Consortium for Small-Scale Modelling

Newsletter

February 2002

No. 2

Deutscher Wetterdienst

MeteoSwiss

Ufficio Generale per la Meteorologia

Hellenic National Meteorological Service

Amt für Wehrgeophysik

Il Servicio Meteorologico Regionale di ARPA

www.cosmo-model.org

Editors: G. Doms and U. Schättler, Deutscher Wetterdienst, P.O. Box 100465, 63004 Offenbach, Germany
Printed at Deutscher Wetterdienst, Offenbach am Main

Table of Contents

1 Introduction

This is the second Newsletter of the Consortium for Small-Scale Modelling (COSMO). It is planned to prepare the Newsletter once a year in January/February, with the opportunity to add special issues at irregular intervals if required.

The basic purpose of the Newsletter is threefold:

- to review the present state of the model system and its operational application and to give information on recent changes;
- to present the principal events concerning COSMO during the last year and to summarize recent research and development work as well as results from the model verification and diagnostic evaluation;
- to provide the meteorological community and especially all external users of the model system with information on COSMO's activities and with new information on the model system and its current forecast quality.

The present Newsletter is organized as follows. Section 2 gives a general overview of the current organizational structure of the COSMO consortium. The present state of the model system, i.e. the LM-package, is summarized in Section 3, including a short description of the model and its data assimilation system, information on the preprocessor programs to provide initial and boundary conditions, and finally remarks on postprocessing utilities and hints on the available model documentation.

Operational and pre-operational applications of the LM-package at the COSMO meteorological centres are described in Section 4. Information about the recent changes to the model system as well as changes in the model set-up at the meteorological centres are outlined in Section 5. Section 6 gives you an overview of the six COSMO Working Groups and their recent research and development activities.

Section 7 provides short information on the main COSMO meetings and events during the last year. Other activities such as internal visits and guest scientist programs are also included. Finally, some forthcoming events planned for this year are announced.

Recent results from the verification of the operational models, both for surface parameters and for vertical profiles, are summarized in Section 8. At the end of this Section, the experiences related to the general model performance and conclusion about model deficiencies are summarized.

Section 9 is devoted to reports on various research topics related to model development and application, including data assimilation, numerics, physics, verification and interpretation. Finally, all COSMO activities related to the LM-system within international and national projects of the member meteorological services are listed in Section 10. This list will be updated in the forthcoming issues.

The Appendices concern the use of the GRIB binary data format for the output and input analyses and forecast fields. These lists will also be updated, and we hope they will be helpful, especially for new users of the LM and its forecast products.

Information about COSMO and the LM can also be obtained from our web-site *www.cosmo-model.org*, which is kindly hosted by HNMS. Many thanks to Theodore Andreadis from HNMS for running, updating and supervising the web-site.

The present organization of the Newsletter is still a first guess. Please contact the editors for any comments and suggestions as well as proposals for items to be included or excluded in the next issue. The editors recognize that typographical and other errors or inconsistencies may be present. We apologize for this, and your assistance in correcting them will be welcome.

We would also like to encourage all the scientists in the COSMO Working Groups to document their work, e.g. in form of a short progress summary or a longer report, to be included in the next Newsletter. Special thanks to all who provided contributions and graphical material for the present issue:

Marco Arpagaus (MeteoSwiss)
Michael Baldauf (Univ. Karlsruhe)
Heinz-Werner Bitzer (AWGeophys)
Carlo Cacciamani (ARPA-SMR)
Ulrich Damrath (DWD)
Pierre Eckert (MeteoSwiss)
Patrizio Emiliani (UGM)
Massimo Ferri (UGM)
George Galanis (HNMS)
Almut Gassmann (DWD)
Frederico Grazzini (ARPA-SMR)
Thomas Hanisch (DWD)
Erdmann Heise (DWD)
Daniel Leuenberger (MeteoSwiss)
Maria Malafouri (HNMS)
Chiara Marsigli (ARPA-SMR)
Enrico Minguzzi (CSI, Torino)
Dmitrii Mironov (DWD)
Andrea Montani (ARPA-SMR)
Fabrizio Nerozzi (ARPA-SMR)
Tiziana Paccagnella (ARPA-SMR)
Ulrich Pflüger (DWD)
Matthias Raschendorfer (DWD)
Thorsten Reinhard (AWI Bremerhaven)
Andrea Rossa (MeteoSwiss)
Christoph Schraff (DWD)
Reinhold Schrodin (DWD)
Jürgen Steppeler (DWD)
Francis Schubiger (MeteoSwiss)
Susanne Theis (Univ. Bonn)
Maria Tomassini (DWD)
Eleftheria Tsiniara (HNMS)
Ulrike Wacker (AWI Bremerhaven)
Emanuele Zala (MeteoSwiss)

To run a complex NWP system at a COSMO meteorological centre requires the continuous effort of many people. Thanks to all of them, especially to those implementing new model versions, maintaining the operations, and organizing the data transfer between the centres:

- Michael Gertz and Thomas Hanisch at DWD,
- Jean-Marie Bettems and Emanuele Zala at MeteoSwiss,
- Theodore Andreadis and George Galanis at HNMS and
- Davide Cesari and Paolo Patruno at ARPA-SMR.

Finally, thanks to all who supported us concerning technical problems during the editorial work. For any comments, suggestions and questions please contact the editors:

Günther Doms
guenther.doms@dwd.de

Ulrich Schättler
ulrich.schaettler@dwd.de

2 Organizational Structure of COSMO

2.1 General

The ***Consortium for Small-Scale Modelling*** (COSMO) was formed in October 1998 at the regular annual DWD/MeteoSwiss meeting. At present, the following national, regional and military meteorological services are participating:

HNMS	Hellenic National Meteorological Service, Athens, Greece
DWD	Deutscher Wetterdienst, Offenbach, Germany
MeteoSwiss	MeteoSchweiz, Zürich, Switzerland
UGM	Ufficio Generale per la Meteorologia, Roma, Italy
ARPA-SMR	Il Servizio Meteorologico Regionale di ARPA, Bologna, Italy
AWGeophys	Amt für Wehrgeophysik, Traben-Trarbach, Germany

The general goal of COSMO is to develop, improve and maintain a non-hydrostatic limited-area modelling system to be used both for operational and for research applications by the members of COSMO. The emphasis is on high-resolution numerical weather prediction by small-scale modelling. COSMO is initially based on the "Lokal-Modell" (LM) of DWD with its corresponding data assimilation system.

A Memorandum of Understanding (MoU) on the scientific collaboration in the field of non-hydrostatic modelling was signed by the Directors of MeteoSwiss, UGM, HNMS and DWD in March/April 1999. Meanwhile, the MoU has been replaced by an Agreement between the four National Meteorological Services.

Figure 1: The Directors of the four COSMO National Meteorological Services signing the COSMO Agreement in Vienna on 3 October 2001. From left to right: U. Gärtner (President of DWD), C. Gkagkaoudaki (Deputy Director of HNMS), R. Sorani (Director of UGM), and D. Keuerleber-Burk (Director of MeteoSwiss).

2.2 Agreement

The structure of the cooperation and both internal and external relationships of COSMO are defined and further detailed in an Agreement between the National Meteorological Services of the participating countries (i.e. DWD, HNMS, MeteoSwiss and UGM). The final version of the COSMO Agreement has been signed by the representatives of the National Meteorological Services on 3 October 2001 (see Figure 1).

There is no direct financial funding from or to either member. However, the partners have the responsibility to contribute actively to the model development by providing staff resources, by making use of research cooperations and by seeking for national funding whenever possible. A minimum of 2 scientists working in COSMO research and development areas is required from each member. In general, the group is open for collaboration with other NWP groups, research institutes and universities as well as for new members. For more details on the Agreement, please contact the Chairman of the Steering Committee, Massimo Capaldo (massimo.capaldo@iol.it).

2.3 Organizational Structure

COSMO's organization, as sketched in Fig. 2, consists of a Steering Sommittee (composed of one representative from each National Meteorological Service), a Scientific Project Manager, Work-package Coordinators and Scientists from the member institutes performing research and development activities in the COSMO working groups. At present, six working groups covering the following areas are active: Data assimilation, numerical aspects, physical aspects, interpretation and applications, verification and case studies, reference version and implementation.

COSMO's activities are developed through extensive and continuous contacts among scientists, work-package coordinators, scientific project manager and steering committee members via electronic mail, special meetings and internal workshops. Once a year there is a General Meeting of the COSMO group in order to present results, deliverables and progress reports of the working groups and to elaborate a research plan with new projects for the next annual period. Following this meeting, a final work plan for each working group is set up. The recent COSMO General Meeting was held on 3-5 October 2001 in Athens.

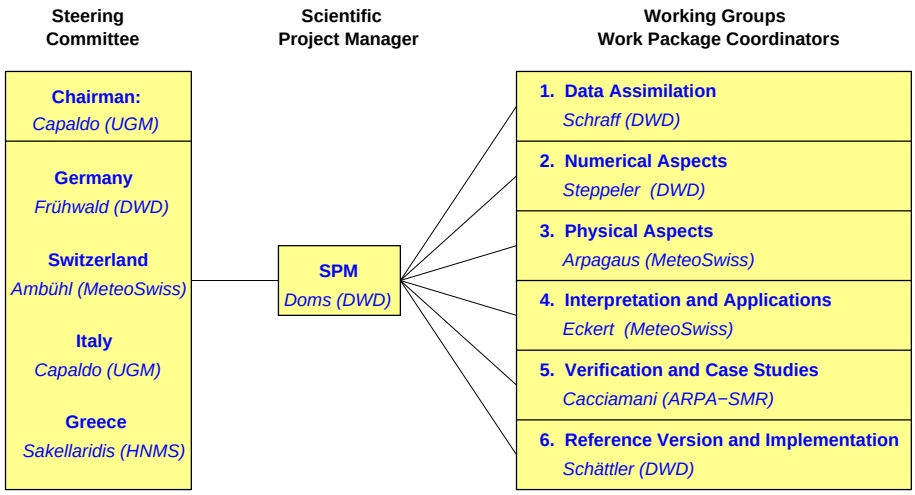

Figure 2: *Organizational structure of COSMO*

3 Model System Overview

The limited-area model LM is designed as a flexible tool for numerical weather prediction on the meso-β and on the meso-γ scale as well as for various scientific applications using grid spacings from 50 km down to about 50 m. Besides the forecast model itself, a number of additional components such as data assimilation, interpolation of boundary conditions from a driving host model and postprocessing is required to run a NWP-system at a meteorological service. In the following sections, the components of the LM-package - as available to the COSMO group - are shortly described.

3.1 Short Description of the LM

This section gives only a brief overview of the Lokal-Modell. For a comprehensive description, the reader is referred to the documentation of the LM package (see section 3.6).

3.1.1 Dynamics and Numerics

The regional model LM is based on the primitive hydro-thermodynamical equations describing compressible nonhydrostatic flow in a moist atmosphere without any scale approximations. A basic state is subtracted from the equations to reduce numerical errors associated with the calculation of the pressure gradient force in case of sloping coordinate surfaces. The basic state represents a time-independent dry atmosphere at rest which is prescribed to be horizontally homogeneous, vertically stratified and in hydrostatic balance. The basic equations are written in advection form and the continuity equation is replaced by a prognostic equation for the perturbation pressure, i.e. the deviation of pressure from the reference state.

The model equations are formulated with respect to a rotated lat/lon-grid with coordinates (λ, φ). The rotated coordinate system results from the geographical (λ_g, φ_g) coordinates by tilting the north pole. In the vertical, we use a generalized terrain-following height coordinate ζ, where any unique function of geometrical height can be used for transformation. Since ζ doesn't depend on time, the $(\lambda, \varphi, \zeta)$-system represents a non-deformable coordinate system, where surfaces of constant ζ are fixed in space - in contrast to the pressure based coordinate system of most hydrostatic models, where the surfaces of constant vertical coordinate move in space with changing surface pressure. By default, a hybrid sigma-type (formulated with respect to the base-state pressure) vertical coordinate is used.

The model equations are solved numerically using the traditional Eulerian finite difference method. In this technique, spatial differential operators are simply replaced by suitable finite difference operators and the time integration is by discrete stepping using a fixed timestep Δt. The model variables are staggered on an Arakawa-C/Lorenz grid with scalars (temperature, pressure and humidity variables) defined at the centre of a grid box and the normal velocity components defined on the corresponding box faces. For a given grid spacing, this staggering allows for a more accurate representation of differential operators than in the A-grid, where all variables are defined at the same point. In general, we use second order centered finite difference operators for horizontal and vertical differencing.

Because the governing nonhydrostatic equations describe a compressible model atmosphere, meteorologically unimportant sound waves are also part of the solution. As acoustic waves are very fast, their presence severely limits the time step of explicit time integration schemes. In order to improve the numerical efficiency, the prognostic equations are separated into terms which are directly related to acoustic and gravity wave modes and into terms which refer to

Table 1: ***LM Model Formulation: Dynamics and Numerics***

Model Equations:	Basic hydro-thermodynamical equations for the atmosphere: - advection form, - non-hydrostatic, fully compressible, no scale approximations, - subtraction of horizontally homogeneous basic state at rest.
Prognostic Variables:	Horizontal and vertical Cartesian wind components, temperature, pressure perturbation, specific humidity, cloud water content; optionally: cloud ice, turbulent kinetic energy.
Diagnostic Variables:	Total air density, precipitation fluxes of rain and snow.
Coordinate System:	Rotated geographical (lat/lon) coordinate system horizontally; generalized terrain-following height-coordinate vertically.
Grid structure:	Arakawa C-grid, Lorenz vertical grid staggering.
Spatial discretization:	Second order horizontal and vertical differencing.
Time integration:	Leapfrog HE-VI (horizontally explicit, vertically implicit) time-split integration scheme by default; includes extensions proposed by Skamarock and Klemp (1992). Additional options for: - a two time-level 2nd order Runge-Kutta split-explicit scheme (Wicker and Skamarock (1998)), - a three time-level 3-d semi-implicit scheme (Thomas et al., 2000).
Numerical Smoothing:	4th order linear horizontal diffusion with option for a monotonic version including an orographic limiter; Rayleigh-damping in upper layers; 3-d divergence damping and off-centering in split steps.
Lateral Boundaries:	1-way nesting using the lateral boundary formulation according to Davies (1976). Option for periodic boundary conditions.

comparatively slowly varying modes of motion. This mode-splitting can formally be written in the symbolic form

$$\frac{\partial \psi}{\partial t} = s_\psi + f_\psi \,, \tag{1}$$

where ψ denotes a prognostic model variable, s_ψ the forcing terms due to the slow modes and f_ψ the source terms related to the fast acoustic and gravity wave modes. f_ψ is made up of the pressure gradient terms in the momentum equations, the temperature and pressure contributions to the buoyancy term in the equation for the vertical velocity, and the divergence term in the pressure and the temperature equation. The subset of equations containing the f_ψ-terms is then integrated with a special numerical scheme.

The default time integration method used in LM is a variant of the Klemp and Wilhelmson (1978) scheme including extensions proposed by Skamarock and Klemp (1992). It is based on a Leapfrog integration for the slow modes from time level $n-1$ to time level $n+1$ using an integration interval of $2\Delta t$. The slow mode tendencies are evaluated at time level n for horizontal advection and at time level $n-1$ for most physical forcings. Tendencies from vertical advection and diffusion are calculated by a quasi-implicit scheme. The integration step is then subdivided into a number N_s of small time steps $\Delta\tau_s$ according to $2\Delta t = N_s \Delta\tau$

and the prognostic equations (1) are stepped forward according to

$$\psi^{\nu+1} = \psi^{\nu} + f_{\psi}^{\nu}\Delta\tau + s_{\psi}^{n}\Delta\tau\,. \tag{2}$$

In the integration of (2), sound waves are treated explicitly for horizontal directions using the forward-backward method while implicitly for the vertical direction (HE-VI scheme). Thus, the small time step $\Delta\tau$ is limited by the CFL stability criterion for horizontal but not for vertical sound wave propagation. This makes the HE-VI scheme numerically very efficient for large grid aspect ratios, i.e. $\Delta x/\Delta z >> 1$, which are typically used in meso-β and meso-γ applications. An additional 3-D divergence damping as well a slight time off-centering in the vertical implicit formulation is applied to damp acoustic modes. On the big time step, the Asselin time filter and a 4th-order horizontal diffusion are used for numerical smoothing.

Two alternative time integration schemes have also been implemented for optional use: a two time-level second-order Runge Kutta method based on the work of Wicker and Skamarock (1998), and a three-timelevel Leapfrog-based Eulerian 3-D semi-implicit scheme according to Thomas et al. (2000). These schemes lead to rather similar results in test cases, but have not yet reached operational efficiency. Table 1 summarizes the dynamical and numerical key features of the LM.

3.1.2 Initial and Boundary Conditions

For operational applications and real data simulations, LM is driven by the new global model GME of DWD using the traditional boundary relaxation technique (see Section 3.3). Information on the GME as well as on recent changes to the global model are summarized in the *Quarterly Report of the Operational NWP-Models of the Deutscher Wetterdienst.* This report series is available online at the DWD web-site (*www.dwd.de*).

A four-dimensional data assimilation cycle based on a nudging analysis scheme (see Section 3.2) can be installed for operational NWP with the LM at COSMO meteorological services. In this case, the initial conditions come from the continuous LM assimilation stream and only boundary data have to be provided by GME forecasts. However, an operational NWP-system can also be set-up without a data assimilation cycle by relying on pure dynamical adaption of large-scale initial fields. In this case, the initial conditions come from interpolated (and initialized) GME analyses. To reduce noise generation and spin-up effects resulting from non-balanced interpolated data, a diabatic digital filtering initialization (DFI) scheme (Lynch et al., 1997) has been implemented. By default, the DFI initialization consists of a 1-h adiabatic backward integration followed by a 1-h diabatic forward integration of the model.

For various research applications as well as for model testing and evaluation, the LM provides a capability to handle idealized cases using user-defined artificial initial and boundary data. For these types of application, periodic lateral boundary conditions can be specified optionally. Additionally, a 2-dimensional model configuration can be used.

3.1.3 Parameterization of Physical Processes

A variety of subgrid-scale physical processes is taken into account by parameterization schemes. A large part of the present physics package of LM has been adapted from the former operational hydrostatic models EM/DM. Current activities of the COSMO physics group concentrate on an upgrade of the physics routines for the operational application. The new physics package will be made up of a new vertical diffusion and surface layer scheme

based on prognostic turbulent kinetic energy, a new grid-scale cloud and precipitation scheme including cloud ice, a new multi-layer soil model, and the Kain-Fritsch scheme for deep moist convection.

Table 2 gives a short overview on the parameterization schemes used by default and on additional options implemented so far.

Table 2: ***LM Model Formulation: Physical Parameterizations***

Grid-scale clouds and precipitation:	Cloud water condensation/evaporation by saturation adjustment; precipitation formation by a bulk parameterization including water vapour, cloud water, rain and snow (scheme HYDOR); rain and snow are treated diagnostically by assuming column equilibrium. Optional: cloud ice scheme.
Subgrid-scale clouds:	Subgrid-scale cloudiness is interpreted by an empirical function depending on relative humidity and height. A corresponding cloud water content is also interpreted.
Moist convection:	Mass-flux convection scheme (Tiedtke, 1989) with closure based on moisture convergence. optional: modified closure based on CAPE.
Radiation:	δ-two stream radiation scheme after Ritter and Geleyn (1992) for short and longwave fluxes; full cloud-radiation feedback.
Vertical diffusion:	Diagnostic K-closure at hierarchy level 2. Optional: a new level 2.5 scheme with prognostic treatment of turbulent kinetic energy; effects of subgrid-scale condensation and evaporation are included. Also, the impact from subgrid-scale thermal circulations is taken into account.
Surface layer:	Constant flux layer parameterization based on the Louis (1979) scheme. Optional: a new surface scheme including a laminar-turbulent roughness layer
Soil processes:	Soil model after Jacobsen and Heise (1982) with 2 soil moisture layers and Penman-Monteith transpiration; snow and interception storage are included. Climate values changing monthly (but fixed during forecast) in third layer.

3.1.4 External Parameters

The parameterization of physical processes, but also the adiabatic model part requires some parameters which are not derived by data assimilation or by interpolation from a driving model. These so-called external parameters are defined in additional data sets. The LM requires the following external parameters: mean topographical height, roughness length, soil type, vegetation cover, land fraction, root depth and leaf area index. The sources for these data are indicated below.

- Mean orography:
  derived from the GTOPO30 data set (30"x30") from USGS.
- Prevailing soil type:
  derived from the DSM data set (5'x5') of FAO.

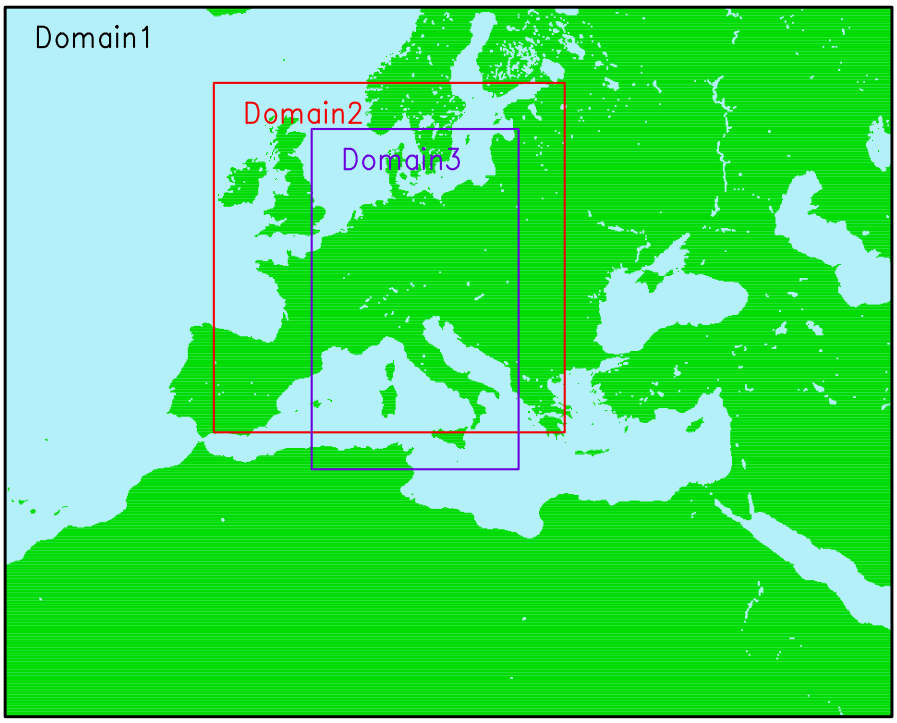

Figure 3: Domains of external parameter datasets used by COSMO partners

- Land fraction, vegetation cover, root depth and leaf area index:
  derived from the CORINE data set of ETC/LC.
- Roughness length:
  derived from the GTOPO30 and CORINE datasets.

External parameters for LM can be derived by a preprocessor program for any domain on the globe at any required spatial resolution. However, this is very time consuming because of the size of the high-resolution global data sets. Within the COSMO group, we thus have prepared some predefined data sets with external parameters on three different domains (see Fig. 3).

Domain 1 covers Europe and surrounding countries; data sets for this domain are available at 28 km, 21 km, 14 km and 7 km grid spacing. The smaller Domain 2 covers Germany and surrounding countries; the corresponding data set gives the external parameters at 7 km resolution. Domain 2 is only used at DWD. Finally, Domain 3 covers central and southern parts of Europe. For this domain, the external parameters are given at 2.8 km resolution. The LM can then be very easily positioned anywhere within these domains.

Details on the location of the three domains are shown in Table 3, where longitude (λ) and latitude (ϕ) of the rotated coordinates and those of the geographical lat-lon grid (λ_g, ϕ_g) are given in degree. The resolution and the corresponding file names (these are required for the interpolation programs to generate initial and boundary data from a host model) are indicated in Table 4. The specifications refer to a rotated lat-lon grid of LM with the north-pole at geographical latitude 32.5° (N) and longitude -170.0° (W).

Table 3: Location of Domains in rotated and in geographical coordinates

Name	Domain corners	λ	ϕ	λ_g	ϕ_g
Domain 1	upper left	- 26.75	9.25	- 42.74	56.07
	upper right	33.25	9.25	70.36	51.49
	lower left	- 26.75	- 38.75	- 11.26	14.54
	lower right:	33.25	- 38.75	35.96	12.34
Domain 2	upper left	- 12.625	4.125	- 15.25	59.26
	upper right	11.125	4.125	32.48	59.77
	lower left	- 12.625	-19.50	- 4.87	36.62
	lower right:	11.125	-19.50	23.15	36.92
Domain 3	upper left	- 6.00	1.00	- 1.37	58.00
	upper right	8.00	1.00	25.06	57.61
	lower left	- 6.00	-22.00	3.19	35.20
	lower right:	8.00	-22.00	19.06	34.97

Table 4: Grid spacing $\Delta\lambda$ (= $\Delta\phi$) in degrees, approximate resolution Δs in m, number of gridpoints and file name of the datasets for the domains

Name	$\Delta\lambda, \Delta\phi$ (°)	Δs (m)	no. of grid points	Filename
Domain 1	0.2500	28000	241 x 193	lm_d1_28000_241x193.g1
	0.1875	21000	321 x 257	lm_d1_21000_321x257.g1
	0.1250	14000	481 x 385	lm_d1_14000_481x385.g1
	0.0625	07000	961 x 769	lm_d1_07000_961x769.g1
Domain 2	0.0625	07000	381 x 379	lm_d2_07000_381x379.g1
Domain 3	0.0250	02800	561 x 921	lm_d3_02800_561x921.g1

3.1.5 Coding and Parallelization

To meet the computational requirement of the model, the program has been coded in Standard Fortran 90 and parallelized using the MPI library for message passing on distributed memory machines. Thus it is portable and can run on any parallel machine providing MPI. Also it can still be executed on conventional scalar and vector computers where MPI is not available.

The parallelization strategy is the two dimensional domain decomposition which is well suited for grid point models using finite differences (see Fig. 4). Each processor gets an appropriate part of the data to solve the model equations on its own subdomain. This subdomain is surrounded by halo grid-lines which belong to the neighboring processors. At present, we use 2 grid-lines for the halo. However, as the number of halo grid-lines is soft-coded, this can be easily changed whenever necessary (e.g., in case of high order advection schemes). During the integration step each processor updates the values of its local subdomain; grid points belonging to the halo are exchanged using explicit message passing. The number of

processors in longitudinal and latitudinal direction can be specified by the user to fit optimal to the hardware architecture.

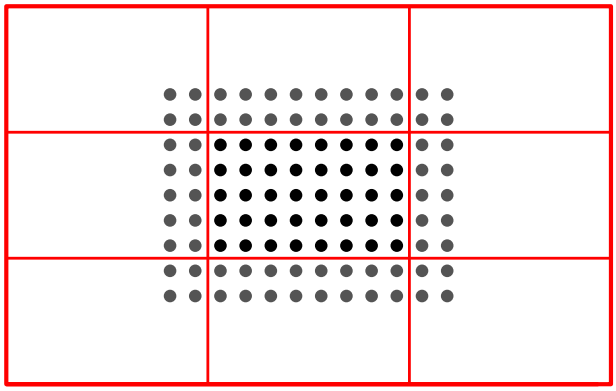

Figure 4: 2-D domain decomposition with a 2 gridline halo

Figure 5 shows timings for one hour of forecast from full-physics test runs with different domain sizes on a Cray T3E. The parallel speedup is illustrated on the log-log-scale, showing that the model scales well to hundreds of processors for appropriate domain sizes.

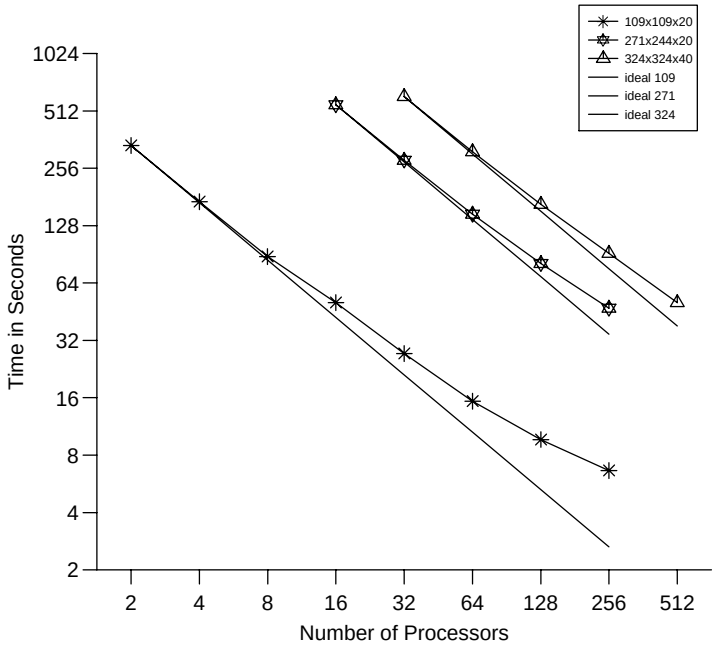

Figure 5: Timings for different model sizes; the straight lines show perfect scalability

3.2 Data Assimilation

The requirements for the data assimilation system for the operational LM are mainly determined by the very high resolution of the model and by the task to employ it also for nowcasting purposes in the future. Hence, detailed high-resolution analyses have to be able to be produced frequently, and this requires a thorough use of asynoptic and high-frequency observations such as aircraft data and remote sensing data. Note that the synoptic scales are largely determined by the lateral boundary conditions provided by the steering model, and the main purpose of the assimilation scheme is to analyze the meso scales.

By design, 3-dimensional analysis methods tend to be less appropriate for this purpose. They do not allow to account for the exact observation time of asynoptic data, and they make it necessary to neglect most of the high-frequent data unless the analysis scheme is applied very frequently at significant computational costs. Moreover, the geostrophic approximation, usually a key ingredient of such schemes, is of limited validity in the meso scale. Therefore, 4-dimensional methods offer potential advantages since they include the model dynamics in the assimilation process directly. Yet, the 4-dimensional variational (4DVAR) method is too expensive for operational application of the LM considering the small amount of time available to produce the analyses and forecasts.

As a result, a scheme based on the observation nudging technique has been developed to define the atmospheric fields. It is based on an experimental nudging analysis scheme which had been developed for DM and the Swiss model version SM (Schraff, 1996; 1997) and which compared favorably with the operational OI-analysis of the DM in various case studies. The new LM-scheme, however, has been adapted to the nonhydrostatic modelling framework and runs on distributed memory machines using domain decomposition. To compute the analysis increments locally for the grid points of each sub-domain, the observational information of the total domain is previously distributed to the sub-domains.

For some of the surface and soil fields, a set of 2-dimensional intermittent analysis schemes is applied in addition. This comprises of the snow analysis, the sea surface temperature (SST) analysis, and the variational soil moisture analysis scheme.

3.2.1 Nudging-Based Assimilation Scheme

Nudging or Newtonian relaxation consists of relaxing the model's prognostic variables towards prescribed values within a predetermined time window (see e.g. Davies and Turner (1977), Stauffer and Seaman (1990)). In the present scheme, nudging is performed towards direct observations which is more appropriate for high-resolution applications than nudging towards 3-dimensional analyses (Stauffer and Seaman, 1994). A relaxation term is introduced into the model equations, and the tendency for the prognostic variable $\psi(\mathbf{x}, t)$ is given by

$$\frac{\partial}{\partial t}\psi(\mathbf{x}, t) \quad = \quad F(\boldsymbol{\psi}, \mathbf{x}, t) \quad + \quad G_\psi \cdot \sum_{k_{(obs)}} W_k \cdot [\psi_k - \psi(\mathbf{x}_k, t)] \tag{3}$$

F denotes the model dynamics and physical parameterizations, ψ_k the value of the k^{th} observation influencing the grid point $\mathbf{x}$ at time t, $\mathbf{x}_k$ the observation location, G_ψ the constant so-called nudging coefficient (currently set to $6 \cdot 10^{-4} s^{-1}$ for all assimilated quantities), and W_k an observation-dependent weight which usually varies between 0 and 1. Neglecting the dynamics and physics and assuming a single observation with a constant weight W_k equal 1, the model value at the observation location relaxes exponentially towards the observed value with an e-folding decay rate of $1/G_\psi$ corresponding to about half an hour.

In practical applications, the nudging term usually remains smaller than the largest term of the dynamics so that the dynamic balance of the model is not strongly disturbed. The coupling between the mass and wind field innovations is primarily induced implicitly by the model dynamics. If the assimilation process is successful the model fields will be close to dynamic balance at the beginning of the forecast, and an initialization step is not required.

The factors W_k determine the relative weights given to the different observations at a specific grid point. For a single observation, this weight (w_k) comprises of the quality (and representiveness) of the observation (ϵ_k) and of weights which depend on the horizontal (w_{xy}) or vertical (w_z) distance respectively temporal (w_t) difference between the observation and the target grid point. If an increasing number of observations influence the grid point the total nudging weight should be limited to avoid the nudging term to become dominant over the dynamics. This is achieved by complementing the individual weight w_t by a relative weight (Benjamin and Seaman, 1985):

$$W_k = \frac{w_k}{\sum_j w_j} \cdot w_k \tag{4}$$

$$w_k = w_t \cdot w_{xy} \cdot w_z \cdot \epsilon_k \tag{5}$$

Currently, only conventional observations are used, namely from TEMP and PILOT (temperature and wind, including the significant levels; humidity up to 300 hPa; geopotential only to derive one pressure increment at the lowest model level), AIRCRAFT (all data), and SYNOP, SHIP and DRIBU reports (station pressure; wind for stations below 100 m above msl; humidity; 2-m temperature is used only for the soil moisture analysis). Note that given a cut-off time of 2.5 hours, observations from up to about 2 hours after the actual analysis time can still be assimilated in the first hours of the operational forecast runs. As a quality control, the observed values are compared with the model fields of the assimilating run itself. For multi-level temperature data, a hydrostatic height and thickness check is included, and a spatial consistency check is performed for the station pressure data.

Equation (3) indicates that in principle the scheme consists of two main steps, i.e. the determination of the observation increments and the computation of the weights. With respect to the vertical interpolation required for the first step, the vertical scale of multi-level temperature and wind observations is adjusted to the vertical model resolution by averaging the observed profile over the thickness of model layers. As a result, the simulated thickness between two pressure levels is automatically relaxed towards the observed thickness when nudging temperature data. In contrast, humidity data are interpolated without averaging in order to capture thin layers of clouds as well as possible. Note that the increments are determined as differences in relative humidity which implies that relative rather than specific humidity is relaxed towards the observed humidity. In this sense, the analyzed quantities are horizontal wind, potential temperature, relative humidity, and pressure at the lowest model level.

Related to the second step, incomplete profiles and single-level increments are vertically extended and provided with vertical weights w_z according to a Gaussian (approx.) in log pressure (correlation scale is $1/\sqrt{3}$ for upper-air wind and 0.2 for upper-air temperature and humidity, and the cut-off is 850 m for surface-level wind resp. the lowest model layer for surface-level humidity). Thereafter, upper-air increments are spread laterally along horizontal surfaces since spreading along the terrain-following model levels as usually applied in nudging-type schemes has disadvantages near steep orography particularly in cases with low stratus (Schraff, 1997). In contrast, surface-level increments are spread along the model levels to limit the area of influence to close to the ground. The spreading includes the computation of the horizontal weights w_{xy} using the function $(1 + \Delta r/s) \cdot e^{-\Delta r/s}$ for the scalar

quantities (Δr being the horizontal distance between observation and target grid point). The wind correlations are split into a longitudinal and transverse part, and this allows to specify the degree of divergence (γ) of the resulting wind analysis increment field (Lorenc et al., 1991). Both the correlation scales s and the non-divergence factor γ increase with height and with distance to the observation time and vary between about 60 km and 160 km resp. 0.4 and 0.7 . The function used for the temporal weights w_t is 1 at the observation time and decreases linearly to zero at 3 hours (for radiosonde data) resp. 1.5 hours (for other data) before and 1 resp. 0.5 hours after the observation time. Hourly or more frequent data are linearly interpolated in time.

Table 5: ***Data Assimilation for LM***

Method	Nudging towards observations
Implementation	continuous cycle of 3-hour assimilation runs
Realization	identical analysis increments used during 6 advection time steps
Balance	1. hydrostatic temperature increments (up to 400 hPa) balancing 'near-surface' pressure analysis increments 2. geostrophic wind increments balancing 'near-surface' pressure analysis increments 3. upper-air pressure increments balancing total analysis increments hydrostatically
Nudging coefficient	$6 \cdot 10^{-4} s^{-1}$ for all analyzed variables
Analyzed variables	horizontal wind vector, potential temperature,relative humidity 'near-surface' pressure (i.e. at the lowest model level)
Spatial analysis	Data are analyzed vertically first, and then spread laterally along horizontal surfaces. vertical weighting: approximately Gaussian in log(p) horizontal weighting: isotropic as function of distance
Temporal weighting	1.0 at observation time, decreasing linearly to 0.0 at 3 hours (upper air) resp. 1.5 hours (surface-level data) before and 1.0 resp. 0.5 hours after observation time; linear temporal interpolation of frequent data.
Observations	SYNOP, SHIP, DRIBU: - station pressure, wind (stations below 100 m above msl) - humidity TEMP, PILOT: - wind, temperature: all standard levels, significant levels up to 150 hPa - humidity: all levels up to 300 hPa - geopotential used for one 'near-surface' pressure increment AIRCRAFT: - all wind and temperature data
Quality control	Comparison with the model fields from assimilation run itself

In the current scheme, the resulting analysis increment fields are partly balanced explicitly in a third major step before being added to the model fields. Three types of balancing are applied. First, a hydrostatic upper-air temperature correction balances the pressure analysis increments at the lowest model layer. It is nearly constant within the lowest 1500 m (therefore hardly modifies the stability within the boundary layer) and decreases rapidly further above

such that the geopotential above 400 hPa is not directly modified by the surface pressure nudging (for hydrostatic conditions). This significantly reduces the vertical extent of the mass field disturbance imposed by the pressure nudging and results in a better adjustment of the wind field and a greatly improved assimilation of the pressure data. Secondly, a geostrophic wind correction partly balances the wind field with respect to the mass field increments imposed by the surface pressure nudging including the temperature correction. Finally, an upper-air pressure correction balances the total analysis increments of the mass field hydrostatically. This is the only feature directly related to the fact that the model is non-hydrostatic. Note that it does not change the non-hydrostatic properties of the full model fields. The correction prevents the introduction of direct sources of vertical wind for which there is no direct control without vertical wind observations being available to be assimilated. This is important since the vertical velocity is still small on the scales to be analyzed with the current scheme and observations (in contrast e.g. to a latent heat nudging scheme). Table 5 summarizes the main features of the LM nudging scheme.

3.2.2 Sea Surface Temperature Analysis

Since the latent and sensible heat fluxes over water depend crucially on the surface temperature, a sea surface temperature (SST) analysis is performed once per day (00 UTC). Starting from the previous analysis as first guess, all the ship and buoy observations from the previous 6 days are used in a correction scheme based on Cressman-type weighting. In data-poor areas, this is blended (via the global SST analysis) with a daily 1° x 1° SST analysis from NCEP which also incorporates satellite data. For the sea-ice cover in the Baltic Sea, an external analysis (from the Bundesamt fuer Seeschiffahrt und Hydrologie) is used.

3.2.3 Snow Depth Analysis

The occurrence of a snow cover strongly influences the radiative absorption and reflection properties of the land surface and therefore the screen-level temperature. The snow water content is a prognostic quantity of the model, and is analyzed once every 6 hours. The method is based on a simple weighted averaging of SYNOP snow depth observations. The weighting depends both on the horizontal and vertical distances to the target grid points. In areas, where the density of these data is not sufficient, an average of snow depth increments derived from SYNOP precipitation, temperature, and weather reports as well as the model prediction are also included.

3.2.4 Soil Moisture Analysis

In land areas without snow, screen-level temperature (and humidity) is significantly influenced by the soil water content on clear-sky days. An inadequate specification of soil moisture can lead to forecast temperature errors of several degrees. The variational analysis scheme (Hess, 2001) derives improved moisture contents once per day by minimizing a cost functional J which depends on the deviations of the forecast temperature $T(\eta)$ from the observed (resp. analyzed) temperature T^o and of the soil moisture η from a given background state η^b:

$$J(\eta) = \frac{1}{2}\Big(T^o - T(\eta)\Big)^T \mathbf{R}^{-1}\Big(T^o - T(\eta)\Big) + \frac{1}{2}\Big(\eta - \eta^b\Big)^T \mathbf{B}^{-1}\Big(\eta - \eta^b\Big) \qquad (6)$$

The observation error covariance $\mathbf{R}$ and background error covariance $\mathbf{B}$ reflect the trust in the observations resp. the background. To solve the minimization problem, two assumptions are made. Firstly, since the 2-m temperature mainly depends on the soil moisture at the same location, the problem can be decoupled horizontally, and a low-dimensional (equal to the number of analyzed soil layers) minimization can be performed for each grid point individually. Secondly, (moderate) changes of soil moisture are assumed to lead to linear changes in temperature. This allows to derive the linear relationships $\mathbf{\Gamma}$ by means of one additional forecast run per analyzed soil layer where each of these forecasts has slightly different values for the initial soil moisture. The minimum of J can then be found by solving $\nabla J(\eta) = 0$ directly without using the adjoint method.

In the current implementation, two additional 15-hour forecasts are required to analyze two (sets of) soil layers for 0 UTC of the previous day by comparing forecast and observed temperature at 12 and 15 UTC. The analysis increments are then added to the soil moisture of the 0 UTC nudging analysis of the current day. The resulting soil moisture is used both as initial state for the operational LM forecast of the current day and as background state for the next soil moisture analysis. This background state η^b is important in order to reduce the daily variation of the soil moisture contents and to stabilize the minimization in cases of weak soil-atmosphere coupling (i.e. cloudy situations). Together with η^b (see above), the background error covariance $\mathbf{B}$ for the following day is provided in a Kalman-filter cycled analysis:

$$(\mathbf{B})^{next} \quad = \quad \mathbf{A} \; + \; \mathbf{Q} \quad , \quad where \;\; \mathbf{A} = (\nabla^2 J)^{-1} = \left(\mathbf{\Gamma}^T \mathbf{R}^{-1} \mathbf{\Gamma} + \mathbf{B}^{-1} \right)^{-1} \tag{7}$$

This takes into account both an increase of confidence in the retrieved soil moisture values due to the utilized screen-level observations (as part of the analysis error covariance $\mathbf{A}$) and a decrease of confidence due to the model error $\mathbf{Q}$ of the soil model. While $\mathbf{A}$ can be computed explicitly, $\mathbf{Q}$ is the main tuning parameter of the scheme. It influences the relative weight given to the past and the present observations and has an impact on the temporal variability of the soil moisture. The scheme has been successfully tested in various case studies and it is operated at DWD since March 2000.

3.3 Boundary Conditions from Driving Models

The LM can be nested in the new global model GME (Majewski, 1998), the former hydrostatic regional models EM or DM of DWD, or the ECMWF global spectral model IFS. The lateral boundary formulation is by the Davies (1976) relaxation technique, where the internal model solution is nudged against an externally specified solution within a narrow boundary zone by adding a relaxation forcing term to the equations.

The external solution is obtained by interpolation from the driving host model at discrete time intervals. The interpolated fields are hydrostatically balanced, i.e. a hydrostatic pressure is prescribed for the nonhydrostatic pressure variable in LM at the lateral boundaries. Within these specified time intervals, the boundary data are interpolated linearly in time (which is done inside the model). Normally the boundary update interval is chosen to be one hour for meso-β scale applications of the LM. The boundary values (and initial values, if no data assimilation suite is operated) are obtained by a preprocessing program from the host model.

- ***GME2LM:***
  interpolation from the new triangular mesh global model GME of DWD.
- ***HM2LM:***
  interpolation from the hydrostatic regional models EM or DM of DWD.
- ***IFS2LM:***
  interpolation from the global spectral model IFS of ECMWF.

A documentation of the GME2LM preprocessor program is available at the COSMO Website. An additional interpolation program LM2LM for one-way self-nesting of LM is in preparation. It is planned to combine all pre-processor routines into a single interpolation program INT2LM.

3.4 Postprocessing

Postprocessing includes all applications that use the direct model output of LM runs. In general, there is a wide range of such applications at each meteorological service, ranging from simple graphical display of weather charts or meteograms for single grid points, or statistical correction of near surface weather elements by Kalman filtering, to more complex derived products supplying information on environment and health, transportation, agriculture and media presentation. Most of these postprocessing tools are very specific to the computer platform, data base system and visualization software of each service and thus cannot be shared within the COSMO group. There is, however, a number of postprocessing programs available within COSMO.

(a) Graphics
Work on two common plotting packages has been completed. The first has been developed at MeteoSwiss and uses Metview with an interface to the GRIB1 LM output data; the other one has been developed at ARPA-SMR and is based on the public domain VIS5D packages; a special routine converts the GRIB1 binary format to the VIS5D data format.

(b) Models
A *Lagrangian Particle Dispersion Model* (LPDM) may be used operationally in case of radioactive accidental releases to predict long-range transport, dispersion, and wet and dry deposition of radioactive material. The calculation of about $10^5 - 10^6$ trajectories of tracer particles is based on wind fields from LM (at hourly intervals) and superimposed turbulent fluctuations (TKE, Monte Carlo method). Radioactive decay and convective mixing are included. The concentration is calculated by counting the particle masses in arbitrary grids.

A *Trajectory Model* may provide guidance on transport routes. The meteorological input is derived from LM at hourly intervals.

An integral part of the NWP-system at DWD is a *Wave Prediction Suite* comprising two models, namely the global model GSM (global sea state model), and a local one (LSM) which covers the Baltic Sea, the North Sea and the Adriatic Sea with a high-resolution mesh. GSM and LSM have been developed by research institute GKSS in Geesthacht (Germany).

(c) Interpretation
An objective weather interpretation scheme (developed at DWD) derives the forecasted 'weather', i.e. the WMO weather code, based on LM output fields. Pressure, temperature, dew point temperature, liquid water content, cloud cover, precipitation and wind speed values are used as input parameters to define the present weather.

3.5 Data Flow of the LM-Package

The various components of the LM Package and the corresponding data flow are illustrated in Figure 6. In case of a set-up without data assimilation (right part of Figure 6), the interpolation programs (GME2LM, IFS2LM or LM2LM) provide initial and boundary conditions for the LM forecast runs (LM-FCT) from the corresponding driving models. This step involves the data set of the external parameters (see Section 3.1.4).

With a system set-up using the LM nudging analysis (left part of Figure 6), the GME2LM provides boundary conditions (LM-BC) from the GME assimilation cycle for the LM runs in nudging analysis mode (LM-NUD) within the assimilation stream. The LM-NUD runs start from a given LM analysis (LM-ANA) to generate an analysis for the next analysis time. The forecasts then start from these LM-ANA initial data using boundary condition from the GME forecast.

To run the LM in nudging mode, a preprocessor program is required which provides the observational data in a special data file format (AOF). The LM analysis file may be modified by incremental analyses of sea surface temperature, snow depth and soil moisture (see Section 3.2). All these programs use GTS and non-GTS obervation data, which are archived in a local data base system. The interface to these data is usually not portable as it depends on the data base system of each meteorological centre.

The LM runs in forecast mode generate direct model output, which includes also fields from the LM internal postprocessing (see Appendix B). These data are then subject to various visualization tools, external postprocessing and other applications such as follow-up models at COSMO Met Services.

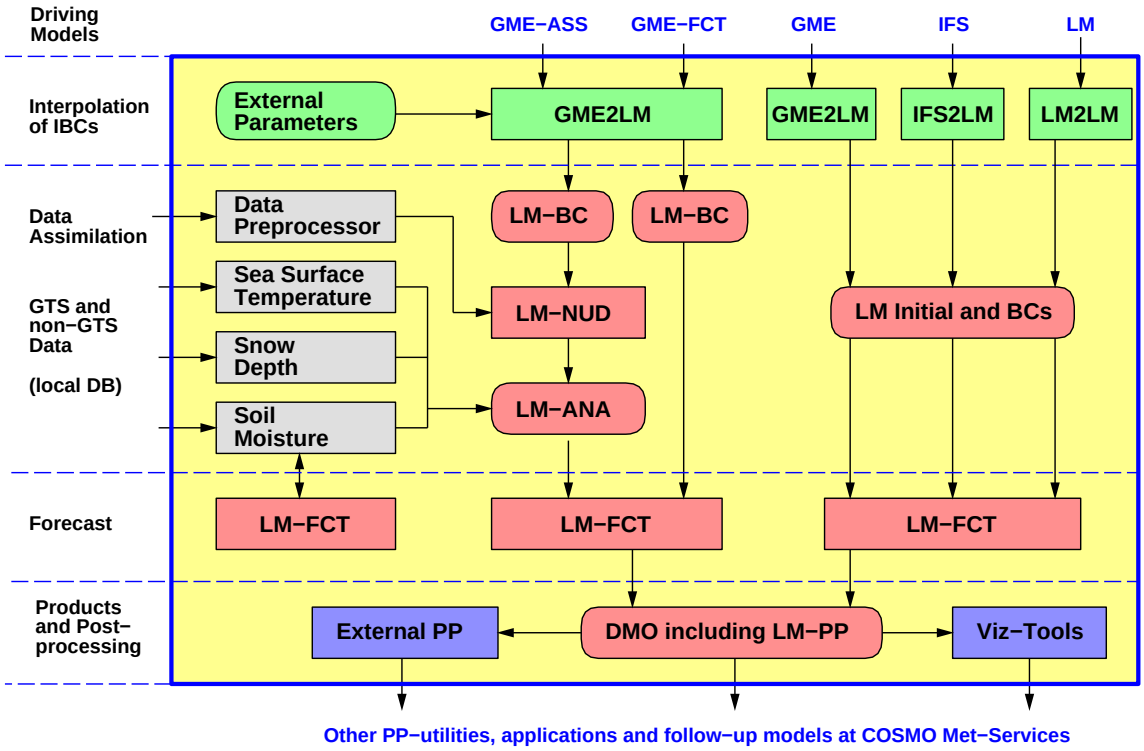

Figure 6: Process and data flowchart of the LM Package for a set-up using data assimilation (left part) and a set-up without data assimilation (right part). Rectangular boxes indicate components of the Package (programs), rounded boxes indicate data files generated by the components.

3.6 Documentation

The following parts of the model system documentation are available at the COSMO website. Unfortunately, these documentation are not up to date. A new release is planned for summer 2002.

(a) The Nonhydrostatic Limited-Area Model LM of DWD

Part I: *Scientific Documentation*
Part II: *Implementation Documentation*
Part III: *User's Guide*
Part X: *Soil Moisture Analysis*

(b) The Interpolation Program GME2LM

4 Operational Applications

The LM is operated in four centres of the COSMO members. Following a 1-year preoperational trial from October 1998 to November 1999, the model became operational at DWD in December 1999. At MeteoSwiss the LM was integrated in a preoperational mode two times a day since July 2000. The model became fully operational in February 2001. In Italy the model runs preoperational twice a day at ARPA-SMR. The HNMS in Greece integrates the LM once a day in parallel to their old operational system. Figure 7 shows the integration domains of the model runs at the COSMO meteorological centres.

All four centres use interpolated boundary conditions from forecasts of the global model GME of DWD. Only a subset of GME data covering the respective LM-domain of a COSMO meteorological centre are transmitted from DWD via the Internet. ARPA-SMR and HNMS start the LM from interpolated GME analyses, followed by an initialization using the digital filtering scheme of Lynch et al. (1997). At DWD, a comprehensive data assimilation system for LM has been installed (see Section 3.2), comprising the LM nudging analysis for atmospheric fields, a sea surface temperature (SST) analysis, a snow depth analysis and the soil moisture analysis according to Hess (2001). Since November 2001, MeteoSwiss also runs a data assimilation system based on the LM nudging scheme.

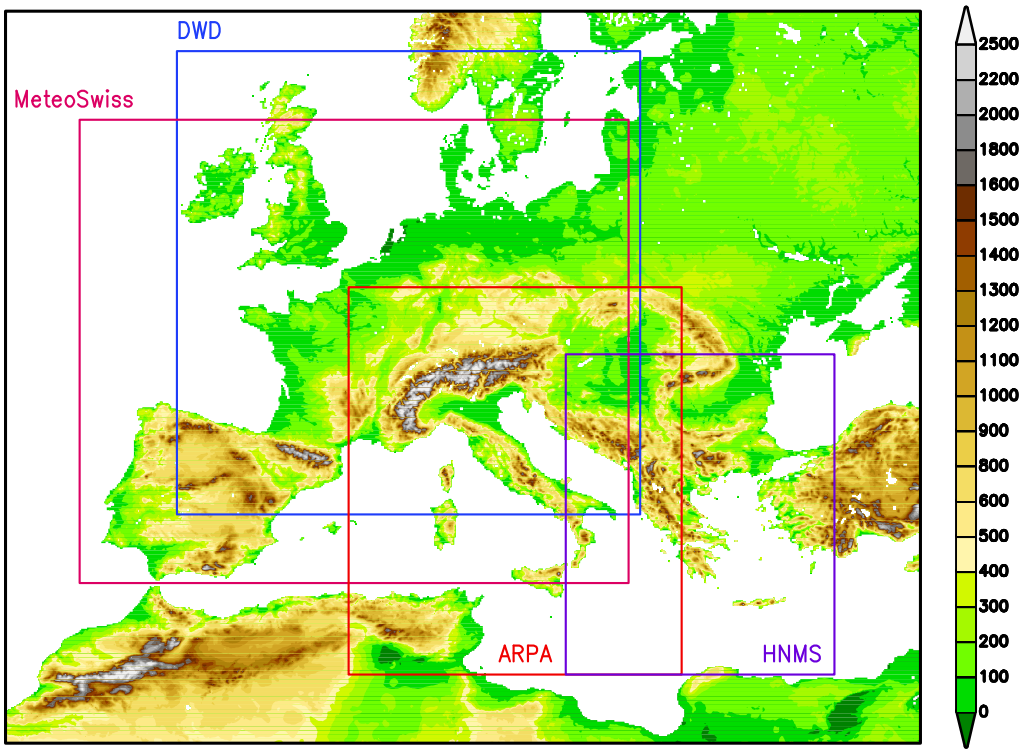

Figure 7: LM integration domains used at DWD, MeteoSwiss, ARPA-SMR and HNMS

The following sections give a brief overview on the configurations of the operational LM systems in the COSMO meteorological centres. During 2001, MeteoSwiss, ARPA-SMR and UGM decided to rename the model within their services:

- the LM application in Switzerland is called ***aLMo*** (Alpine Model),
- the LM application in Italy is called ***LAMI*** (Limited Area Model Italy).

4.1 ARPA-SMR (Bologna)

Basic Set-Up of LM

The regional meteorological service ARPA-SMR in Bologna operates the LM (as LAMI) at 7 km grid spacing. The rotated lat-lon coordinates of the lower left and the upper right corner of the integration domain are ($\lambda = -5°, \phi = -24.0°$) and ($\lambda = 9.5625°, \phi = -7.0625°$), respectively. See Figure 7 for this model domain. The main features of the model set-up are summarized in Table 6.

Table 6: Configuration of the LAMI at ARPA-SMR

Domain Size	234 x 272 gridpoints
Horizontal Grid Spacing	0.0625° ($\sim$ 7 km)
Number of Layers	35, base-state pressure based hybrid
Time Step and Integration Scheme	40 sec, 3 time-level split-explicit
Forecast Range	48 h
Initial Time of Model Runs	00 UTC and 12 UTC
Lateral Boundary Conditions	Interpolated from GME at 1-h intervals
Initial State	Interpolated from GME, initialized by DFI scheme
External Analyses	None
Special Features	Use of filtered topography
Model Version Running	lm_f90 2.12
Hardware	IBM SP3 (using 32 of 64 processors)

4.2 DWD (Offenbach)

Basic Set-Up of LM

The LM runs operationally at DWD using a 7 km grid spacing and 35 vertical levels. The rotated lat-lon coordinates of the lower left and the upper right corner of the integration domain are ($\lambda = -12.5°, \phi = -17.0°$) and ($\lambda = 7.75°, \phi = 3.25°$), respectively. See Figure 7 for this model domain. The main features of the model set-up are summarized in Table 7.

Data Assimilation

At DWD, a comprehensive data assimilation system for LM has been installed. Besides the analysis by observational nudging, three external analyses are run: a sea surface temperature (SST) analysis (00 UTC), a snow depth analysis (00, 06, 12 and 18 UTC) and a variational soil moisture analysis (00 UTC).

The data assimilations for the models GME and LM proceed as parallel streams which are coupled only via the boundary data. (see Fig. 8). The GME analysis is based on a 3-D multivariate optimum interpolation (OI) of deviations of observations from 6-h forecasts(first guess), generating an intermittent assimilation cycle with 6-h analysis frequency. All observations within a time window of $\pm$ 1.5 hours are considered as instantaneous, i.e. to be valid at analysis time. Thereby, a certain amount of observation data – those between the time windows – is lost. In order to include these measurements, the analysis update frequency has to be increased. A new intermittent GME-assimilation cycle with a 3-h period will be introduced in February 2002.

Table 7: **Configuration of the LM at DWD**

Domain Size	325 x 325 gridpoints
Horizontal Grid Spacing	0.0625° (∼ 7 km)
Number of Layers	35, base-state pressure based hybrid
Time Step and Integration Scheme	40 sec, 3 time-level split-explicit
Forecast Range	48 h
Initial Time of Model Runs	00 UTC, 12 UTC, 18 UTC
Lateral Boundary Conditions	Interpolated from GME at 1-h intervals
Initial State	Nudging data assimilation cycle, no initialization
External Analyses	Sea surface temperature (00 UTC) Snow depth (00, 06, 12, 18 UTC) Variational soil moisture analysis (00 UTC)
Special Features	Use of filtered topography, new TKE-scheme new surface-layer scheme
Model Version Running	lm_f90 2.12
Hardware	CRAY T3E (using 484 of 812 processors)

The 6-h GME forecasts to produce the first guess are used to generate boundary data at 1-h intervals for the LM assimilation cycle. The nudging scheme produces a continuous analysis stream, where data are assimilated at the time they are observed - but using a time-weighting function to spread the information in time. For practical reasons, 3-hour LM assimilation runs are done. LM analysis files are written every hour.

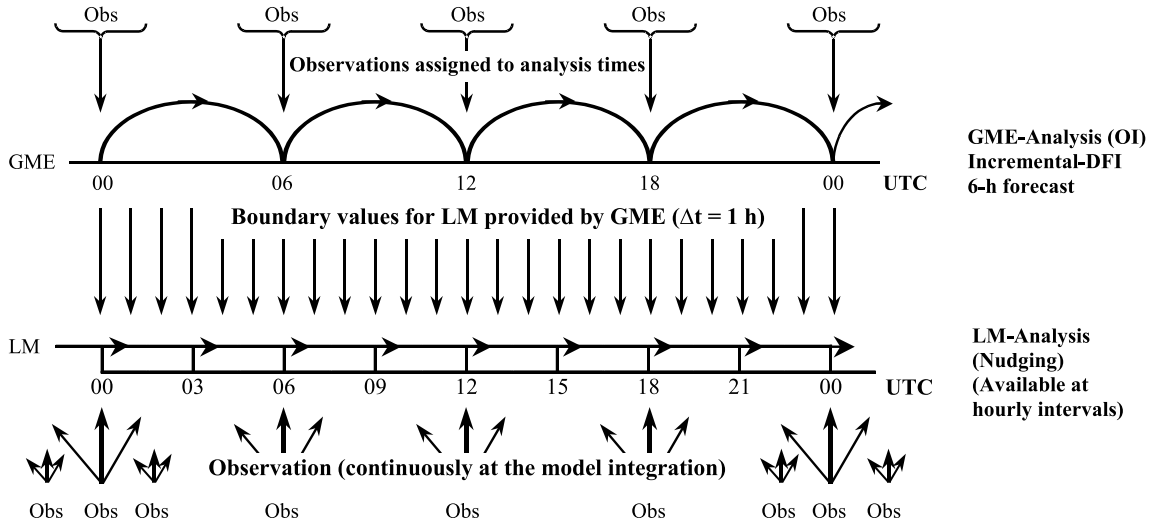

Figure 8: 4-D data assimilation for GME and LM

Operational Schedule

The operational schedule is structured by data assimilation for GME every six hours, i.e. for 00, 06, 12 and 18 UTC. The LM data assimilation is implemented with a continuous cycle of 3-hour assimilation runs. The data cut-off time for the 00 UTC and 12 UTC model runs of both GME and LM is 2 h 14 min. Based on this analyses, GME performs a 174-h forecast,

and LM performs a 48-h forecast. Another 48-h prediction of both models is performed starting at 18 UTC with a data cut-of time of 4 hours. Besides the forecast models, a wave prediction suite comprising a global and a local sea state model (GSM and LSM) is run operationally. Some detail of the operational schedule is given in Figure 9.

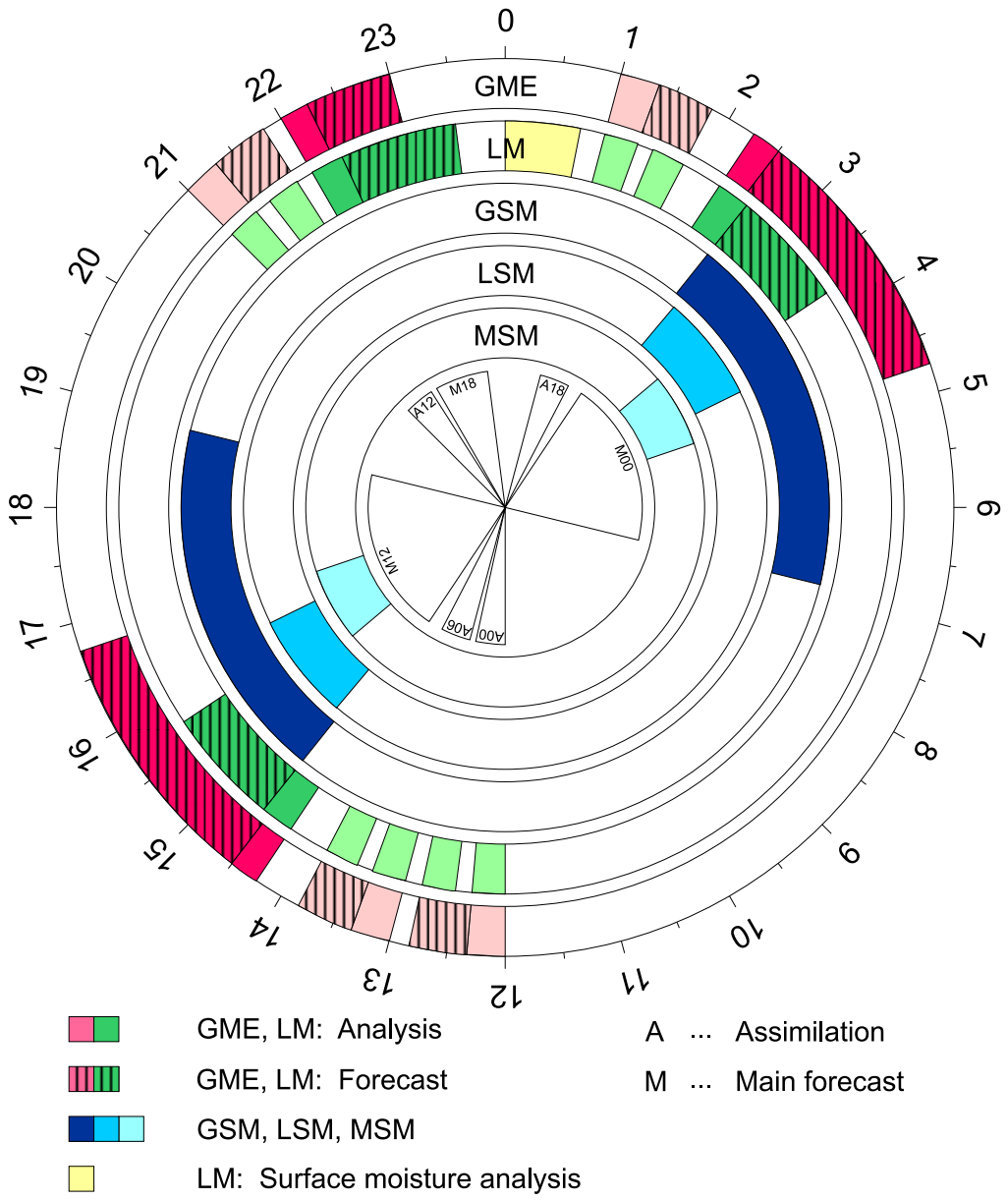

Figure 9: Operational timetable of the forecast models GME, LM, GSM and LSM at DWD

Current and New Computer System

At present, a powerful Cray T3E 1200 distributed memory MPP (massively parallel processors) system is the main number cruncher at DWD. This computer consists of 792 application PEs (processing elements, 20 with 0.5 GByte, 772 with 128 MByte of memory), 12 command PEs, and 12 operation PEs. Each PE has a nominal peak performance of 1.2 GFlop/s (floating point operations per second); for typical NWP programs a sustained speed of nearly 64 GFlop/s has been realized using all application PEs. Programs running on the Cray T3E use standard MPI (message passing interface) routines to exchange data between the processors.

A SGI Origin 2000 system with 2 x 16 processors, 16.4 GByte memory and 2337 GByte disk space (configured as fail-save RAID system) is used as data server (DAS1 and DAS2). All observations (BUFR code) and model results (GRIB1 code) are stored in huge *ORACLE* data bases. For example, one GME forecast run up to 174 h produces more than 12 GByte of data, and one LM forecast up to 48 h about 5 GByte. The daily NWP production exceeds 40 GByte of data. Archiving of the NWP data is based on *AMASS* (Archival Management and Storage System) with about 75 TByte of data on REDWOOD cassettes. Most pre- and post-processing, like observation decoding and graphics, is performed on so-called 'operational servers', a *SGI Origin 2000* system with 8 + 14 processors and 6.1 + 7.9 GByte of memory (RUS1 and RUS2). Figure 10 gives an overview of the hardware configuration at DWD.

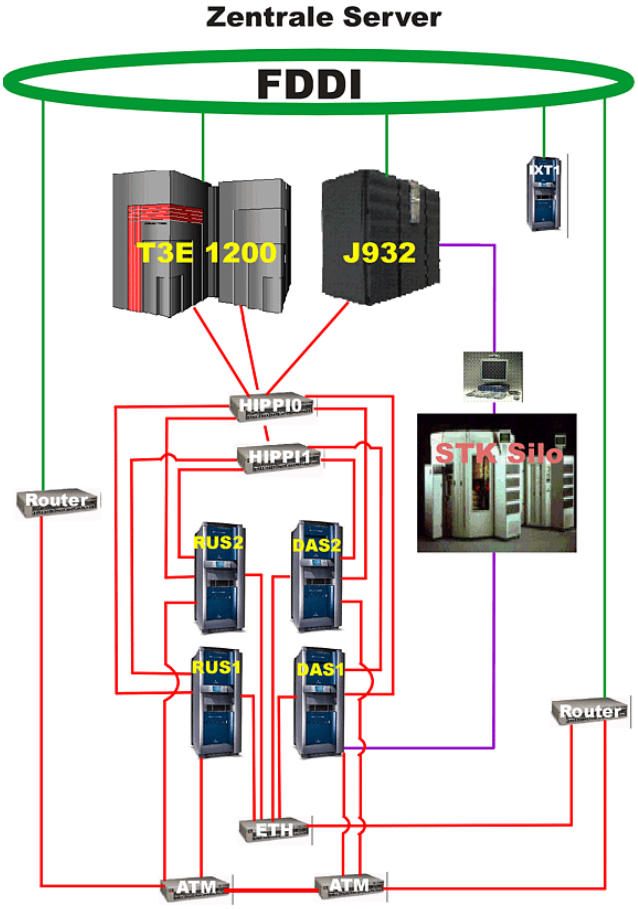

Figure 10: Present configuration of hardware at DWD

Starting in spring 2001, a new high performance computer system has been installed at DWD. The IBM system RS/6000 SP3 consists of 80 nodes with 16 processors each. The processors are equipped with a 375 MHz CPU (Power3-II). Most of the nodes possess 8 GByte of shared memory, some possess 16 GByte. The peak performance of the total 80-node system (1280 PEs) is around 2 Teraflop/s. The sustained performance for typical NWP codes is about 3.5 to 5 times larger than the performance of the current Cray T3E 1200 system. The 80-node IBM system has passed the acceptance tests in December 2001. At present, the operational complete NWP system is ported to the IBM SP3. It is planned to switch off the Cray T3E by the end of February 2002.

4.3 HNMS (Athens)

Basic Set-Up of LM

The national meteorological service of Greece, HNMS in Athens, operates the LM in a pre-operational mode at 14 km grid spacing. The rotated lat-lon coordinates of the lower left and of the upper right corner of the integration domain are ($\lambda = 4.5°, \phi = -24.0°$) and ($\lambda = 16.25°, \phi = -10.0°$), respectively. See Figure 7 for this model domain. The main features of the model set-up are summarized in Table 8.

Table 8: **Configuration of the LM at HNMS**

Domain Size	95 x 113 gridpoints
Horizontal Grid Spacing	0.1250° ($\sim$ 14 km)
Number of Layers	35, base-state pressure based hybrid
Time Step and Integration Scheme	80 sec, 3 time-level split-explicit
Forecast Range	48 h
Initial Time of Model Runs	00 UTC
Lateral Boundary Conditions	Interpolated from GME at 1-h intervals
Initial State	Interpolated from GME, initialized by DFI scheme
External Analyses	None
Special Features	Default model version
Model Version Running	lm_f90 1.9
Hardware	CONVEX (using 14 of 16 processors)

4.4 MeteoSwiss (Zürich)

(E. Zala, MeteoSwiss)

The Lokal-Modell (named as aLMo at MeteoSwiss) runs on a NEC SX5 placed at the Swiss Centre for Scientific Computing (CSCS) in Manno. During the operational forecasting slots the SX5 enters dedicated mode: 8 CPUs are then reserved for the model integration, 1 for the interpolation of the initial and lateral boundary fields provided by DWD. The operational suite is steered by the LM Package. This is a set of scripts running on SUN workstations.

Basic Set-Up of aLMo

The aLMo domain extends from 35.11 N -9.33 E (lower left) to 57.03 N 23.41 E (upper right). This domain is covered by a grid of 385x325 points with a horizontal resolution of 7 km (see Figure 7). The borders are placed prevalently over sea in order to reduce negative interferences generated at the transition zone of the orographies of the driving model (GME) and aLMo. The main features of the model set-up are summarized in Table 9.

Vertical Coordinates

In operational mode the model runs with 45 levels vertically distributed as shown in Figure 11.

Hardware and Communications

The computational work of the aLMo suite is managed by 3 systems:

Table 9: **Configuration of the aLMo at MeteoSwiss**

Domain Size	385 x 325 gridpoints
Horizontal Grid Spacing	0.0625° (∼ 7 km)
Number of Layers	35, base-state pressure based hybrid
Time Step and Integration Scheme	40 sec, 3 time-level split-explicit
Forecast Range	48 h
Initial Time of Model Runs	00 UTC and 12 UTC
Lateral Boundary Conditions	Interpolated from GME at 1-h intervals
Initial State	Nudging data assimilation cycle, no initialization
External Analyses	Merging of LM-DWD snow analysis
Special Features	Use of filtered topography
Model Version Running	lm_f90 2.12
Hardware	NEC SX5 (using 8 of 8 processors)

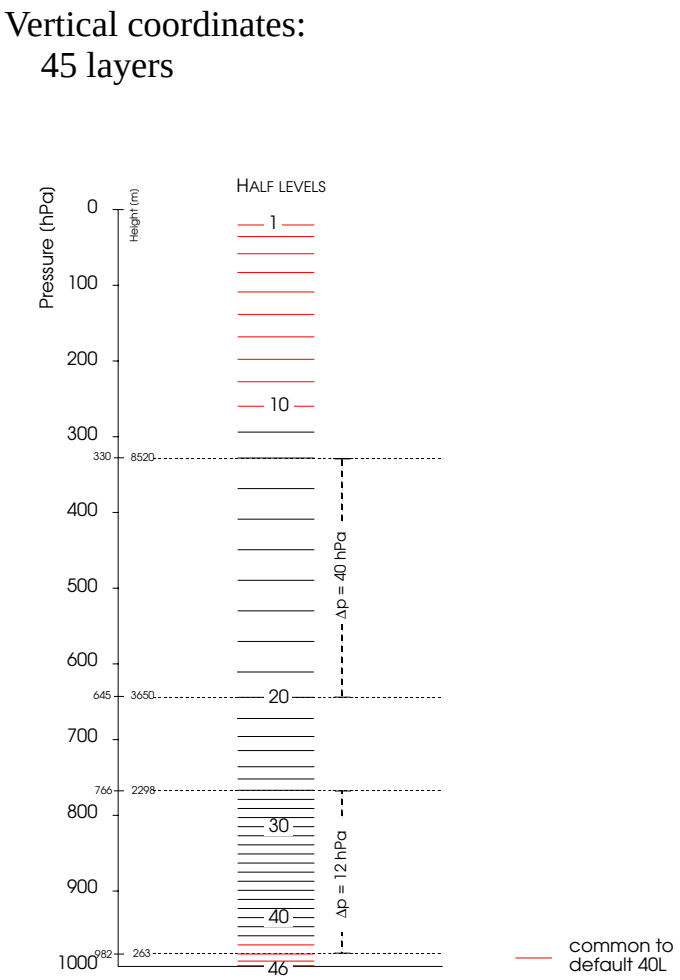

Figure 11: Vertical distribution of levels used at MeteoSwiss

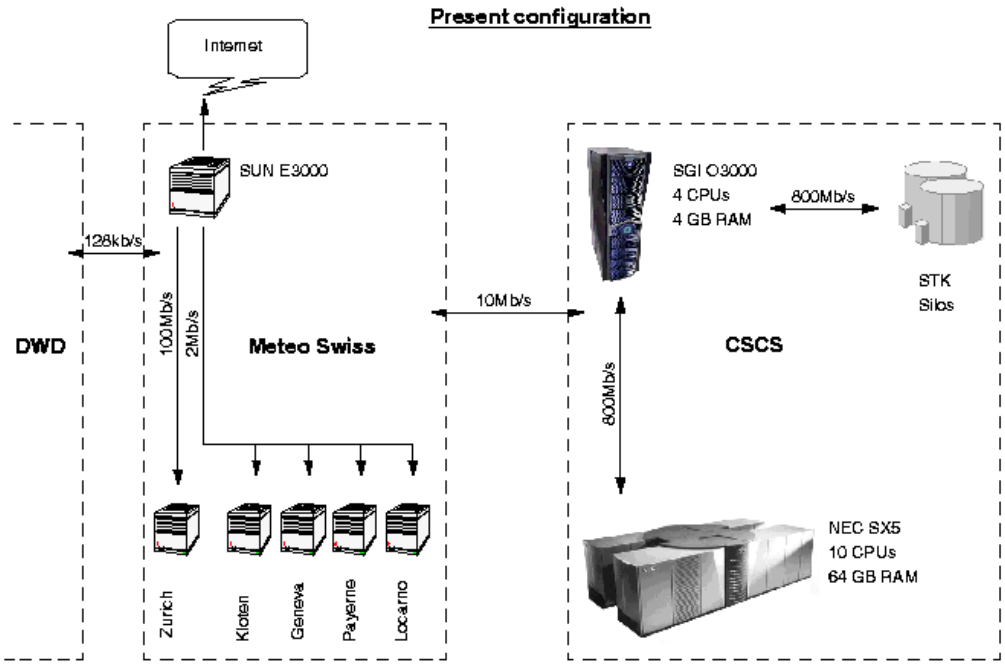

Figure 12: Present configuration of hardware and communications at MeteoSwiss

- SUN Enterprise 3000	at Meteo Swiss	(conduct, dissemination)
- SGI Origin 3000	at CSCS	(postprocessing)
- NEC SX5	at CSCS	(GME2LM, aLMo, LPDM)

Figure 12 shows the present configuration of hardware and communication used for the operational application of aLMo.

Data Flow
Figure 13 sketches the dataflow of the operational system.

LM Package
The operational suite is driven by "LM Package", a software developed at Meteo Swiss. It has a modular structure and is composed by 50 C-shell scripts. It can be executed in three different modes: operational, test and personal mode. In operational mode preprocessing, aLMo and postprocessing are running concurrently; warnings and exits are transmitted to operating which has the possibility of manual intervention.

Products
- 2-D plots: produced by MetView every 6 hours
- Animations: Hourly loops produced with IDL
- Tables, extracts of the model output in different formats
- Trajectories
- Concentrations from LPDM module

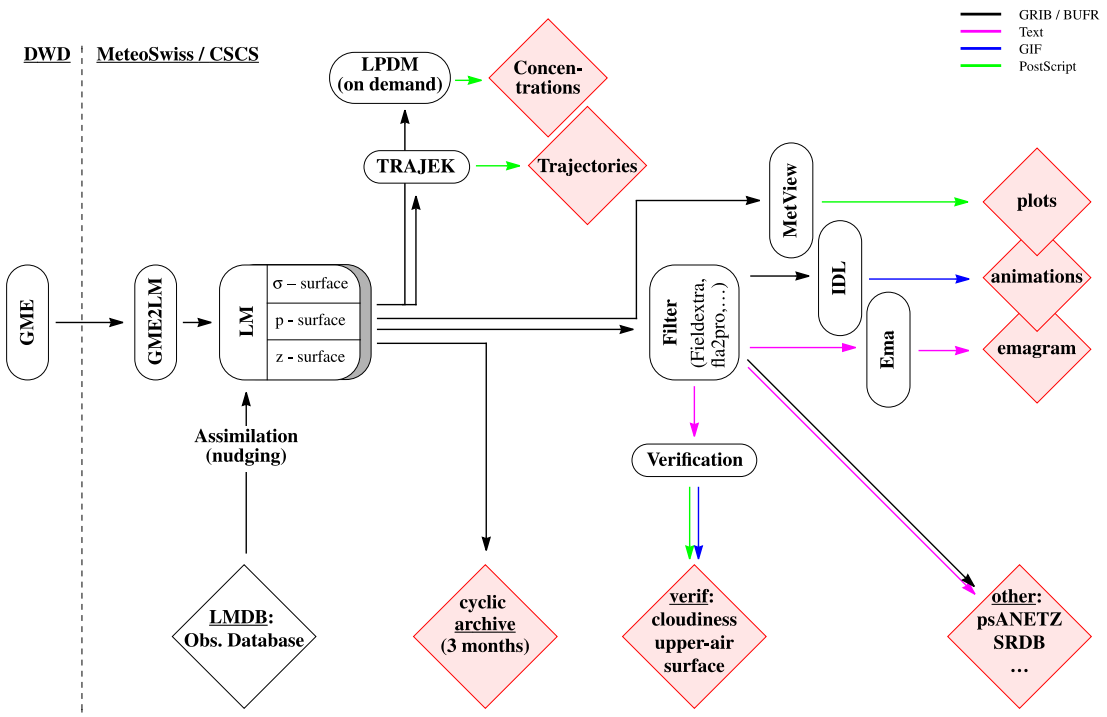

Figure 13: Dataflow of the current operational system at MeteoSwiss

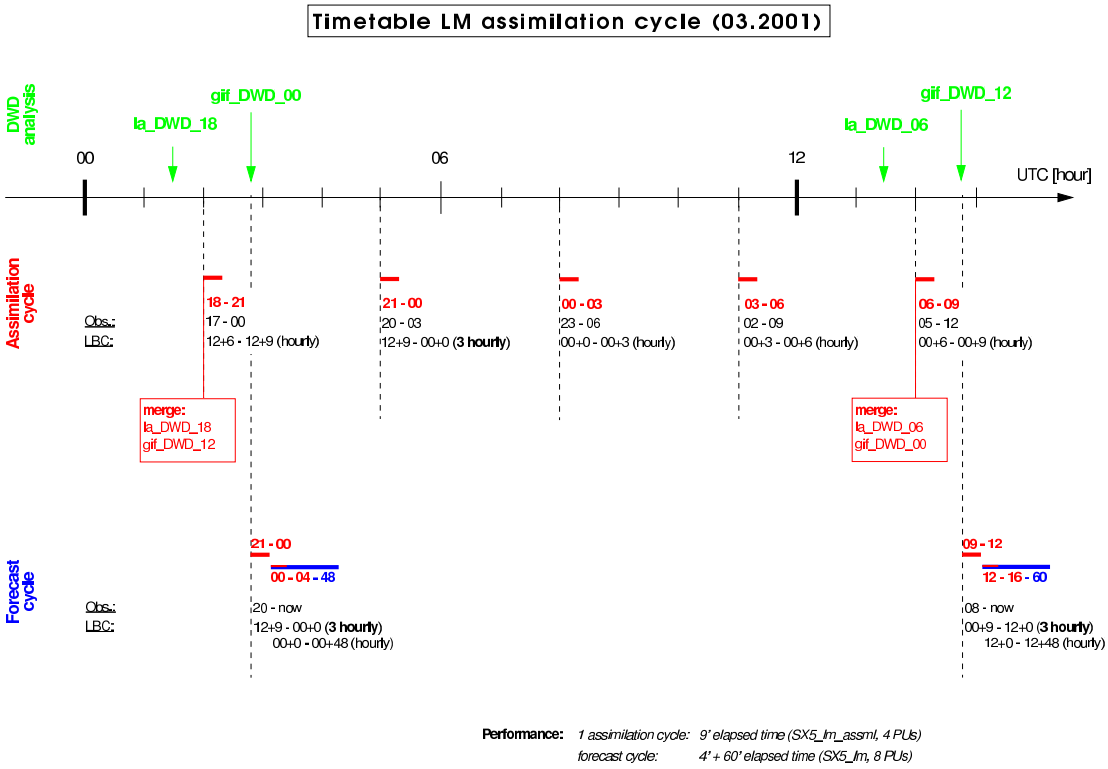

Figure 14: Time table of the aLMo assimilation cycle at at MeteoSwiss

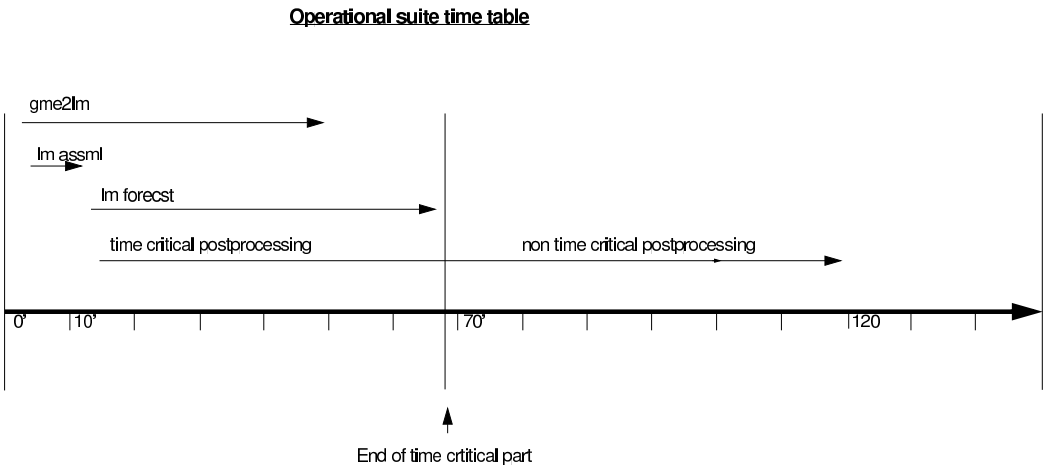

Figure 15: Time table of the operational suite at MeteoSwiss

Assimilation Cycle
The data assimilation at MeteoSwiss is implemented with 3-hour assimilation runs. Cut off time is 5 hours. The observations are taken from the aLMo data base, basically a copy of the ECMWF message/report data base. During the 06-09h and 18-21h assimilation runs the ozone, vegetation and soil parameters are updated from the GME analysis. In a similar way the LM snow analysis from DWD is merged into aLMo initial conditions.

Time Table
The analysis used by the main 48h forecasts is produced just ahead of the main runs (lm forecast) with a 3h run of aLMo in assimilation mode (lm assml). During the main forecast runs assimilation continues during the first 4 hours. The postprocessing is divided into a time critical and a non time critical part. During the first part the crucial products for Meteo Swiss internal clients (mainly forecasters) are generated and disseminated. During the second part the remaining products for internal and external clients are created. Archiving and statistics take place at the very end of the task.

Verification
The output of the Model undergoes three different types of verification:

- Surface verification: The surface parameters are compared to measurements taken by synoptical and automatic stations.
- Upper air verification: verification of the model against measurements from radiosonde ascents;
- Cloud verification: verification of the model cloudiness based on METEOSAT visible images.

5 Changes to the Model System

In this section, important changes to the LM-system which have been introduced during the last year are briefly described, and the possible impact on the forecast products are summarized. Of course, changes in the host model GME can also have a significant impact on the LM forecasts. Important changes to GME and its data assimilation are summarized below.

- The program for the analysis of mass, wind and humidity (ANA-MWH) now provides the analysis increments on the icosahedral-hexagonal model grid directly. Before, an interpolation from the analysis grid (regular geographical grid with mesh size 0.75° x 0.5°) to the model grid was performed (February 2001).
- The gravity wave drag has been decreased after verification results and diagnostic evaluations suggested that GME overestimates this effect (February 2001).
- Within the GME data assimilation cycle, the data cut-off time is reduced from 3h 40min to 2h 14min past analysis time. The former early runs with a short cut-off time are no longer performed (March 2001).
- The incremental digital filtering initialization of GME is performed in vertical mode space. Only the external mode and the first nine internal modes are subjected to the filtering procedure. This reduces the impact of initialization on the analysis in data sparse areas (June 2001).

For more detailed information on changes to GME and its data assimilation, please refer to the *Quarterly Report of the Operational NWP-Models of the Deutscher Wetterdienst, No. 26-28* (available at www.dwd.de).

5.1 Major Changes to LM

Cycle 2 of the LM software library lm_f90 was introduced in August 2000. The new version resulted from a basic redesign of the code and has a strongly increased modularity. This allows for faster compilation of the code. Also, due to the reduced interdependency of the modules, the simultaneous work on the code by different groups has become much more easy.

During 2001, there have been a number of correction updates of LM. But also a few more significant changes to the model code have been introduced, mainly the implementation of a new scheme for horizontal diffusion and a modification in the diagnostic interpretation of the subgrid-scale cloud water content for the radiation scheme. Within the nudging module, a large number of both technical and scientific updates have been introduced, focusing on the operational assimilation of aircraft data (AMDARs) and a better quality control of surface and radiosonde data.

Notes on lm_f90 Version 2.4

This version was created on 29 January 2001. It includes several changes to the data assimilation.

- Modifications necessary for the operational assimilation of aircraft data. In particular, preservation of specific instead of relative humidity at the nudging of temperature is

introduced as (operationally active) option for the whole model domain or only for the vicinity of convectively precipitating grid points (namelist parameter `khumbal`). Also, due to the lack of a check of aircraft position, aircraft temperature is rejected whenever the wind observation is rejected, and vice versa.

- Measures to (prepare to) improve the assimilation of surface pressure data. Namely, a spatial consistency check is introduced as additional quality control (making a larger nudging coefficient for pressure data more feasible for the future). And the quality weight is optionally enhanced for pressure data when the observed pressure tendency is large (namelist parameter `qcfpst`).

- Reorganization of loops to enhance the efficiency of the spreading of observations in the nudging and of the 2-d surface analysis scheme on vector processors (based on proposals by CSCS, Manno).

- Introduction or modification of factors and variances used for quality control thresholds (partly following the ECMWF data pre-processing).

- Some (minor) bug corrections, and formal code changes. Change of the defaults of many namelist parameters related to data assimilation. Most of these defaults are now set to the operational namelist values. Removal of namelist parameters `qctf` and `qctfsu`.

- Exchange of boundaries prior to using model values in the nudging scheme, to ensure results independent from the domain decomposition.

There is no direct meteorological impact, except within the assimilation cycle due to a better quality control.

Notes on lm_f90 Version 2.5

This version was created on 1 June 2001. It includes changes to the data assimilation, a modification to the surface- runoff and a bug-correction in the soil model.

- Observation (pre-)processing: Introduction of flight track checks for aircrafts, including an explicit check for missing sign at the reported longitude, and checks for exaggerated horizontal or vertical collocation of the reports. Also, frequent single-level aircraft reports at approximately the same pressure level are thinned.

- Observation (pre-)processing: Introduction of wind shear and lapse rate checks for multi-level data. Modification of limits for gross error checks. Additional data events.

- Introduction of a new namelist variable `yaofpath`, which denotes the name of the path of the observation input file AOF.

- Some (minor) bug corrections. Formal code changes, e.g. in `organize_nudging` to distinguish more clearly between sections with and without communication between PE's. Safety tests at memory allocation of arrays.

- Modification of the surface-runoff for GRIB-output. The number of layers contributing to surface runoff has been changed from 1 to 0 (i.e surface-runoff only).

- An error in the constant for the soil water flux corresponding to 10 % of pore volume was corrected in the soil model.

Both a better use of aircraft and radiosonde data due to quality controls improve the LM analysis. The correction of the error in the soil model has no noticeable impact to the forecasts.

Notes on lm_f90 Version 2.6

This version was created on 12 June 2001. It includes changes to the radiation scheme and a few correction updates.

- The interpretation of the in-cloud and area-average cloud liquid water content for the input to the radiation scheme is changed (routine `organize_radiation.incf`). The in-cloud value for the stratiform clouds is now set to the maximum of 0.5 % of the saturation specific humidity and of 0.5 times of the predicted cloud water. The in-cloud value for convective clouds is now simply set to 0.2 g/kg. For the area average cloud water content, these values are weighted with the corresponding area fraction of cloud cover. The Namelist input variables `icldm_rad=3` and `icldm_rad=4` now do the same interpretation of cloud water for the radiation scheme. The option `icldm_rad=4` will be removed in a future update.
- An error in the data exchange related to the cloud-ice scheme was corrected (routines `lmorg.f90` and `src_leapfrog.f90`).
- Tuning of flight track check thresholds in the data assimilation part of the model. Message on thinning of aircraft reports introduced.

The change in the interpretation of sub-grid scale cloud water content has a significant impact: the positive bias of 2-m temperature below low and medium level clouds (which have been too transparent for solar radiation) is removed to a large extend.

Notes on lm_f90 Version 2.7

This version was created on 26 June 2001. It is a pure correction update for an allocation-deallocation bug in the analysis scheme, which was accidentally introduced in version 2.6. There is no meteorological impact.

Notes on lm_f90 Version 2.8

This version was created on 6 July 2001. It includes mainly the technical organization of I/O and several optimizations for vectorization.

- Reorganization of the I/O handling: Some control structures (especially for the variable table of the meteorological fields) have changed; some new structures have been added. The input is now controlled by the new Namelist-variables `yvarini` and `yvarbd` (analogous to the output).
- Minor Bugs were corrected in the routines for GRIB output and for time measuring.
- Optimizations for better vectorization have been introduced in several routines. Especially, a 2D vertical interpolation to p- and z-levels – allowing for vectorization – has been introduced.

- Some preparations for the future implementation of the new multi-layer soil model have been included by introducing new fields and control variables.
- The following new NAMELIST variables have been introduced in various NAMELIST groups (with modification in the corresponding routines).
  - in `/runctl/ (src_setup)`:
    `lreorder`: specifies whether the PEs can be reordered in the cartesian MPI-communicator
  - in `/phyctl/ (organize_physics)`:
    `lmulti_layer`: to run the new multi-layer soil model
    `lmelt`: to run with melting processes in the soil
    `ke_soil`: number of levels in multi-layer soil model
    `isoillevels`: for specifying the depth of the levels
  - in `/ioctl/ (organize_data)`:
    `nvers`: for documenting purposes (mainly in GRIB-Code)
    `ymode_read`: to specify the mode how files are opened
    `ymode_write`: (in GRIB-Code)
  - in `/gribin/ (organize_data)`:
    `yvarini`: list of initial variables for input
    `yvarbd`: list of boundary variables for input

There is no meteorological impact from this changes. A better performance on vector machines is achieved.

Notes on lm_f90 Version 2.9

This version was created on 16 July 2001. The new scheme for horizontal diffusion has been implemented and some correction updates concerning the reorganized Grib I/O from version 2.8 have been included.

The new horizontal diffusion scheme uses direct monotonic flux-limiting and an additional orographic flux-limiter. The scheme can be used optionally. The following NAMELIST input parameter have been introduced in `/dynctl/`:

Parameter	Definition / Purpose	Default value
`itype_hdiff`	a switch to select a scheme for horizontal diffusion =1: regular 4th-order linear horizontal diffusion =2: new monotonic 4th-order scheme	`itype_hdiff = 2`
`hd_max:`	the threshold value H_{max} in the quadratic form of the orographic flux limiter in m.	`hd_max = 250`
`hd_cor_t:`	a factor by which the standard coefficient for numerical diffusion is reduced in case of temperature and pressure smoothing.	`hd_cor_t = 0.75`
`hd_cor_q:`	a factor by which the standard coefficient for numerical diffusion is reduced in case of humidity and cloud water smoothing.	`hd_cor_q = 0.50`

The scheme is switched on by default. It requires about five percent more CP-time on scalar machines. The meteorological impact is quite large, especially in mountainous regions with

steep topography. Here, the peak precipitation over mountain tops is reduced and the dry valley effect is removed; the spatial distribution of precipitation over complex terrain agrees better to available observations.

Notes on lm_f90 Version 2.10

This version was created on 24 July 2001. It is mainly an optimization update to reduce the computational overhead due to the new horizontal diffusion. The module routine `slow_tendencies.incf` has been removed from module `src_leapfrog.f90` to become an external subroutine `slow_tendencies.f90`. Several optimizations have been included, especially a more efficient algorithm for solving the tridiagonal systems of equations. Also, some corrections concerning CALLs to the intrinsic MIN/MAX functions and GRIB-output routines have been done. There is no meteorological impact from these changes.

Notes on lm_f90 Version 2.11

This version was created on 28 September 2001. Some minor bugs which accidentally have been introduced the preceding versions have been corrected. An extensive use of the internal function `LEN_TRIM` (was very slow on the NEC) has been eliminated, and a few modifications have been made in the nudging analysis routines to port the program on the IBM. New 3-d arrays have been introduced to read cloud ice optionally from interpolated GME initial and boundary fields (if present, otherwise cloud ice is diagnosed from cloud water). Digital filtering of cloud ice is also included. Corresponding control variables in NAMELIST-input have been defined:

Parameter	Definition / Purpose	Default value
`lana_qi`	if .TRUE., take cloud ice values from the analysis file, else, cloud ice is diagnosed in the model.	.FALSE.
`llb_qi`	if .TRUE., take cloud ice values from the lateral boundary files, else, cloud ice boundary values are diagnosed in the model.	.FALSE.

There is no meteorological impact from these changes, except when using cloud ice values from initial and lateral boundary files.

Notes on lm_f90 Version 2.12

This version was created on 7 November 2001. It includes several minor corrections in routines related to the nudging scheme. As a significant change, a bugfix was introduced in the new surface layer scheme to avoid unrealistic oscillations of the 2m-temperature and 2m-dewpoint in case of very stable stratification. Also, a minimal roughness length over water surfaces was introduced. These changes do not only affect the diagnostic screen level values, but also the surface layer resistances (i.e. the transfer coefficients for heat and momentum). However, the overall meteorological impact of these changes showed to be small.

Planned Releases

Also in 2002, there will be a number of new model versions – not only due to error corrections and optimizations, but also due to the implementation of new physics packages and changes in the model dynamics. By now, the following releases are planned.

– Implementation of the Kain-Fritsch convection scheme
– Implementation of the SLEVE-coordinate
– Implementation of the new multi-layer soil model TERRA_LM
– Tuning of the cloud-ice scheme
– Code re-organization and optimization of the TKE-scheme
– Implementation of a new 2-timelevel integration scheme with 3rd-order advection
– Reformulation of the interpolation of diagnostic screen-level values

5.2 Major Changes to GME2LM

The interpolation program GME2LM has been extended to include a couple of new features, which are mainly related to the new multi-layer soil model and the cloud ice scheme. The following release notes summarize the changes.

Notes on GME2LM Version 1.8

This version of GME2LM was created on 19 December 2000. It includes vectorized versions of routines that transform the wind speeds from the rotated system to the geographical and vice versa. These routines improve the performance of GME2LM on vector processors significantly. Also, the interfaces for the asynchronous I/O-module have been adapted to the new version of `mpe_io.f90`.

Notes on GME2LM Version 1.9

This version of GME2LM was created on 24 August 2001. Besides some bug corrections, new features for the interpolation were added in this version of GME2LM.

- Possibility to create LM initial data from an older GME forecast: Can be specified with the new NAMELIST-variable `ydate_bd` (start of GME forecast).
- Possibility to compute initial data for the (new) multi-layer soil model for the LM (under development). Can be specified with the NAMELIST-variables `lmulti_layer, ke_soil, czhl_soil`.
- Possibility to compute initial and boundary data for the z-coordinate version of the LM (under development). Can be specified with the (old) NAMELIST variables `ivctype=2, vcflat=0.0` and appropriate `vcoords` (in meter above ground).

The following new NAMELIST-variables were added.

Input Group	Parameter	Definition / Purpose
/input_contrl/	lreorder	allows reordering of PEs in the cartesian MPI-communicator
	ydate_bd	start of GME forecast for boundary values; if ydate_bd is older than ydate_ini, old GME data are used to construct LM initial data.
	lmulti_layer	to compute initial data for the new multi-layer soil model
	ke_soil	number of levels in multi-layer soil model
	czhl_soil	for specifying the depth of the half levels (in meters)
/input_data/	nvers	for documenting purposes (mainly in GRIB-Code)
	ymode_read	to specify the mode how files are opened
	ymode_write	(in GRIB-Code)

Notes on GME2LM Version 1.10

This version of GME2LM was created on 14 September 2001. It contains changes that allow to compute only certain variables for the LM initial file, in order to mix initial fields from this program with fields from other programs (external analyses, LM Nudging, ...) in the assimilation cycle. Also for that purpose, a different height correction of the climatological soil temperature (T_CL) has been implemented. Additionally, the interpolation of cloud ice from GME to LM grid has been implemented. Also, some more bugs have been corrected.

The following Namelist variables have been added.

Input Group	Parameter	Definition / Purpose
/input_contrl/	lprog_qi	interpolate cloud ice from GME
	qvmin	minimum value of specific humidity (security)
	qcmin	minimum value of cloud water content (security)
	qimin	minimum value of cloud ice content (security)
	lt_cl_corr	if .TRUE., a different kind of height-correction of T_CL is performed
/input_data/	yvarini	list of initial fields for LM
	yvarbd	list of boundary fields for LM These lists correspond to the same lists in the LM. Only the variables that occur in these lists are written for initial and boundary data files, resp.

Notes on GME2LM Versions 1.11, 1.12 and 1.13

These Versions, created on 27 September, 15 October and 18 October, respectively, are pure correction updates.

5.3 Changes to Model Configurations at COSMO Centres

During winter 2000/2001 all meteorological centres running the LM at 7-km grid spacing have switched to use a weakly filtered orography (by applying a 10th-order Raymond filter with filter parameter $\epsilon = 0.1$, see the contribution of A. Gassmann in Newsletter No.1).

December 2000
Use of a prototype version of the new scheme for horizontal diffusion at MeteoSwiss for operational production.

January 2001
ARPA-SMR switches from the former 32-layer to a 35-layer model version.

February 2001
The LM becomes fully operational at MeteoSwiss with a 45-layer model version.

April 2001
The new turbulence scheme based on prognostic turbulent kinetic energy is switched on in the operational production at DWD. Additionally, a new parameterization to calculate the surface fluxes of heat, moisture and momentum is applied. For details on the statistical evaluation of a parallel test suite, see COSMO Technical Report No.1 by M. Raschendorfer and D. Mironov (2001).

June 2001
The assimilation of aircraft data is introduced operationally to the LM data assimilation cycle at DWD.

November 2001
MeteoSwiss introduces a nudging-based aLMo assimilation cycle operationally.

November 2001
The new horizontal diffusion scheme is switched on at DWD. For a detailed description of the scheme and the impact to forecast products, see COSMO Technical Report No.3 (Doms, 2001). Additionally, the option for a spatial average of convective forcings as input to the convection scheme is applied (also at MeteoSwiss).

6 Working Groups

COSMO's scientific and technical activities are organized in *Working Groups* (WG) which cover the main research areas related to a NWP-system. Each Working Group is headed by a *Work Package Coordinator* (WPC), who is responsible for the consistency of the execution of the work packages and for the coordination, planning, and supervision of the scientific and technical activities related to the work packages in his group.

This section gives an overview on the current personnel composition of the WGs. All scientists contributing actively to the work packages are included in the lists, also those from outside COSMO member institutions. For each WG, the main research activities from the recent COSMO period (Oct 2000 - Oct 2001) are briefly summarized and a short note on the planned activities for the present period (Oct 2001 - Oct 2002) is given. The work plan lists as well as a detailed description of each work package within a WG, are available at the member area of our web-site.

6.1 Working Group 1: Data Assimilation

This working group considers various aspects of 4-dimensional assimilation of observation data using the nudging analysis technique. For soil moisture and some surface fields, a set of 2-dimensional intermittent analysis schemes is applied in addition. The group is headed by Christoph Schraff (DWD) as WPC. The following scientists are members of this group.

Name	Institution	e-mail
Paolo Alberoni	ARPA-SMR	palberoni@smr.arpa.emr.it
Theodore Andreadis	HNMS	andrea@hnms.gr
Jean-Marie Bettems	MeteoSwiss	jean-marie.bettems@meteoswiss.ch
Michael Buchhold	DWD	michael.buchhold@dwd.de
Davide Cesari	ARPA-SMR	dinamici@smr.arpa.emr.it
Massimo Ferri	UGM	m.ferri@ecmwf.int
Guergana Guerova	University of Bern (CH)	guergana.guerova@mw.iap.unibe.ch
Christian Häberli	MeteoSwiss	christian.haeberli@meteoswiss.ch
Reinhold Hess	DWD	reinhold.hess@dwd.de
Daniel Leuenberger	MeteoSwiss	daniel.leunenberger@meteoswiss.ch
Andrea Rossa	MeteoSwiss	andrea.rossa@meteoswiss.ch
Georgio Sakellaridis	HNMS	nwpapa@hnms.gr
Christoph Schraff	DWD	christoph.schraff@dwd.de
Panageotis Skrimizeas	HNMS	pskrim@hnms.gr
Friedrich Theunert	AWGeophys	friedrichtheunert@awg.dwd.de
Maria Tomassini	DWD	maria.tomassini@dwd.de
Helmut Walter	AWGeophys	helmutwalter@awg.dwd.de

The main research activities of WG 1 for the period Oct 2000 - Oct 2001 covered the following points.

- Work on the assimilation of aircraft data (AMDAR) within the nudging scheme has been continued. In order to avoid wrong positions of aircraft (caused by instrument or transmission errors), a flight track check has been introduced as a model-independent quality control step. Test experiments have shown a significant positive impact to parameters of the free atmosphere (wind, temperature, humidity) for 12 UTC and 18 UTC runs, which is noticeable up to 24-h forecast time. The experiments revealed a

neutral impact on precipitation, and a slightly better prediction of low level stratus in winter (see *Assimilation of aircraft observations* in Section 9). Aircraft data are assimilated operationally at DWD since June 2001.

- The development work to assimilate integrated water vapour, derived from GPS-data of about 80 stations in or near Germany, has been continued. In one of the case studies (3 May 2001), a heavy precipitation event in Germany was better simulated by using GPS and aircraft data. An erroneous reproduction of the diurnal cycle of integrated water vapour by the model, however, can sometimes result in problems with the assimilation of GPS data (see *Monitoring of integrated water vapour from ground-based GPS observations and their assimilation in a limited-area NWP model* in Section 9).

- A 27-day observation system experiment was conducted at MeteoSwiss for the EU-COS programme of EUMETNET. A scenario with a drastically reduced number of radiosonde stations over Europe but with a higher observation frequency of the remaining stations and with additional AMDAR aircraft data was prescribed. The experiment showed that the reduction of the radiosonde soundings resulted in a deterioration of the forecasts (measured by scores for vertical profiles of wind velocity, wind direction, temperature and relative humidity). This loss in forecast quality could not be compensated by a higher frequency of soundings and the additional use of aircraft data. A detailed report by J.-M. Bettems will appear as COSMO Technical Report No. 4.

- A long-term parallel test experiment with the LM nudging scheme was run at MeteoSwiss. Compared to the operational runs starting from interpolated GME analyses, the use of the nudging-based data assimilation revealed an overall positive impact, especially on precipitation amount, for forecast periods of up to 18 hours (see also *Comparison of forecasts with and without nudging: surface parameters over Switzerland for April - December 2001* in Section 9).

The major work packages for 2002 include further evaluation and tuning of the nudging scheme, especially with respect to the temporal weights, the vertical correlation functions and the assimilation of surface-level wind and humidity data. Another topic is the use of additional observations: several work packages deal with the assimilation of radar data, of GPS-derived integrated water vapour, of wind profiler data, of cloud analysis data and of SATOB wind data. Also, a detailed documentation of the nudging analysis scheme is planned for 2002. Furthermore, work on an extension of the current variational soil-moisture analysis scheme is planned to begin in 2002 as part of the 3-year EU-project ELDAS (see Section 10 for more information about ELDAS).

6.2 Working Group 2: Numerical Aspects

The WG on numerical methods and basic model dynamics is headed by Jürgen Steppeler (DWD) as WPC. Currently, the following scientists are members of this group.

Name	Institution	e-mail
Heinz-Werner Bitzer	AWGeophys	heinz-werner.bitzer@dwd.de
Günther Doms	DWD	guenther.doms@dwd.de
Almut Gassmann	DWD	almut.gassmann@dwd.de
Daniel Leuenberger	MeteoSwiss	daniel.leuenberger@meteoswiss.ch
Annemarie Link	DWD	annemarie.link@dwd.de
Tiziana Paccagnella	ARPA-SMR	t.paccagnella@smr.arpa.emr.it
Yannis Papageorgiou	HNMS	nwpapa@hnms.gr
Peter Prohl	DWD	peter.prohl@dwd.de
Maria Refene	HNMS	diso@hnms.gr
Georgio Sakellaridis	HNMS	nwpapa@hnms.gr
Jürgen Steppeler	DWD	juergen.steppeler@dwd.de
Lucio Torrisi	UGM	torrisi@ecmwf.int

The main research activities of WG 2 for the period Oct 2000 - Oct 2001 covered the following points.

- The present terrain-following coordinate system will result in large and presumably not acceptable numerical errors in case of steep topography. Thus, work on a z-coordinate system version of LM for high-resolution applications has been continued. The following progress was achieved:
  - establishment of a 3-d version of the z-coordinate LM,
  - improvement in generating smooth mountain waves.
- The evaluation of the 2-time-level RK split-explicit integration scheme has been continued. A version of the scheme to be combined with any advection scheme was developed. Tests involving idealized test situations perform adequate. Problems remain to be investigated for real data cases (see contribution by A. Gassman in Section 9).
- For applications on the meso-γ scale the full 3-D transport of rain and snow has to be considered instead of the present column-equilibrium approximation. A test version using positive definite transport and a time-splitting approach for the fallout of precipitation has been developed (see contribution by A. Gassman in Section 9). Further development of this scheme will follow the 2-time-level integration scheme.
- The current leapfrog scheme with centered differencing for humidity advection is not very accurate. A monotonic scheme for the advection of humidity variables has been implemented (in the framework of the 2-time-level integration scheme).
- Artificial horizontal diffusion is required to control small-scale noise on the 2dx interval. The current linear 4th-order scheme, however, introduces new errors on the resolvable scales via the Gibbs phenomena. A monotonic version of the scheme, which lacks over- and under-shootings and gradually reduces diffusive fluxes with increasing steepness of the topography, was implemented and has recently been introduced operationally (see COSMO Technical Report No.3).

The major work packages for 2002 include further development work for the new z-coordinate, which is considered to be essential for NWP on the meso-γ scale. This work package aims at the derivation of a full 3-D model version including physics in late autumn this year. Other points of interest are the operational application of the 2-time-level integration scheme, the introduction of the SLEVE vertical coordinate (see contribution of D. Leuenberger in Section 9), and the use of ECMWF frames as initial and boundary conditions for LM.

6.3 Working Group 3: Physical Aspects

The main effort of this working group is to develop new physics packages for future operational applications and to improve existing parameterizations. The WG on physical processes is headed by Marco Arpagaus (MeteoSwiss). The following scientists are members of this group.

Name	Institution	e-mail
Euripides Avgoustoglou	HNMS	euri@hnms.gr
Marco Arpagaus	MeteoSwiss	marco.arpagaus@meteoswiss.ch
Claudio Cassardo	Università di Torino	cassardo@ph.unito.it
Günther Doms	DWD	guenther.doms@dwd.de
Erdmann Heise	DWD	erdmann.heise@dwd.de
Hans-Joachim Herzog	DWD	hans-joachim.herzog@dwd.de
Pirmin Kaufmann	MeteoSwiss	pirmin.kaufmann@meteoswiss.ch
Nicola Loglisci	Università di Torino	loglisci@ph.unito.it
Massimo Milelli	SMR Piemonte	massimo.milelli@csi.it
Dmitrii Mironov	DWD	dmitrii.mironov@dwd.de
Renata Pelosini	SMR Piemonte	renata.pelosini@csi.it
Matthias Raschendorfer	DWD	matthias.raschendorfer@dwd.de
Reinhold Schrodin	DWD	reinhold.schrodin@dwd.de
Jan-Peter Schulz	DWD	jan-peter.schulz@dwd.de

The main effort of this working group is to develop new physics packages for future operational applications and to improve existing parameterizations. Some of the topics the group has been working on during the last COSMO period are the following:

- A new turbulence scheme (level 2.5) based on a prognostic treatment of turbulent kinetic energy (TKE) as well as a new surface layer scheme based on the TKE approach have been implemented for optional use. Both schemes are operational at DWD since the beginning of April 2001. A technical report on parts of this work package ("Evaluation of Empirical Parameters of the New LM Surface-Layer Parameterization Scheme") can be obtained on the COSMO website at http://www.cosmo-model.org/cosmoPublic/technicalReports.htm.

- A new multi-layer version of the soil model TERRA has been developed. The new version includes freezing and melting of soil layers and a revised formulation of the snow model. The new scheme is currently being evaluated and tuned. A technical report describing the changes to TERRA ("The Multi-Layer Version of the DWD Soil Model TERRA_LM") is available on the COSMO website at http://www.cosmo-model.org/cosmoPublic/technicalReports.htm.

- Implementation work has started to add the Kain-Fritsch convection scheme as an optional cumulus parameterization scheme. First tests have been done and show promising results. This work will be continued in 2002.

- A cloud-ice scheme has been developed and implemented into both LM and GME. Final tests are currently under way. Operational implementation is planned for 2002, but needs an organizational effort since all local area models depending on GME boundary data should switch simultaneously to prevent systematic errors.

- Some tuning of the cloud-radiation interaction has been done to tackle the known problem of near surface temperatures being to high under moderately dense cloud

cover. However, no conclusive results have been achieved yet and therefore the work will be continued in the next COSMO period.

The plans for 2002 include further work on all the packages mentioned above. For the new turbulence scheme, this consists of parameter tuning, further extension of the scheme as well as writing up a documentation. The soil model and the cloud-ice scheme mainly await operational implementation, and the implementation of the Kain-Fritsch convection scheme as well as the tuning of the cloud-radiation interaction is "work in progress".

New packages for the work plan of 2002 include a sensitivity study for the roughness length (wind speeds at mountainous stations are forecasted systematically too low when observations are compared to the nearest grid-point), the parameterization of boundary layer clouds & sub-grid scale cloudiness (either within the new turbulence scheme or an entirely new package) and first tests of various parameterization packages as well as the implementation of a 3D turbulence formulation for LM runs at 2.8 km or even smaller grid-spacing. Last but not least, there are two work packages focusing on the observed but yet not understood differences of the precipitation amounts for different LM versions and the overestimation of weak precipitation events.

In addition, there will be a joint workshop with working group 5 in early February in Torino to discuss interpretation, verification and tuning issues related to the new boundary layer schemes (turbulence, surface-layer).

6.4 Working Group 4: Interpretation and Applications

The activities of the working group started in 2001 with the nomination of Pierre Eckert (MeteoSwiss) as the work package coordinator. The following scientists are members of this group:

Name	Institution	e-mail
Günter Doms	DWD	guenther.doms@dwd.de
Pierre Eckert	MeteoSwiss	pierre.eckert.@meteoswiss.ch
Massimo Ferri	UGM	m.ferri@ecmwf.int
George Galanis	HNMS	galan@hnms.gr
Chiara Marsigli	ARPA-SMR	cmarsigli@smr.arpa.emr.it
Andrea Montani	ARPA-SMR	a.montani@smr.arpa.emr.it
Tiziana Paccagnella	ARPA-SMR	t.paccagnella@smr.arpa.emr.it
Volker Renner	DWD	volker.renner@dwd.de
Susanne Theis	Universität Bonn	susanne.theis@uni-bonn.de

The activities in 2001 have mainly been organizational, but some scientific work has already been done. The group met once in April 2001 in Bologna together with WG5. The definition and the activities of the work packages are presented below.

- *WP 4.1 LAM EPS.* The goal of this activity is to run the LM with initial and boundary conditions given by the ECMWF ensemble in order to catch probabilities of extreme events with more spatial accuracy. The first step is to connect the LM to the ECMWF IFS and this has been done. Some MAP cases have been run in hind-cast mode. The next step is to implement an operational suite in real time. The corresponding demands have been addressed to ECMWF. The group decided to use a 10km resolution LM on

a domain gathering the domains of all participating states. We also decided to study statistical methods for the forecast of extremes so as to fix a benchmark for the heavier dynamical methods.

- *WP 4.2 Statistical post-processing.* The post-processing has been divided in internal and external. Internal is when the computing needs a lot of data from the model, like model level information or internal parameters. Production of radar-type animations, instability indices or significant weather codes can be counted among these. External post-processing happens when it is produced from limited output files from the model. It mainly has the goal of correcting systematic deficiencies of the model. Kalman filtering and MOS methods are examples. A first questionnaire has been circulated in 2001. Techniques for producing precipitation probabilities from surrounding grid point information have also been investigated at DWD.

- *WP 4.3 Presentation.* It has been decided not to include in WG4 the software aspects of the graphical presentation. This will be treated by WG 6. What rests to WG4 is to propose guidelines on parameters to present for instance to get an overall view of the synoptic evolution or to catch various meteorological mesoscale phenomena. We also will investigate the possibilities of 3d animations. Finally guidelines for the bench forecasters will be produced in form of a user guide.

6.5 Working Group 5: Verification and Case Studies

This Working Group takes care for the verification of operational model forecasts, for the development of new verification methods and diagnostical tool as well as for case studies with the LM. The WG is headed by Carlo Cacciamani (ARPA-SMR) as WPC. The following scientists are members of this group.

Name	Institution	e-mail
Marco Arpagaus	MeteoSwiss	marco.arpagaus@meteoschweiz.ch
Jean-Marie Bettems	MeteoSwiss	jean-marie.bettems@meteoswiss.ch
Riccardo Bortolotti	ARPA-SMR	rbortolotti@smr.arpa.emr.it
Carlo Cacciamani	ARPA-SMR	ccacciamani@smr.arpa.emr.it
Ulrich Damrath	DWD	ulrich.damrath@dwd.de
Massimo Ferri	UGM	m.ferri@ecmwf.int
George Galanis	HNMS	galan@hnms.gr
Stefano Gallino	CMIRL (Genova)	stefano@cmirl1.ge.infn.it
Pirmin Kaufmann	MeteoSwiss	pirmin.kaufmann@meteoswiss.ch
Enrico Minguzzi	SMR Piedmont	enrico.minguzzi@csi.it
Tiziana Paccagnella	ARPA-SMR	t.paccagnella@smr.arpa.emr.it
Renata Pelosini	SMR Piemonte	renata.pelosini@csi.it
Ulrich Pflüger	DWD	ulrich.pflueger@dwd.de
Andrea Rossa	MeteoSwiss	andrea.rossa@meteoswiss.ch
Francis Schubiger	MeteoSwiss	francis.schubiger@meteoswiss.ch

The main activities of WG 5 for the period Oct 2000 - Oct 2001 covered the following points.

- The operational verification of predicted surface weather parameters is done at each COSMO site for the corresponding LM application. The observational basis are SYNOP stations and regional high resolution networks. Results are summarized in verification reports which are distributed on a quarterly basis on the COSMO web-site.

An internal Mini-Workshop on the verification of LM was held on 10-11 April 2001 in Bologna, together with the new working group on interpretation and applications. The participants addressed the following items.

  - Set-up of a limited area ensemble prediction system, based on a ECMWF super-ensemble, using LM at 10 km resolution,
  - Postprocessing tools and products,
  - Identification of deficiencies in the model performance as noticed from recent verification results,
  - New methods for the verification of precipitation,
  - Set-up of a common verification package for a LM test suite running at ECMWF.

- Development of a TEMP-verification package at DWD and MeteoSwiss has been completed. Results are distributed on a quarterly basis. A summary of the annual scores for 2001 can be found in COSMO Newsletter No.2.

- Verification of precipitation using high resolution precipitation analyses from ARPA-SMR for the Emilia Romagna region. The analyses are available every hour and are obtained by using surface raingauges and calibrated radar data.

- Daily verification of cloudiness with the Meteosat VIS channel at 12UTC. Coupling of VIS and IR data to define an objective method of cloud classification .

- Verification of precipitation forecasts using the Radar composite network.

The major work packages for 2002 include a continuation of the current operational verification of surface parameters using both GTS and special observational data from regional networks. Also, work on the verification of vertical profiles at TEMP stations and the verification of LM cloudiness using Meteosat VIS and IR data will be continued. A central aspect will be the definition of a common verification system to be used for a new parallel test suite at ECMWF.

6.6 Working Group 6: Reference Version and Implementation

The WG on code maintenance, reference version, documentation and implementation is headed by Ulrich Schättler (DWD) as WPC. The following scientists are members of this group.

Name	Institution	e-mail
Theodore Andreadis	HNMS	andrea@hnms.gr
Euripides Avgoustoglou	HNMS	euri@hnms.gr
Jean-Marie Bettems	MeteoSwiss	jean-marie.bettems@meteoswiss.ch
Davide Cesari	ARPA-SMR	dinamici@srm.arpa.emr.it
Helmut Frank	DWD	helmut.frank@dwd.de
Guy de Morsier	MeteoSwiss	guy.de.morsier@meteoswiss.ch
Paolo Patruno	ARPA-SMR	p.patruno@smr.arpa.emr.it
Jean Quiby	MeteoSwiss	jean.quiby@meteoswiss.ch
Ulrich Schättler	DWD	ulrich.schaettler@dwd.de
Jan-Peter Schulz	DWD	jan-peter.schulz@dwd.de
Lucio Torrisi	UGM	torrisi@ecmwf.int

In the period Oct. 2000 - Oct. 2001 the following work was done by WG 6:

- Procedures for filtering the orography have been included in the interpolation program GME2LM.
- Work on the interpolation programs has been carried on:
  - GME2LM has been updated to provide initial- and boundary conditions also for the new z-coordinate version of the LM and for the new multi-layer soil model. It also includes now optimizations for vectorization.
  - IFS2LM has been provided to nest LM into the ECMWF model.
  - Work on LM2LM to nest LM into itself is still going on.
- The reference versions of GME2LM and LM, which are maintained at DWD, have been updated and are installed and running at all COSMO member sites and at ECMWF. A formal procedure how to update and test new reference versions has been proposed at the Annual Meeting in Athens.
- The grib2v5d-project (Grib to Vis5d) has evolved and has its own web page now at http://grib2v5d.sf.net. There is a link in the COSMO web page.
- The public and the member area of the COSMO web page have been installed by HNMS.

Ongoing work of WG 6 in the next period is the update of the programs and their installation and testing at all sites. For this purpose, test suites for single cases and fixed time periods will be installed at ECMWF. Another task is the maintenance and update of the COSMO web page. Special tasks are the integration of all parts of the interpolation programs into a single INT2LM and the update of the model documentation. And finally, work on the 2-way interactive nesting version will be carried on.

7 COSMO Meetings and Events

This section summarizes the main meetings, workshops and seminars as well as management decisions from the previous year. Other COSMO activities such as guest scientists and internal visits are also considered. Finally, an overview of the forthcoming activities in the present COSMO working period is given.

7.1 Meetings in 2001

(1) COSMO Workshop on Verification and Interpretation

The members of Working Group 4 for Interpretation and Application and of Working Group 5 for Verification and Case Studies met on 10-11 April 2001 in Bologna at ARPA-SMR for a joint internal COSMO workshop.

The first day of the workshop started with six presentations of WG4. Three talks concerned the ARPA-SMR activities in the field of Limited Area Ensemble Predictions (LEPS) by presenting the methodology, case study results and the probabilistic evaluation of LEPS. The following talks considered the use of the Kalman filtering technique, an approach for downscaling of weather elements and a method for a statistical interpretation of high resolution surface weather parameters. The afternoon of the first day continued with presentations of WG 5. The first part of these talks focused on recent results of verification of the operational models in Germany, Switzerland, Italy and Greece using Synop observations. In the second part, various alternative methods for model verification and validation were addressed, such as the verification of precipitation against radar data, verification of cloud coverage using satellite data, a verification method depending on weather type, verification of precipitation using high-resolution non-GTS data for case studies or within hydrographical basins. Also, the state of advancements of the study on objective cloud classification using IR and visible meteosat data have been presented.

The second day of the workshop continued with separate discussions in WG4 (concerning the LM-LEPS, the use of statistical postprocessing methods, additional postprocessing products and guidelines for forecasters), and in WG5 (concerning basic verification methods, the set-up of a list with deficiencies of the model performance with respect to various surface parameters, organization of the exchange of observation data and of verification results between members), followed by a final plenary discussion. The plenum addressed mainly the set-up of a common verification package at ECMWF, where LM is installed and will be used for MAP case studies and for longer test suites (as reference runs for model changes) as well as for the LM-LEPS at 10 km resolution (covering a COSMO superdomain). A list of action was decided in order to achieve this objective in the near future.

A detailed workshop report has been prepared by C. Cacciamani and P. Eckert. This report has been distributed and is available on our web-site.

(2) Seminar on Scientific Applications of the LM

This seminar was organized by Jürgen Steppeler and was held at DWD in Langen, 21-23 May 2001. It was dedicated to research activities with the LM at various universities and covered various scientific topics. Central issues have been numerical methods for nonhydrostatic models and physical processes. Proceedings of the seminar have not been published, but two papers from this seminar (by Michael Baldauf and by Thorsten Reinhardt and Ulrike Wacker) appear in Section 9 of this Newsletter.

(3) Meeting of the Work Package Coordinators

The work package coordinators (WPCs, i.e. C. Schraff, J. Steppeler, M. Arpagaus, P. Eckert, C. Cacciamani and U. Schättler), the scientific project manager (SPM, G. Doms) and the chairman of the Steering Committee (M. Capaldo) met at DWD on 14 September 2001 in Offenbach. The first part of the meeting was dedicated to review the progress in the work packages, to identify problems and delays in specific WPs and to set up a list with model deficiencies and technical problems. The second part concerned some preparations for the next General Meeting in Athens: set-up of the agenda, proposals for new work packages, interdependencies and priorities of WPs, definition of goals for 2002 and items for the strategic discussion. The minutes of this meeting are available on the web-site.

(4) COSMO Workshop on Numerical Methods

The Members of the COSMO numerics group (WG2) met one day before the General Meeting on 2 October 2001 in Athens. The participants discussed the current state of dynamics and numerics in European NWP models. J. Steppeler gave an overview on numerical activities within SRNWP and within COSMO. Crucial questions, such as the efficiency of semi-Lagrangian schemes for nonhydrostatic modelling and problems in very high resolution simulation of mountain flow systems have been addressed. Also, problems of a more long-term interest, such as conservation form of the equations, adaptive meshes and global nonhydrostatic modelling have been discussed. The minutes of this internal workshop are available on our web-site.

(5) 3rd General Meeting of the COSMO Consortium

The recent COSMO general meeting was held in Athens (Greece) on 3-5 October 2001. It was hosted by HNMS and took place at the National Museum of War close to the centre of Athens. With about 40 participants (see Fig. 16), the meeting was well attended. It was a very stimulating meeting with many interesting presentations, with many discussions on various subjects, and with much organizational work on concrete work packages. The Director of HNMS, A. Economou, opened the meeting by a welcome address. G. Sakellaridis, the head of the HNMS Research Department welcomed us in Athens and presented further details about the organization of the meeting. The Chairman of the STC, M. Capaldo gave an account of the work of the Steering Committee and G. Doms summarized the activities of SPM and the WPCs during the year.

The first (public) part was organized in six main sessions according to our working group structure. The work package coordinators gave an overview on progress in the various research and development activities of the working groups, followed by presentations on selected issues by the responsible scientists. Each session was closed by a general discussion on central topics. Summaries of the talks including the slides are available on our web-site. Section 9 contains a number of contributions which emerged from the presentations in Athens.

The second (internal part) of the meeting was dedicated to formulate the research plan for the next period (Oct 2001 - Oct 2002). Delayed work packages and proposals for new ones have been presented by the WPCs and discussed in the plenum. Allowing time for this plenum discussion on future work packages was found to be a good idea and useful, not only for a cross-checking of interdependencies but also for more scientific input and ideas to the following workshops of the WGs. The proposals for work packages were oriented along some basic guidelines for the next working period.

Figure 16: Participants at the 3rd COSMO General Meeting 3-5 October 2001 in Athens. Front row (from left to right): Massimo Milelli, Elena Oberto, Andrea Rossa, Dieter Frühwald, Massimo Capaldo, Renata Pelosini, Tiziana Pacagnella, Davide Sacchetti, Simone Campagna, Christoph Schraff, Günther Doms, Ryzard Klejnowski. Second Row: Almut Gassmann, Jean Quiby, Matthias Raschendorfer, Sabine Theiss, Andrea Montani, Lucio Torrisi, Jürgen Steppeler, Heinz-Werner Bitzer, Maric Djordje, Jean-Marie Bettems. Back row(s): Erdmann Heise, Euripides Avgoustoglou, Panagiotis Skrimizeas, Jan-Peter Schulz, Konstantina Zeini, George Galanis, Pierre Eckert, Maria Refene, Dmirtii Mironov, Georges Sakellaridis, Davide Cesari, Carlo Cacciamani, Stefano Tibaldi, M. Arpagaus, Massimo Ferri, Ulrich Schättler, Ulrich Damrath. Jaques Ambühl is taking the photo.

- Consolidation, Upgrade and Documentation of the LM
  - tuning and optimization for both model and data assimilation components
  - operational use of the new physics package
  - increased quality of the precipitation forecasts
  - assessment of the 'realism' of high-resolution forecasts
  - continue work on 2-way interactive self-nesting
  - update and complete the documentation of the model system
- Application and Interpretation
  - installation of a limited area EPS system based on the ECMWF ensemble
  - statistical interpretation of high resolution forecasts
  - new postprocessing products
- Towards the Meso-γ Scale
  - continue work on the z-coordinate version of the model
  - experimental work and test suites
  - development of a 3-D turbulence scheme
  - inclusion of graupel and hail in the microphysics scheme
  - development of a shallow convection scheme

Detailed work plans have then been set-up by the working groups in separate workshops, which afterwards were presented to the plenum. The last part of the meeting was dedicated to a general discussion on goals and perspectives. The final version of the work plans and a short description of each work package is available on the member area of our web-site.

(6) 6th Meeting of the COSMO Steering Committee

The 6th meeting of the STC wos held on 5 October 2001 during the COSMO general meeting in Athens (participants: M. Capaldo, G. Sakellaridis, D. Frühwald, J. Ambühl and R. Klejnowski). M. Capaldo informed the STC on the recent signature of the COSMO Agreement, and welcomed Dr. Ryszard Klejnowski as an invited observer from IMGW of Poland. The STC agreed on certain steps of action concerning computer resources at ECMWF for the COSMO LEPS. Another topic has been COSMO products and their use in the framework of EUCOS rules for commercialization. Also, staff resources for the maintenance and the definition of the LM reference version have been discussed. Regarding the COSMO perspective and goals for the comming period, the STC expressed that quality items of precipitation forecasts were considered of paramount importance, together with product-oriented post-processing.

R. Klejnowski confirmed the intention of IMGW to join the COSMO group. In this framework, a copy of the final version of the Agreement as well as the template of the Declaration of Membership page has been provided to Dr. Klejnowski for further analysis by the relevant authority. R. Klejnowski kindly offered to organize the next COSMO annual meeting in Warsaw on 25-27 September 2002.

(7) 7th Meeting of the COSMO Steering Committee

The 7th meeting of the COSMO Steering Committee was held in Roma at UGM/CNMCA on 20 December 2001 (participants: M. Capaldo, G. Sakellaridis, D. Frühwald, J. Ambühl and G. Doms). The SPM presented the draft work plans for upcoming COSMO period as prepared by the WPCs. All work packages have been approved, some with a couple of modifications. The final version of the work plans are available at the member area of our web-site. Further points of discussion have been computer resources for COSMO LEPS and COSMO products. M. Capaldo also reported on latest informations from IMGW in Poland. Minutes of this meeting will be available on the member area of our web-site.

7.2 Guest Scientists

Luca Bonaventura from the University of Trento (Italy) stayed at DWD as a guest scientist for three weeks in April and for two weeks in May 2001. During his first visit, the concrete work on the new z-coordinate was continued and specific numerical questions related to the shaved element discretization have been addressed.

For 2001, we had planned to have Jack Kain (NSSL, Norman, USA) as a guest scientist at MeteoSwiss for final implementation and tuning of his convection scheme. And DWD had invited Louis Wicker (NSSL, Norman, USA) for implementation and testing of his new two-time level integration scheme. Unfortunately, both scientists had to cancel their visits due to certain circumstances. We hope that we can reorganize these visits at later time.

7.3 Internal Visits

E. Avgoustoglou from HNMS visited DWD two weeks in April 2001. He has taken responsibility for the work package on 2-way interactive nesting. Together with U. Schättler, he worked on the re-implementation of the existing but old test version into the recent model cycle. First successful runs on single cases were performed. The final permanent implementation into the source code will be done later.

In spring 2001, M. Arpagaus from MeteoSwiss visited DWD. The current status, progress and problems in work packages in WG 3, which mostly reside at DWD, have been discussed.

7.4 Upcoming COSMO Meetings

The following COSMO workshops and meetings are planned for 2002. Some other meetings related to COSMO are also included.

6-8 February 2002: COSMO-Workshop on Verification and Physics
at CSI Piemonte, Torino (I)
Discussion on the status and problems of the activities in WG3 and WG5.

April/May 2002: Meeting of the Work-Package Coordinators
at DWD, Offenbach (D).
Assessment of the progress of WPs, identification of problems and delays, and some preparations for he next General Meeting. The SPM will invite for this meeting during March.

27-29 May 2002: LM User Seminar
at DWD, Langen (D)
This seminar is dedicated to research activities and scientific applications of the LM at various universities and research institutes. The this years seminar will also include tutorials on numerics and on the LM Package. For information on the seminar and the preliminary agenda, please contact J. Steppeler (juergen.steppeler@dwd.de).

24 September 2002: COSMO-Workshop on Numerical Methods
IMWG, Warsaw, Poland
Discussion on new numerics and dynamical cores. J. Steppeler will invite for this workshop during the year.

25-27 September 2002: 4th General Meeting of the COSMO Consortium
IMWG, Warsaw (Poland)
Progress Reports from the Working Groups and presentation of results from the work packages; discussion and set-up of a scientific work plan for 2003.

November 2002: Meeting of the Steering Committee
UGM, Rome (I)
Regular business meeting, revision of work packages and definition of the final COSMO work plan for 2003.

7.5 Announcements

At the recent COSMO general meeting we agreed to have more active participation at international conferences, workshops and seminars. This section lists a number of meetings which are of specific interest for active participation. Of course, this list is by no means complete.

MAP Meeting 2002 with the 10th AMS Conference on Mountain Meteorology
17-21 June 2002, Park City UT, USA (www.ametsoc.org/AMS/meet/FAINST/10mount02.-html).

European Conference on Severe Storms
26-30 August, Prague, Czech Republic (www.chmi.cz/ECSS2002).

International Conference on Quantitative Precipitation Forecasting (QPF)
2-6 September 2002, University of Reading, UK (www.met.rdg.ac.uk/qpf).

ECMWF Seminar on Recent Developments in Predictability Studies
9-13 September 2002, Reading, UK (www.ecmwf.int/services/training/index.html).

October 7-10: 24rd EWGLAM and 9th SRNWP meeting
KNMI, De Bilt, Netherlands
The scientific topic of this meeting is *Clouds and Precipitation at High Resolution.*

Second European Conference on Radar Meteorology (ERAD)
18-22 November 2002, Delft, Netherlands (www.copernicus.org/erad/index2002.html).

Also, three SRNWP workshops are scheduled for. One of the Lead Centre for variational methods, one of the Lead Centre for numerical techniques, and one of the Lead Centre for statistical and physical adaptations. The exact dates and locations are not yet fixed. Please refer to the SRNWP Homepage (srnwp.cscs.ch) for more information.

8 Verification of the Operational Models

This section summarizes some of the operational verification results for the LM forecasts at various COSMO meteorological centres. More detailed detailed verification results are presented on a quarterly basis at the COSMO web-site.

8.1 Verification of Surface Weather Parameters

8.1.2 Operational Verification at DWD

(Ulrich Damrath, DWD)

For objective verification of surface weather elements predicted by the LM running at DWD, the standard verification package of the research and development department is used. Verification scores are derived on a daily, weekly and monthly basis for various sets of SYNOP observation stations.

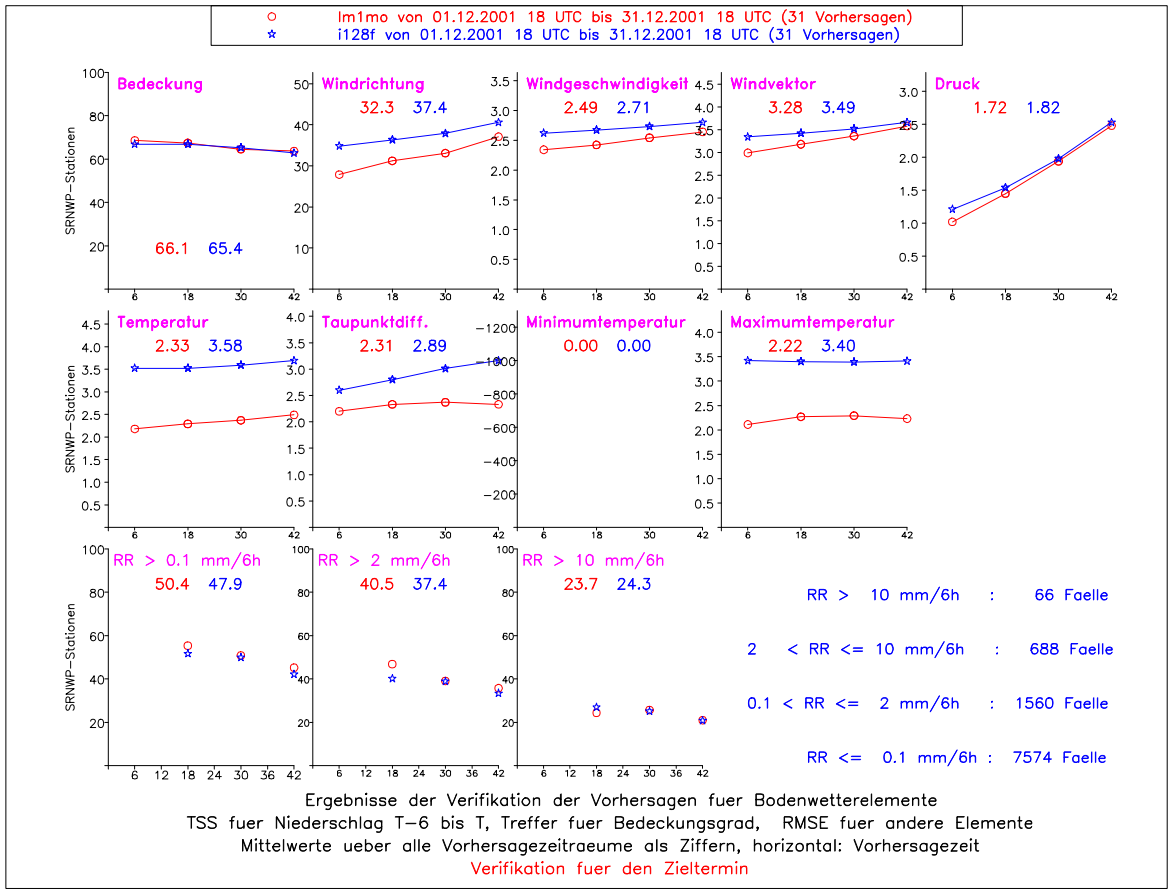

Figure 17: Mean verification scores for December 2001, valid at 18 UTC, as a function of forecast time (06,18,30 and 42 hrs) at all SRNWP-stations in the integration domain. Red: LM, blue: GME. RMSE for all elements except for cloud cover (hit rate) and precipitation (TSS); numbers are mean values over all forecast times. Top: cloud cover, wind direction, wind speed, wind vector and surface pressure (from left to right). Middle: temperature, dew point difference, minimum and maximum temperature (from left to right). Bottom: 6 hr precipitation amounts for 3 thresholds: 0.1mm, 2mm and 10mm. The observed numbers of observations in each class is also indicated.

As an example, Figure 17 shows the verification results for LM and the driving global model GME obtained for December 2001 for all SRNWP-stations in the LM integration domain. These stations have been selected by the EWGLAM NWP-group to be representative for a larger horizontal domain, thus allowing for a direct comparison with gridpoint model output with an only small systematic error. The root mean square errors of predicted wind direction, wind speed and wind vector as well as of surface pressure are smaller in LM than in the coarse grid global model GME. This is expected because the impact of the topography is much better represented in a high resolution model. The root mean square errors of 2m-temperature, dew point and maximum 2m-temperature are significantly smaller than in GME. They are also much smaller than the scores from winter 1999/2000. This might indicate a positive impact of the new TKE-based turbulence and surface-layer scheme. No clear advantage can be seen for cloud cover where the hit rate has about the same values in LM and in GME. For predicted precipitation, the LM has a slight advantage compared to GME, especially for the yes/no-decision (>0.1mm class) and for thresholds > 2mm/6h. For heavy precipitation events (>10mm class), the scores are similar.

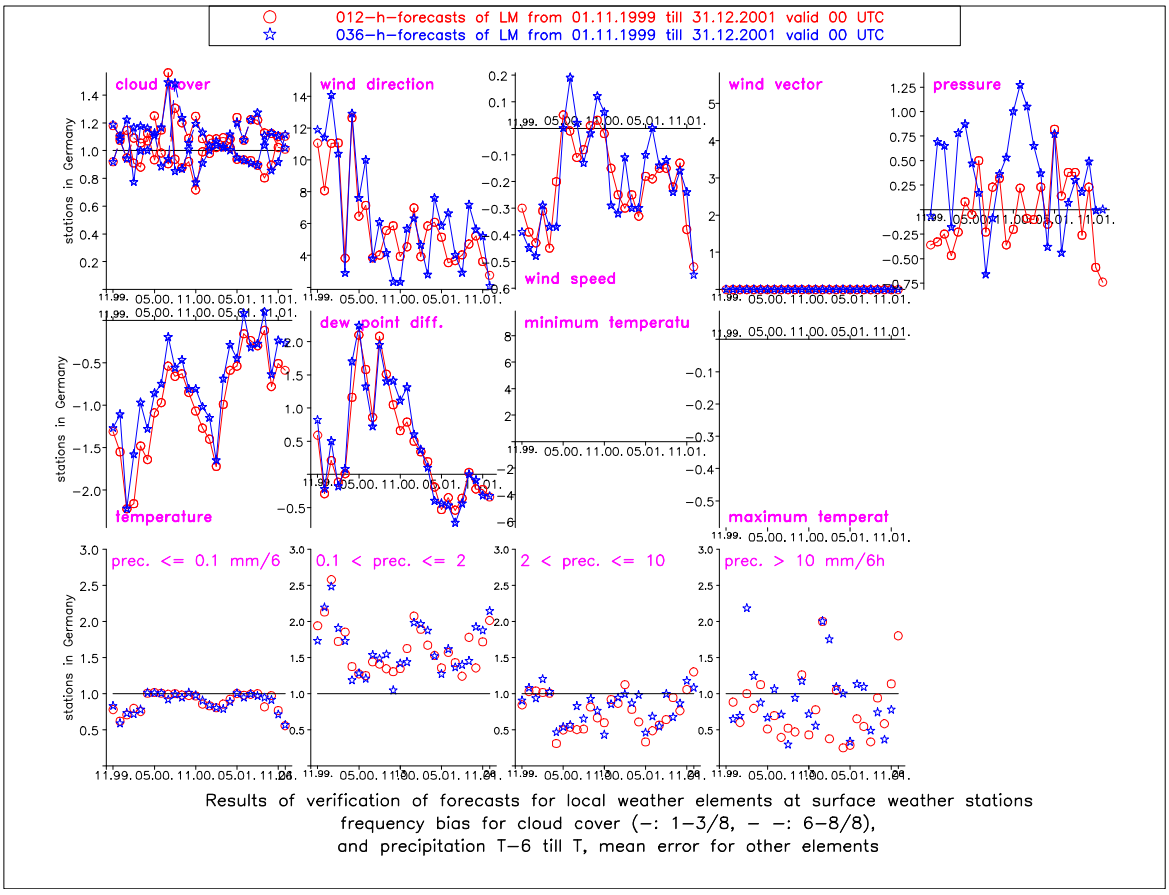

Figure 18: Mean monthly verification scores at all stations in Germany valid at 00 UTC as a function of time (from November 1999 until December 2001) for two forecast times (red: + 12h, blue: + 36h). Mean error for all elements except for cloud cover (frequency bias) and precipitation (frequency bias). Top: cloud cover, wind direction, wind speed, wind vector and surface pressure (from left to right). Middle: temperature, dew point difference, minimum and maximum temperature (from left to right). Bottom: 6 hr precipitation amounts for 3 thresholds: 0.1mm, 2mm and 10mm.

The time evolution of the mean monthly scores at all stations in Germany from November 1999 until December 2001 is shown in Figures 18 and 19 for two forecast times: 12 h and 36 h. Verification time is 00 UTC. The mean errors of wind speed and (Fig. 18) show

an annual variation with a large negative bias during winter/spring, whereas a smaller bias occurs during the summer months. Also, the rmse error of wind speed and wind vector is smallest during summer (Fig. 19). A seasonal variation of the scores for cloud cover can also be noticed: the hit rate (Fig. 19) is highest during autumn/winter and smaller during spring/summer. This indicates a problem in the parameterization of convection and convective cloud cover.

A similar effect can be seen for temperature: the mean errors have a large negative bias during winter and spring, which becomes much smaller in the summer and autumn months. (Fig. 18). The 2m-temperature rmse error is also smallest for the summer season (Fig.19). In the course of 2000/2001, there is a clear trend for a reduction of the rmse errors for the predicted of 2m-temperature and 2m-dewpoint. This can be attributed to the impact of the soil moisture analysis and the new turbulence scheme.

The precipitation scores (frequency bias in Fig. 18, thread skill score in Fig. 19) do also show some annual variation. Medium and heavy precipitation events (> 2mm/6h and > 10mm/6h) appear to be underpredicted. On the other hand, light rain in the range from 0.1 to 2 mm/6h is overpredicted, especially during winter.

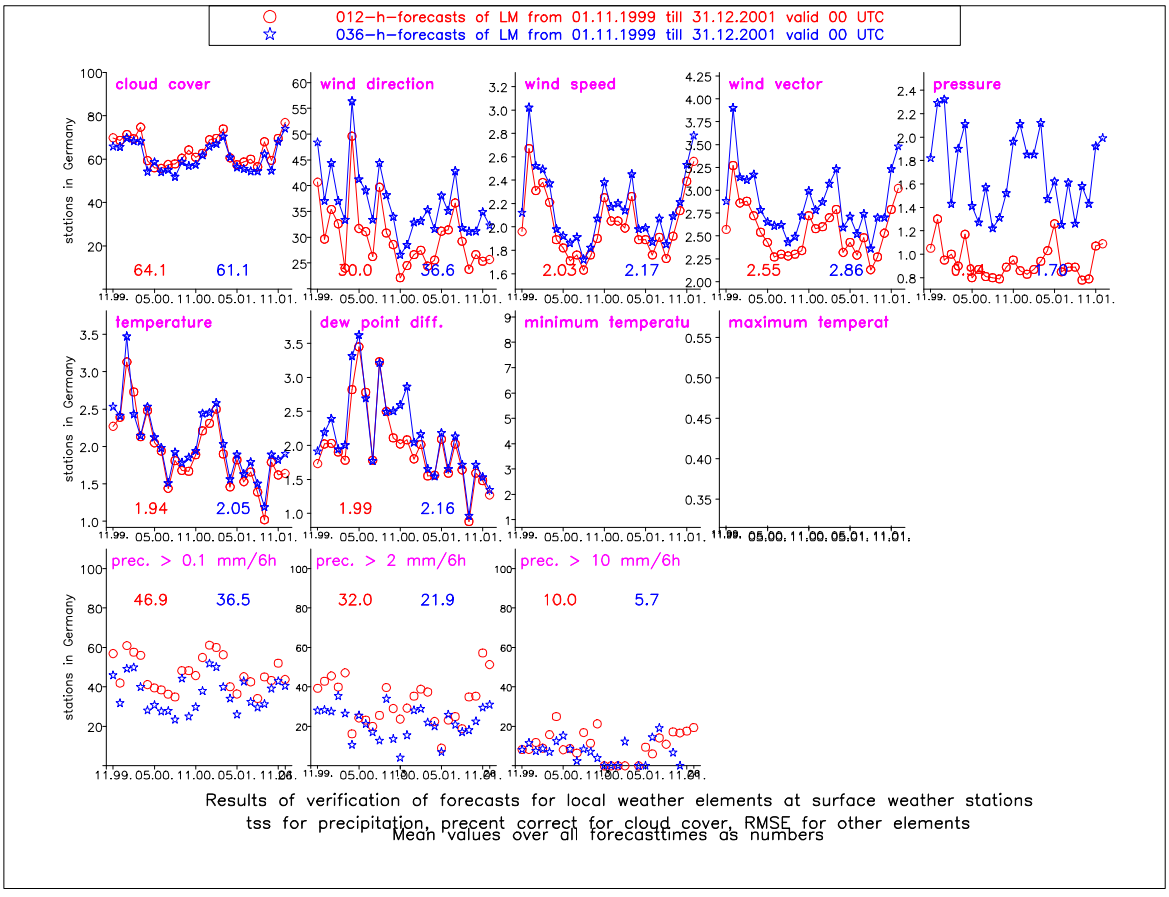

Figure 19: Mean monthly verification scores at all stations in Germany valid at 00 UTC as a function of time (from November 1999 until December 2001) for two forecast times (red: + 12h, blue: + 36h). RMSE for all elements except for cloud cover (hit rate) and precipitation (TSS); numbers are mean values over all forecast times. Top: cloud cover, wind direction, wind speed, wind vector and surface pressure (from left to right). Middle: temperature, dew point difference, minimum and maximum temperature (from left to right). Bottom: 6-hr precipitation amounts for 3 thresholds: 0.1mm, 2mm and 10mm.

8.1.2 Operational Verification at MeteoSwiss

(F. Schubiger, MeteoSwiss)

The following nomenclature for LM is used in the text below: aLMo means the LM version operational at MeteoSwiss since July 2001, LMD means the operational LM version of DWD.

(a) High Resolution Verification of Daily Cycle over Switzerland

Results of aLMo and LMD have been computed monthly and seasonally for 2m-temperature, 2m-dewpoint and 2m-dewpoint depression, 10m-wind, precipitation (hourly sums for daily cycle and 6h sums for scores) and for cloud cover (3-hourly intervals). Different testversion of aLMo have also been verified. These non-operational verification results are discussed in Chapter 9.

The following points are of main interest:

- The 2m-temperature cooling in the night is too pronounced and the diurnal amplitude is too large (with the exception of Summer for gridpoints < 800m) and the daily maxima is reached ~ 1.5 hour too early. Till Summer 2001, the diurnal amplitude was ~ 0.5 K larger in LMD than in aLMo. The 2m-temperature negative bias is quite pronounced in wintertime. During nighttime in the winter 2000/2001 it was of the order of 3K for gridpoints < 800m and even ~ 5K for gridpoints > 1500 m.

- The 2m dewpoint depression shows the great impact of the new TKE scheme operational at DWD since April 2001. The daily cycle of aLMo (without that modification) is much too little (aLMo always too dry during nighttime) and the daily cycle is not well reproduced (see Section 9 *"Verification results of aLMo with/without new TKE-scheme"*).

- The results for precipitation show differences between aLMo and LMD especially in Spring and early Summer. LMD gives less precipitation than aLMo (see Figure 5a on report *"Comparison for forecasts with/without nudging"* in Section 9: LMD (blue dotted line) gives 20% less than aLMo during Summer 2001). Table 10 summarizes the scores of frequency bias of the four seasons for the thresholds 0.1, 2, 10 and 30 mm/6h for aLMo and LMD. The high amounts of precipitation (10 mm/6h) are underestimated in LMD by $\sim 40\%$ and in aLMo by only $\sim 5\%$. The rare events of very high amounts (30 mm/6h; observed in 0.23% of all cases) showed great differences between aLMo and LMD: strong overestimation in aLMo, strong underestimation in LMD. The causes of such differences will be investigated more in detail.

- Verification of 10m-wind (for stations below 800m) gave an overestimation of the windspeed of ~ 0.5-1.0 m/s both in aLMo and LMD.

- Total cloudiness gave similar results in aLMo and LMD. In summer the mean daily cycle is not well reproduced (maxima at $\sim$ 06 UTC instead of $\sim$ 15 UTC; see Figure 6a in report of *"Comparison for forecasts with/without nudging"* in Section 9).

(b) Daily verification of LMS/SM cloudiness with the Meteosat VIS-Channel

This verification is operational for the full aLMo domain.

(c) Verification of the vertical profiles at TEMPs stations

See Section 8.2.1 for the operational verification of vertical profiles.

Table 10: Frequency bias (%) of predicted precipitation over Switzerland. For all 6-h sums from + 6h till + 48h of all 00 UTC and 12 UTC forecasts, compared to 69 ANETZ stations. The LM precipitation is the mean over 5 gridpoints.

Threshold	Winter 00	Spring 01	Summer 01	Autumn 01
0.1 mm / 6 h				
aLMo	139	137	148	130
LMD	121	112	107	112
SM	129	114		
2.0 mm / 6 h				
aLMo	101	124	115	112
LMD	86	92	80	89
SM	87	102		
10 mm / 6 h				
aLMo	69	113	93	105
LMD	52	66	51	72
SM	55	122		
30 mm / 6 h				
aLMo	74	133	182	112
LMD	22	14	73	62
SM	100	290		

(d) Subjective verification of LMS by bench forecasters

The bench forecasters of MeteoSwiss continued in 2001 their subjective verification of aLMo (see COSMO Newsletter No.1, p. 51). Emphasis is given to the general performance of aLMo and to the relative performance as compared (a) to the SM till July 2001 and (b) to testversions of aLMo since August 2001 (aLMo-forecasts issued from nudging assimilation in Geneva and aLMo with prognostic TKE scheme in Zurich). The results obtained for the comparison aLMO vs SM showed that the forecasters judged the aLMo quite similar as the SM: aLMo provides a little bit superior forecasts compared to SM for fronts (structure and timing) and 10m-windfields. Precipitation were judged a bit worse in aLMo than SM (especially in June-July 2001). Results for the forecasts issued from nudging assimilation showed – compared to those issued transformed GME-fields – a positive impact in the time range +0..+18h for 10m-windfield and especially for precipitation.

8.1.3 Operational Verification at ARPA-SMR

(Frederico Grazzini, ARPA-SMR, Bologna)

At the moment, the operational verification procedure at ARPA-SMR is performed only for the first integration (D+1) day with 6h step. The following models are verified: ECMWF (run starting at 00 UTC), LAMBO (run starting at 00 UTC) and LM (ARPA-SMR version ALMO, run starting at 00 UTC). Various scores are calculated for the surface weather parameters

– 2-m temperature
– 2-m dew point temperature
– 10-m wind
– total cloud cover

– 6h total precipitation amount

Figure 20 shows the distribution of the stations used for verification. Stations were divided in classes according to their geographical location; mountain stations (> 700m) are indicated with red circles, inner lowland stations with green circles, cyan and blue circles indicate coastal stations.

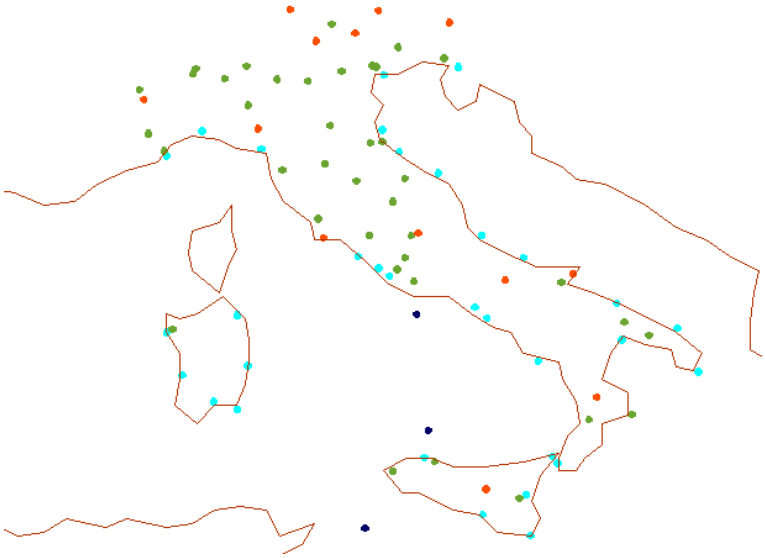

Figure 20: Italian Synop Stations-Type Classification. Blue and Cyan: Coastal; green: Lowland; orange: Mountain H > 700m.

Station subdivision in classes has designed in order to check systematic errors related with different geographical and surface conditions. This approach can give two type of results: information about models ability in reproducing correct surface processes through a correct climatology in different geographical areas, indication of possible error source through error comparison in different areas.

Following COSMO WG5 specification, we decided to adopt nearest grid point interpolation, provided the grid point was a land type and the altitude mismatch with synop height was lower than 100 m. If one of these two conditions it is not satisfied, for example the latter, we chose among the four surrounding grid-point, the one that is land type and that minimize the altitude mismatch. This criteria is applied for the whole set of variables.

The main results for Winter 2000/01 and Spring 2001 are summarized below (here, only a few examples are shown; more detailed verification results are presented on a quarterly basis at the COSMO web-site).

2-m Temperature
Cold Bias for all models in all areas, more pronounced in Lambo and Lokal Modell. Small error sensitivity respect to different flat areas as coastal and lowland. In these two areas MAE (Mean Absolute Error) is about 2 and 3 degrees. The comparison with mountain stations shows higher MAE and a bigger daily error cycle, especially for LM, with a strong cooling during night.

2-m Dew Point Temperature
Very different behaviour among models. ECMWF shows a very little negative bias, Lambo a constant positive bias and LM, on the contrary, a very strong negative bias. Bias in LM

goes to zero only at 12 UTC.

10-m wind

Wind error intensity happen to be quite sensible respect to different areas. ECMWF has a tendency to underestimate intensity while Lambo and LM to a lesser extent, to overestimate. Over mountain area all models show an negative bias. Also MAE shows differences ranging from 1.5 - 2 m/s in lowland areas up to 2.5 - 3 m/s in mountain areas (see Figure 21).

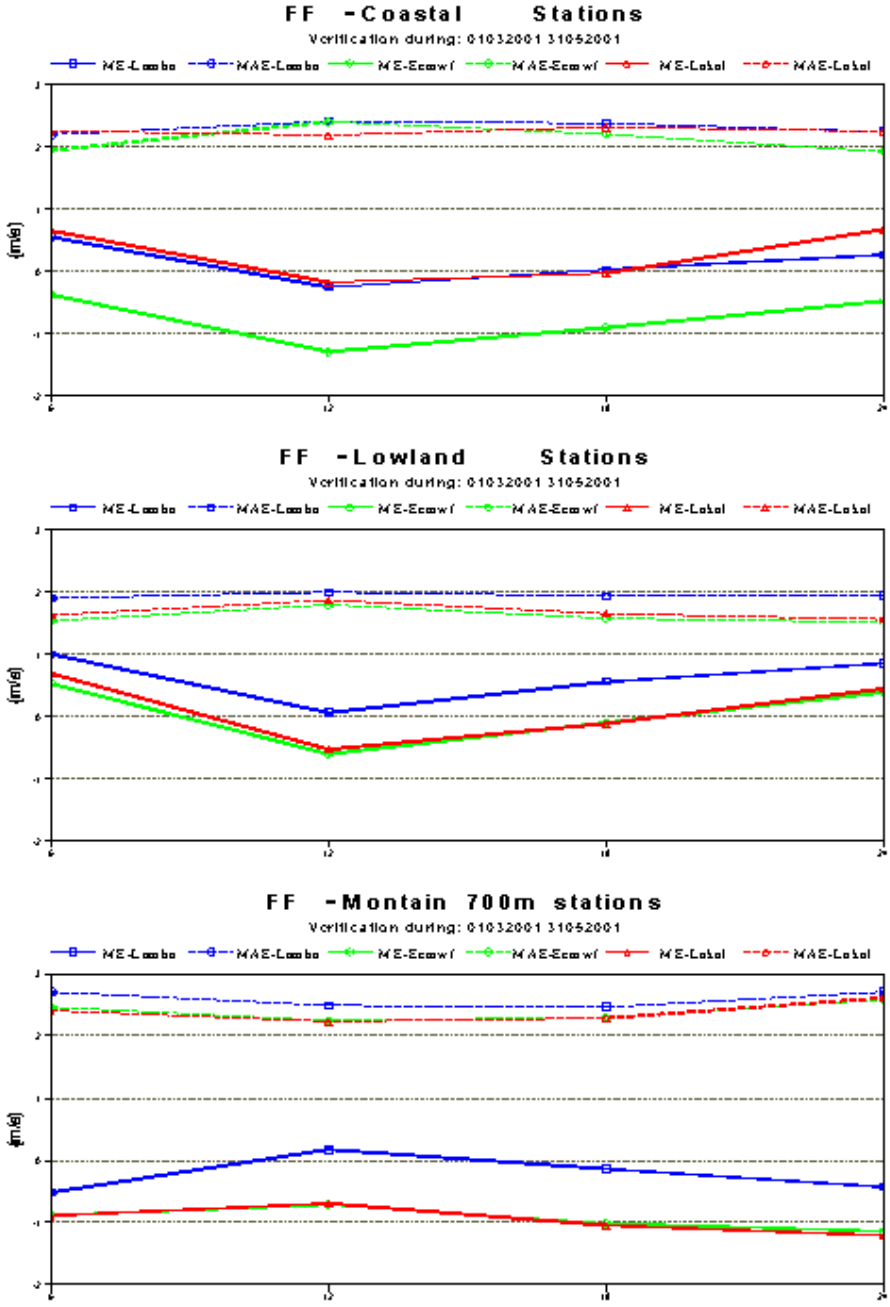

Figure 21: Mean error (ME, full lines) and mean absolute error (MAE, dashed lines) of 10-m wind speed (in m/s) for Spring 2001 as function of forecast time (0, 12, 18 and 24 h) for coastal stations (top), lowland stations (middle) and mountain stations (bottom). Lambo: blue, ECMWF: green, Lokal Model: red.

Total Precipitation
The POD and FAR scores for 6-h precipitation amount (calculated from contingency tables for all stations and forecast times) reveal an advantage of LM respect to the other models in terms of POD at higher thresholds (10mm and 20mm thresholds). However, together with POD, also FAR is increasing even if it is about on the same level of other models. To check if this increase in POD is not due to a unreal tendency of producing lot of high precipitation events we check also forecast precipitation frequency distribution against observed. Results are that LM seems to be the best with the closest distribution respect to observed at all thresholds (see Figure 22).

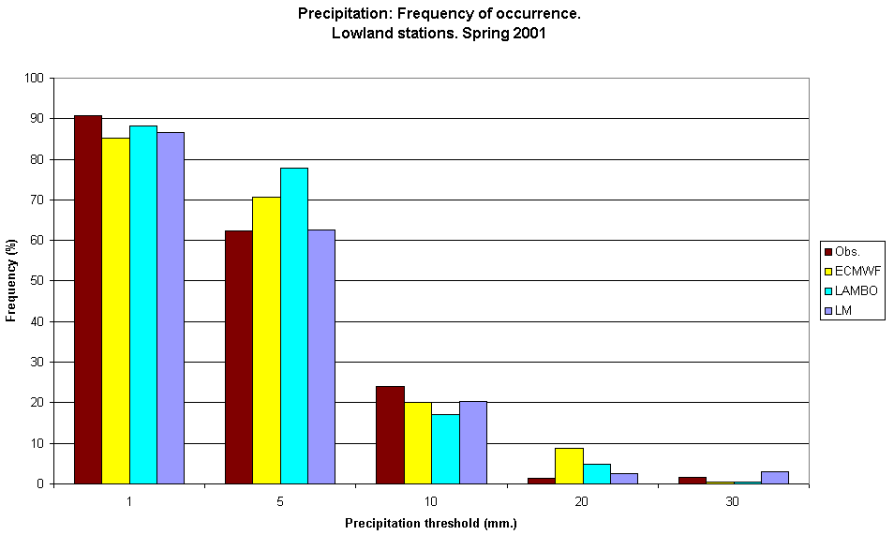

Figure 22: Frequency of occurrence computed for 6h total precipitation amount at different thresholds for Lambo (light blue), ECMWF (yellow) and Lokal Model (purple). Observations in red.

8.1.4 Operational Verification at HNMS

(George Galanis, Eleftheria Tsiniari, Maria Malafouri, HNMS)

In this note we present an outline of the operational verification procedure held in Hellenic National Meteorological Service concerning the direct outputs of LM on surface weather parameters. More precisely, we checked the performance of the model during the year 2001 for:

– 2-m Temperature,
– Sea Level Pressure,
– 10-m Wind Speed,
– 10-m Wind Direction.

The Synop stations used were those of Athens (16716), Thessaloniki (16622), Herakleion (16754), Corfu (16641), Larissa (16648), Limnos (16650), Naxos (16732), Santorini (16744) and Kozani (16632). In order to obtain the forecast values over the area of each station we interpolate the results of the five nearest grid points, a fact that leads, at least in some cases, to systematic errors. However, by using certain types of Kalman filtering, we achieve to eliminate the greatest part of the aforementioned problems.

The main conclusions form the verification of surface parameters are summarized as follows.

- We encountered significant systematic errors, especially at near coast locations during the summer period.
- The Kalman filtering used gives excellent results towards the improvement of the final forecast, since it eliminates the systematic error and decreases the standard deviation of the absolute error.
- There is a 24-hour periodicity at the distribution of errors and its standard deviation in forecast time.
- The model presents better performance at the winter period.
- We observed increasing with time error and deviation of it for the sea level pressure.
- Wind parameters behave better at island stations

In the following Figures 23 - 25 we present some characteristic results of the methodology adopted.

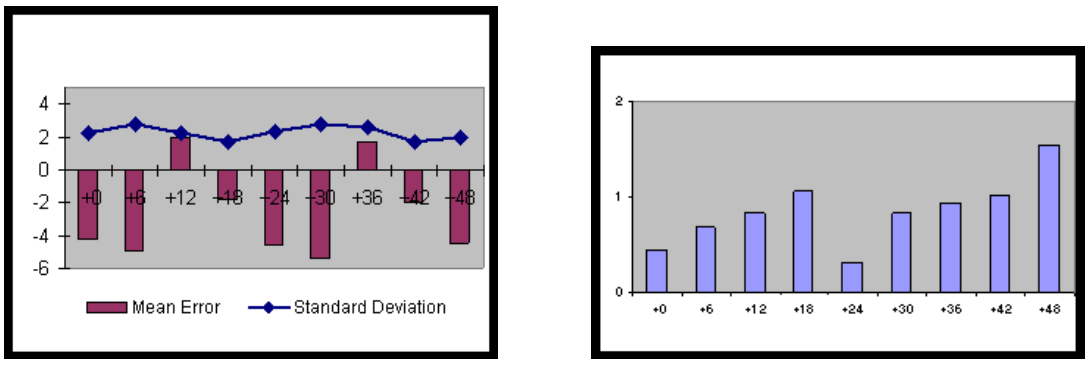

Figure 23: Left: Evolution in forecast time of the mean error and of the standard deviation of 2-m temperature at the Station of Corfu for the period September - December 2001. Right: Evolution in forecast time of the root mean square error of sea level pressure at the station of Naxos for the period September - December 2001.

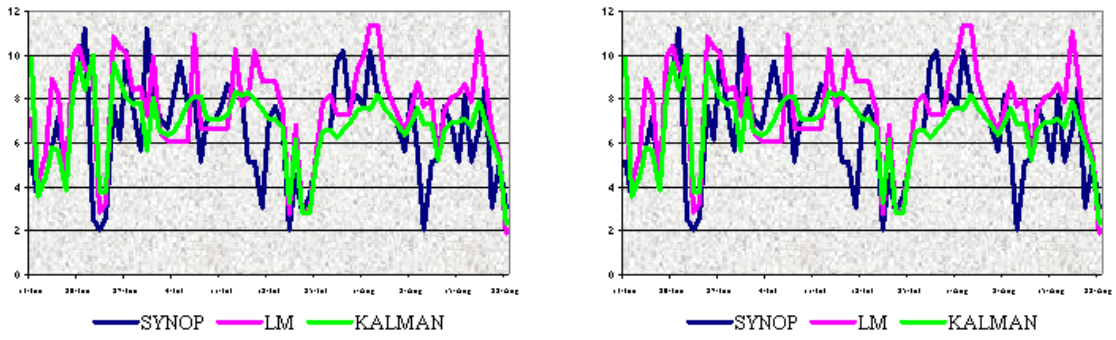

Figure 24: Left: Athen's 2-m temperature at 18 UTC corrected by Kalman filtering for the period June - August 2001. Right: Santorini's 10-m wind speed at 12 UTC corrected by Kalman filtering for the period June - August 2001.

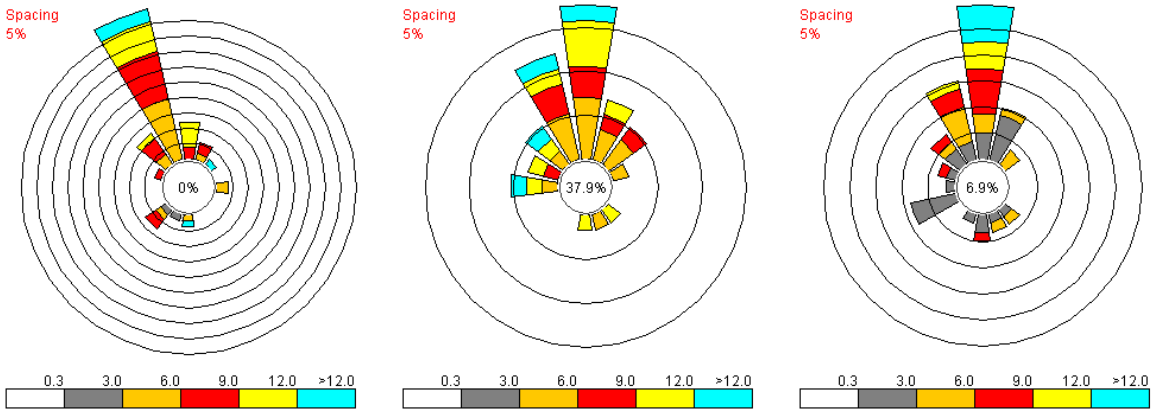

Figure 25: Wind Roses for the station of Athens at 00 UTC. The first one corresponds to the observed values, the second to the analysis of the model and the third to the 24th hour forecast.

8.2 Verification of Vertical Profiles

Both at MeteoSwiss and DWD a software package for the verification of the vertical structure by comparison of the model atmosphere with radiosonde data has been developed and is operational. The packages allow for monthly, seasonal and yearly verification at individual TEMPs stations and for sets of stations.

8.2.1 Operational Verification at MeteoSwiss

(*Marco Arpagaus, MeteoSwiss*)

The operational upper-air verification at MeteoSwiss uses a set of 28 TEMP stations all over the integration domain to verify the vertical structure of the forecasts. For the operational setup of the Alpine Model (aLMo), refer to section 4.4 in this Newsletter. In particular, note that aLMo forecasts start from their own analysis fields (nudging scheme) since 1st of November 2001.

Figures 26–30 show the average vertical structure for all 28 stations for the full climatic year 2001 (averaged over verification times 00 & 12 UTC). More results are available within the member area of the COSMO website at http://www.cosmo-model.org.

The most prominent feature in the verification plots for *geopotential* (c.f. figure 26) and *temperature* (c.f. figure 27) is the drastic increase of the geopotential mean error in the stratosphere. The reason for this is probably related to an error in the interpolation scheme for pressure and temperature.

In the lower troposphere, temperature and geopotential validate very well. From the middle atmosphere up to the tropopause, a significant negative bias in the temperature profile hints to a systematic model deficiency, which is not yet understood.

At and above the tropopause level, the mean error for the temperature fluctuates back and forth and produces a saw-like structure. The reason for this is most probably linked to the behaviour of the geopotential mean error discussed above. Concerning the standard deviation, both geopotential and temperature consistently show largest spread around the tropopause level.

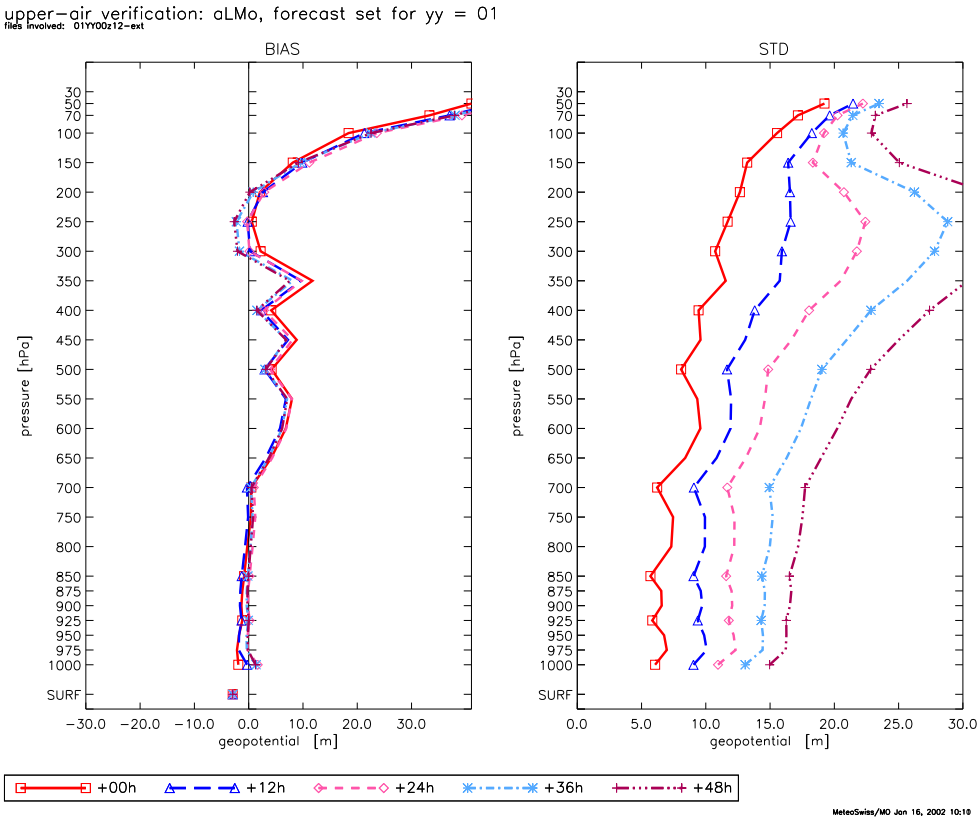

Figure 26: Mean error (BIAS) and standard deviation (STD) for the geopotential. Various forecast times with verification times 00 & 12 UTC for the climatic year 2001 (1.12.2000–30.11.2001).

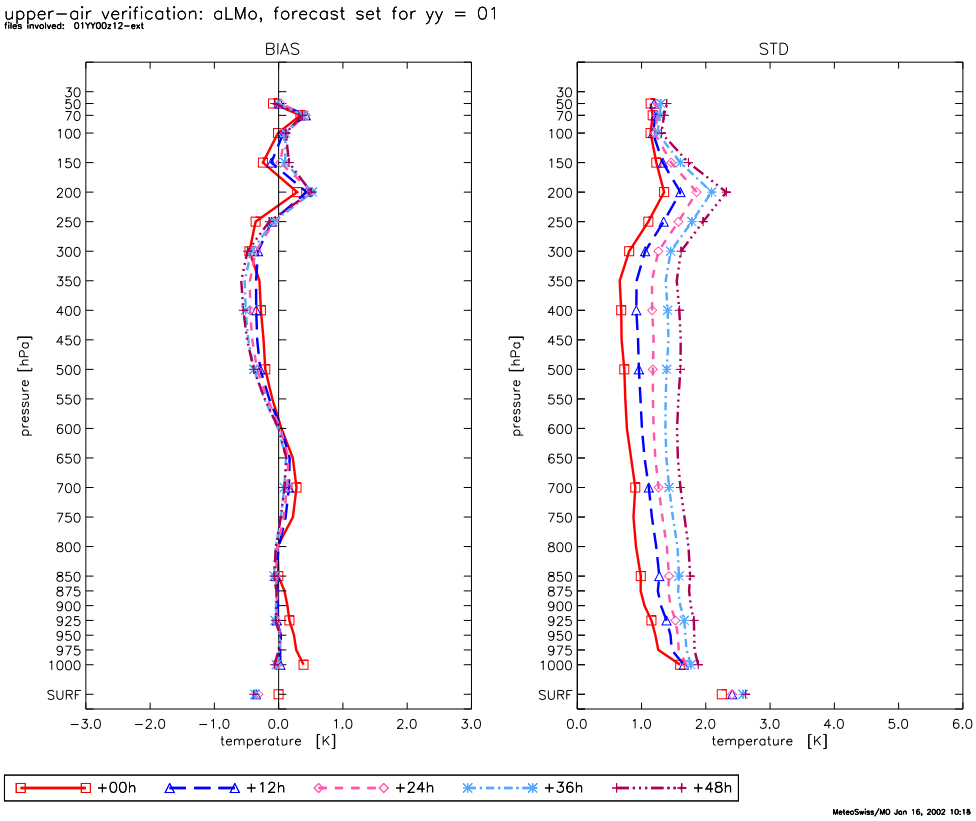

Figure 27: Mean error (BIAS) and standard deviation (STD) for temperature. Various forecast times with verification times 00 & 12 UTC for the climatic year 2001 (1.12.2000–30.11.2001).

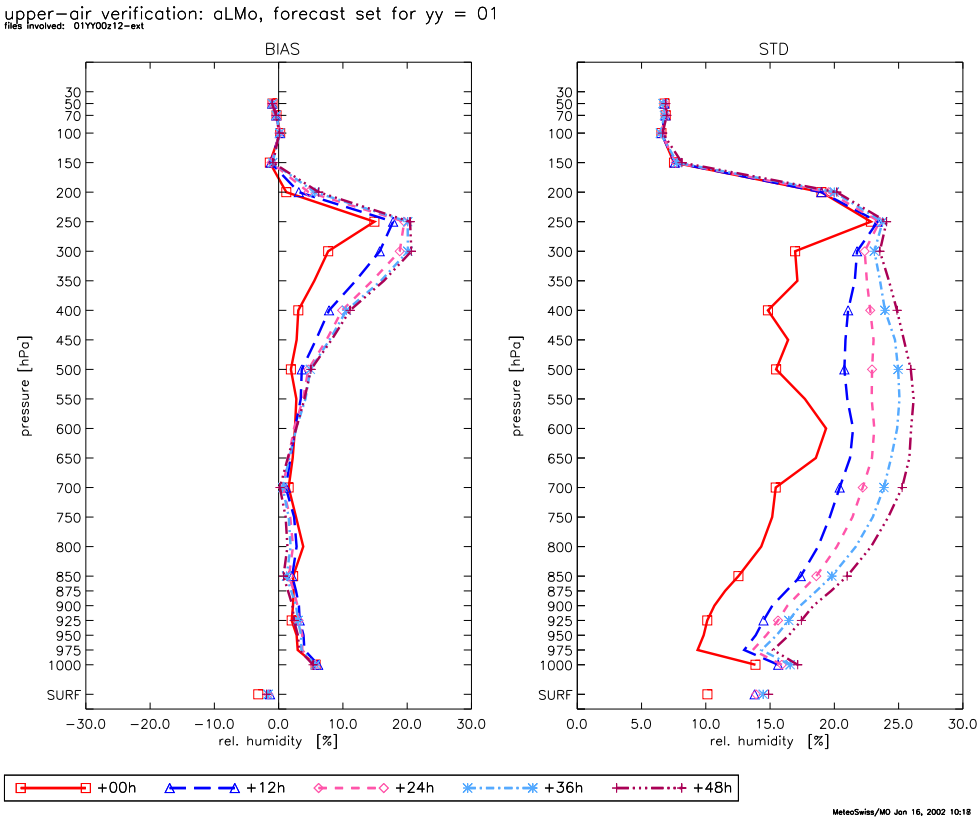

Figure 28: Mean error (BIAS) and standard deviation (STD) for relative humidity with respect to water. Various forecast times with verification times 00 & 12 UTC for the climatic year 2001 (1.12.2000–30.11.2001).

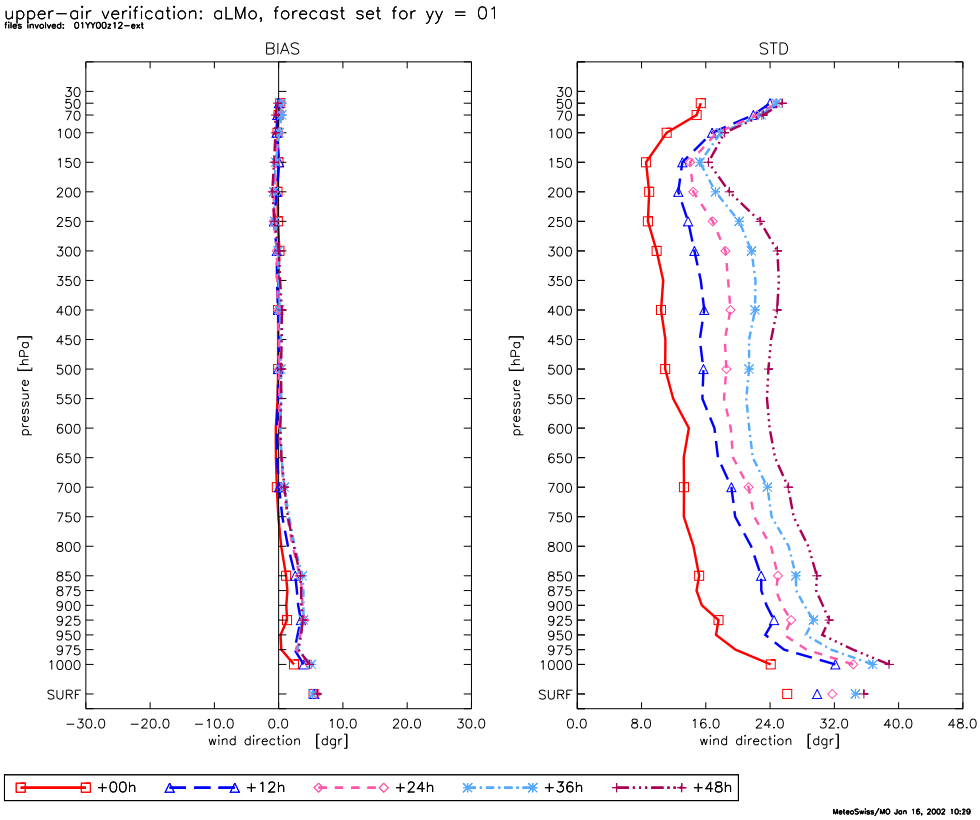

Figure 29: Mean error (BIAS) and standard deviation (STD) for wind direction. Various forecast times with verification times 00 & 12 UTC for the climatic year 2001 (1.12.2000–30.11.2001).

Up to 700 hPa, the mean error for the forecasted *relative humidity* (c.f. figure 28) is reasonably small, with a tendency to positive values towards the surface. Above 700 hPa, relative humidity with respect to water is not a good quantity to look at and the results should therefore be interpreted with great care.

The mean error of the *wind direction* (c.f. figure 29) is small,especially above the boundary layer. As expected, there is a clear increase for both mean error and standard deviation towards the surface. A deterioration of the standard deviation is also observed in the stratosphere.

The mean error of the *wind speed* (c.f. figure 30) is fairly small. The largest bias is observed for the boundary layer and at the tropopause height. The standard deviation is largest at the tropopause, consistent with the highest winds at this level.

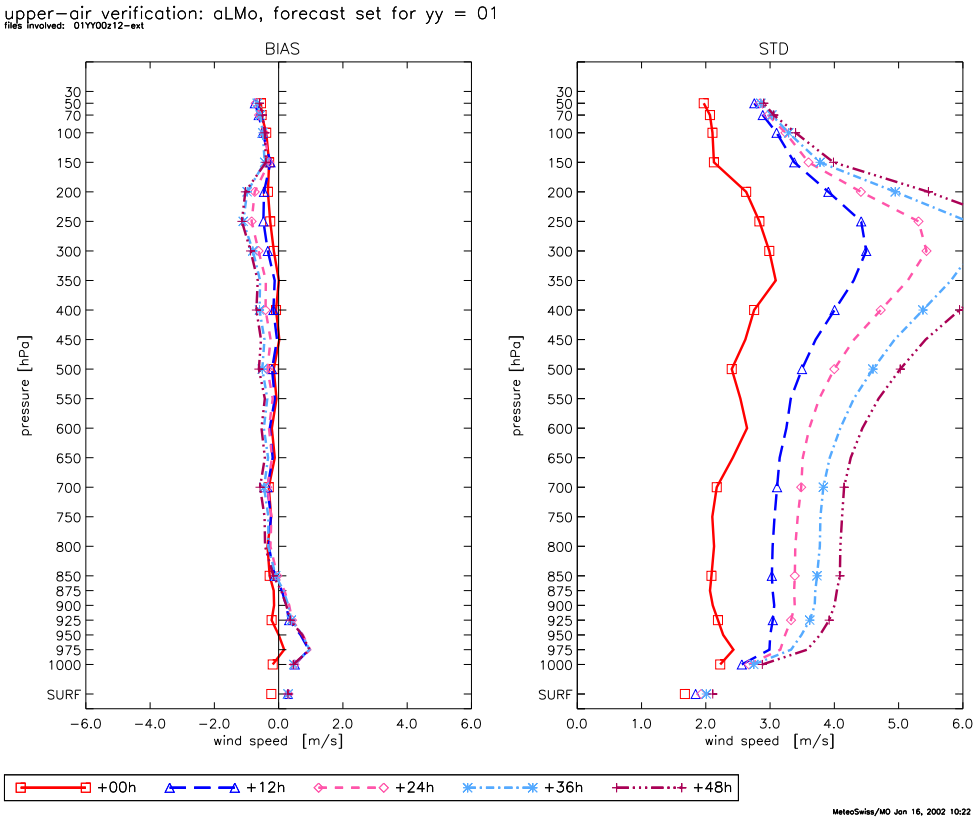

Figure 30: Mean error (BIAS) and standard deviation (STD) for wind speed. Various forecast times with verification times 00 & 12 UTC for the climatic year 2001 (1.12.2000–30.11.2001).

8.2.2 Operational Verification at DWD

(*Ulrich Pflüger, DWD*)

The operational upper-air verification of LM at Deutscher Wetterdienst uses all available TEMP and PILOT stations within the integration domain to verify the vertical structure of the forecasts. Vertically the atmosphere is divided into discrete bins with steps of 25 hPa below 800 hPa and with steps of 50 hPa above the 800 hPa level. Complying with its height, every measurement respective every forecast increment is allocated to one bin.

Figure 31 shows the mean error (left column) and the root mean square error (right column) in the year 2001 (01.01.2001 - 31.12.2001) averaged over the verification time 00 UTC for geopotential, relative humidity, temperature, wind direction and wind speed. To the right of each chart the bin occupancy is shown as a bar chart. Figure shows the same illustration but averaged over the verification time 12 UTC.

Most noticeable in the verification plots for geopotential and temperature is the strong increase of mean error above 250 hPa. The reason for this is assumed in an error in the interpolation scheme for temperature and pressure. Below 600 hPa mean error of geopotential is nearly constant with height and has negative values for the analysis. The forecasts for 00 UTC have always a positive bias whereas bias of 12 UTC forecasts is varying from -1.5 m to 1.5 m. Between 600 hPa and 250 hPa the mean error in the forecasts changes from positive to negative values respectively becomes more negative, whereas the values for the analysis stay nearly constant at both verification times.

The bias for relative humidity looks very well, 00 UTC forecasts tends to positive values below 800 hPa and negative values above. Absolute values are less than 5 %. 12 UTC forecasts always have a positive mean error with maximum values near 5 %.

Between 900 hPa and 300 hPa the bias of temperature analysis is nearly constant with a value of about -0.1 K. Below 900 hPa at 00 UTC the mean error decreases to -0.3 K whereas the bias at 12 UTC increases and becomes even positive (0.1 K). Below 600 hPa the forecasts mean error for both verification times is same or even less than analysis mean error. Between 600 hPa and 400 hPa the bias in forecasts becomes more negative and reaches values down to -0.6 K in the 48 h forecasts. In November and December, this decrease already had begun above 850 hPa. Above 400 hPa the mean error increases strong and reaches maximum values between 0.6 K (analysis) and more than 1 K (48 h forecast). Above 200 hPa the mean error fluctuates back, forth and back again and produces a saw-like structure.

The mean error in wind direction is very small above the boundary layer with a tendency to negative values below 600 hPa and positive values above 600 hPa. 00 UTC analysis changes in the boundary layer from negative to positive values and stays positive below 950 hPa. 12 UTC analysis also shows this change in the boundary layer but with a very small zone of positive values and a change back to a small negative value near ground. The forecast bias is close to the analysis bias, except at verification time 12 UTC and below 850 hPa, where the bias of wind direction reaches maximum absolute values of about 3 degrees.

The mean error in wind speed is positive through the whole atmosphere at both verification times, except for a small zone above the boundary layer, where the forecasts mean error has values less than zero. The largest bias can be noted for the boundary layer and at the tropopause height. The bias of the forecasts is also close to the bias of the analysis except for the upper tropopause and the tropopause height, where the bias of the 48 h forecast reaches values of more than 2 m/s (analysis < 1 m/s).

The root mean square error for all five parameters is increasing nearly linear between forecast time 12 h and 48 h. Except for geopotential (which isn't nudged) there is a gap between analysis (00 h forecast) and the remaining forecasts. The reason for this is probably related to the nudging procedure, it seems that the nudging scheme forces the 00 h forecast too strong to the measurements.

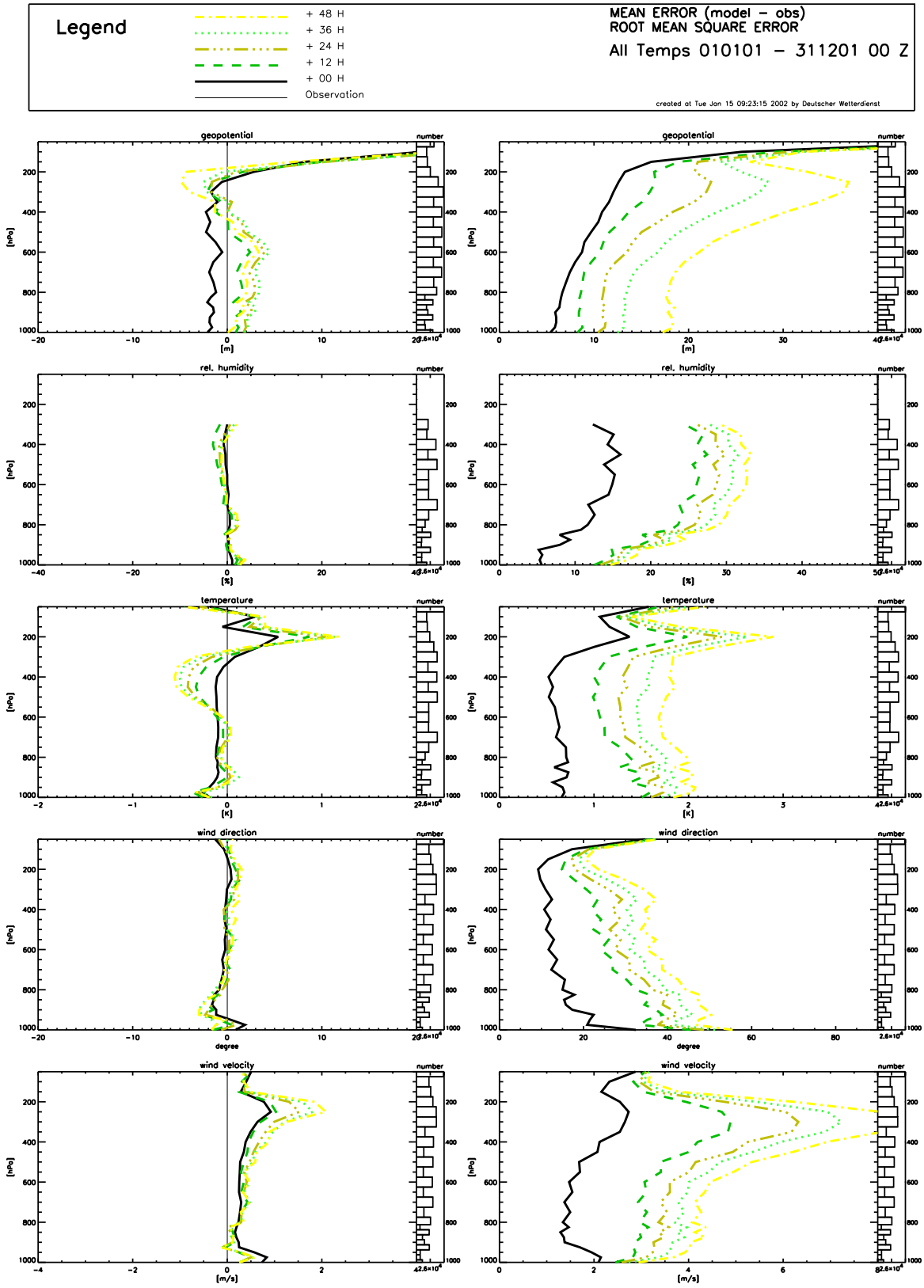

Figure 31: Mean error (left column) and root mean square error (right column) in the year 2001 (01.01.2001 - 31.12.2001) averaged over verification time 00 UTC for geopotential, relative humidity, temperature, wind direction and wind speed. Right of each chart the bin occupancy is shown as a bar chart.

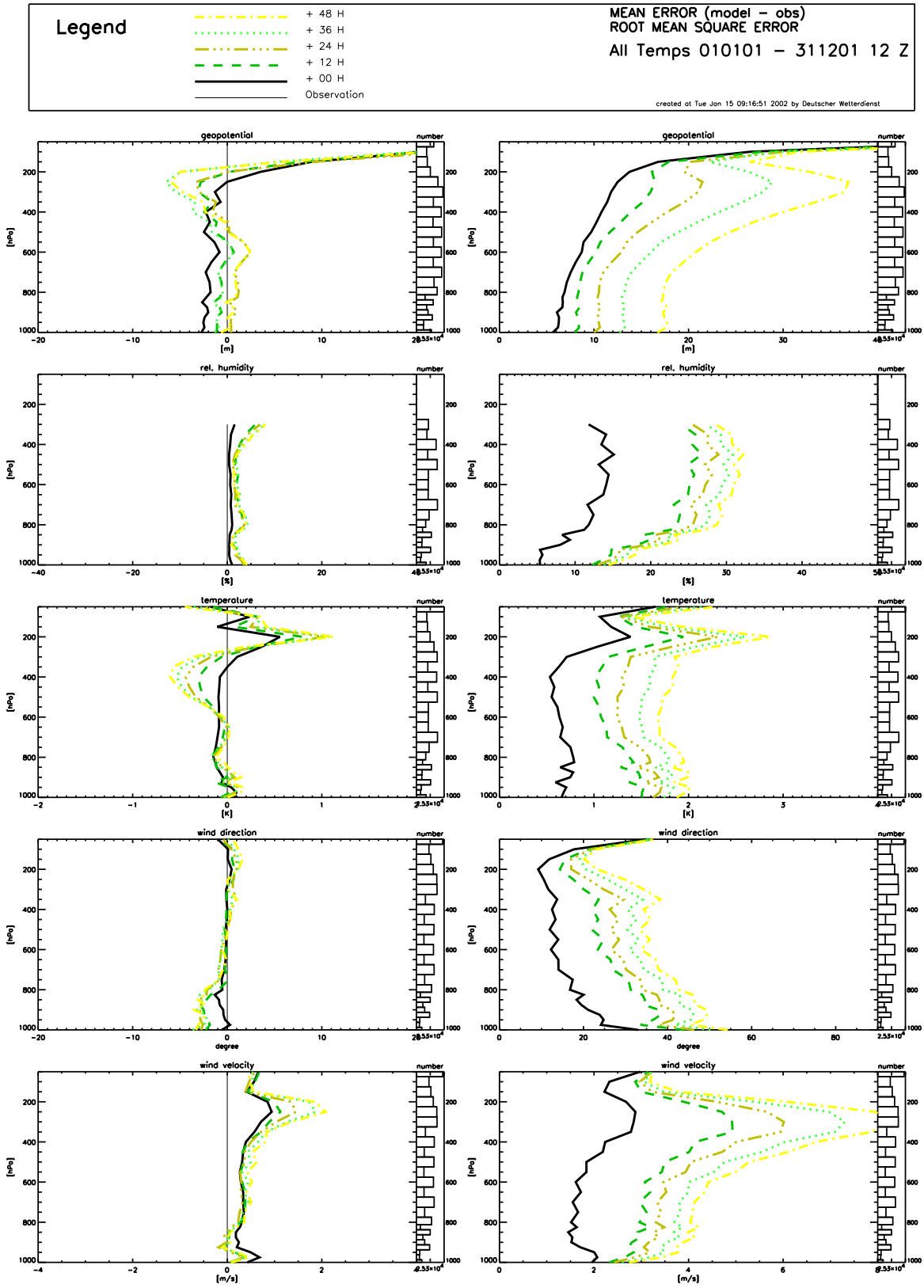

Figure 32: Mean error (left column) and root mean square error (right column) in the year 2001 (01.01.2001 - 31.12.2001) averaged over verification time 12 UTC for geopotential, relative humidity, temperature, wind direction and wind speed. Right of each chart bin occupancy is shown as a bar chart.

8.3 Verification of Precipitation

Precipitation is a very important weather parameter and a demanding task for numerical weather prediction. To find a valid analysis of precipitation measurements to compare with gridded model results of precipitation forecasts is equally demanding and not yet conclusively resolved. A specific problem, especially at high model resolution, is that the spatial and temporal variability of precipitation is much larger than those of the standard observations.

The operational daily verification of precipitation at meteorological centres is mostly based on the coarse SYNOP observations. This section summarizes work of the COSMO verification group which is related to regional verification of precipitation using special observational networks of high resolution in space and/or time.

8.3.1 Spatial Distribution of Precipitation over Germany and Switzerland

(Ulrich Damrath, DWD)

This verification product is based on the climate observation networks of DWD and MeteoSwiss. The data have a high spatial resolution (more than 5000 stations in Germany and Switzerland), but a coarse temporal resolution (24 h precipitation sums).

Figure 33 shows the distribution of monthly precipitation amounts for September 2001 as obtained from the climate networks and form the corresponding 00 UTC LM runs at DWD. The results from corresponding GME runs and from the LM assimilation cycle are also included in the Figure. Most details resulting from orographical forced enhancement of precipitation are well represented by the LM forecasts, e.g. the high rain amounts along the northern ridge of the Alps, over the Black Forest and over various low mountain ranges in Germany and along its southeastern border. Similar topographical structures are also present in the results from the assimilation cycle. Here, the pattern is more close to the observations than in the forecasts, especially in northern Germany where the LM tended to underpredict the precipitation amount. In most of these mountainous areas the peak values are somewhat overestimated. Also, the lee-effect downstream of mountain ranges (for instance the Black Forest) is overestimated (too dry). The area mean value of monthly precipitation, however, is close to the observed one. Almost no topographical structures are visible in the GME precipitation field due to the coarse horizontal resolution of the model.

The corresponding verification results for the spatial distribution of precipitation in 2000 revealed a tendency of the model to strongly overestimate the rain amounts over mountain tops and to suppress the intensity of cold fronts north of the Alps in case of southerly Föhn-flow (see Section 8.3.1 in COSMO Newsletter No.1). As a short-term remedy to cure this problem, a filtered topography has been introduced in December 2000. The impact of the filtered topography can be seen in Figure 34, which compares the monthly precipitation sums along various west-east cross sections in southern Germany across the Black Forest for September 2000 (using the grid-scale mean topography) and 2001 (using the filtered topography).

In September 2000, the model showed a strong overestimation of peak precipitation near steep topography. In some locations, the rain amounts are 2-3 times larger than the observed ones. There is also a tendency to shift the maximum to the windward side of the mountains. Also, the lee-effect is overestimated, i.e. the rain amounts are underpredicted downstream of the mountains. The situation is different in September 2001, when the filtered topography is used (clearly, there is no one-to-one correspondence in Figure 34 because the meteorological

situation is not the same). Here, the peak precipitation amounts are at the same level of the observed ones. Unfortunately, the lee-effect is still present: the rain amounts downstream of the mountain range is severely underestimated, which results in too small values for the area-mean precipitation. Also, there is still a shift of the peak precipitation to the windward side of the mountain slopes.

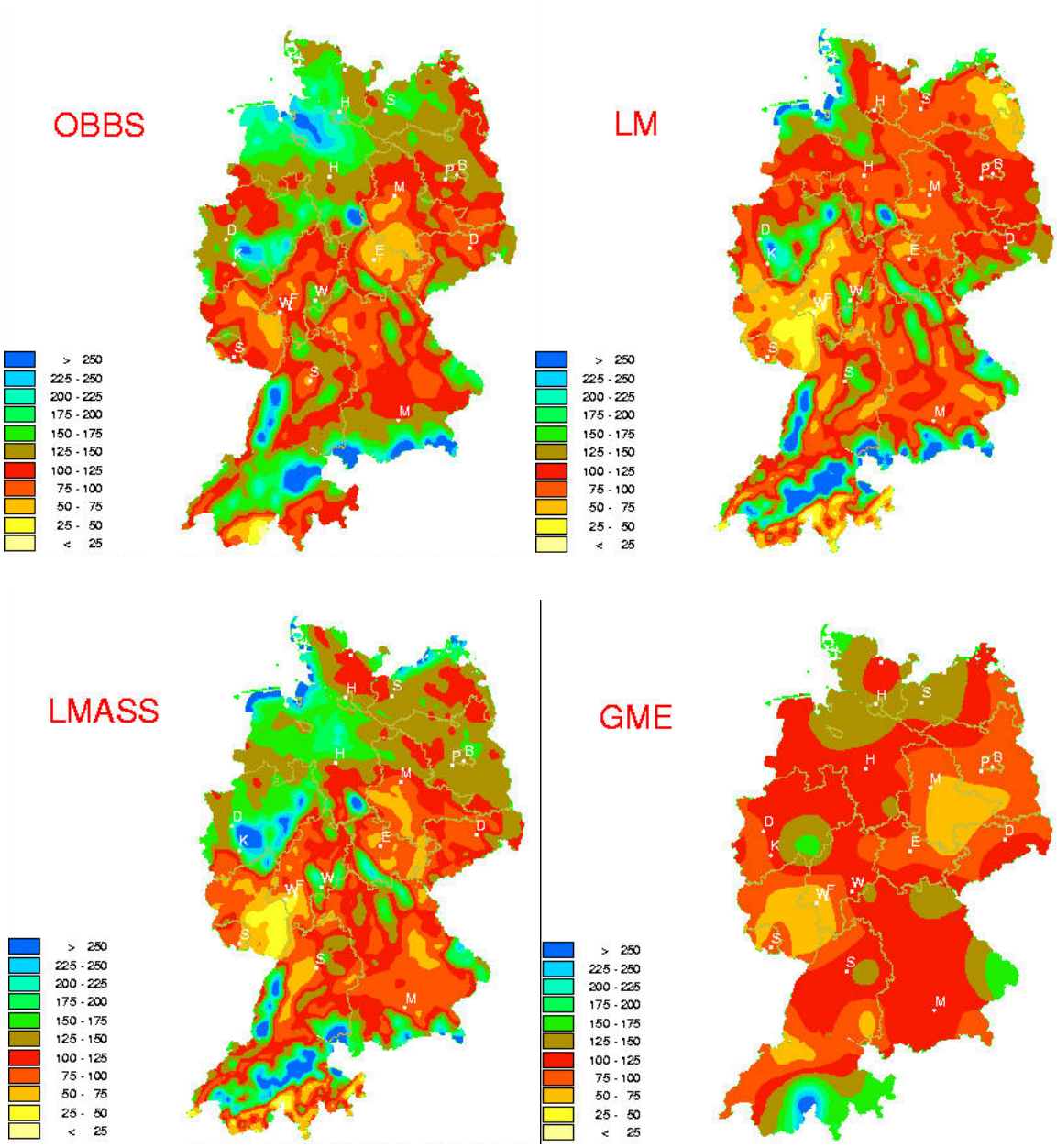

Figure 33: Monthly precipitation sum (mm) for September 2001 as observed (OBBS) by climate networks (max: 503 mm, mean: 135 mm) and derived from 00 UTC forecasts (LM) at DWD (max: 867 mm, mean: 129mm). The results from the LM-assimilation stream (LMASS; max: 934 mm, mean: 141 mm) and from forecasts of the global model GME (max: 329 mm, mean: 128 mm) are also shown.

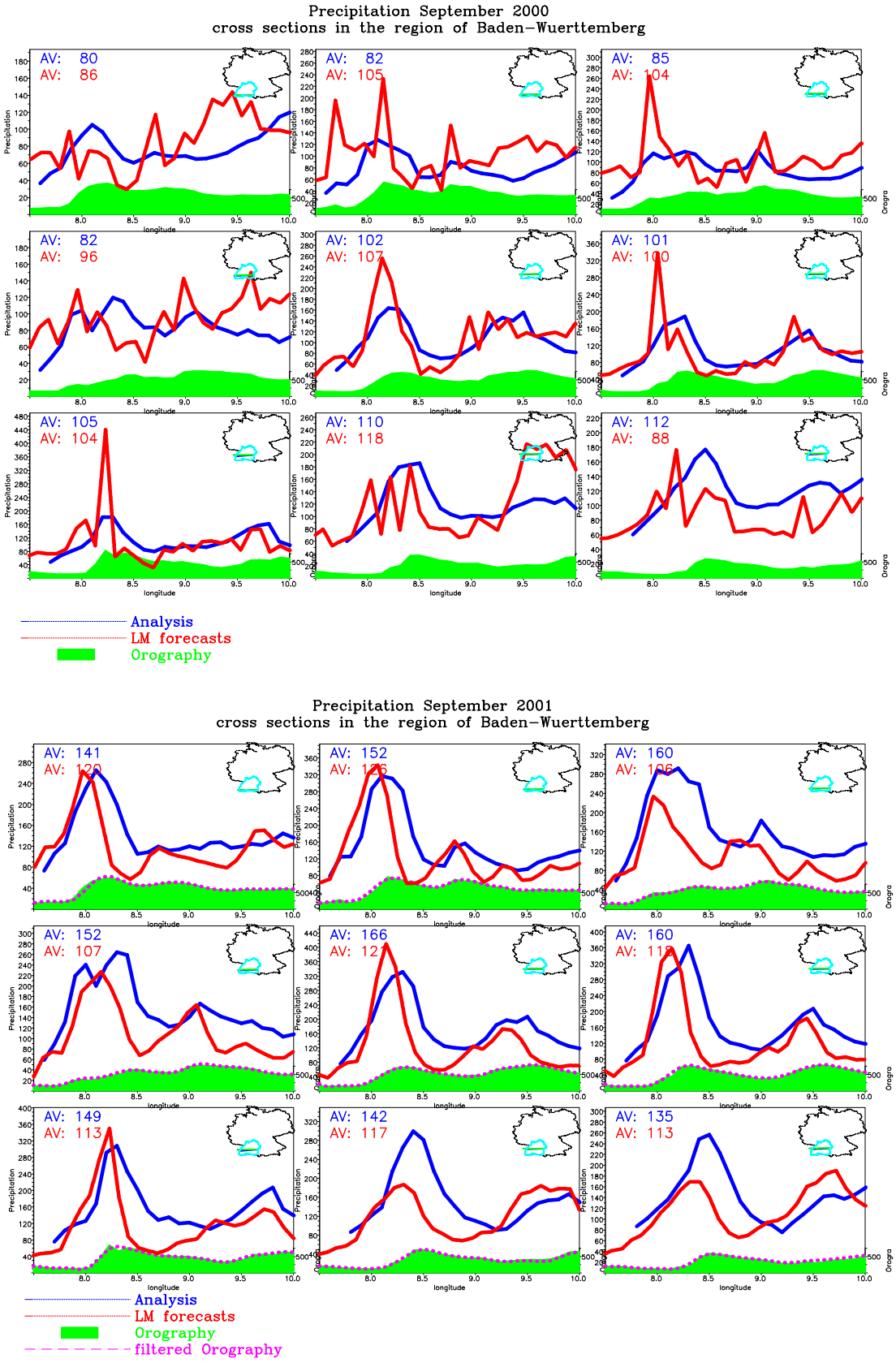

Figure 34: Monthly precipitation sum as observed by a high resolution network (blue line) and by operational LM forecasts (red line) for various west-east cross sections over south-east Germany (from the Rhine Valley over the Black Forest, as indicated on the top right in each figure). Top: September 2000, using the grid-scale topography (shaded). Bottom: September 2001, using the filtered topography (dashed line in bottom figure).

8.4 Assessment of Model Performance

This section summarizes certain aspects of the general model behaviour in the operational application. Also, some conclusions on model deficiencies from the recent verification results as well as from diagnostic evaluations and from case studies are summarized.

(a) General

During the course of the operational and pre-operational applications of the LM at COSMO meteorological centres, the model has proven to run stable, robust and efficient. Only one blow-up (due to a CFL instability) for the Lothar Christmas Storm (24 December 1999) has been recorded up to now.

Also, no significant problems related to the lateral relaxation boundary conditions or to the use of nonhydrostatic dynamics have been encountered. In general the relaxation boundary conditions with an updating frequency of 1 hour work well despite of the quite large GME/LM grid spacing aspect ratio of about 1:9. Unlike for inflow boundaries, where the flow systems in general are adapted consistently from the driving model (even for fast moving storm systems) problems may sometimes arise along the outflow boundaries whenever the inner solution evolves much different from the imposed solution of the driving model (e.g a faster movement of fronts or a different evolution of convective systems). As the two solution do not fit, the relaxation results in artificial divergence or convergence generating vertical accelerations. In such cases, this can produce narrow bands of clouds and precipitation along the lateral boundaries. However, any significant detrimental impacts on the inner solutions have not been observed so far.

Grid-point storm like effects have not been noticed up to now. This is a clear advantage compared to hydrostatic models, which at high resolution often tend to generate grid-point storms (which even may result in blow-ups) in case of convectively unstable stratification. In such situations, the nonhydrostatic model dynamics seems to be much more robust. Also, no worrying numerical problems have been encountered from using a large-scale convection scheme at 7 km grid-spacing in a nonhydrostatic dynamic framework.

The prediction of cyclones and of frontal clouds and precipitation is in general well simulated by the LM. Exceptions occur for large errors in position and timing of storm systems from the driving model along the lateral boundaries. The simulation of convective systems such as squall-lines or air-mass thunderstorms seems to be of about the same quality as with the old hydrostatic model DM (or SM), but with the known deficiencies: Position and timing errors occur quite often, but a better localization of air-mass convection is achieved when topographical forcings are relevant; and as with the old models, the diurnal cycle of convection is not well represented.

(b) Model Deficiencies

From the verification results for the last year, we can summarize some basic problems:

- During nighttime the 2m-temperature has a quite large cold bias, especially during winter. The verification results form DWD reveal that this effect is much less pronounced when the new TKE turbulence and surface layer scheme is used, together with the soil moisture analysis.
- The mean diurnal cycle of 2m-temperature is represented by the model, but with a too large amplitude (for both the old and new turbulence schemes). Also, the maximum is achieved too early (at noon) and the temperature starts to decrease too early in the

afternoon.

- The diurnal cycle of the 2m-dewpoint-temperature is not well captured. However, with the new TKE turbulence and surface layer scheme the diurnal cycle is much better represented by the model.
- 10-m winds appear to be too high over Switzerland for stations below 800m in both aLMo and LM-DWD. A special effect is seen in LM-DWD using the TKE scheme for stations above 800m: Here, the 10-m wind is strongly underestimated. This effect was found to occur in all regions with a high roughness length, e.g. also for big cities.
- In summer, the mean daily cycle of both total cloudiness and precipitation is not well represented. Especially, the precipitation peaks too early (at noon) by about 6-12 h.
- Low precipitation amounts appear to be overestimated by the model. This may result from convective drizzle or from a too slow evaporation of rain below stratiform clouds.
- Over regions with complex and steep topography (especially over the Alps), the simulated precipitation patterns are still not very satisfactory. However, some progress has been made by introducing the filtered topography.
- The verification results for precipitation over Switzerland show marked differences between aLMo and LM-DWD for spring and summer 2001. In general, LM-DWD gives less precipitation than aLMo (by about 25%). Very high precipitation amounts are strongly underestimated in LM-DWD, and strongly overestimated in aLMo. The reason for this behaviour is not yet clear.

At the recent COSMO meeting, several new work packages have been defined to investigate these problems and to find short-term remedies. The problem with precipitation over steep terrain seems to be related to a more general deficiencies in the model formulation: The use of terrain-following coordinates implies that

(1) the errors in the pressure gradient term discretization increases with increasing steepness of topography at higher resolution,

(2) the errors in 3-d advection increase at higher resolution and

(3) the errors from horizontal diffusion will also increase.

As a short-term remedy for errors resulting from horizontal diffusion, a new scheme based on a monotonic formulation with an orographic limiter has been developed, which has recently been put into operations. On the long-term, we aim at the introduction of the z-coordinate using shaved element discretization to get rid of the numerical topography problem.

9 Model Development and Application

This section includes several reports on various research topics and model applications as well as progress and status reports of the COSMO Working Groups. Within this section, we omit a subdivision by themes and the numbering of equations and figures refers to each paper. The contributions are ordered such that follow the topics of WG1 – WG6.

Most of the papers included in this section are write-ups from the COSMO annual meeting 2001 in Athens. Two contributions (by Michael Baldauf and by Thorsten Reinhard and Ulrike Wacker) from the LM User Seminar in Langen have also been included. Many thanks to all who provided contributions for the present issue of the Newsletter.

We have not included longer reports that have been or are going to be published in the COSMO Technical Report (TR) series. The TRs are intended for a documentation of research activities, to present and discuss results from model applications and from verification and interpretation, and to document technical changes and new components of the LM package. The purpose of these reports is to communicate results, changes and progress related to the LM model system relatively fast within the COSMO consortium. The following TRs appeared in 2001 (available at www.cosmo-model.org).

No. 1, Dmitrii Mironov and Matthias Raschendorfer (2001): *Evaluation of Empirical Parameters of the New LM Surface-Layer Parameterization Scheme. Results from Numerical Experiments Including the Soil Moisture Analysis.*

No. 2, Reinhold Schrodin and Erdmann Heise (2001): *The Multi-Layer Version of the DWD Soil Model TERRA_LM.*

No. 3, Günther Doms (2001): *A Scheme for Monotonic Numerical Diffusion in the LM.*

The following issues are planned so far for 2002. Of course, any additional paper is welcome, and we would like to encourage all of you to submit a contribution.

No. 4, Jean-Marie Bettems: *EUCOS Impact Study Using the Limited-Area Non-Hydrostatic Model in Operational Use at MeteoSwiss.*

No. 5, Matthias Raschendorfer: *A New TKE-Based Scheme for Vertical Diffusion and Surface-Layer Transfer.*

No. 6, Hans-Joachim Herzog, Ursula Schubert, Gerd Vogel, Adelheid Fiedler and Roswitha Kirchner: *LLM – The High-Resolving Nonhydrostatic Simulation Model in the DWD – Project LITFASS. Part I: Modelling Technique and Simulation Method.*

No. 7, Günther Doms: *The LM Cloud Ice Scheme.*

Assimilation of Aircraft Observations

Christoph Schraff

Deutscher Wetterdient, Offenbach am Main, Germany

1 Introduction

Up to May 2001, only synoptic observations of type TEMP, PILOT, SYNOP, SHIP, and BUOY have been used operationally in the nudging-based data assmilation scheme developed for the LM. For the specification of detailed mesoscale initial conditions, however, the use of additional asynoptic data is mandatory. An increasing number of European aircrafts provide wind and temperature observations of excellent quality. In fact, the total number of typically about 15000 single-level aircraft reports per day already exceeds the number of TEMP and PILOT observations in the LM domain nowadays. In particular, the sequences of data from flight ascents and descents provide a promising source of information for mesoscale data assimilation since they are often delivered with a high vertical resolution.

Figure 1 shows a typical distribution of aircraft reports for a 6-hour period during the daytime. Specifically, the left panel displays the positions of groups of reports with good vertical resolution in the lower an middle troposphere, the right panel the positions of the other reports located mainly in the middle and upper troposphere. It indicates that in the lower troposphere, most of the data are located near one of a rather small number of big airports, and the data density is less uniform than for radiosondes. The observation time for almost all the reports lies between 5 and 22 UTC. As a consequence, a significant impact from the aircraft data can be expected mainly for forecasts starting during the daytime, e.g.

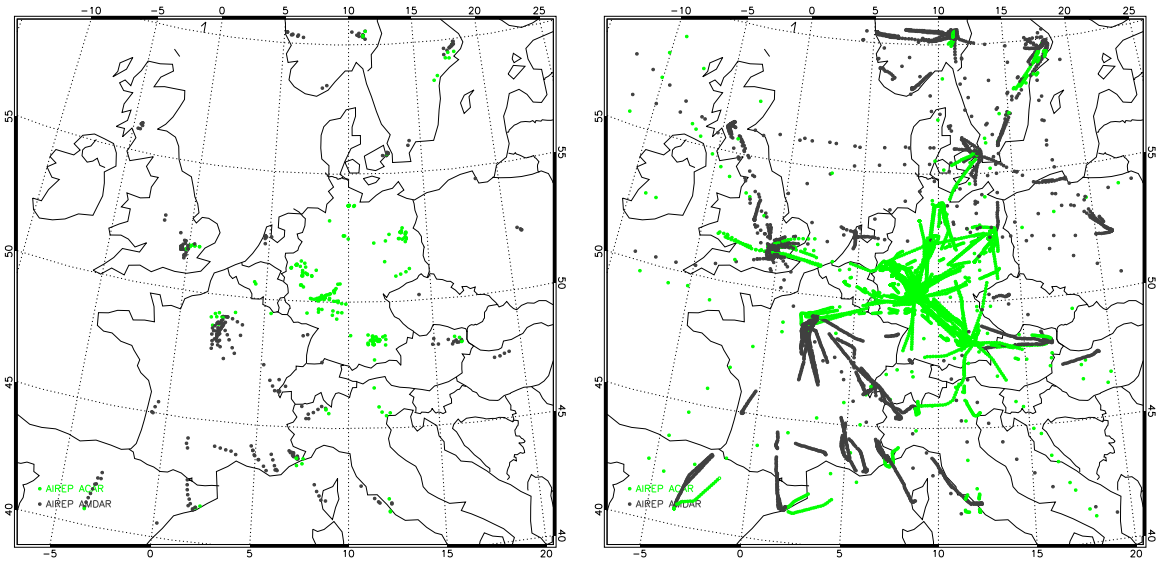

Figure 1: Distribution of positions of aircraft reports from 6 to 12 UTC on August 17, 2001. Black dots: AMDAR reports; green dots: ACAR reports. Left panel: groups of reports with good vertical resolution during flight ascents or descents, located mostly in the lower and middle troposphere; right panel: the other reports as single-level reports, located mostly in the middle and upper troposphere.

at 12 or 18 UTC. The benefit for the 0-UTC LM runs should be more limited due to the fact that in this case, aircraft data are only available to improve the model state prior to rather than during or after the assimilation of the radiosonde data set around 23 UTC to 0 UTC.

The assimilation of the aircraft observations is included in the scheme developed for the LM based on the nudging technique. An outline of the concept and basic features of the scheme can be found in Doms et al. (2002). In the present contribution, section 2 describes the additional steps that are specific to the processing of aircraft reports. Section 3 presents results from several 5- to 10-day assimilation and forecast cycle experiments. It includes comparisons between cycles with and without using aircraft data, and is complemented by concluding remarks.

2 Processing Steps Specific to Aircraft Data

A feature common to the following processing steps is that they relate only to sets of reports from the same aircraft. All the aircraft data are presented to the scheme as single-level reports which therefore have to be grouped according to aircraft identifiers prior to these steps. Note that as these steps are worked in parallel for the different sets (i.e. aircrafts) on distributed memory machines, the collection of such sets requires communication where completely different (amounts of) data are exchanged for each pair of nodes.

Flight Track Checking

The flight track checking is a model-independent quality control step. Given a complete set of reports with the same well-defined aircraft identity, the reports are first sorted in a unique way according to their probable chronological order. This is done by sorting them according to time at first. Groups of 'simultaneous' reports, i.e. reports assigned to the same minute, are then sorted vertically such that the vertical distance to the report prior to the group minus the distance to the subsequent report will increase from one to the next report in this group. Finally, simultaneous and vertically colocated reports are sorted horizontally in an analogous fashion.

A first check is about exaggerated horizontal colocation of the reports which may be caused by instrument or transmission errors. All the reports from an aircraft are rejected if more than 50 % of them have the same horizontal coordinates and at least 3 of the colocated reports are more than 12 minutes apart from each other. The latter condition helps to avoid the rejection of aircrafts (e.g. from Lufthansa) which issue identical coordinates for the frequent reports in the first 2 or 3 minutes after take-off (up to about 800 hPa). In a similar way, a check for exaggerated vertical colocation is performed below level flight levels.

The actual flight track check is based on an idea following the ECMWF position checking for ships to derive a confidence by comparing the reported horizontal position with estimates extrapolated linearly from pairs of previous positions. In the present scheme, however, the estimates are computed from previous reports not only with respect to the chronological order, but also to the reverse order. The two resulting confidences are then combined to make the final decision. In this sense, the flight track check is performed both in forward and backward direction. This significantly improves the reliability to reject the erroneous reports and at the same time reduces the probability to reject correct reports due to previous erroneous reports. In an analogous way, estimates and confidences for the vertical positions are computed for an independent vertical check. It is noted, that some tuning is required for the specification of the rejection limits and of parameters used to determine the confidences.

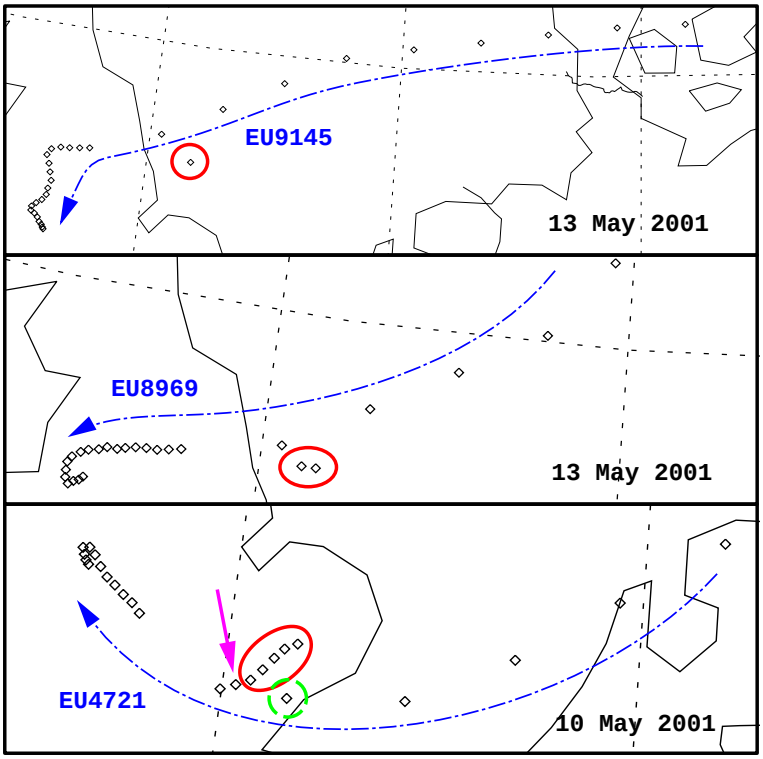

Figure 2: Sequences of aircraft reports from 3 different flights. Black diamonds: reported positions; long blue arrows: flight directions; red solid circles: enclosing reports with erroneous positions (missing sign at longitude) and rejected by the flight track check; green dashed circle: enclosing correct report rejected by the track check; pink arrow: pointing to an erroneous report not rejected; solid black lines: (English, Dutch, etc.) coastlines. Zero degree longitude is indicated by the dotted black lines next to the red circles. Aircraft identifiers are given in blue and dates in black.

Furthermore, an iterative check for missing sign at the reported longitude is done in advance. This type of error appears relatively frequently with reports located at a longitude between 0 and -1 degrees. For that purpose, horizontal 'reversed-sign' confidences for the forward and backward trajectories are computed in addition by reversing the sign for every reported positive longitude value. Reports are rejected if their original confidence is low and the 'reversed-sign' confidence is high. It is done iteratively to first sort out the most doubtful reports which are then omitted in the subsequent iterations, and this may alter the confidences derived for the other reports.

Figure 2 shows three examples where the sign of some of the reported longitudes has been missing. While the first case (top panel) with a single erroneous position is relatively easy to diagnose, the second case is already more difficult since the two erroneous positions support each other. And a case such as the third one would be completely misinterpreted if only a simple foreward trajectory check was applied. Since the position error of the first report with missing sign is still small, the resulting confidence would be high enough for acceptance. The same would apply to all the subsequent erroneous reports since they would be supported by one or several previous erroneous reports. In contrast, due to the large jump in the trajectory from last erroneous to the subsequent correct reports, three of the latter would be assigned a low confidence and therefore be rejected by mistake. The inclusion of the backward trajectory greatly improves the diagnosis, and with the addition of the iterative check for missing sign, all the erroneous reports except the one with the smallest error are rejected, and only one correct report is also rejected (see bottom panel).

Construction of Piecewise Vertical Profiles

During the ascent and descent flight phases, the sequences of single-level reports from individual flights often have a high vertical resolution, in many cases about 10 to 20 hPa in the lower troposphere. Due to the vertical spreading of the single-level increments by applying the vertical correlation function, a model grid point can be influenced by many observations from one aircraft. This will result in a vertical smoothing of the observational information. In order to take better advantage of the high vertical resolution, some of the single-level reports are grouped into piecewise vertical profiles which can then be assimilated in a way analogous to the nudging of radiosonde profiles.

The base report for such a group is usually selected to be the lowest report that has not yet been used for another multi-level report. Its observation time and horizontal location is assigned to the whole multi-level report in construction. Further single-level reports with strictly decreasing pressure are added, until no reports can be found within a time radius of 15 minutes and a specifyable horizontal radius from the base report, and within 55 hPa from the previously added report. If no more than 2 reports can be added the base report will be assimilated as single-level report, and the process is repeated with the next report as base report.

With the operational choice of 20 km for the horizontal tolerance radius, the temporal and horizontal position errors introduced are not considered significant. The extent of the lowermost multi-level report close to the ground is then typically about 100 hPa for the descent phase and 150 hPa for the steeper ascent phase. It can even reach more than 400 hPa if the aircraft reverses its direction during the ascent. Further above, there are often 1, 2, or even more shorter multi-level reports. As a result, most aircraft data are assimilated as part of a multi-level report below 700 hPa and as original single-level report above 400 hPa.

Note that the scheme allows to assimilate all aircraft data as single-level reports by setting the tolerance radius to zero. However, the assimilation as piecewise vertical profiles is computationally far more efficient due to the inherent limitation of the vertical spreading.

Horizontal Thinning of Aircraft Reports

In order to reduce both the computational costs and the variation of the data density related to quasi-colocated data, sequences of vertically (nearly) colocated single-level reports from the same aircraft are thinned horizontally. Specifically, all reports within less than $\pm$ 5 hPa and at most 4 minutes from a previous active report are set passive. Assuming a regular time interval between the reports, this corresponds to a horizontal distance of at most 150 km which is of the order of the 2-folding decay length of the horizontal correlation functions. Thus, the data coverage remains very good, and the number of assimilated single-level aircraft reports is reduced by about 10 %.

Reduction of the Vertical Correlation Scale

In order to further reduce vertical smoothing of observational information and variations of the effective data density, the scale of the vertical correlation function can be decreased by some factor for reports with a small (but non-zero) vertical distance between each other. Such a factor is computed for each pair of reports from the same flight. In case of perfect temporal and horizontal colocation, it is chosen such that the 2-folding decay height of the resulting vertical correlation function will be equal to the maximum of half the vertical distance between the two reports and half the model layer thickness at the reports. With

decreasing temporal and horizontal overlap between the two areas of influence, the factor approaches 1. The factors finally applied for the upward (downward) spreading of a specific report are equal to the minimum of all the factors derived from pairs which consist of this report and another report further above (below). Thus, the correlation functions may vary from report to report. The procedure is applied both to the single-level and the multi-level reports.

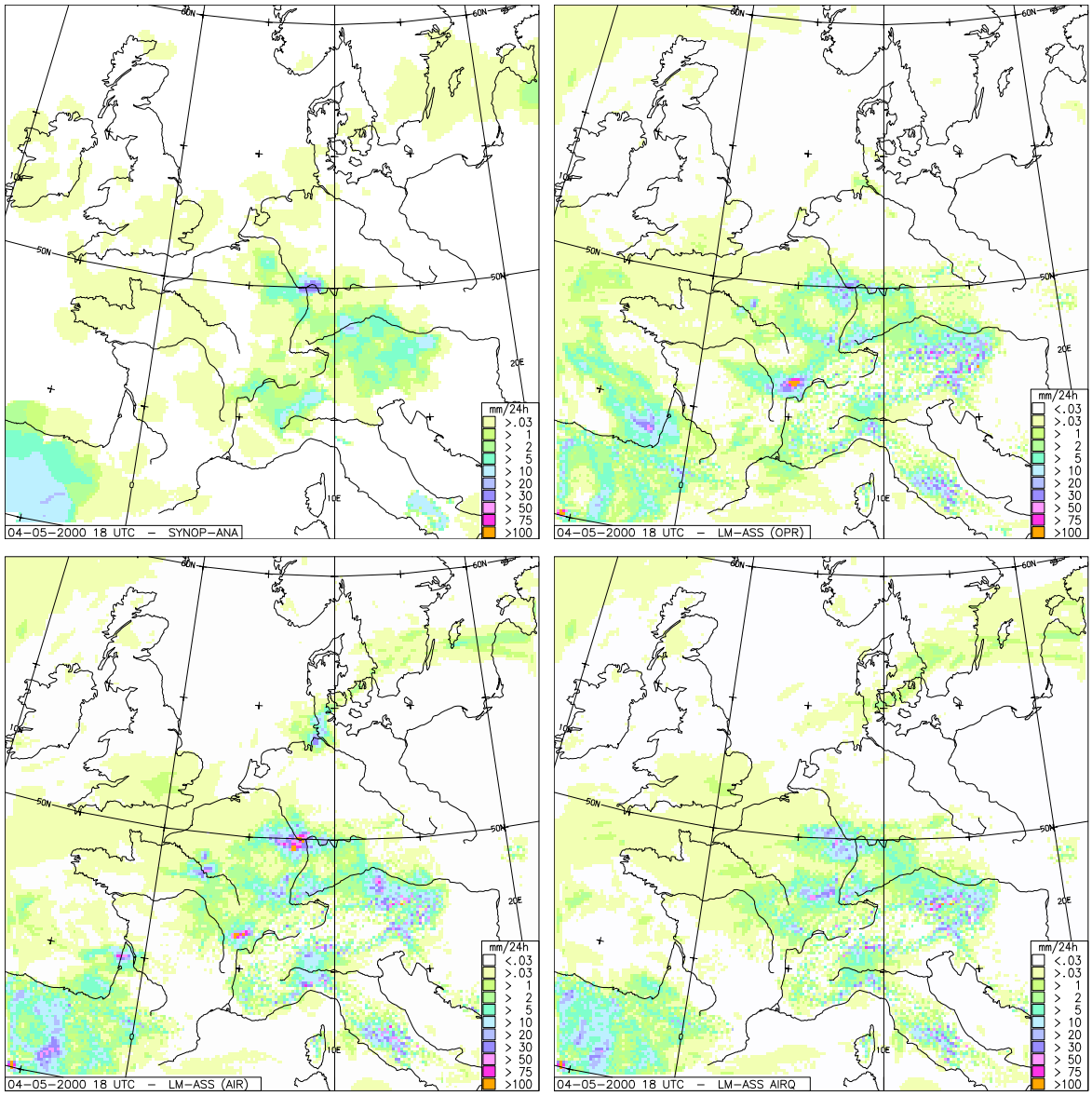

Figure 3: 24-hour precipitation from 3 to 4 May 2000, 18 UTC. Top left: verifying analysis derived from SYNOP observations; top right: assimilation run without aircraft data; bottom left: assimilation run with aircraft data; bottom right: assimilation run with aircraft data and preservation of specific instead of relative humidity at temperature nudging.

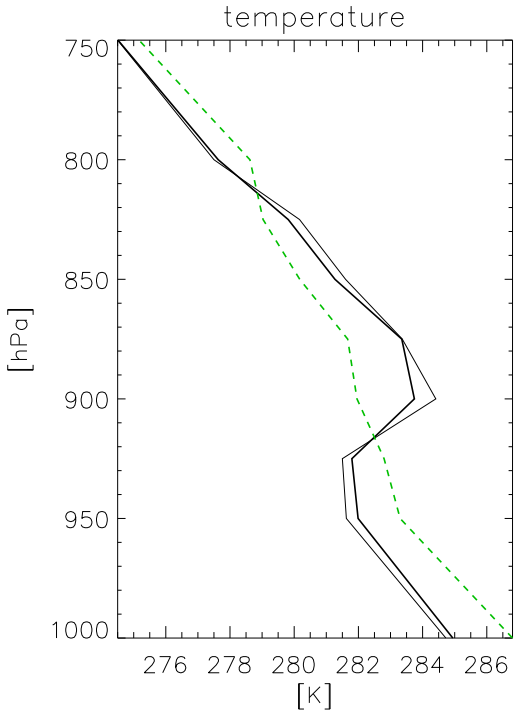

Figure 4: Vertical temperature profiles derived by averaging over data which are gathered from all the locations where aircraft temperature has been reported in the close vicinity of Paris between 18 and 24 UTC on 3 May 2000. Thin black line: aircraft observations; green dashed line: 6 - 12 hour LM forecast (i.e. starting at 12 UTC); thick black line: LM assimilation run with aircraft data.

3 Results

Humidity Preservation at Temperature Nudging

Although the prognostic humidity variable of LM is specific humidity, the humidity observation increments are expressed in units of relative humidity in the nudging scheme. This implies that relative rather than specific humidity is relaxed towards the observed humidity. This should allow the model to create more realistic cloudiness in the initial state even if there are temperature errors. Also, relative humidity has been preserved so far within the process of nudging temperature observations by adapting the specific humidity. The choice of the humidity variable to be preserved during the temperature nudging is of secondary importance as long as the temperature data come along with usable humidity observations, as is normally the case with radiosondes. Possible humidity errors infered by the temperature nudging can then be corrected by simultaneous nudging towards the humidity data.

This is not the case for the aircraft reports which are lacking of humidity information. When preserving relative humidity, problems with the convective precipitation have occurred in a few cases during the assimilation. For one case, this is indicated in Figure 3 by the distinct precipitation maxima around several airports (e.g. Paris, Bordeaux, Frankfurt, Munich) neither present in the verifying analysis nor in the assimilation run without aircraft data. The vertical temperature profiles over Paris (Figure 4) help to understand the type of processes causing this rainfall. An elevated inversion observed by several aircrafts during the evening was not predicted by a very short-range forecast which can be regarded as a first guess for the assimilation. Increasing the temperature above the inversion by nudging these aircraft observations then implies increasing the specific humidity. Dynamical, physical or numerical model processes cause some vertical smoothing and prevent the model from ever reaching exactly the temperature gradients. The temperature increment, although greatly reduced in the assimilation runs, remains positive, and the specific humidity is increased all the time, until mid-level convection sets in eventually. This in turn stabilizes the convective area above the inversion and strongly counteracts the assimilation process, so that a lot of rain can be produced in a relatively short time.

The problem does not occur when specific humidity is preserved at the temperature nudging. A third formulation where the preservation of specific humidity is confined to the vicinity of convectively precipitating grid points also solves the problem. For these two versions, the differences in the resulting precipitation patterns are rather small, and the quality is very similar. However, preserving specific humidity everywhere has been found to give better cloud analyses and forecasts in cases of low stratus. Here, the vertical smoothing tends to introduce a positive temperature error below the inversion and a negative bias in (specific) humidity and cloudiness. Preserving the relative humidity will then increase this bias. As a result, preserving specific humidity everywhere constitutes the best version overall and is used further on.

Multi-level Versus Single-level Reports

In order to establish the benefit from constructing piecewise profiles as described in section 2.2, a comparison has been made between the standard version which makes use of these profiles and a version which assimilates aircraft data only as single-level reports. In this version, the sequences of reports in ascents and descents have been thinned allowing a minimum

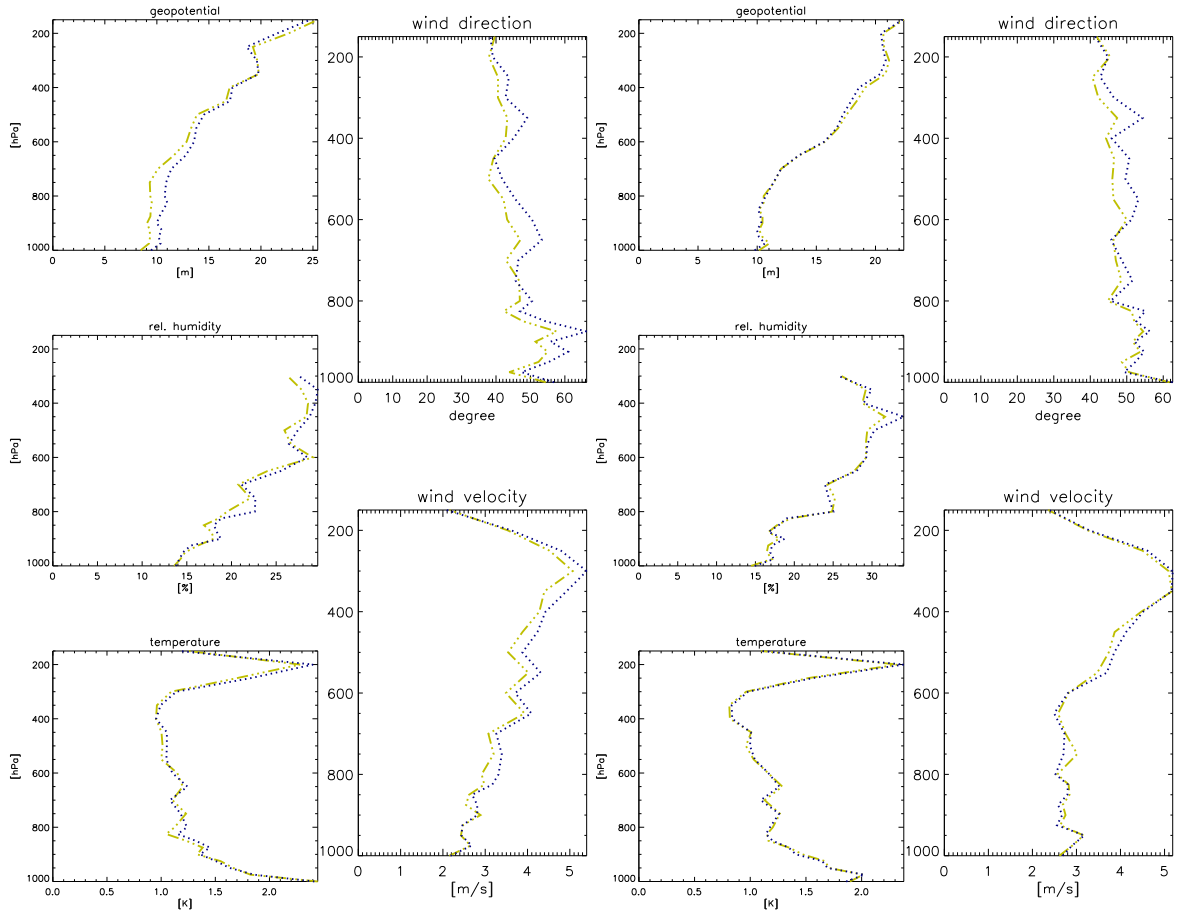

Figure 5: Upper-air verification against all radiosonde data (TEMP and PILOT) for the period of 28 April, 12 UTC, to 5 May 2000, 0 UTC. Left and right group of 5 panels each shows the vertical profiles of rms errors of geopotential, relative humidity, temperature, wind direction, and wind speed for 24-hour forecasts from continuous assimilation and forecast cycle experiments. Left group: 12-UTC forecast runs (i.e. forecasts starting at 12 UTC); right group: 0-UTC forecast runs. Blue dotted lines: without use of aircraft data; yellow dash-dotted lines: with use of aircraft data.

vertical distance of nearly 25 hPa between two successive reports so that the computer time used for two versions was similar. The comparison has been done for a wintertime low-stratus type period with inversions, where the vertical resolution of the assimilated observations is expected to be more important than in other situations. It has turned out, however, that the superiority of the standard version is negligible.

General Impact of the Aircraft Data

For several 5 to 10 day periods, assimilation cycles with 3 daily 36 hour forecasts using aircraft data have been compared to control experiments or the operational runs that did not use aircraft data. For the 18 UTC runs (i.e. forecasts starting at 18 UTC), the overall differences between the two versions are found to be very similar to those of the 12 UTC runs despite the difference in the number of available observations. At 18 UTC, there are less radiosondes than at 12 UTC and about the same amout of aircraft data so that a somewhat larger impact might have been expected.

In the upper-air verification against radiosonde data, the impact for the 12 UTC runs ranges from neutral for an advective period to significantly positive for a more quiet and convective period (late April to early May 2000, see Figure 5) for forecast lead times of up to at least 24 hours. The error reduction is more pronounced for geopotential and wind than for temperature and humidity. It is even larger if the influence of the lateral boundaries which are identical in all experiments is reduced by neglecting the radiosondes within the outermost 60 grid rows of the LM domain in the verification (Figure 6). Note that the improvement in the humidity profiles is a result of nudging aircraft wind and temperature data. The modified way to preserve (specific instead of relative) humidity at the temperature nudging has shown little effect on the upper-air statistics in this period. It has, however, improved the humidity profiles in a wintertime anticyclonic period. In contrast, the overall impact for the 0-UTC LM runs is close to neutral for most periods and all forecast lead times (see e.g. Figure 5). As an exeption, some positive impact is found for the 12-hour forecasts in the last test period before operational implementation (Figure 7).

In the surface verification against SYNOP reports (not shown) for the late April to May 2000 period, the impact is generally small. There is a slight negative tendency for cloud cover at the 0 UTC runs and for 10-m wind, and small improvements for cloud cover, 2-m temperature, and surface pressure at the 12 and 18 UTC runs. The scores for precipitation

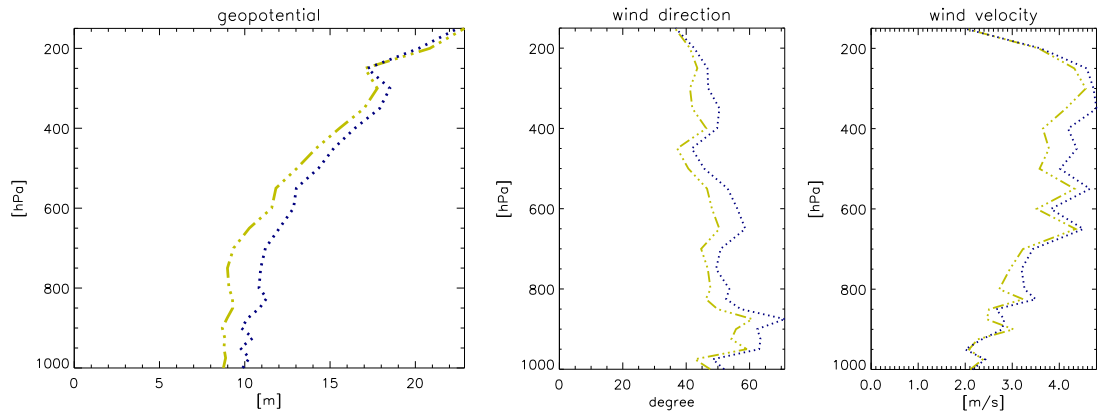

Figure 6: As Fig. 5, except that the radiosondes within 60 grid rows from the lateral boundaries of the LM domain are neglected in the verification, and only geopotential, wind direction, and wind speed are shown for the 12-UTC forecast runs.

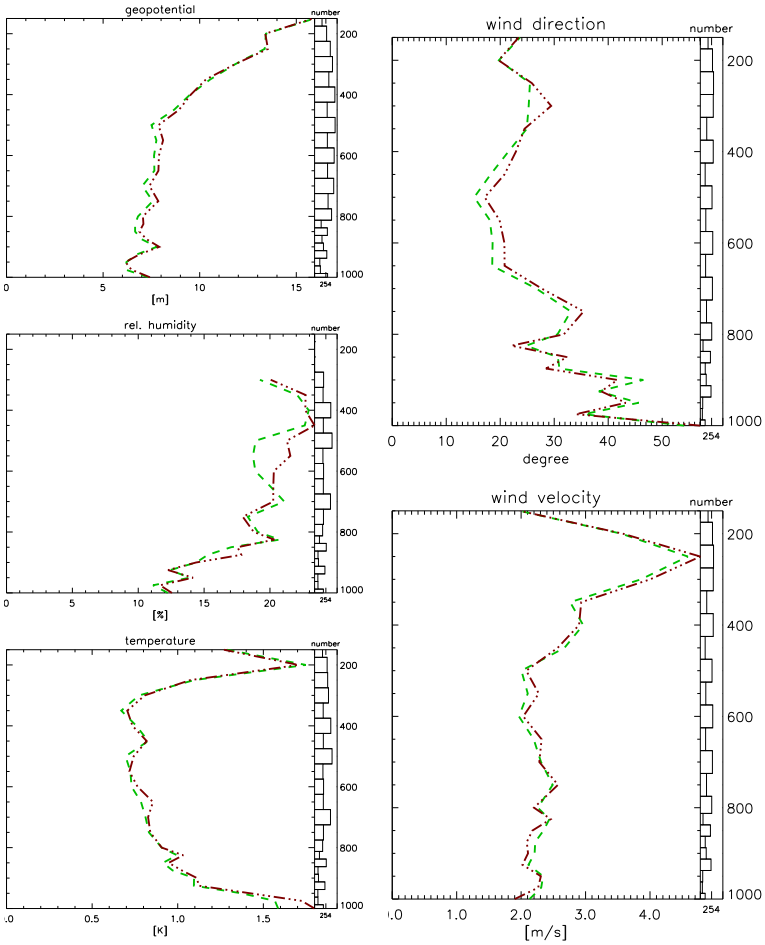

Figure 7: Upper-air verification against the radiosonde data for 10 - 14 April 2001. The 5 panels show the vertical profiles of rms errors of geopotential, relative humidity, temperature, wind direction, and wind speed for 12-hour forecasts starting at 0-UTC from continuous assimilation cycles. Red dash-dotted lines: without use of aircraft data; green dashed lines: with use of aircraft data. The horizontal bars on the right edge of the panels indicate the numbers of observations used to compute the corresponding rmse values. Radiosondes within 60 grid rows from the lateral boundaries of the LM domain are neglected in this verification.

are mixed. While the true skill statistics are somewhat decreased (using thresholds of 0.1, 2, 10 mm / 6 hours), the bias frequency scores and percent correct rates are slightly higher.

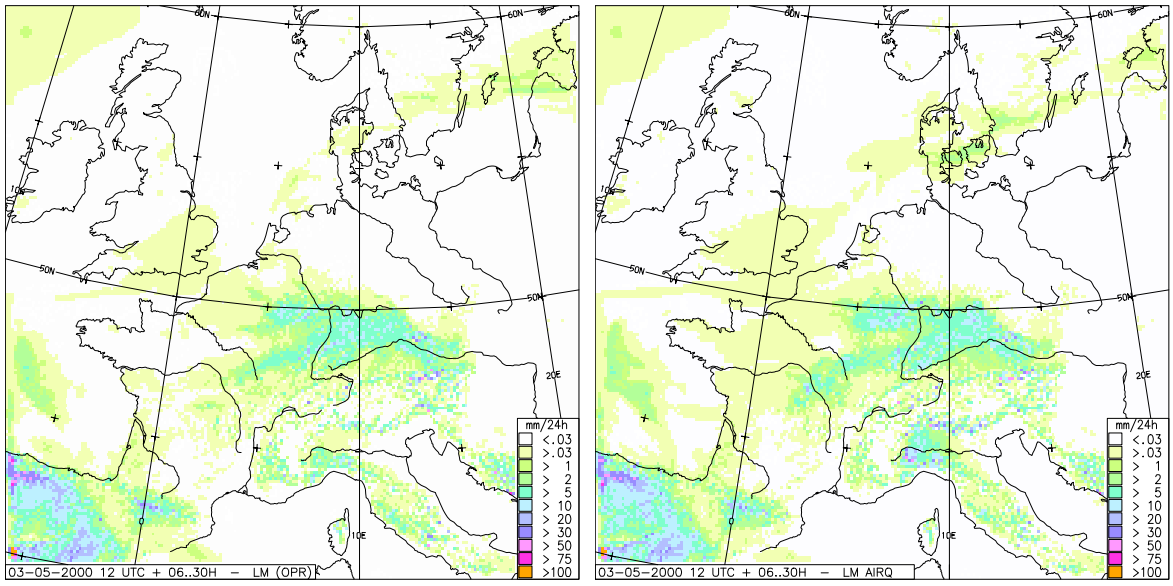

Figure 8: 6 - 30-hour precipitation forecasts for 4 May 2000, 18 UTC. Left: without the use of aircraft data; right: with the use of aircraft data for the initial state.

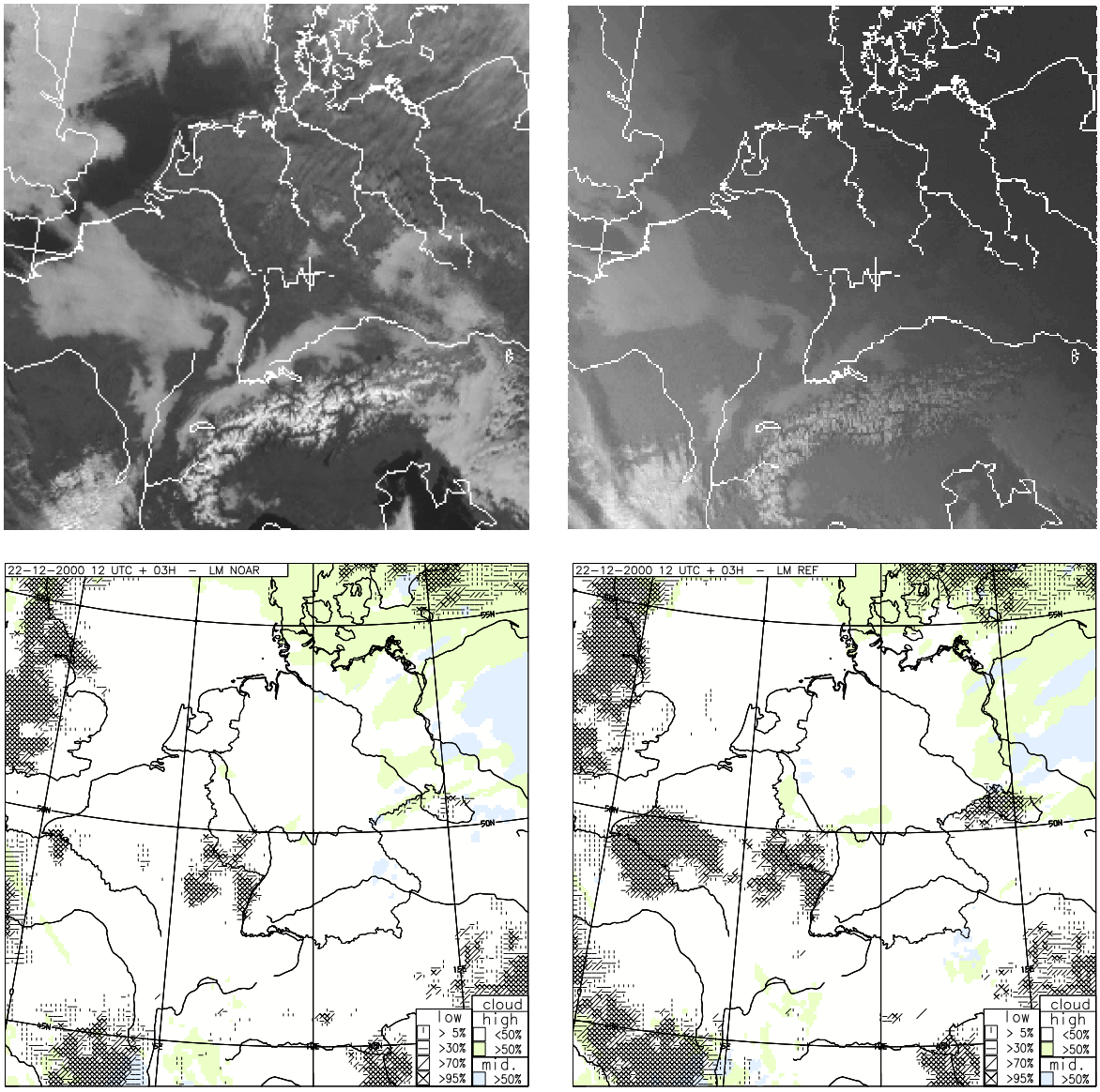

Figure 9: Top row: Meteosat VIS image for 22 December 2000, 12 UTC (left) and 15 UTC (right). Bottom row: 3-hour forecasts of low cloud cover (symbols), mid-level and high cloud cover (grey and green shading) for 15 UTC starting from an assimilation cycle without using (left) respectively with using (right) aircraft data. In both experiments, specific humidity is preserved at the temperature nudging.

Subjective evaluation of 24-hour precipitation patterns from LM assimilation runs and forecasts against analyses derived from SYNOP observations have not revealed a clear tendency either. A similar number of positive and negative cases have been found, and the differences are usually much larger during the assimilation than in the forecasts. As shown in Figure 3 for the case of 4 May 2000 as an example, the use of aircraft data clearly improves the LM analysis over Spain, southwestern France, and north of Lyon, and degrades it north of the Jura Mountains. The 6 - 30 hour precipitation forecast (Figure 8) gives a somewhat better indication of the rain in the western Po Valley than the control forecast, but at the same time tends to enhance erroneous rainfall in central France.

Similar results are obtained in an analogous evaluation of cloud cover except for a anticyclonic wintertime period in December 2000. Several analyses and very short range forecasts benefit from the assimilation of the aircraft data with respect to the representation of low stratus.

The most significant impact at daytime has been found for the 3-hour forecast shown in Figure 9 (the 12-UTC Meteosat VIS image is added to complement the information content of the 15-UTC image which is limited by the lack of daylight).

4 Concluding Remarks

Due to the impact range from neutral to significantly positive, the assimilation of the aircraft observations has been introduced operationally at DWD in June 2001. At the same time, the nudging scheme has been modified to preserve specific instead of relative humidity at the nudging of temperature data.

The impact of the conditional reduction of the scale of the vertical correlation functions still awaits to be thoroughly established. The lack of significant impact from the assimilation of aircraft data as piecewise vertical profiles instead of single-level reports could be related to this scale reduction which also has the effect to decrease vertical smoothing.

The lack of benefit from the aircraft data for precipitation forecasts may be related to the fact that no humidity observations are available from aircrafts. There is some hope that humidity information from other observing systems, e.g. GPS derived integrated water vapour, may in some way complement the wind and temperature information from aircrafts, and that this could lead to improvements in precipitation forecasts.

References

Doms, G., A. Gassmann, E. Heise, M. Raschendorfer, C. Schraff, R. Schrodin, 2002: Parameterization issues in the non-hydrostatic NWP-model LM. *ECMWF Seminar on Key issues in the parameterization of subgrid physical processes, 3 - 7 September 2001, Seminar proceedings,* to appear.

Monitoring of Integrated Water Vapour from Ground-Based GPS Observations and their Assimilation in a Limited-Area NWP Model

M. Tomassini[1)], G. Gendt, G. Dick, M. Ramatschi, C. Schraff[1)]

GeoForschungsZentrum, Potsdam, Germany

[1)] *Deutscher Wetterdient, Offenbach am Main, Germany*

Abstract

Detailed short-range numerical weather prediction (NWP) requires observational information of good quality and with high spatial/temporal resolution. Due to various limitations, important quantities such as tropospheric water vapour are often inadequately covered by conventional observations from radiosondes or by meteorological satellite systems. The Global Positioning System (GPS) is developing into a powerful source of humidity information for fine-scale regional models. Since May 2000, the GeoForschungsZentrum in Potsdam has been processing the data from a dense network of German GPS ground stations in near real time. The final product, Integrated Water Vapour, has been monitored at the Deutscher Wetterdienst, and preliminary assimilation experiments have been carried out to test the impact of the new observations in the operational non-hydrostatic limited-area NWP model.

1 Introduction

For the GPS Atmosphere Sounding Project (GASP) of the Helmholtz Society, the GeoForschungsZentrum (GFZ), Potsdam, has started activities in 1999 establishing a GPS ground network at some synoptic sites of the Deutscher Wetterdienst (DWD). This network has been extended by including GPS stations of the Satellite Positioning Service of the German National Survey (SAPOS) and of the International GPS Service (IGS), and it consists at present of approximately 100 sites. Since May 2000, GFZ has produced hourly estimates of Integrated Water Vapour (IWV) using predicted orbits. From February 2001 the process is running in near-real time (NRT). The main objective of the work presented here is the assimilation of the GPS IWV data into the limited-area NWP model of DWD, namely the "Lokal Modell" (LM). For this purpose a continuous monitoring of the GPS data has first been established using the operational assimilation cycle of LM as reference. After having assessed that the quality of the data is sufficient to consider them for assimilation purposes several numerical experiments have been performed to test and tune the use of GPS IWV for the LM. The basic concept followed for the assimilation of GPS data is described in Kuo et al., (1993), and it consists in relaxing the model IWV values towards the observed ones.

2 The GPS Data

The network of GPS stations included in the NRT analysis at GFZ and monitored at DWD is shown in Figure 1. Most of the stations transmit the GPS data in hourly batches directly to GFZ via ftp with a delay of less than 5 minutes, but some stations transmit with a delay of up to 25 minutes. The analysis is performed with the GFZ EPOS software (Gendt et al., 2001) using parallel analysis of stations in clusters with Precise Point Positioning (PPP) strategy in sliding 12-hour data windows shifted by one hour. Available hourly data from the global

IGS network are used for estimation of high quality GPS orbits and clocks, needed for the PPP analysis. The elevation cut-off angle is 15° and the sampling rate is 2.5 minutes. The predicted GFZ Ultra Rapid Orbits are used as initial values and the station coordinates are held fixed, once determined with sufficient accuracy. The final product, as hourly estimate of Zenith Path Delay (ZPD) and IWV (for stations where also meteorological data are measured or can be interpolated), is available within one and a half hours from the nominal observation time or solution epoch (30 minutes from epoch, 30 minutes data transfer delay and about 15 minutes processing). The current software allows the automatic operation of up to 200 stations and ZPD estimates at 15 minute intervals without increasing the processing time of 15 minutes. The major limitation of the whole processing is still in the data acquisition, because data from many stations are arriving too late for the NRT usage.

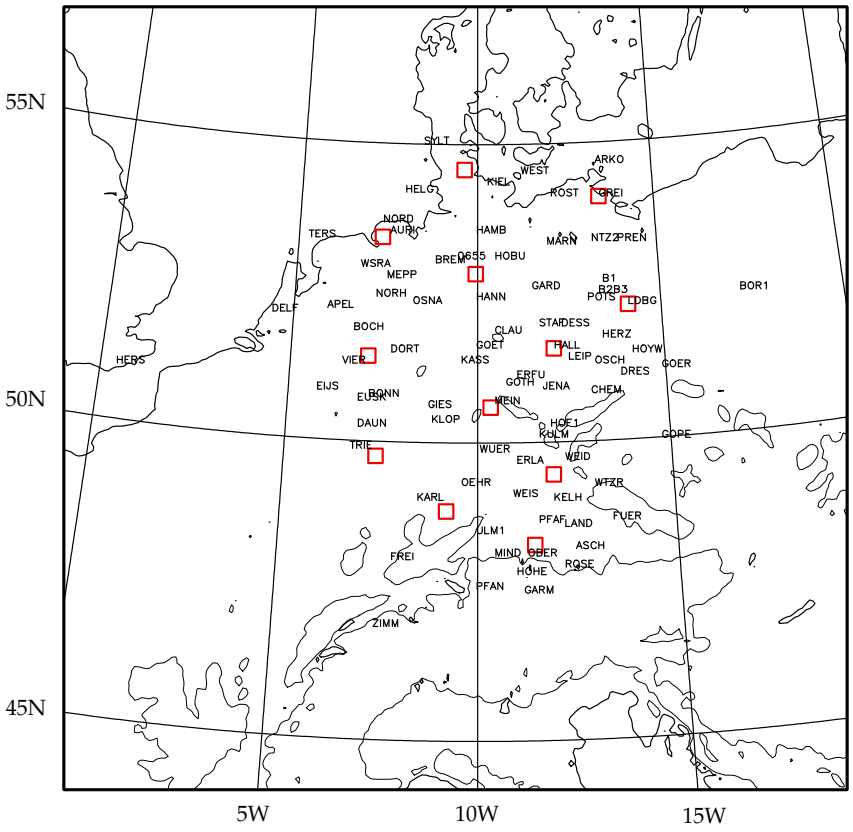

Figure 1: The GPS stations processed at GFZ and monitored at DWD (status as April 2001). German radiosonde stations (squares) are also shown for reference.

3 Monitoring

A routine monitoring of GPS data processed at GFZ has been set up at DWD. The observed hourly IWV data are compared against the IWV computed from the LM analysis fields. The LM analysis is obtained with a continuous assimilation cycle by nudging the model variables towards observations (from surface and radiosonde stations and since June 2001 also from aircraft platforms). The height difference between the location of the GPS antenna and the model orography has been taken in account for the sites above the model orography (the integration starts at the model level just below the antenna), whilst for the stations below the orography the integration starts from the lowest model level.

Table 1 shows the results of the comparison GPS minus LM IWV for the period May-August 2001. For this comparison 83 stations processed by GFZ and located within the LM domain have been considered (see Figure 1). Out of these stations, 26 are equipped with meteorological sensors providing measurements of pressure and temperature (MET) and 57 are not (NOMET). Not all stations supplied data regularly, and the number of data is approximately 70% of the possible total amount. In order to monitor all the data received, the model pressure and temperature interpolated to the station location have been used as input for the algorithm applied to derive IWV from the ZPD (Bevis et al. 1994). This does not significantly affect the results for the MET stations, since the LM analysis has used the same measurements of pressure and temperature from these sites. The mean difference for all stations and during the four-month period is 0.6 kg m-2, i.e. a small wet bias of the GPS data with respect to LM analysis, and the root mean square (rms) difference is 2.4 kg m-2. For the same period, a positive bias of 1.4 kg m-2 has also been found comparing the GPS data from the Lindenberg station (LDBG) against IWV derived from the radiosonde measurements available at this site.

Table 1. Comparisons of hourly IWV GPS observations against the operational LM analyses for 2001 for 83 stations (ALL), for 26 stations with meteorological sensors (MET) and for 57 without (NOMET). For each period in 2001 the table shows the mean difference GPS minus LM analysis (bias), the standard deviation (std), the root mean square (rms), the mean observed value of GPS (GPS) in kg m-2, and the number of observations (no).

	bias	std	rms	GPS	no
ALL					
May	0.4	2.1	2.1	17.2	44565
June	0.7	2.0	2.1	19.5	42990
July	0.6	2.4	2.5	25.1	43440
August	0.6	2.6	2.7	26.9	46715
May-August	0.6	2.3	2.4	22.3	177710
MET					
May-August	0.4	2.2	2.3	21.7	114406
NOMET					
May-August	0.7	2.3	2.4	22.6	63304

The reason of this bias is not clear and will be investigated further, especially because previous studies (Emardson et al. 1998; Koepken, 2001) showed an overall small dry bias of GPS data in comparison to radiosondes. Separate statistics for MET and NOMET stations reveals (Table 1) that the former have a smaller bias and rms difference than the latter, in the order of 0.3 kg m-2 and 0.1 kg m-2 respectively. In the context of data assimilation, such a small difference indicates that the quality of the humidity information from both types of stations is similar.

An interesting result of the monitoring is that the GPS observations exhibit a diurnal cycle which differs from the one of the model analysis. Figure 2 shows the monthly mean of the diurnal variation for May-August 2001 for 23 stations (selected because providing data more regularly than the others). An increase of IWV by more than 1 kg m-2 starting after 6 UTC

(8 local time) is observed by GPS. In the afternoon, around 18 UTC, the GPS IWV starts to decrease. The behaviour of the model tends to be the opposite, with a small decrease of humidity content during the morning and an increase of IWV in the afternoon. A diurnal cycle similar to the one of the GPS IWV has been observed with the microwave radiometer located in Potsdam, Germany, during the whole of a summer season, and it has been related to evapotranspiration around the site, which starts some time after sunrise and ceases at sunset (Güldner and Spänkuch, 1999). Therefore the disagreement on the diurnal cycle of the atmospheric humidity content is likely to be related to a shortcoming of the model and/or to the poor time resolution of the observations available for the LM operational analysis.

Since February 2001 the GPS data available in NRT have been used to monitor the operational output of LM. Every day the LM IWV analysis field at 00 UTC, from which the 48 hour forecast is started, is plotted together with the GPS observations. This type of monitoring is very useful to promptly detect problems either with the model output or with the GPS data processing. For example it has been possible to spot stations providing erroneous data due to changes affecting the antenna handling or position not known at GFZ.

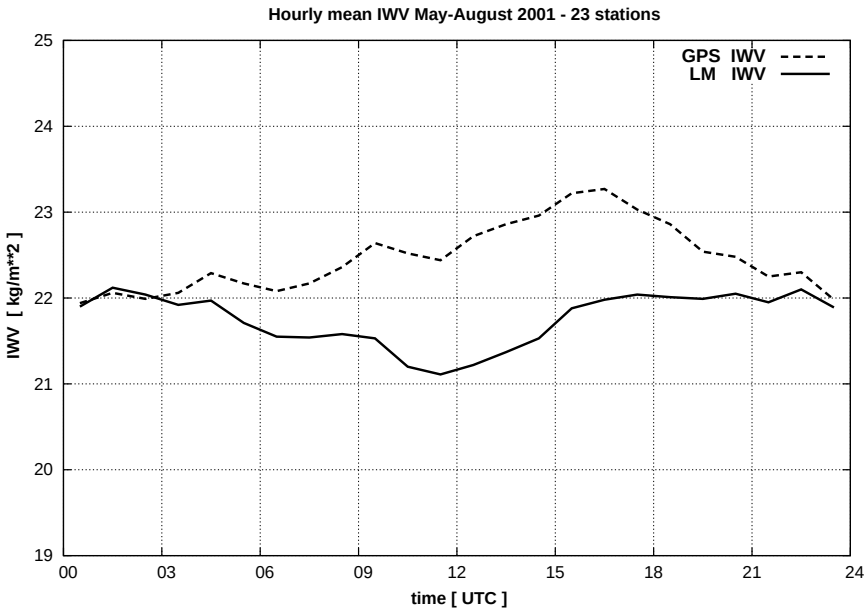

Figure 2: Monthly mean of diurnal variation of IWV in the LM analysis (full line) and derived from GPS observations (dashed line) for 23 stations during the period May-August 2001.

4 Assimilation of GPS Data

At DWD, the current version of LM, a non-hydrostatic regional model for central and western Europe, has a spatial grid resolution of approximately 7 km and 35 layers in the vertical. The assimilation scheme of LM is based on nudging towards observations. A relaxation term is introduced in the prognostic equation so that, assuming a single observation, the tendency of the prognostic variable $\psi(x,t)$ is given by:

$$\frac{\partial}{\partial t}\psi(x,t) = F(\psi,x,t) + G \cdot [\psi^{obs} - \psi(x^{obs},t)]$$

The first term F denotes the dynamical and physical model. The second term consists of the observation increment (i.e. the difference between the observation ψ^{obs} and the corresponding

model value $\psi(x^{obs}, t)$) multiplied by a weight G which depends on the constant nudging coefficient and the spatial and temporal distance between the observation and the time-space model grid point (for more details see Schraff, 1996). In the present operational implementation, the LM uses data from surface and aerological reports and computes the observation increments once every 6 advection time steps of 40 seconds.

The nudging of GPS IWV has been implemented following Kuo et al. (1993). A "pseudo-observed" profile of specific humidity based on the observed IWV and the vertical structure of the model humidity field is derived and then nudged at each single vertical level of the model. Model pressure and temperature are used to derive IWV from ZPD for all station types (the monitoring results showed that this has not a significant influence on the data quality). In order to avoid modifications of the humidity field at upper levels which contribute very little to the GPS measurement, the retrieved GPS profile is neglected above 500 hPa. At present the GPS derived profiles are treated like radiosonde profiles, i.e. the same vertical weight function is used above and below incomplete profiles. They have also the same lateral radius of influence of approx. 120 km, which appears to be reasonable for the reduced network of 50 stations used for the tests presented here but which may have to be modified for a denser network. It is worth to mention that no quality control (except a gross error check) has been implemented yet for the GPS observations.

In order to assess the impact of the IWV nudging on the analyses and the sensitivity to the new observations, several assimilation experiments using GPS data have been carried out and compared to the operational assimilation run. The experiments cover 24-hour periods in different seasons. The IWV nudging is found to draw the model fields significantly towards

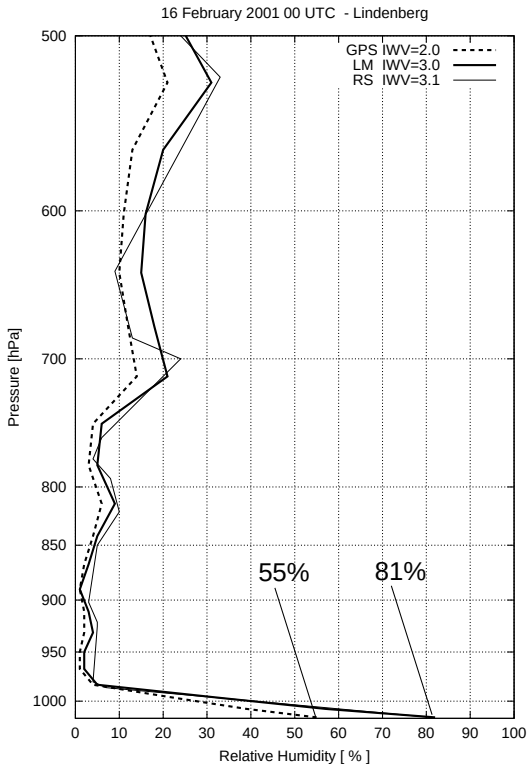

Figure 3: Relative humidity vertical profiles at station Lindenberg on 16 February 2001 at 00 UTC: profile from the vertical sounding corresponding to 3.1 kg m-2 (thin line), profile from the operational model LM corresponding to 3.0 kg m-2 (thick line) and the profile retrieved from the operational LM profile and the GPS observation of 2.0 kg m-2 (dashed line).

the GPS observations. For instance, the rms difference between the GPS and the model IWV is reduced from 2.0 kg m-2 to 1.3 kg m-2 on 3 April 2000. For a wintertime low-level inversion case (16 February 2001), however, a problem occurred. At low levels the humidity analysis of the experiment using GPS data starting from 00 UTC became rapidly drier than the routine analysis. For example, at station LDBG at 03 UTC the relative humidity of the lowest model level is 75% in the experiment and 89% in the routine.

The reason of this is illustrated in Figure 3. The humidity profile from the routine analysis, as well as that from the radiosonde data available at the site, describes an inversion associated with a very thin layer close to saturation immediately above the ground, a strong vertical humidity gradient, and very dry conditions further above. At the beginning of the experiment, i.e. at 00 UTC, the routine profile is used as input to retrieve the GPS profile. The observed GPS IWV is lower than the model value, and the small absolute difference in the order of 1 kg m-2 results in a GPS retrieved profile which is too dry at the low-levels. As a preliminary measure, a minimum threshold (2 kg m-2) has been introduced for the assimilation of GPS IWV. Further work will be dedicated to implement a check on the vertical humidity gradient to avoid unrealistic modifications of the model vertical structure by the IWV nudging.

For another case (3 May 2001) with strong rainfall in the North Rhine-Westphalia region, the impact on precipitation has been evaluated (Figure 4. At 18 UTC, the 12- hour accumulated precipitation analysis based only on SYNOP observations (Figure 4a) shows one cell of heavy rain around the station of Osnabrück (OSNA) which reported 34 mm. The precipitation field as derived from radar data (Figure 4b), although quantitatively less accurate, offers a more realistic picture of the rainfall pattern with two distinct cells. The operational assimilation run of the LM (Figure 4c) neither captures the detailed structure nor produces more than 5 mm in the area of interest. On the other side, the experiment which includes the GPS data after 00 UTC (Figure 4d) analyses this rainfall event significantly better, with two cells of more than 10 mm of accumulated precipitation. Note, however, that the impact is not everywhere positive. Over south-west Germany, the experiment produces more rain not confirmed by the observations. This is related to the assimilation of GPS IWV from two stations, Freiburg (FREI) and Karlsruhe (KARL), which indicate more humidity than the model. Therefore, further efforts are required to evaluate, understand, and improve the overall impact of GPS data on precipitation.

5 Conclusions

The results of monitoring the GPS data processed by GFZ indicate that their quality is acceptable for data assimilation purposes. In particular the very similar outcome for stations with and without meteorological sensors gives confidence in using IWV derived from the ZPD with the aid of model pressure and temperature. Another interesting finding is that sequences of hourly GPS data reveal a diurnal cycle not correctly captured by the model. First assimilation tests have shown that the model IWV is relaxed towards the GPS IWV successfully during the assimilation period, and that care must be taken in nudging IWV in some particular weather conditions, e.g. in the presence of strong vertical humidity gradients or at low IWV. The signal in the precipitation field is mixed, with the GPS data improving the analysis of a severe rain case but also tending to deteriorate the analysis in some areas without precipitation. Further work has to be dedicated to the tuning of IWV nudging, in particular with respect to the vertical distribution of the observational information and to its lateral spreading (e.g. testing a radius of influence smaller than 120 km). Assimilation experiments over longer time periods and the subjective and statistical evaluation of the

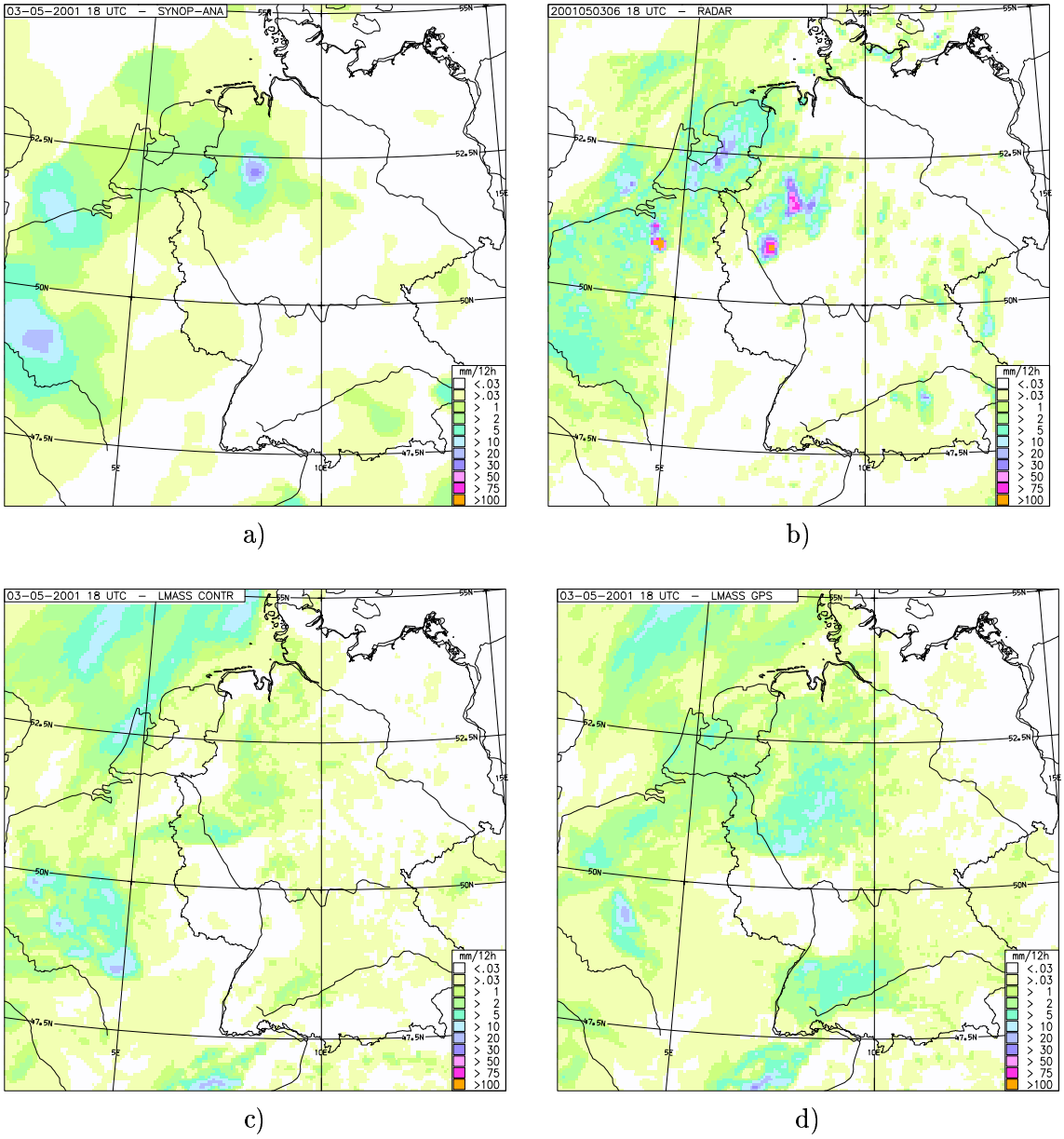

Figure 4: Accumulated precipitation from 6 to 18 UTC on 3 May 2001 from a) SYNOP observations, b) radar data, c) analysis of the operational model and d) analysis experiment with GPS data.

resulting forecasts, with a focus on the precipitation, are required to assess the impact of GPS data. It will be also interesting to carry out these experiments using the additional data from European stations available within the European Co-operation in Scientific and Technical Research (COST) Action 716.

Acknowledgments
This study was carried out under the grant of the German Federal Ministry of Education and Research (BMBF) No. 01SF9922/2.

Remarks
This paper will be published in "Physics and Chemistry of the Earth".

References

Bevis, M., S. Businger, S. Chiswell, T. A. Herring, R. A. Anthes, C. Rocken and R. H. Ware, 1994: GPS Meteorology: Mapping Zenith Wet Delay onto Precipitable Water. *J. Appl. Meteor.*, 33, 379-386.

Emardson, T. R., G. Elgered and J. M. Johansson, 1998: Three months of continuous monitoring of atmospheric water vapour with a network of global positioning system receivers. *J. Geophys.Res.*, 103, 1807-1820.

Gendt, G., C. Reigber, G. Dick, 2001: Near Real-Time Water Vapour Estimate in a German GPS Network - First Results from the Ground Program of the HGF GASP Project, *Phys. Chem. Earth (A)*, 26, 413-416.

Güldner, J. and D. Spänkuch, 1999: Results of Year-Round Remotely Sensed Integrated Water Vapour by Ground-Based Microwave Radiometry. *J. Appl. Meteor.*, 38, 981-988.

Koepken, C., 2001: Validation of Integrated Water Vapour from Numerical Models using ground-based GPS, SSM/I, and Water Vapor Radiometer measurements. *J. Appl. Meteor.*, 40, 1105-1117.

Kuo Y., Y. Guo and E. Westwater, 1993: Assimilation of Precipitable Water Measure-ments into a Mesoscale Numerical Model. *Mon. Wea. Rev.*, 121, 1215-1238.

Schraff, C., 1996: Data assimilation and Mesoscale weather Prediction: a Study with a Forecast Model for the Alpine Region. Publication No. 56, available from the Swiss Meteorological Institute, Zürich, CH.

A Two Timelevel Integration Scheme for the LM

Almut Gassmann

Deutscher Wetterdient, Offenbach am Main, Germany

The current three timelevel integration scheme for the LM has several disadvantages and should be improved or even replaced by an other scheme. The main drawbacks are its low order of approximation for advection, its need for a relatively large number of small time steps for the fast waves integration, its need of the Asselin time filter and its incompatibility to any positive definite advection scheme desired for the moisture variables.

By searching for an alternative one should turn the attention to a numerical consistent, stable and efficient scheme. In the framework of the split-explicit time integration every two timelevel advection scheme should fit for these requirements. The philosophy behind the split-explicit time integration scheme is to split slow and fast terms of the equations and to treat the fast sound and gravity wave terms with a shorter timestep than the others. During this short time step integration, the advective or slow tendency remains a constant. Besides the known three time level scheme of Klemp and Wilhelmson (1978), a two timelevel scheme was presented by Wicker and Skamarock (1998). But this scheme has the disadvantage that it only works in connection with a Runge-Kutta scheme of second order in time and its stability and phase properties are not excellent.

A new scheme works only a bit different than that of Wicker and Skamarock (1998). First, it integrates only the fast wave terms until the center of the time step and one gets result values ϕ^*. Second, from this ϕ^*-values advective tendencies are computed. These might be calculated with any stable two timelevel scheme. In a short notation they read as

$$\left(\frac{\partial \phi}{\partial t}\right)_{ADV} = \frac{\phi^{n+1} - \phi^n}{\Delta t} = F(\phi^*).$$

Here $F(\phi^*)$ denotes the advective tendency calculation. In the third step, short time steps are calculated from the beginning of the large time step till its end by retaining the slow (or advective) tendencies constant. A sketch of this scheme is given in Figure 1. The stability analysis of this scheme shows eigenvalues smaller than one almost everywhere. That means the scheme is stable and reliable. The stability analysis was performed for several advection schemes (Runge-Kutta scheme of second order in time, Lax-Wendroff scheme, semi-implicit scheme). They all exhibit good stability properties.

In the framework of the LM the new scheme needs only 6 short time steps in our configuration (instead of 7 in the current scheme). The Runge-Kutta scheme of second order in time with third order spacial upstream differences is chosen for advection in the horizontal direction

$$\begin{aligned} \tilde{\phi} &= \phi^* + \frac{\Delta t}{2} R(\phi^*) \\ F(\phi^*) &= R(\tilde{\phi}), \text{ with} \\ R(\phi) &= -\frac{u}{6\Delta x}\left(\phi_{i-2} - 6\phi_{i-1} + 3\phi_i + 2\phi_{i+1}\right) \text{ and } u > 0. \end{aligned}$$

The vertical advection has to be a Runge-Kutta scheme of second order, too. Thereby, centered differences work well despite of the Runge-Kutta scheme with centered spacial differences is slightly unstable taken for itself. But the scheme is stable in connection with the

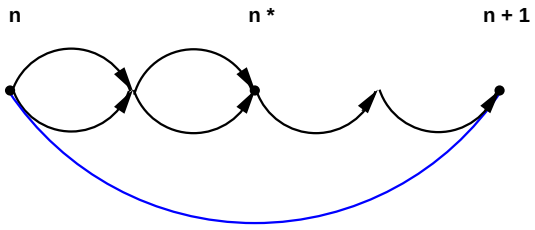

Figure 1: A sketch of the new time splitting scheme. The blue line symbolizes the advection step with the advective tendency evaluated for the provisional n* values, the black arrows mark the small time step integration.

splitting algorithm as can be shown by a stability analysis. Third order upstream horizontal differences should also be taken into account for the metric terms appearing in the calculation of the contravariant vertical velocity

$$\dot{\zeta} = -\frac{1}{\sqrt{\gamma}} \left(\frac{u}{a \cos\varphi} \frac{\partial p_0}{\partial \lambda} + \frac{v}{a} \frac{\partial p_0}{\partial \varphi} + g \rho_0 w \right)$$

and of the lower boundary condition for w which is free slip and the contravariant vertical velocity vanishes ($\dot{\zeta}_{N_\zeta+1/2} = 0$). Tendencies of the physics calculation are added to the advective ones to complete the slow tendencies. Thus they are easily included in the framework of the split-explicit scheme. Moisture variables are treated with a positive definite van-Leer advection scheme. No horizontal diffusion is added because a slight diffusion effect is present in the advection scheme anyway.

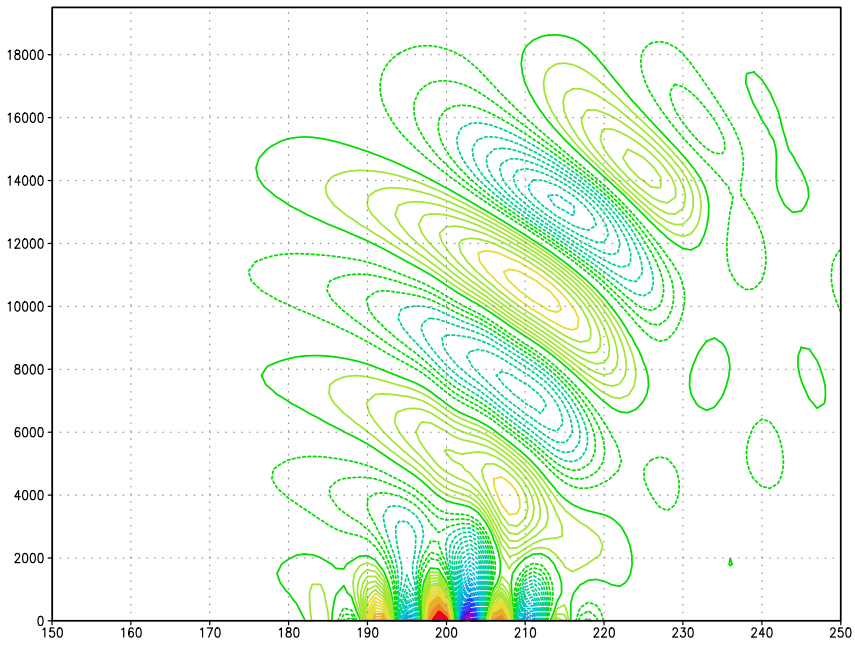

Figure 2: w-field for the idealized flow over a hilly orography, contour intervall 0.05 m/s

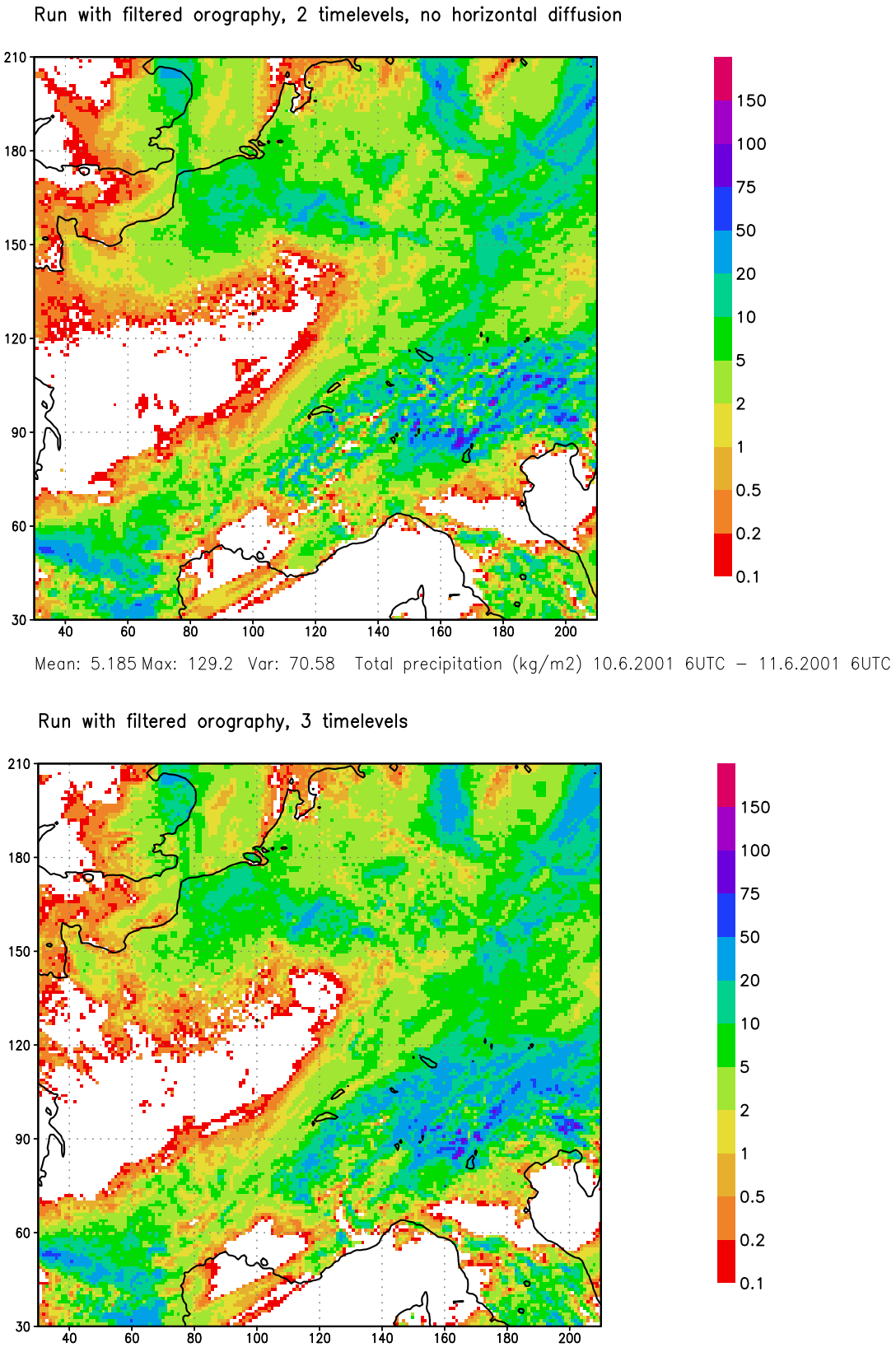

Figure 3: 24-h precipitation amount for an arbitrary test run. Top: with the two timelevel scheme. Bottom: with the three timelevel scheme

First, idealized 2-dimensional test runs with a dry atmosphere flow over a bell shaped mountain with small-scale terrain variations were performed, as done in Schär et al (2001). If the flow field is not exactly balanced, this test fails and a very distorted wave pattern appears. In our simulations, this test performs very well and the result for the w-field (Figure 2) is comparable to the analytic solution. It is noticeable that the test succeeds also with the three timelevel scheme.

Results of realisic simulations suggest that the scheme is working, but the predicted field of precipitation is noisier in mountainous regions than that of the current scheme (see Figure 3). This behaviour is not astonishing, because some of the diffusive and damping mechanisms are no longer present now and the order of approximation in the horizontal advection terms has increased. Remarkable is that the overall amount of precipitation is now slightly lower, whereas its maximum ist comparable to the three timelevel run. Focusing on the eastern Bavarian part, which lies on the lee side of the Alps, the precipitation amount is relatively smaller in the two timelevel run than in the three timelevel run. May be that other effects as the horizontal transport of precipitation become necessary. Other predicted fields look similar for both runs. The stability and the performance seem to be satisfactory with the new configuration, but the code is not yet optimized. There is still work to be done, above all more experiments on realistic cases. All together the two timelevel scheme is promising.

References

Klemp, J. B. and R. B. Wilhelmson, 1978: The Simulation of Three-Dimensional Convective Storm Dynamics. J. Atmos. Sci., 35, 1070-1096.

Schär, C., D. Leuenberger, O. Fuhrer, D. Lüthi and C. Girard, 2001: A new terrain-following vertical coordinate formulation for atmospheric prediction models. Submitted to Mon. Wea. Rev.

Wicker, L. J. and W. C. Skamarock, 1998: A Time-Splitting Scheme for the Elastic Equations Incorporating Second-Order Runge-Kutta Time Differencing. Mon. Wea. Rev., 126, 1992-1999.

Integration by Time-splitting in Mesoscale Models

Michael Baldauf

Institut für Meteorologie und Klimaforschung
Forschungszentrum Karlsruhe/Universität Karlsruhe

1 Introduction

In compressible models arises the problem, that fast processes (especially the acoustic waves) require small timesteps Δt for the reason of numerical stability, although these processes are not of meteorological interest. For the interesting slow processes timesteps ΔT are sufficient, which often are much bigger than Δt. There exist mainly two ways to circumvent a complete (and therefore inefficient) integration with the small timestep Δt: use of full implicit three-dimensional solvers for the sound or time-splitting. Whereas full implicit solvers need a lot of computer storage, time-splitting schemes are easier to implement. Here the fast processes are solved with the small timestep Δt and calculated more often, while the slow processes are calculated with a big timestep and accordingly more seldom. The whole scheme is more efficient because normally slow processes (above all advection and diffusion) require a lot of computing time whereas a sound timestep can be calculated in a relatively short time. Therefore a time-splitting scheme is required which solves the equations with an as large as possible time-splitting ratio $n_s := \Delta T/\Delta t$.

In the literature several time-splitting schemes have been discussed. The additive splitting (or complete operator splitting) first calculates the slow process and afterwards with the updated fields n_s times the fast processes. This scheme is relatively efficient, it uses 1 times the slow process and n_s times the fast process. But stability ist guarantied only, if the processes themselves are stable *and* commutable (Leveque and Oliger,1983). In the applications, one often observes a more ore less strong noise. Therefore the additive splitting is not recommended if the operators do not commute.

A second group of methods is due to the idea of Klemp and Wilhelmson (1978) (sometimes called partial operator splitting): to every fast process one adds a certain amount of the slow process. With that there follows a stronger coupling between the fast and the slow processes in comparison with the additive splitting. Consequently this method is much less influenced by noise. This basic idea can be realised with different time discretisation schemes like the leapfrog-scheme, the Euler-forward- or the Runge-Kutta-method.

The original method by Klemp and Wilhelmson (1978) uses a leapfrog-scheme and therefore is a real 3-timelevel-scheme. This not only is more expensive in programming and requires more computer storage, but also excludes the usage of some efficient advection schemes. It needs more computing time than the additive splitting because one has to carry out twice as many fast timesteps. Nevertheless this is an important method because it is stable, if a weak Asselin-Filter (which inhibits the chessboard instability of the leapfrog scheme) and a divergence filter (see below) is used (Skamarock and Klemp, 1992).

To circumvent the problem with three timelevels, Wicker and Skamarock (1998) proposed the Runge-Kutta-method in the Klemp-Wilhelmson framework instead of the leapfrog-scheme. Whereas values of the fields are calculated in a middle timelevel it is a real 2-timelevel-method. However, the calculation amount again is increased: 2 times the slow process and

$1.5n_s$ times the fast processes. The stability of this scheme with a sound-advection-system has been showed (Wicker and Skamarock, 1998).

In principle simpler as the both previously discussed methods is the combination of the Klemp-Wilhelmson-method with an Euler-forward-scheme. The calculation amount is equal to the additive time-splitting and has the advantage to be a 2-timelevel-scheme. Nevertheless this method was seldom used because a stability analysis by Skamarock and Klemp (1992) showed, that this method is unstable. In this work, a more detailed stability analysis is shortly presented, which shows that under certain circumstances, the Euler-forward-scheme becomes numerically stable.

2 The Linearised Sound-Advection System

Mostly these stability considerations are carried out with the following linearised, one-dimensional sound-advection-system

$$\frac{\partial u}{\partial t} + c_A \frac{\partial u}{\partial x} = -c_S \frac{\partial p}{\partial x} \quad (1)$$

$$\frac{\partial p}{\partial t} + c_A \frac{\partial p}{\partial x} = -c_S \frac{\partial u}{\partial x} \quad (2)$$

because it is on the one hand a very simple model (it contains only 2 variables and considers only one space direction), on the other hand it contains the two processes, which generally influence the stability of the Klemp-Wilhelmson-scheme.

For the stability analysis of the whole system we assume a simple upstream-differencing for the advection with constant velocity c_A and the forward-backward-scheme by Mesinger (1977) for the acoustic waves with constant sound speed c_S (for the space derivatives centered differences are used). For simplicity we assume a non-staggered grid with grid width Δx. One can introduce the two Courant-numbers $C_S := c_S \Delta t/\Delta x$ and $C_A := c_A \Delta T/\Delta x$. As everybody knows, the upstream-scheme is stable for $C_A < 1$; above this limit all the wavelengths become unstable. The forward-backward-scheme is stable for $C_S < 2$; above this limit the $4\Delta x$-waves become unstable first.

In the following, some results of a von-Neumann-stability analysis are presented. For the additive splitting the above mentioned limits for C_A, C_S are valid furthermore. The reason is that the sound-advection-system is special in so far, as the two operators for sound and advection commute (see the remark above).

In contrast to this, the stability range of the Klemp-Wilhelmson-Euler-forward-scheme is drastically reduced. This is shown in Figure 1 (left side), here already for a small time-splitting ratio $n_s = 2$. The reason for this are the long waves ($k \approx 0$), which are stable only in the range

$$C_A < 1 - C_S(1 + n_s).$$

So for increasing time-splitting ratios the stability range decreases.

This instability caused by the long waves cannot be cured by a smoothing filter which acts only on small wavelengths. Already Skamarock and Klemp (1992) pointed out that a divergence filter can increase the stability of the Klemp-Wilhelmson-leapfrog-scheme. A divergence filter is formulated as a gradient of the velocity divergence, which is added to the equations of motion. Taking the divergence of the equation of motion one gets with this term a diffusionlike equation for the divergence. Because only the meteorologically unimportant

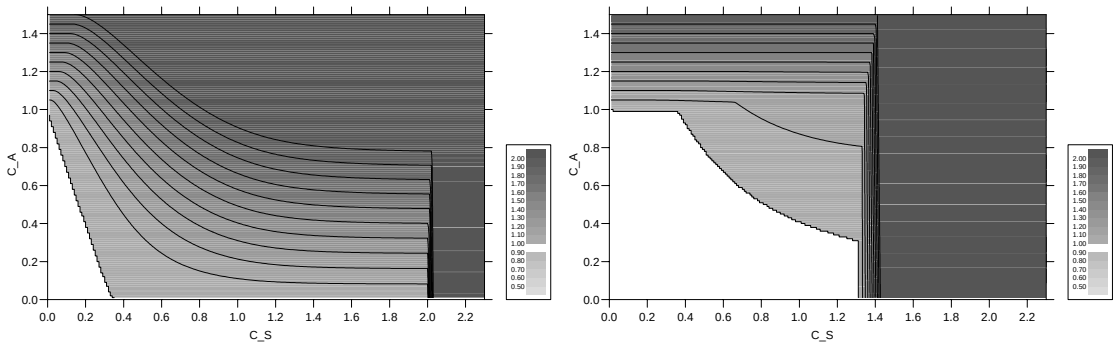

Figure 1: Stability diagram of the Klemp-Wilhelmson-scheme: the maximum absolute eigenvalue $|\lambda|_{max}$ in dependency from the Courant-numbers C_A and C_S. On the left side without divergence damping and for a time-splitting ratio $n_s = 2$, on the right side with divergence damping ($C_{div} = 0.45$) and $n_s = 4$.

sound waves are significantly divergent[1], one accepts this artificial term. Equation (1) is therefore supplemented by

$$\frac{\partial u}{\partial t} + \ldots = \ldots + \alpha_d \frac{\partial}{\partial x}\left(\frac{\partial u}{\partial x}\right)$$

By introduction of the Courant-number $C_{div} = \alpha_d \Delta t / \Delta x^2$ and using an explicit differencing scheme the divergence filter is stable for $C_{div} < 1/2$.

If one carries out the analysis with this divergence filter one gets a significant increase of the stability range (see Figure 1, right side). Now the condition for the stability of the long waves is

$$1 - C_A - C_S > \left(C_S - \frac{C_{div}}{C_A}\right) n_s.$$

This condition can easily be fulfilled in the case of strong divergence damping

$$C_{div} > C_S C_A$$

In this case, there exist no upper limit for the time-splitting ratio n_s.

In contrast to this the analysis of Skamarock and Klemp (1992) delivered an instability of the Euler-forward-scheme. The reason for this is that they aspired to solve the stability problem fully analytic and first made a spatial fourier transform of the equations. This seems to deliver a too careful limit for the stability range. One should pronounce that the stability analysis shown here assumes the rather diffusive upstream scheme for the advection.

3 Conclusion

The Klemp-Wilhelmson-Euler-forward-scheme seems to be useable in mesoscale models if one takes a sufficient strong divergence damping. In our model KAMM2 (Karlsruher Atmosphärisches Mesoskaliges Modell, version 2) a damping factor $\alpha_d = 0.1 c_S^2 \, \Delta t$, which is also given by Skamarock and Klemp (1992), is sufficient. It is interesting, that from a viewpoint of stability there exist no upper limit for the time-splitting ratio. In KAMM2 we nevertheless limit the ratio in the most cases by $n_s \leq 20$ (in spite of the fact that also simulations

[1]With the exception of the bouyancy term in the equation of heat, when formulated with the absolute temperature. But this term can be expressed equivalent to the Boussinesq-Approximation.

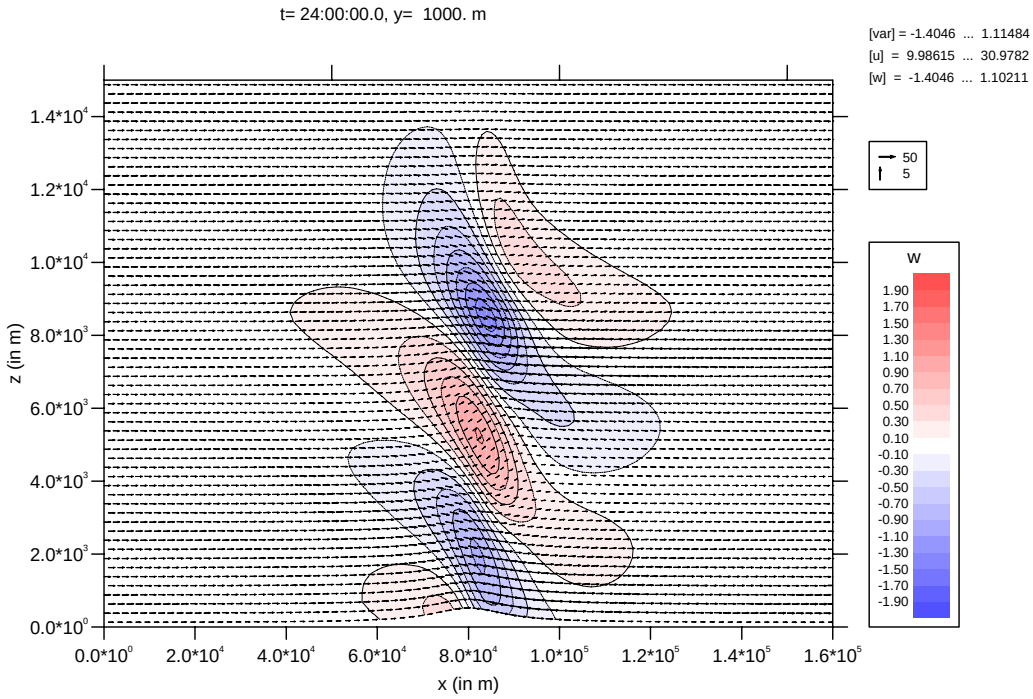

Figure 2: Simulation of a 2-dimensional flow over a mountain with the Klemp-Wilhelmson Euler-forward method.

with $n_s \leq 50$ were stable). As an example a 2-dimensional flow over a wide mountain in the isothermal case, that means a relatively strong thermal stability, is shown in Figure 2. The simulation remains stable at least for 24 hours.

References

J. B. Klemp and R. B. Wilhelmson, 1978: The simulation of three-dimensional convective storm dynamics. *J. Atm. Sci.*, 35, 1070–1096.

R. J. LeVeque and J. Oliger, 1983: Numerical methods based on additive splittings for hyperbolic partial differential equations. *Math. Comp.*, 40(162), 469–497.

F. Mesinger, 1977: Forward-backward scheme, and its use in a limited area model. *Beitr. Phys. Atm.*, 50, 200–210.

W. C. Skamarock and J. B. Klemp, 1992: The stability of time-split numerical methods for the hydrostatic and the nonhydrostatic elastic equations. *Am. Met. Soc.*, 120, 2109–2127.

L.J. Wicker and W.C. Skamarock, 1998: A time-splitting scheme for the elastic equations incorporating second-order Runge-Kutta time differencing. *Mon. Wea. Rev.*, 126, 1992–1999.

The SLEVE Coordinate in LM

Daniel Leuenberger

MeteoSwiss, Krähbühlstrasse 58, 8044 Zürich, Switzerland

1 Introduction

Most numerical weather prediction models, including the LM, are written in terrain-following coordinates. The height of the model levels thus depend on the underlying topographic structure. Over complex mountainous areas the inhomogeneities in the levels may cause truncation errors in the numerical schemes. *Schär et al.* (2001) have recently suggested a new SLEVE (Smooth Level VErtical) coordinate formulation which produces a smooth computational mesh at mid and upper levels. Unlike traditional formulations, e.g. the well known pressure based Sigma coordinate or the height based Gal-Chen coordinate, which are both implemented in the LM, the new SLEVE coordinate transformation is characterized by a scale dependent, exponential vertical decay of the terrain structure. This allows for a fast decay of small-scale topography components, leading to a fast transition from terrain-following to smooth levels.

The present report contains a brief description of some properties of the new SLEVE formulation and shows first results of both idealized and realcase studies with LM. It is shown that the use of the SLEVE coordinate can have a significant influence on the forecast results.

2 Definition and properties of the SLEVE coordinate

Definition

For the definition of the SLEVE coordinate the terminology and the notation of the section about terrain-following coordinates in *Doms and Schättler* (1999) is used. The height-based SLEVE coordinate μ is a non-normalized coordinate taking the values $\mu = 0$ at the terrain surface h and $\mu = \mu_T = z_T$ at the model top. Similar to the definition of the Gal-Chen coordinate, the inverse transformation for the SLEVE coordinate is given by

$$z(\lambda, \varphi, \mu) = a(\mu) + b_1(\mu) h_1(\lambda, \varphi) + b_2(\mu) h_2(\lambda, \varphi) \tag{1}$$

where λ and φ are rotated longitude and latitude used in LM, respectively. The topography parts h_1 and h_2 denote the large-scale and the small-scale components of the topography $h(\lambda, \varphi)$ and satisfy the relation

$$h(\lambda, \varphi) = h_1(\lambda, \varphi) + h_2(\lambda, \varphi) \tag{2}$$

The mapping functions $a(\mu)$ and $b_i(\mu)$ of a *hybrid version* of the SLEVE coordinate are given by

$$\begin{aligned} a(\mu) &= \mu, \\ b_i(\mu) &= \begin{cases} 0 & : \ \mu_F \le \mu \le \mu_T \\ \frac{\sinh((\mu_F - \mu)/s_i)}{\sinh(\mu_F/s_i)} & : \ 0 \le \mu < \mu_F \end{cases} \end{aligned} \tag{3}$$

where the subscript $i = 1$ refers again to the large-scale part and $i = 2$ to the small-scale part of the topography. The decay constants s_i define the vertical decay rate of the respective topography component, i.e. at a height s_i the contribution of h_i to the level height has fallen to a factor of $1/e$ of the value at the surface $z = h$. $\mu_F = z_F$ denotes the height, where the terrain-following surfaces change to horizontal z-surfaces.

The *original* SLEVE formulation is obtained by setting z_F to the height z_T of the model domain, i.e. $\mu_F = \mu_T$. It can be noted that the use of the hybrid SLEVE formulation mitigates the problem of the discontinuity in the determinant of the inverse Jacobian matrix at $\mu = \mu_F$ since $|\frac{\partial b_i}{\partial \mu}|_{\mu=\mu_F}$ is smaller compared with the Gal-Chen formulation.

Invertibility condition and choice of vertical decay rates

Since any vertical coordinate transformation must be unique, the function (1) must be strictly monotone. A sufficient (but not necessary) condition can be expressed as

$$\frac{\partial z}{\partial \mu} \geq \gamma > 0 \tag{4}$$

where

$$\gamma = 1 - \frac{h_{1,max}}{s_1} \coth\left(\frac{\mu_F}{s_1}\right) - \frac{h_{2,max}}{s_2} \coth\left(\frac{\mu_F}{s_1}\right) \tag{5}$$

Here, $h_{i,max}$ denote the maxima of the topography parts in the computational domain. From this condition it becomes clear that the choice of the decay rates s_1 and s_2 is not free but depends on the topography, the decomposition filter and the inter-facial height μ_F. In practice it is desirable that the *small-scale* component decays as fast as possible because these structures cause the most serious transformation errors. Therefore s_2 must be chosen as small as possible. Since the well resolved topography structures are much less responsible for errors, s_1 may be set to a larger value than s_2 resulting in slowly varying levels even in the upper part of the domain.

3 Idealized study

In this section results from an idealized study of stably stratified, dry flow impinging upon a two-dimensional mountain are presented. The background flow of the atmosphere is defined by a constant Brunt-Väisällä frequency $N = 0.01\ s^{-1}$ and by the velocity in x-direction $U = 10\ m/s$. Together with the upstream surface temperature ($T_0 = 288\ K$) and pressure ($p_0 = 1000\ hPa$), this fully determines the background profile.

The topography has a bell-shaped structure with superposed complex variations:

$$h(x) = h_0 \exp\left[-\left(\frac{x}{a}\right)^2\right] \cos\left(\frac{\pi x}{\lambda}\right)^2 \tag{6}$$

with $h_0 = 250\ m$, $a = 5\ km$ and $\lambda = 3\ km$. The mountain waves forced by this terrain have two major components, one large-scale component which propagates with height and a small-scale wave which decays rapidly with height. The horizontal grid length is $\Delta x = 500\ m$, so the wavelength of the fine-scale structure is $6\ \Delta x$. The vertical discretization is done on 65 levels with a uniform level spacing of $300\ m$.

Two simulations using the two-dimensional version of the LM are performed, one with the traditional Gal-Chen coordinate and one with the SLEVE coordinate using values of $s_1 = 5000\ m$ and $s_2 = 2000\ m$. Figure 1 shows the steady-state solution of the vertical velocity computed with a) a linear model based on Fourier decomposition (see *Schär et al.* (2001)),

b) LM with the Gal Chen coordinate and c) LM with the SLEVE coordinate. The simulation using the Gal-Chen coordinate shows fine-scale noise in the large-scale waves, which is very likely caused by transformation errors, where with the SLEVE coordinate this noise can be reduced substantially.

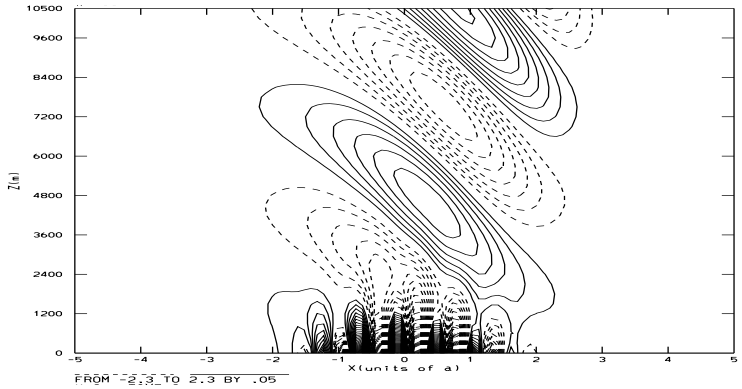

a) Linear solution

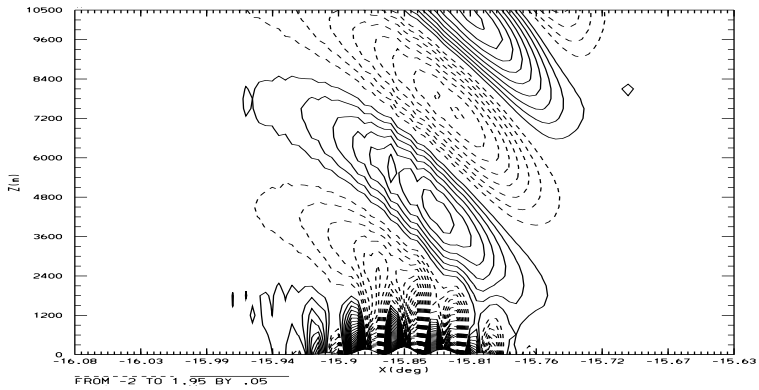

b) LM with Gal-Chen coordinate

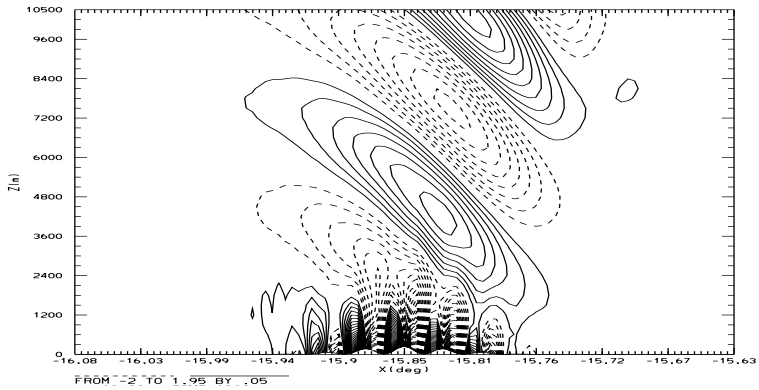

c) LM with SLEVE coordinate

Figure 1: Results from the idealized study of dry, stratified flow against a two-dimensional mountain. Isolines of the steady state solution of vertical velocity computed with a) a linear model (reference solution), b) LM with Gal-Chen coordinate c) LM with SLEVE coordinate. Positive contours are solid, negative contours are dashed, contour interval is 0.05 m/s

4 Real-case studies

Here we consider results from two real-case studies demonstrating the performance of the SLEVE coordinate in the realcase environment of LM. For both cases, forecasts are computed with the operational settings used at MeteoSwiss (hereafter referred to as operational simulation) and compared to simulations using the SLEVE coordinate. The settings are identical except for the type of vertical coordinate: the operational setting uses pressure hybrid coordinates with 45 levels and horizontal z-coordinates above $\mu_F = 11357\ m$. The SLEVE setting uses the same number of levels and vertical decay rates of $s_1 = 10000\ m$ and $s_2 = 2000\ m$. Figure 2 shows vertical west-east cross-sections at 46.5N of the level structure for the operational (panel a) and for the SLEVE coordinate (panel b).

Additional simulations have been performed using a SLEVE *hybrid* coordinate with the same inter-facial height as in the operational setup. The results are found to be very similar to those obtained with the SLEVE coordinate and are thus not shown here. These simulations, however, confirm that the SLEVE formulation can also be used in a hybrid form.

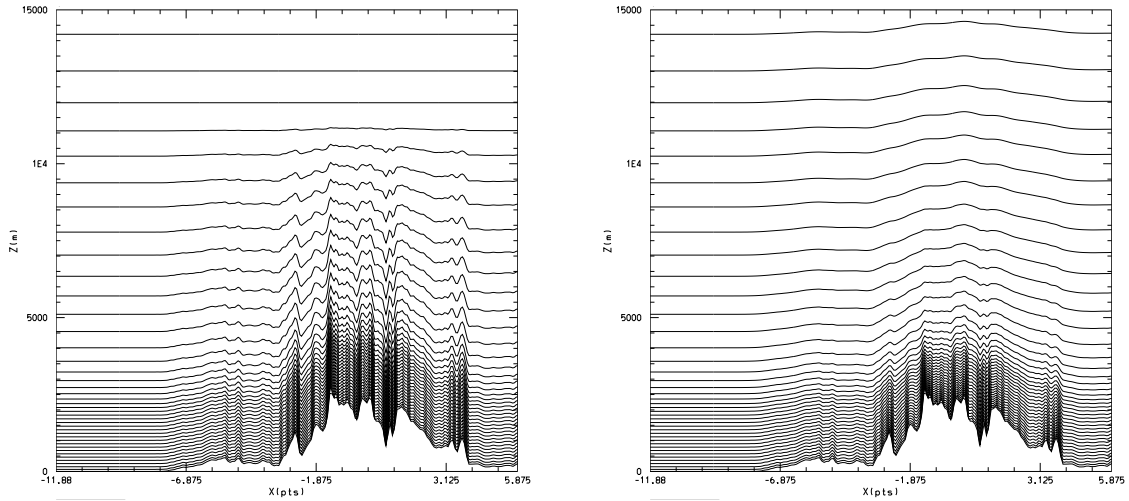

Figure 2: Vertical West-East cross-sections of the height of the computational surfaces for a) hybrid pressure coordinate (operational at MeteoSwiss) and b) SLEVE coordinate. Only the lower 15 km of the domain are shown.

Strong-wind case of 18.1.2000

The first case is characterized by a strong northerly flow against the alps resulting in large horizontal and vertical winds over the alpine topography and a blocked low-level air mass at the north side of the alps accompanied with stratiform precipitation. The forecasts are initialized at 18.1.2000 00h from GME output. Figure 3 shows vertical west-east cross-sections at 46.5N of the V-component of the horizontal velocity and isolines of potential temperature at forecast time +08h computed with a) the operational setting and b) the SLEVE coordinate. The jet of strong northerly wind with a maximum of more than 50 m/s over the eastern part of the alps is clearly visible.

Results computed with the SLEVE coordinate show overall smoother fields in heights between 2000 m and 12000 m. This is the region where the largest differences in the structure of the computational levels between the two coordinate types can be found. It is likely that some of the upper level fine-scale structures observed in the operational simulation are caused by transformation errors of the same type as those obtained in the idealized study.

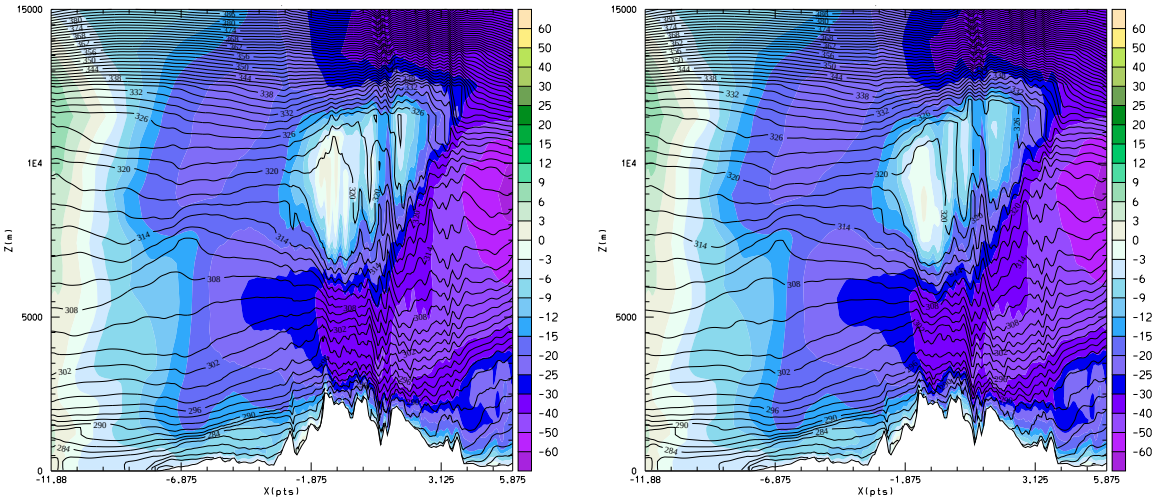

a) b)

Figure 3: Vertical West → East cross-sections of the V-component of the horizontal velocity and isolines of potential temperature computed with a) the operational setting and b) the SLEVE coordinate. Only the lower 15 km of the domain are shown.

Convective case of 27.6.2001

Next we consider a summer case characterized by heavy prefrontal convective activity over the alpine area having caused considerable amounts of precipitation at different locations in the Swiss Alps. The forecasts are initialized at 27.6.2001 00h from GME output. Figure 4 shows vertical south-north cross-sections at 7.2E of the relative humidity and isolines of equivalent potential temperature at forecast time +10h computed with a) the operational setting and b) the SLEVE coordinate.

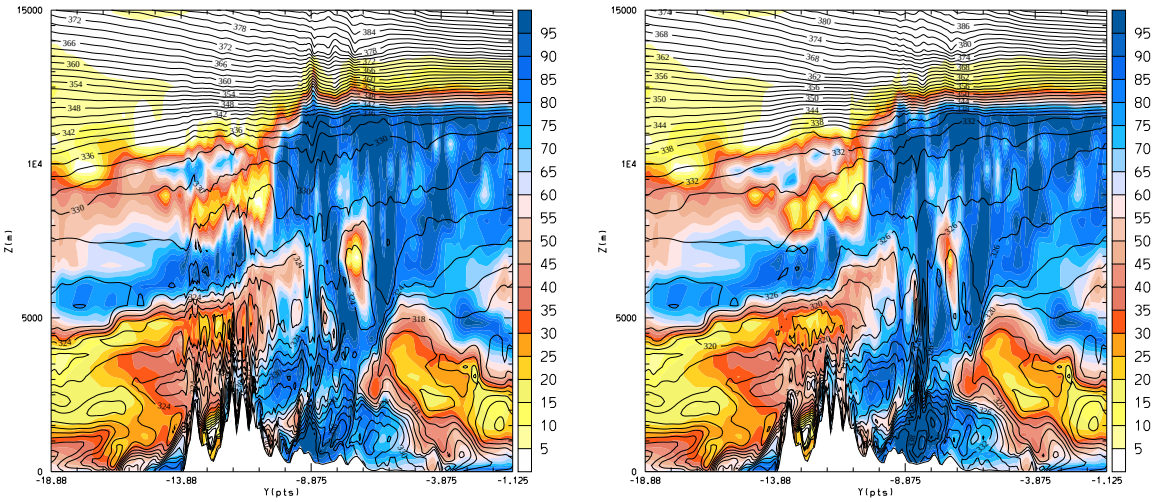

a) b)

Figure 4: Vertical South → North cross-sections of the relative humidity and isolines of equivalent potential temperature computed with a) operational setting and b) SLEVE coordinate. Only the lower 15 km of the domain are shown.

The differences in the results are more pronounced than in the winter case. The fields computed with the operational setup show fine-scale structures even in regions up to the height of the tropopause (Figure 4a). The fact that these structures are confined to regions of complex topography and are of columnar shape aligned with underlying topography struc-

tures suggest that these structures are caused by numerical rather than physical effects. The results obtained with the SLEVE coordinate are much smoother in regions over complex topography and much of the fine-scale noise in mid and upper levels is reduced considerably.

An investigation of the precipitation fields has shown that even over small topography elevations a considerable difference in the structure and amplitude of the precipitation computed with the different coordinates can be observed. A comparison with radar observations over Switzerland, indicates that the performance of the SLEVE coordinate in predicting precipitation is not superiour to that of the operational setup. However, the overall structure of the fields is smoother and more coherent with the SLEVE coordinate.

5 Summary and Conclusion

The use of the new SLEVE coordinate in LM has proven to be able to reduce fine-scale noise in computed fields over poorly resolved topography structures by generating smoother computational levels in mid and upper parts of the domain compared to traditional coordinates like the Sigma coordinate or the Gal-Chen coordinate. The convective summer case simulation is more sensitive to the structure of the levels than the strong-wind winter case. The computational overhead for the calculation of the SLEVE levels is neglectable.

References

Schär, C., D. Leuenberger, O. Fuhrer, D. Lüthi and C. Girard, 2001: A new terrain-following vertical coordinate formulation for atmospheric prediction models. *Submitted to Monthly Weather Review.*

Doms, G. and U. Schättler, 1999: The Nonhydrostatic Limited-Area Model LM (Lokal-Modell) of DWD: Part I, Scientific Documentation, *http://www.cosmo-model.org/*

The Z-Coordinate Version of the LM

Jürgen Steppeler and [1)]Heinz-Werner Bitzer

Deutscher Wetterdient, Offenbach am Main, Germany

[1)] *Amt für Wehrgeophysik, Traben-Trarbach, Germany*

Meso scale models in terrain following coordinates generate strong erroneous forces near mountains, which lead to artificial circulations even with a horizontally stratified atmosphere. An obvious remedy of this problem is the use of a Z-coordinate, with the effect that the orography cuts into the lower model levels. With such an approach it is necessary to be careful in formulating the lower boundary condition. It is necessary to allow for a sufficiently smooth representation of the orography (see Kröner,1997). Step function representations of the lower boundary can have problems in representing the orography smoothly and therefore can produce problems in representing the flow around hills (Gallus and Klemp, 2000).

The aim of this short paper is to give an introduction to the z - coordinate version of the LM. A more detailed paper suitable as a documentation for those wishing to work with it is in preparation.

The approach presented here is based on the finite volume approach using shaved cells. These are obtained by cutting a regular rectangular grid with an orographic function which is represented as a continuous bilinear spline. A number of further approximations are applied in order to make the scheme practical for operational use. The equations of motion are the same as described in the LM-documentation, but specialised to the case with a flat orography. Fig. 1 shows the grid for the two dimensional case. For cells not cut by the orography the finite difference equations are the same as with the operational LM. For the computation of the fast waves in the cut cells it is essential to use weights derived from the distances which the orography cuts out of a grid cell. As an example, the derivation of the discretization of the divergence from the finite volume principles is derived. Let $D_{i,k}$ be the amplitudes for the divergence representation, to be defined for integer i, k. $V_{i,k}$ is the volume of the cut cell. For the definition of the other symbols refer to Fig. 1. The discretization formula is derived by integrating the divergence over a cell volume:

$$\begin{aligned} D_{i,k}V_{i,k} = \int \left(\frac{\partial u}{\partial x} + \frac{\partial w}{\partial z}\right) dxdz \quad &= \quad dx'_{i,k-1/2} \cdot w_{i,k-1/2} - dx'_{i,k+1/2} \cdot w_{i,k+1/2} \\ &\quad + dz'_{i+1/2,k} \cdot u_{i+1/2,k} - dz'_{i-1/2,k} \cdot u_{i-1/2,k} \end{aligned}$$

We make the thin wall approximation. For cells which are not cut we have dx'=dx and dz'=dz and therefore the equation above is the centred difference approximation, as used in the operational LM.

For the discretization of the slow modes, centred difference approximations are used, which require posing boundary values at points under the mountain. These boundary values for the computation of the advection terms are computed by interpolating into the mountain using planes determined by three points which are outside the mountain.

The scheme is implemented now in three space dimensions. A numerical experiment was performed using a circular mountain of height 400m and half width 10 km with 36 levels changing from 100m to 200m near the surface. The upper layers were 1200m. The horizontal grid length was 2 km. According to Gallus and Klemp (2000) the generation of a hydrostatic

gravitational wave generated by a smooth bell shaped mountain is a crucial test for Z-coordinate models. Boundary treatments of the step mountain type often create solutions which are not very smootth and can even be entirely wrong.

Fig. 2 shows the u-velocity of the solution after 2.5 hrs, corresponding to a cross section through the centre of the mountain. It corresponds well to the analytic solution of this problem.

References

Gallus, W. and J. Klemp, 2000: Behaviour of flow over Steep Orography. *Mon. Wea. Rev.*, 128, 1153-1164.

Kröner, D., 1997 Numerical Schemes for Conservation Laws, Wiley, N. Y., pp 507.

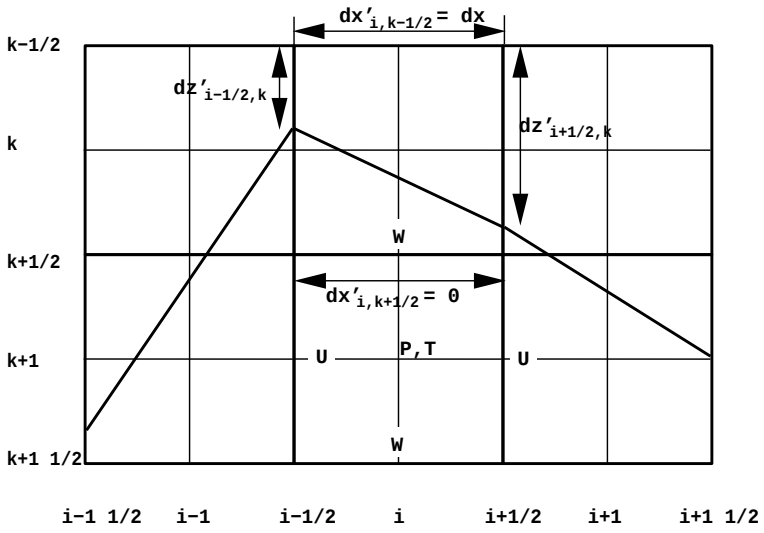

Figure 1: The grid for the z-coordinate representation

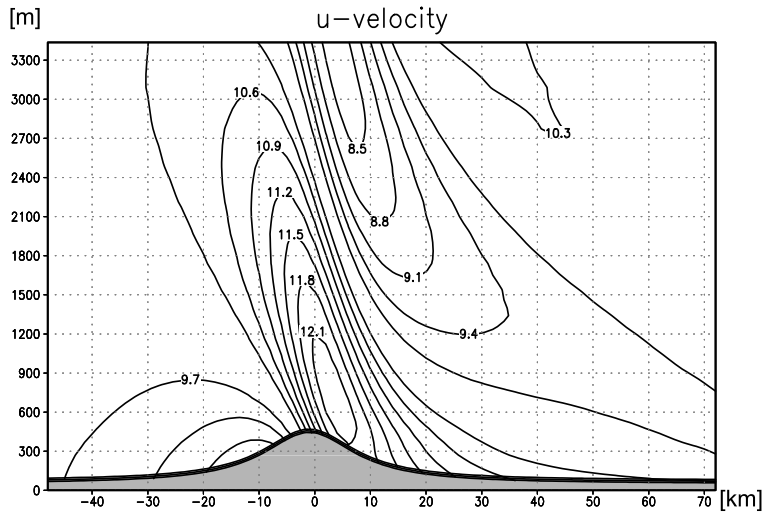

Figure 2: The u-velocity of the 2.5 hr forecast with the z-coordinate LM

3D-Transport of Precipitation

Almut Gassmann

Deutscher Wetterdient, Offenbach am Main, Germany

The current scheme for gridscale precipitation assumes column equilibrium for sedimenting constituents like rain or snow. That is, sedimentation can be considered to be a fast process compared to the characteristic time of cloud development. In the model's framework rain or snow are falling through all lower model levels within a single time step. Consequently, the precipitation fluxes of rain P_r and snow P_s are used as dependent model variables and are used to compute the various source terms. The full prognostic equation for the mass fraction of rain q^r or snow q^s degenerates to the diagnostic expression

$$-\frac{1}{\rho}\frac{\partial P_x}{\partial z} = S_x \tag{1}$$

in which x stands for r (rain) or s (snow), respectively.

With the refinement of the model to the meso-scale the assumptions made above get more and more unrealistic. Cumuliform clouds come into a resolvable scale. Thus, the vertical and horizontal advection and inside cloud temporal interactions of rain and snow can't be ignored any longer for a realistic forecast. Even for the stratiform generation of precipitation horizontal advection must be taken into account. The time scale it takes before a raindrop or a snowflake reach the ground can be about 15 minutes and the horizontal scale it passed during this time may be several 10th of kilometers. Although q^c (cloud water) and q^v (specific humidity) are advected in the current model, the lee side precipitation is not sufficiently recognized by the model. With a prognostic scheme this lack is hoped to be reduced.

In contrast to (1), the full prognostic equation for rain or snow reads

$$\frac{\partial q^x}{\partial t} + \vec{v}\cdot\nabla q^x - \frac{1}{\rho}\frac{\partial P_x}{\partial z} = S_x. \tag{2}$$

Thus, the reformulation of the model requires the use of q^x as dependent and now prognostic model variables instead of P_x, the explicit treatment of the sedimentation term and a positive definite advection scheme for the moisture variables.

The reformulation of the model in terms of $q^x = \rho^x/\rho$ is easily done by the use of the relation

$$P_x = \alpha_x \left(\rho^x\right)^{e_x} \tag{3}$$

where α_x is a constant factor and e_x is a constant exponent. These numbers follow from the parameterization assumptions of the Kessler scheme. The reformulation of the source terms S_x is now straightforward.

The explicit treatment of the sedimentation term turns out to be more difficult. The terminal velocity v_z is a nonlinear function of the specific amount itself. It is sometimes larger than allowed by the Courant number, especially in the boundary layer where the model layers become thin. If the rain is falling with a terminal velocity of 4 m/s and the model's time step is 40 seconds, the Courant number for the lowest model layer gets 7.5 which exceeds greatly the allowed number of one. Due to the nonlinear behaviour of the terminal velocity an implicit treatment of the sedimentation term is impossible. But the explicit treatment

of sedimentation requires a smaller time step. In our approach, the time step is adjusted to the layer thickness and a number of intermediate shorter time steps are used only when required. But this requires the use of a first order upstream scheme

$$(\rho^x)_k^{\nu+1} = (\rho^x)_k^{\nu} - \frac{\Delta t_i}{\Delta z_k} \left(v_{z,k}^{\nu} \, (\rho^x)_k^{\nu} - v_{z,k-1}^{\nu} \, (\rho^x)_{k-1}^{\nu} \right) . \tag{4}$$

Here, ν counts the intermediate time steps which have the length of Δt_i. The sum of the intermediate time steps equals one model time step $\sum_i \Delta t_i = \Delta t$. In practice, the loop is done from the highest model layer to the lowest (the direction of decreasing layer thickness). If it turns out that the time step has to be reduced the time step is halved. The flux over one intermediate time step is assumed to be constant. So, the sedimentation scheme requires only information from the current and the next upper layer. Furthermore, no fluxes have to be interpolated. Despite of the diffusivity and the numerical costs this scheme has the advantage to avoid unnecessary computations and is automatically positive definite. We hope that because of the relatively small number of time steps for sedimentation the effect of the diffusivity of the scheme is of minor importance. Moreover, process splitting (Strang-splitting) is done so that first sedimentation is computed for $\Delta t/2$, then the microphysical conversion rates and source terms are evaluated and last, a second $\Delta t/2$ sedimentation step is done. Other methods for the treatment of the sedimentation term are possible but are not implemented or tested. For instance, the highest occuring Courant number can determine the small time step for the whole column in combination with a higher order sedimentation scheme (Dudhia et al, 1993). An other possibility is the use of the flux-form semi-Lagrangian technique which avoids small time steps at all (Kato, 1995).

Advection of q^r and q^s is done with a positive definite van-Leer scheme as for advection of cloud ice q^i. Advection as well as sedimentation are discretized as schemes acting on two timelevels. Whitin a three timelevel environment this causes problems in mass and energy conservation because other related variables such as q^c, q^v and T are defined on three timelevels. The scheme thus requires the LM as a two timelevel discretization. Work is in progress on that topic, too. Besides, a formulation with the use of partial densities ρ^x would be more consistent in relation to the conservation of mass.

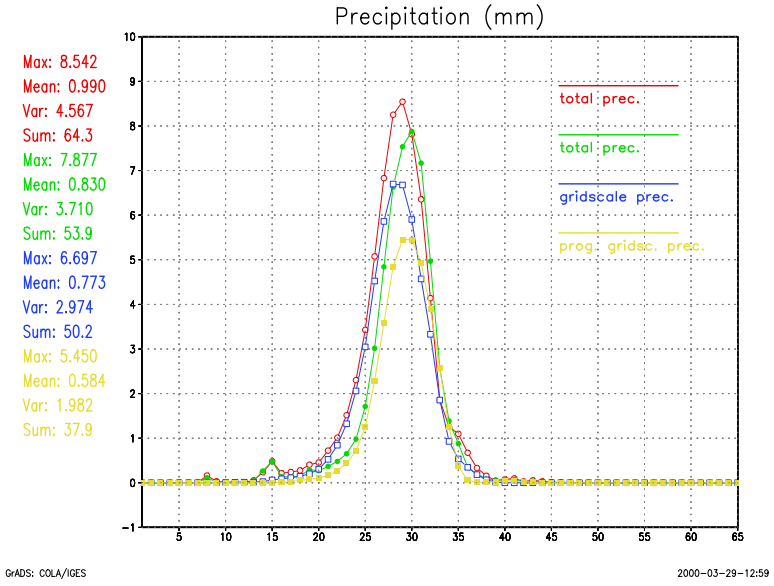

Figure 1: Idealized 2D test case: Total and gridscale Precipitation.

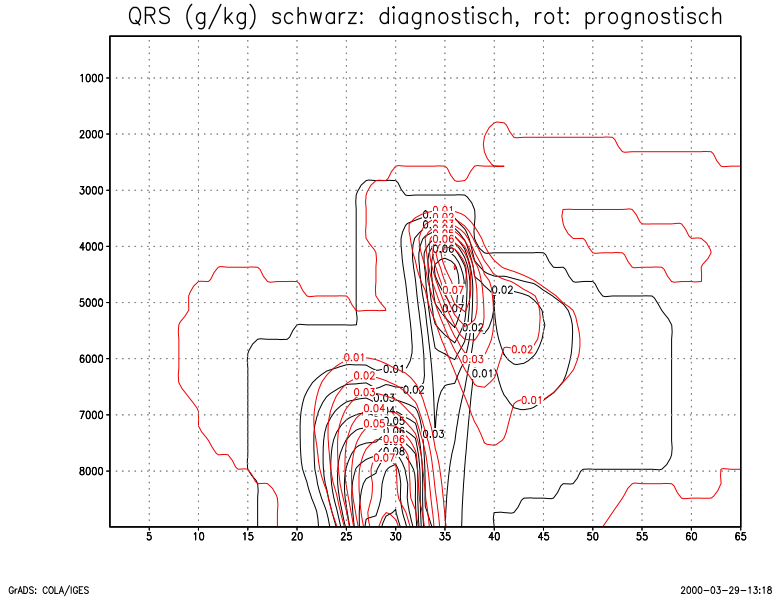

Figure 2: Idealized 2D test case: Sum of rain and snow content for the diagnostic scheme (black) and the prognostic scheme (red).

A simple test case is the 2-dimensional flow over a mountain ridge in a wet atmosphere. In the experiment, the mountain has a maximum height of 1000 m and a half width of 50 km on a 7 km mesh, its peak is located at gridpoint 33 in the following figures. A flow of 10 m/s wind speed is coming from the left and the atmosphere has a relative humidity of 95% in the middle troposphere. As shown in figure 1 after 12 hours of integration, the total amount of rain and snow $q^{r,s}$ is advected to the right in comparison to the diagnostic scheme where precipitation particles are not advected at all. The sedimentation velocity of snow is sometimes as small that snow is more advected than sedimented which diffuses these particles troughout the model domain in a very small concentration. This is indicated in this figure by the large area covered with a very small snow amount. Figure 2 shows the total amount of precipitation after 12 hours. The maximum precipitation amount is shifted to the right by about 1 mesh size. This seems to be plausible. The overall amount of precipitation is lower (84%) than that of the compared diagnostic scheme. This effect is also significant in other experimental studies (see below). It might be due to the larger evaporation of rain below and outside the cloud.

A first realistic test case is the Brig case. The Brig flood in September 1993 caused a lot of damage in the Brig valley. It was not sufficiently forecasted by the LM with the diagnostic precipitation scheme, it even gave no precipitation for the Brig grid point itself. The station data in figure 3 show the luv side (and even the lee side) of the Alps with a considerable amount of precipitation. Figure 4 compares LM forecasts[2] with prognostic and diagnostic gridscale precipitation schemes. With the diagnostic precipitation scheme the lee side of the mountains has little precipitation and the upper Rhone valley is almost completely without precipitation. The maximum amount of precipitation is found to be in the southwestern part of the domain. With the prognostic precipitation scheme, the lee side of the Alps gets more precipitation, there are no dry valleys and the maximum precipitation amount for a single gridpoint is reduced to about one half of that achieved with the diagnostic scheme. The region of maximum precipitation has moved northeast and is thus more towards the region of observed maximum precipitation. The precipitation field is much smoother. This

[2]These were performed without fitered orography.

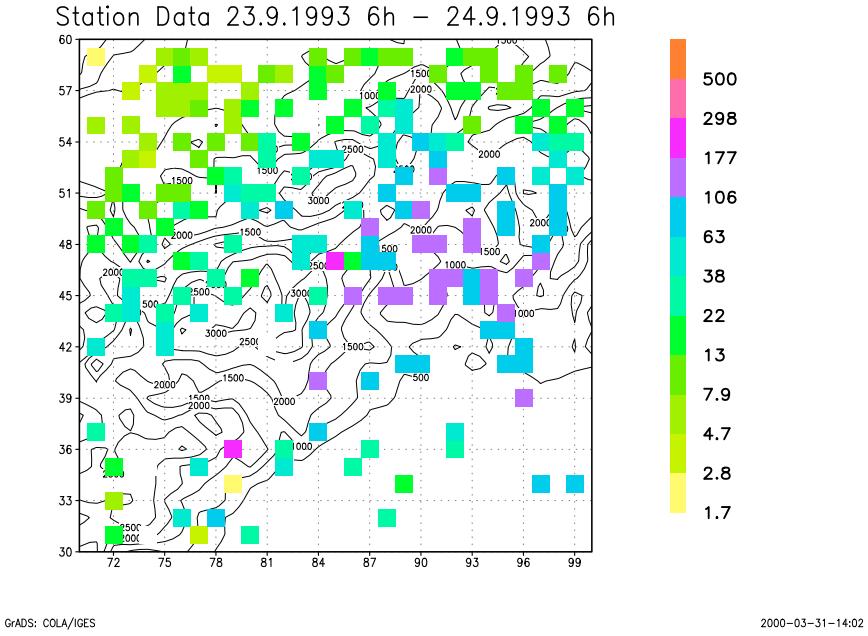

Figure 3: Brig case: Station data for precipitation

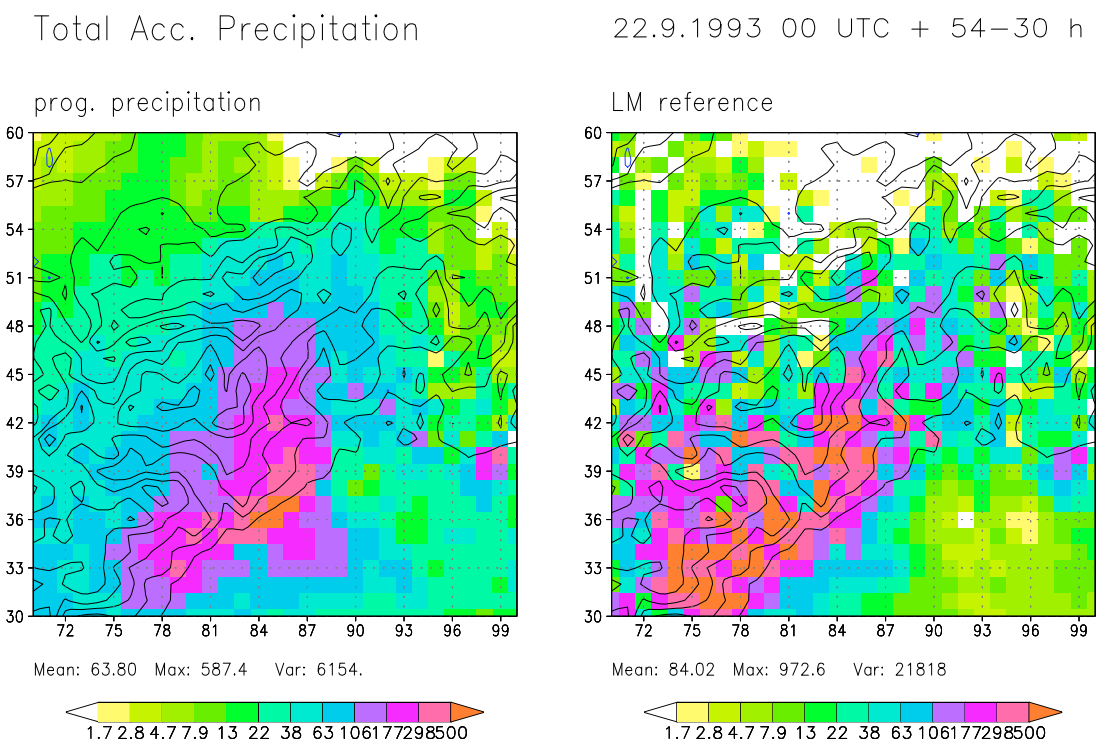

Figure 4: Brig case: Prognostic and diagnostic scheme precipitation results

is an encouraging result for the prognostic precipitation scheme. Again, the total amount of precipitation in the considered domain is reduced by about 25%.

An other example shows impressively the transport of precipitation over large distances. Figure 5 shows the distribution of total amount of rain and snow in a west–east vertical

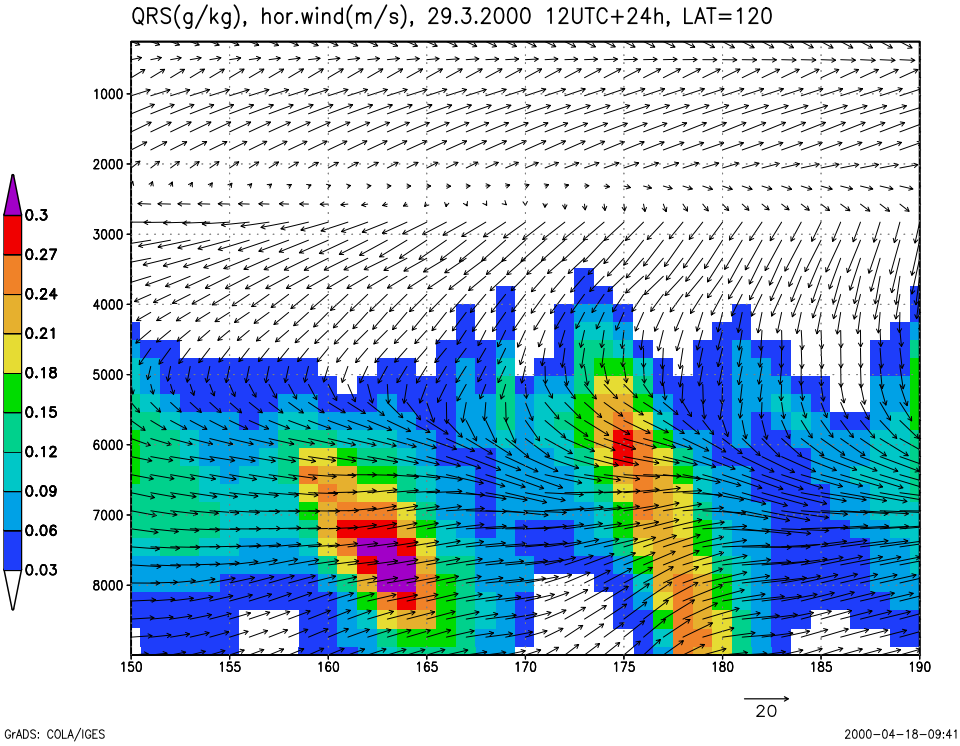

Figure 5: Vertical west–east cross section over the Rhine valley near Freiburg

cross section over the Rhine valley near Freiburg. Arrows indicate horizontal wind vectors and vertical spacing is on model levels. The result is that $q^{r,s}$ can be advected over about 5 gridpoints (35 km) before reaching the surface. As a result, the lee side of the mountains can get more precipitation.

The gridscale precipitation scheme with prognostic treatment of specific contents of rain and snow shows encouraging results and seems to overcome problems in the forecast of precipitation, especially in mountainous regions. Surely, the numerical implementation can be improved to come to a more efficient formulation. For future versions of LM this precipitation scheme should be taken into account.

References

Kato, T., 1995: A Box-Lagrangian Rain-Drop Scheme. J. Meteor. Soc. Japan, 73, 241-245

Grell, G. A., J. Dudhia and D. R. Stauffer, 1994: A Description of the Fifth-Genereation Penn State/NCAR Mesoscale Model (MM5). National Centre for Atmosperica Research, Mesoscale and Microscale Meteorological Division. Boulder, Colorado, USA.

Impact of Parameterization Assumptions on Cloud Physical Quantities

Thorsten Reinhardt and Ulrike Wacker

Alfred-Wegener-Institut für Polar- und Meeresforschung, D-27515 Bremerhaven

1 Introduction

Atmospheric ice particles show a great variety of shapes. A compilation of natural shapes is given in the classification of Magono and Lee (1966) or in the paper of Locatelli and Hobbs (1974). Further examples of ice particle forms are found e. g. in Rauber and Grant (1986) and in Uttal et al. (1988) for wintertime situations over Colorado, in McFarquhar and Heymsfield (1996) for cirrus clouds over the equatorial Pacific and in Korolev et al. (1999) for arctic clouds.

In atmospheric prediction models cloud microphysics is considered in terms of a parameterization. Thereby the natural variety of ice particle types cannot be considered. Instead, usually only a few categories of ice particles are taken into account and their shape parameters are prescribed. E. g. Walko et al. (1995) use in their model RAMS five categories of ice particles (pristine ice crystals, snow, aggregates, graupel, and hail) while the operational forecast models of the British (Wilson and Ballard, 1999) and German (Doms and Schättler, 1999) weather services consider only one species of ice particles.

In this paper we study the influence of differing assumptions for ice particle properties on model results. To this end we start with the derivation of generalized expressions of the transformation rates for accretion/riming, deposition, and the sedimentation flux. Based on sensitivity studies with the Lokal-Modell (LM) of the DWD we will then evaluate the sensitivity of simulated fields of condensate and precipitation rate to the prescribed properties of the ice particles.

2 Generalized Parameterization Equations

The studies shown in this paper refer to a parameterization of the type of a Kessler scheme considering the H_2O categories water vapor, cloud water, rain, ice. In such schemes each species is characterized by one moment of the particle size distribution, i. e. the partial density. Such concepts require the relationships between mass and size and between sedimentation velocity and size. It is common practice to use relationships which are fits to observations in the form of power laws:

$$m(D_*) = aD_*^x \qquad \text{and} \qquad v(D) = v_0 D^y \,, \tag{1}$$

with D_*: characteristic particle diameter, D: equivalent diameter of a spherical water drop with same mass, a, v_0, x, y: fitted parameters. The relationships (1) used in this study are taken from Locatelli and Hobbs (1974) for ice particles and from Kessler (1969) for rain drops. With assumptions analogous to those in the Kessler scheme and the given relationships (1), expressions for the riming and accretion rates can be derived. To this end it is assumed that the size distribution of precipitation particles is of an exponential form (so-called Marshall-Palmer distribution): $f(D) = N_0 \exp(-\lambda D)$, with $N_0 = const.$ Integration over the particle

spectrum yields the following equation for the riming and accretion rates:

$$Q_{\mathrm{rim/acc}} = bCP_{\mathrm{i,r}}^{\beta} \,. \tag{2}$$

with C and P: mass fractions of cloud water and precipitation (ice/rain). Using similar assumptions the mass sedimentation flux comes out as:

$$F = \tilde{d}P_{\mathrm{i,r}}^{\delta} \,. \tag{3}$$

The coefficients b and $\tilde{d}$ and the exponents β and δ are uniquely determined. They depend on, among other things, the parameters a, v_0, x, y from Eq. (1) and hence, carry the information on the particular particle type. A detailed derivation of (2) and (3) can be found in Wacker (2000).

The particle growth rate by water vapor deposition reads:

$$\dot{m} = \frac{4\pi c(D_*) d_{\mathrm{v}}}{1 + H_{\mathrm{i}}} F_{\mathrm{v}}(D) \rho_{\mathrm{a}} (q_{\mathrm{v}} - q_{\mathrm{v,sat}}) \,, \tag{4}$$

(e. g. Pruppacher and Klett, 1997). Thereby q_{v} denotes the mass fraction of water vapor, $q_{\mathrm{v,sat}}$ the saturation mass fraction of water vapor with respect to ice, ρ_{a} the density of the air, d_{v} the molecular diffusion coefficient of water vapor, H_{i} the Howell-factor for ice taking into account the temperature difference between the particles and their environment, and F_{v} the ventilation coefficient describing the effect of the particle's motion relative to the air. The effect of the particle's shape enters via the function $c(D_*)$, which is given by the electrostatic capacitance of a conducting body of the same shape. For thin circular disks of diameter D_* the capacitance is given by $c = D_*/\pi$ and for spheres by $c = D_*/2$. The deposition rate of the particle ensemble is given by:

$$Q_{\mathrm{dep}} = \frac{1}{\rho_{\mathrm{a}}} \int \dot{m} f(D) \, \mathrm{d}D = \alpha_1 (1 + \alpha_2 P_{\mathrm{i}}^{\gamma_1}) (q_{\mathrm{v}} - q_{\mathrm{v,sat}}) P_{\mathrm{i}}^{\gamma_2} \,, \tag{5}$$

wherein we have assumed that the particle shape can be approximated by thin circular disks or by spheres. The coefficients α_1 and α_2 and the exponents γ_1 and γ_2 are determined and they depend on the particle type in a similar way as b, $\tilde{d}$, β, δ in Eqs. (2) and (3). The melting rate is derived analogously.

In Figs. 1 and 2 the riming/accretion and deposition rates as functions of the mass fractions of ice and rain are compared for several ice particle types and for rain drops. The transformation rates related to the different particle types can differ at a given precipitation mass fraction by a factor of up to ten. Thus it can be expected that these large differences in the transformation rates for different particle types also affect model results when choosing different precipitating ice particle types in the parameterization.

3 An Analytic Solution for the Steady State Profile of Precipitation Concentration

To calculate the field of precipitation concentration, the full budget equation for precipitation mass is replaced in many models by a diagnostic relationship. It is assumed that the cloud physical source rates, here summarized as Q, always balance the divergence of the sedimentation flux (so-called "Säulen-Gleichgewicht"):

$$\frac{1}{\rho_{\mathrm{a}}} \frac{\partial F(P)}{\partial z} = -Q \,. \tag{6}$$

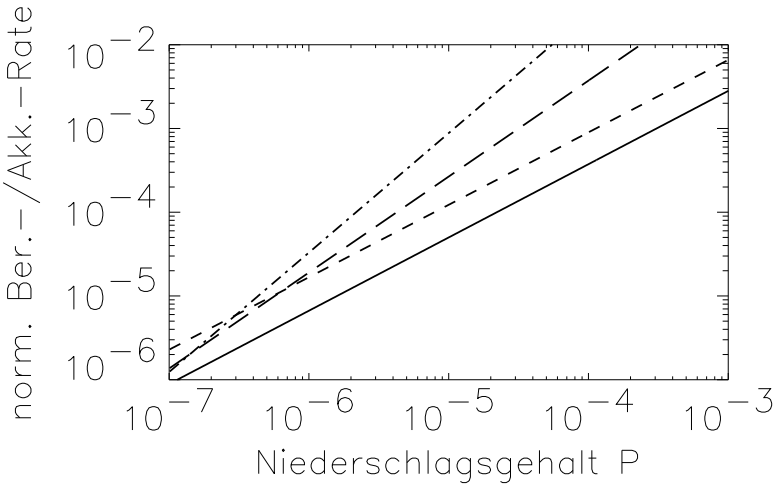

Figure 1: Riming and accretion rates, $Q_{\mathrm{rim/acc}}$ (in s^{-1}) per mass fraction of cloud water C, as functions of mass fraction of ice and rain P for the following particle types: raindrops (———), unrimed aggregates (- · - · - ·), densely rimed aggregates (— — —), lump graupel (- - - - -).

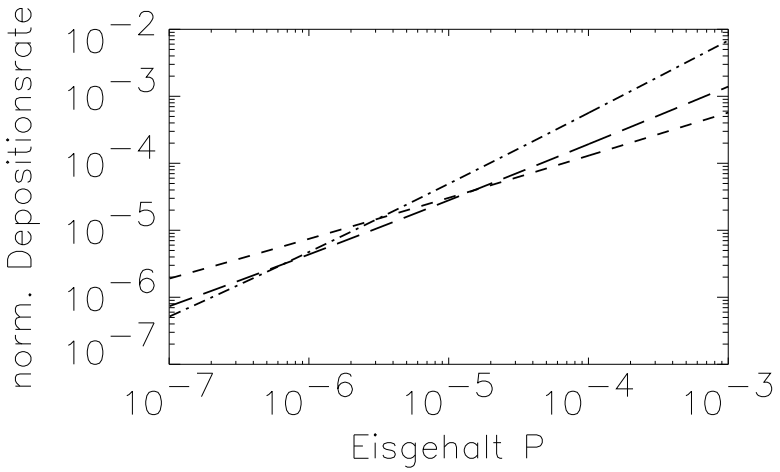

Figure 2: Deposition rate normalized to ice supersaturation, $Q_{\mathrm{dep}}/(q_{\mathrm{v}} - q_{\mathrm{v,sat}})$ (in s^{-1}), as function of mass fraction of ice P, for $T = -10\,^{\circ}\mathrm{C}$, $p = 800\,\mathrm{hPa}$. Particle types as in Fig. 1.

Thereby, tendency term and advective effects are all neglected. This approximation may be justified for models with sufficiently large time steps and grid sizes. It is widely used for the sake of computational efficiency, and also at present in LM (Doms and Schättler, 1999). In this section, solutions of the diagnostic equation (6) are derived, and we will discuss the vertical structure of the profile of precipitation concentration $P(z)$ in dependency on the prescribed particle type. For further information the reader is referred to Wacker (2000).

Parameterization equations are used for the source rates and the sedimentation flux in forms of the power laws as given in (2), (3), (5). In the following, only accretion or riming is considered; however, the elaboration could be done, at least approximately, for depositional growth likewise.

Suppose we neglect the dependency of the source rate Q and the sedimentation flux F on air density. Then the flux is a function of precipitation concentration P alone, and gives Eq. (6) as a differential equation for P:

$$\frac{\partial P}{\partial z} = -\frac{bC}{\tilde{d}\delta} P^{\beta-\delta+1} \tag{7}$$

Assuming a vertically constant cloud water content, the differential equation is readily solved. Thereby three cases are to be distinguished with respect to the exponent $\beta - \delta + 1$.

(i) $\beta - \delta + 1 = 1$, i.e. $\beta = \delta$.
For equal exponents β and δ we find *exponential growth*:

$$P(z) = P_0 \exp[\frac{bC}{\tilde{d}\delta}(z_0 - z)] \tag{8}$$

with $P_0 = P(z = z_0)$. This case corresponds to the ice particles chosen e. g. in the LM-parameterization.

(ii) $\beta - \delta + 1 < 1$, i. e. $\beta < \delta$
In case of coagulation, $\beta < \delta$ holds for particle types of spherical-like form such as drops, graupel and so on. The solution

$$P(z) = [P_0^{\delta-\beta} + (\delta - \beta)\frac{bC}{\tilde{d}\delta}(z_0 - z)]^{1/(\delta-\beta)} \tag{9}$$

describes a *parabolic growth law of precipitation concentration.*

(iii) $\beta - \delta + 1 > 1$, i.e. $\beta > \delta$
The third case holds for riming of flat ice particles such as snowflakes and describes *hyperbolic growth*, which is faster than exponential growth:

$$P(z) = [\frac{1}{P_0^{\beta-\delta}} - (\beta - \delta)\frac{bC}{\tilde{d}\delta}(z_0 - z)]^{-1/(\beta-\delta)} \; . \tag{10}$$

The different regimes will now be characterized in terms of one point: In the first two cases, an infinite precipitation concentration isn't reached but for an infinite long distance $z \to -\infty$. For flat particles, however, we find a finite critical level z_{crit} where $P(z = z_{\text{crit}}) \to \infty$:

$$z_{\text{crit}} = z_0 - \frac{1}{P_0^{\beta-\delta}}\frac{\tilde{d}\delta}{bC}\frac{1}{\beta - \delta} \; . \tag{11}$$

Note that this level of singularity depends not only on the boundary condition, but also on the assumed particle type. This behavior will be illustrated by two case studies.

Firstly, an ensemble of conical graupel with $\beta < \delta$ is considered falling through a thick layer with high constant cloud water content of $C = 10^{-4}$. The steady state profile increases parabolically up to a concentration 10 times the upper boundary value, see Fig. .

Secondly, an ensemble of aggregates of densely rimed dendrites is considered with a β-value only slightly larger than δ. *These flat particles fall slowly and grow by riming very fast*; thus they give rise to this explosive like increase of precipitation concentration, see Fig. 4.

Problems with this kind of instability have not been reported from numerical simulations up to now, at least as far as the authors know. Maybe, ice particles are not interpreted as such flat types in other model parameterizations.

Furthermore the vertical integration is usually to be done numerically, and frequently used simple numerical integration schemes of forward type act damping. Thus, the increase of $P(z)$ is damped the more, the larger mesh size is chosen (see Figs. 3 and 4). Nevertheless a much faster growth of P is found for flat ice particles than for graupel.

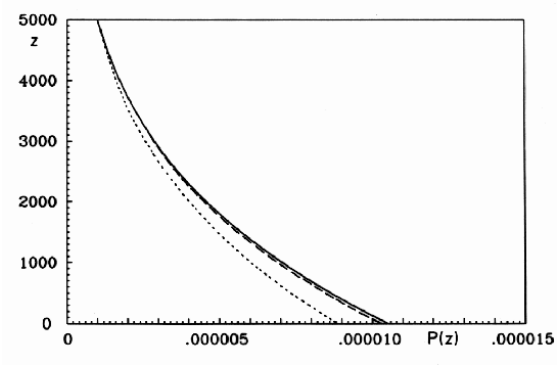

Figure 3: Steady state vertical profile of precipitation mass fraction $P(z)$ for conical graupel. Height z in m. Analytic solution (———) and numerical soultions for Δz = 50 m (— — —) and $\Delta z = 500$ m ($\cdots$). Model conditions: $C = 10^{-4}$, $\rho_a = 10^{-3}$ g/cm^{-3}.

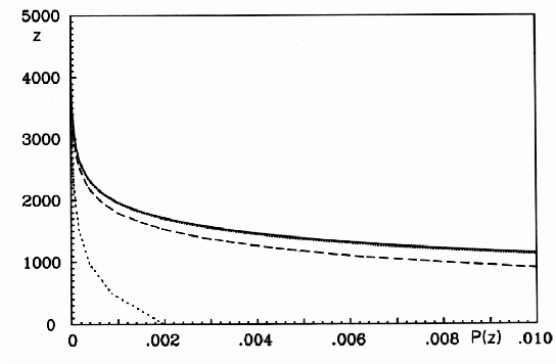

Figure 4: Same as Fig. but for densely rimed aggregates.

The studies presented in Figs. and 4 are carried out assuming a constant high cloud water concentration throughout the layer. Even if a more realistic profile $C(z)$ is prescribed, the profiles for the different ice particle types distinguish considerably, see Wacker (2000).

Another point is, that in prognostic model simulations feedback mechanisms are present, by which the diagnostic precipitation concentration and the cloud water content interact with each other. If cloud water is strongly depleted by e. g. riming, only little precipitation may be formed subsequently. And in any case, the depletion of cloud water is limited by its present content. This feedback is neglected in the analytic model presented here. Nevertheless, the unrealistic increase in precipitation may become visible in model simulations, if this feedback is suppressed by a continuous supply of cloud water as e. g. near the boundary of a nested model. Such a case study will be presented at the end of the following section.

4 Sensitivity Studies with LM

In this section we present sensitivity studies carried out with the Lokal-Modell (LM) with respect to different prescribed ice particle types. The grid-scale cloud parameterization in LM is a Kessler-type scheme extended by the ice phase (Doms and Schättler, 1999). The H_2O categories considered are water vapor, cloud water, rain, and precipitating ice. The transformation rates for riming (2) and deposition (5) and the magnitude of the mass sedimentation flux (3) depend on the assumptions on the particular ice particle type, as shown in Section 2.

To detect the impact of the assumptions about the ice particle type on the model results, we firstly discuss case studies of a two-dimensional flow over a bell-shaped mountain. For these sensitivity studies, all other parameterized physical processes are neglected.

The sensitivity of the model results with respect to the prescribed particle type is found in the surface precipitation rate as well as in atmospheric fields like those of cloud water or water vapor concentrations. An example of the differences in the simulated cloud water concentration fields is shown in Figs. 5 and 6. In those model runs the solid precipitation particles are interpreted as unrimed aggregates and as lump graupel, respectively. The situ-

ations shown are quasi-stationary states four days after the start of the simulation. If the ice particle type is assumed to be graupel, the cloud water content is everywhere higher than in the simulation assuming the ice particles to be unrimed aggregates. The maximum value of the cloud water content in the case "graupel" is about five times higher than that in the case "unrimed aggregates". Also the positions of the maximum in cloud water contents differ. In the case "graupel", the maximum is found at a height of about 1.5 km while in the case "unrimed aggregates" the height is 3.4 km. Overall, we find in the case "graupel" a higher cloud water content and less precipitation compared with the case "unrimed aggregates", because unrimed aggregates convert more cloud water by riming and deposition into precipitation than graupel and therefore cause – in spite of the lower cloud water content – a larger precipitation rate than graupel. The sensitivity studies also show that the less efficient formation of precipitation in the case "graupel" leads to a higher downstream advection of cloud water to the lee, where it evaporates and thus, increases the relative humidity compared to the case "unrimed aggregates" (no figure).

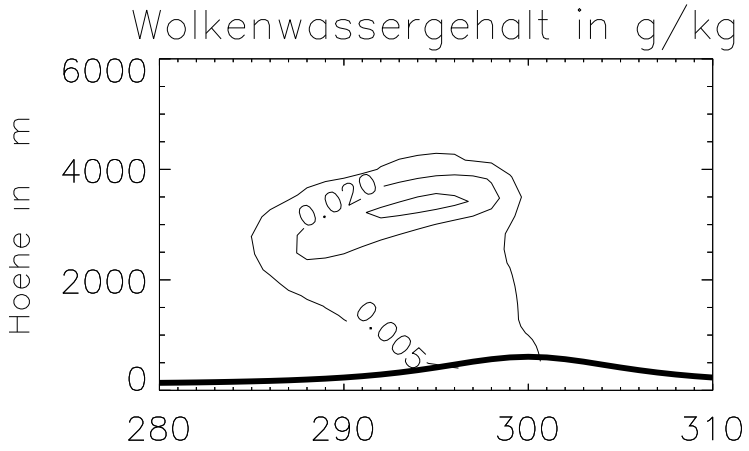

Figure 5: Vertical cross section of the mass fraction of cloud water C in g/kg (thin lines). Ice particles are interpreted as unrimed aggregates. x-axis: distance from boundary in gridpoints (mesh size 7 km). Isolines: 0.005 g/kg, 0.02 g/kg, 0.03 g/kg. The maximum of C is 0.033 g/kg. Thick line: surface height.

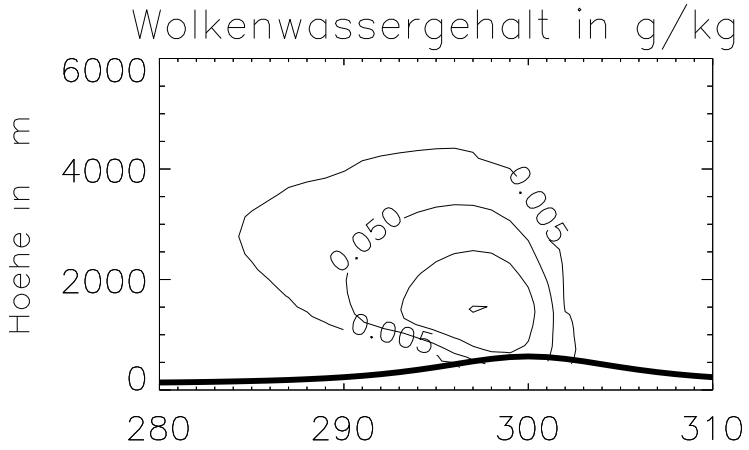

Figure 6: As Fig. 5, but for graupel. Isolines 0.005 g/kg, 0.05 g/kg, 0.1 g/kg, 0.15 g/kg. The maximum of C is 0.15 g/kg.

The sensitivity of the model results with respect to the choice of the ice particle types varies depending on the other model assumptions like the shape of the mountain and the initial conditions. Table 1 shows the surface precipitation rate for three ice particle types and four model configurations. Case 1 is the reference case: surface temperature: 5 °C, vertical

Table 1: Surface precipitation rate (in mm/d) at time $t = 4$ d depending on the chosen ice particle type. Given are mean values over ca. 140 km in x-direction. For explanation of the four cases see text.

Cases		Unrimed. agg.	Dens. rim. agg.	Graupel
1	Total Prec.	9,51	8,83	7,05
	Rain	6,82	4,49	3,05
	Snow	2,69	4,34	4,00
2	Total Prec.	32,2	31,4	28,9
	Rain	10,9	7,8	5,8
	Snow	21,3	23,5	23,1
3	Total Prec.	9,34	8,42	5,71
	Rain	6,64	3,97	2,12
	Snow	2,71	4,46	3,59
4	Total Prec.	8,60	8,23	7,19
	Rain	0,02	0,07	0,20
	Snow	8,58	8,61	6,99

temperature gradient: 6.5 K/km, relative humidity at the surface: 75 %, relative humidity in the mid troposphere: 90 %, height of the montain: 500 m, width of the mountain: see Figs. 5 and 6. In each of the cases 2 to 4 one parameter is varied in comparison with the reference case. In case 2 the height of the mountain is increased from 500 m to 1000 m. In case 3 the mountain is only half as wide as in the reference case. (We ensured that the differences in model results are due to the increased steepness and not due to smaller mesh size.) In case 4 the temperature at the surface is decreased to 0 °C.

All these cases have in common that the model precipitation is stronger for ice particles interpreted as flat "unrimed aggregates" than for ice particles interpreted as densely rimed aggregates and graupel; but, however, the relative differences vary.

As to be expected, the simulated precipitation increases with montain height (case 2), but the relative differences between simulations with different ice particle types are smaller than in the reference case. In case 3 (steeper and narrower mountain) nearly the same precipitation as in the reference case is found, if unrimed aggregates are assumed, while selecting graupel, the surface precipitation is reduced noticeably compared to case 1. Also in case 4 (colder atmosphere) the differences related to different ice particle shapes are smaller than in the reference case.

Note also the differences in the precipitation rate for liquid and solid particles: The "unrimed aggregates" case provides a greater portion of rain in the surface precipitation than the "densely rimed aggregates" case, and these again more rain than the "graupel" case. This finding is not surprising: Ice particles with more effective depositional growth may gain larger size; however, they are likewise characterized by a higher melting rate and thus convert a greater portion of solid precipitation into rain.

These four cases reveal the following trend: The differences for simulations related to different ice particle types increase if the air masses are lifted on a smaller distance, hence spend less time in the upwind region where most of the cloud forming processes occur (case 3 compared to case 1). In contrast, the differences decrease if, due to stronger orographic forcing (case 2) or lower temperatures (because of the higher efficiency of the ice phase in forming condensate;

case 4), a larger share of the water vapor influx from the boundary is converted into surface precipitation.

The impact of the prescribed ice particle type on model results can also be found in simulations of real weather situations. Figure 7 shows the fields of 24-h precipitation sums from Dec. 9 1998 0–24 UTC simulated with LM. The model domain is located in South-West Germany and France, boundary conditions come from GME data.

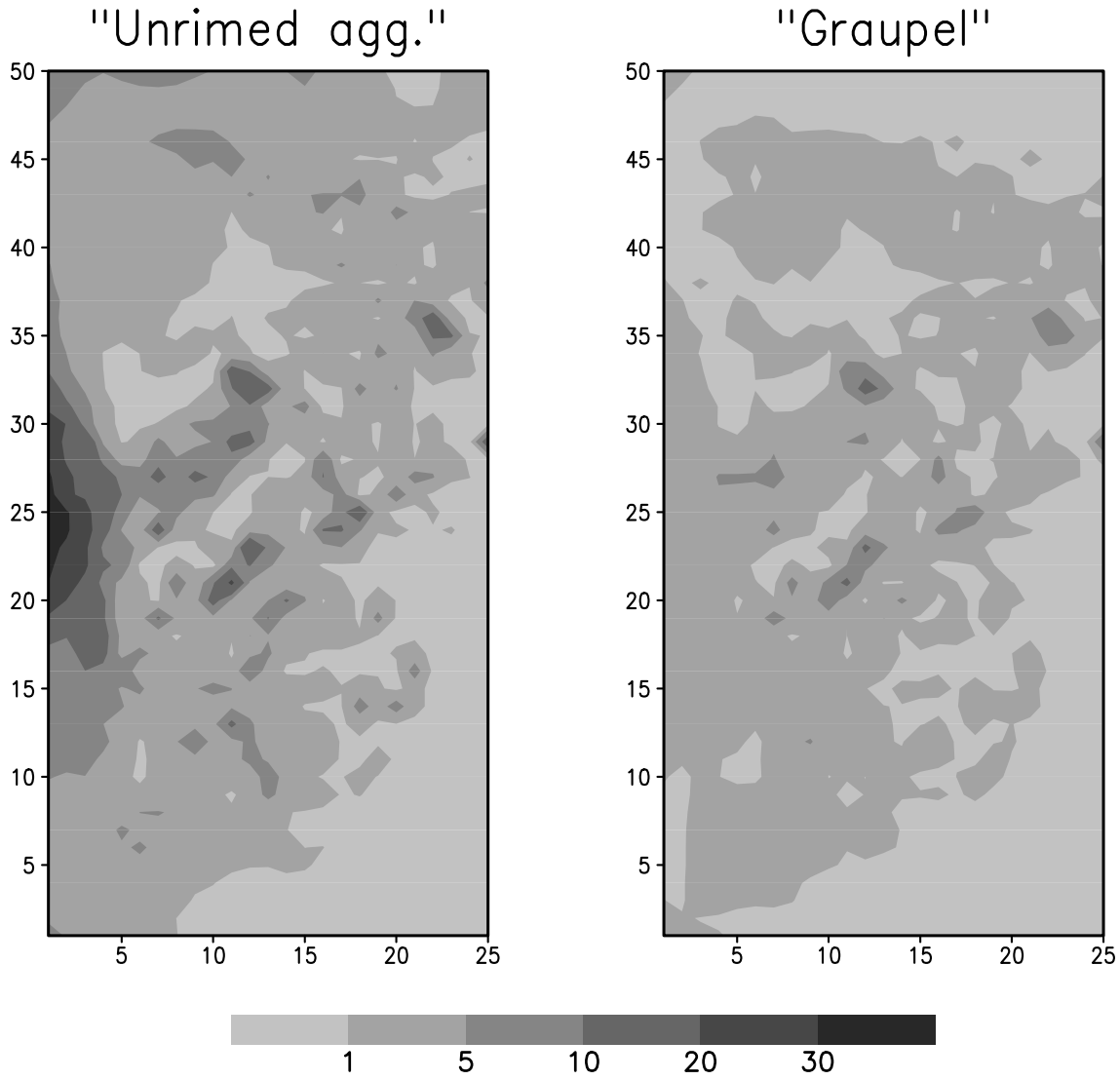

Figure 7: Horizontal distribution of 24-h precipitation sum (in mm) of the LM simulation at Dec. 9 1998, 0–24 UTC. Ice particles are interpreted as unrimed aggregates (left) and graupel (right). Axes: gridpoints (mesh size 7 km).

Firstly we disregard the boundary region, i.e. each five gridpoints next to the boundary. LM simulates widespread up to 2 mm more precipitation in the case "unrimed aggregates" than in the "graupel" case, with a maximum difference of about 10 mm. On the other hand, at single gridpoints larger precipitation rates are found in the "graupel" case, however, not exceeding 0.5 mm. Mean area values of surface precipitation amount to 1.55 mm for the case "graupel" and to 2.48 mm for the case "unrimed aggregates". In general, this comparative study reveals similar trends as in the previously discussed two-dimensional case studies, namely higher surface precipitation in the case "unrimed aggregates" than in the "graupel" case. This documents that also in the simulation of three-dimensional non-stationary atmospheric

evolution the choice of the particular ice particle type in the parameterization scheme may influence the simulated surface precipitation to a nonnegligible amount.

Let us still have a look at the western boundary. In the case "unrimed aggregates" ($\beta > \delta$) we find in the boundary region a very high precipitation rate, which does not appear in the case "graupel" ($\beta < \delta$). If the model domain is enlarged, this high precipitation disappears at that geographical location, but a similar effect eventually shows up near the new boundary. This boundary effect can be explained as follows: At the boundary the prognostic quantities, amongst them cloud water content, are provided by the large-scale model. They are consistent with the GME parameterization in which the particles are interpreted as flat disks with $\beta = \delta$. Therefore, the C-values in the boundary region are higher than those which would result from the LM-run in the case "unrimed aggregates". As cloud water concentration is prescribed at the boundary, the feedback between riming and cloud water concentration, which prevents unrealistically high precipitation, is suppressed as in the analytic study in Section 3. Therefore a similar effect occurs as addressed there: Under the conditions of fixed cloud water content and flat particles with $\beta > \delta$ in Eq. (7) an unrealistically high precipitation rate can occur.

This example shows that results near the boundaries should be interpreted carefully, when the model concepts, e. g. in the parameterization assumptions, of the nested and the larger-scale model differ.

5 Discussion

It has been shown that both in strongly idealized two-dimensional model studies as well as in the simulation of real weather situations the choice of the particular ice particle type in the cloud microphysics parameterization can have great impact on simulated fields of condensate contents and of surface precipitation. To document this effect, two very different particle types were chosen, i. e. graupel and unrimed aggregates, which denote opposite extremes. Of course, unrimed ice particles will change their habits towards those of rimed particles when growing by riming. On the other hand particles consisting mostly of rime like graupel can occur only *after* heavy riming. So in general the uncertainty caused by prescribing a somehow "mean" ice particle type should be smaller than the range of model results shown in this study.

In current parameterization schemes, however, it is unavoidable to prescribe a certain ice particle type. The results shown in this paper make clear that in these schemes the choice of just these ice particle types are relevant for simulated fields of condensate contents and precipitation rates. Remedy to that uncertainty would be the development of parameterization schemes which specify the ice particle type depending on the current conditions.

6 Acknowledgements

The authors are grateful to the staff of DWD's Geschäftsbereich Forschung und Entwicklung for providing LM and for their support. This research was supported by the Deutsche Forschungsgemeinschaft (grant WA 1334/1-1).

References

Doms, G. and U. Schättler, 1999: *The nonhydrostatic Limited-Area Model LM (Lokal-Modell) of DWD. Part I: Scientific Documentation.* DWD, GB Forschung und Entwicklung.

Kessler, E., 1969: *On the distribution and continuity of water substance in atmospheric circulations.* Amer. Meteor. Soc., Boston.

Korolev, A.V., G.A. Isaac, J. Hallet, 1999: Ice particle habits in Arctic clouds. *Geophys. Res. Lett. 26*, 1299–1302.

Locatelli, J.D. and P.V. Hobbs, 1974: Fall speeds and masses of solid precipitation particles. *J. Geophys. Res. 79*, 2185–2197.

Magono, C. and C.V. Lee, 1966: Meteorological classification of natural snow crystals. *J. Fac. Sci. Hokkaido Univ. Ser. 2, 1*, 321–362.

McFarquhar, G.M. and A.J. Heymsfield, 1996: Microphysical characteristics of three anvils sampled during the Central Equatorial Pacific Experiment. *J. Atmos. Sci. 53*, 2401–2423.

Pruppacher, H.R. and J.D. Klett, 1997: *Microphysics of clouds and precipitation.* Dordrecht: Kluwer Acad. Publ., 954 p .

Rauber, R.M. and L.O. Grant, 1986: The characteristics of cloud water over the mountains of northern Colorado during wintertime storms. Part II: Spatial distribution and microphysical characteristics. *J. Climate Appl. Meteor. 25*, 489–504.

Uttal, T., R.M. Rauber and L.O. Grant, 1988: Distributions of liquid, vapor, and ice in an orographic cloud from field observations. *J. Atmos. Sci. 45*, 1110–1122.

Wacker, U., 2000: Influence of the type of condensate particles on cloud physical quantities. *Phys. Chem. Earth (B) 25*, 91–99.

Walko, R.L., W.R. Cotton, M.P. Meyers and J.Y. Harrington, 1995: New RAMS cloud microphysics parameterization. Part I: The single-moment scheme. *Atmos. Res. 38*, 29–62.

Wilson, D.R. and S.P. Ballard, 1999: A microphysically based precipitation scheme for the UK Meteorological Office Unified Model. *Q. J. R. Meteorol. Soc. 125*, 1607–1636.

The LM Cloud Ice Scheme

Günther Doms

Deutscher Wetterdient, Offenbach am Main, Germany

1 Introduction and Background

Cloud processes take place on scales that are significantly smaller than those resolved by the grid boxes of a NWP-model. In large-scale models not only cumulus clouds but also precipitating stratiform frontal clouds are of subgrid nature and need to be represented by a suitable prognostic cloud fracion paramterization (e.g. Sundqvist, 1988; Smith, 1990; Tiedtke, 1993; Rasch and Kristjansson, 1998)). The formation of precipitation from subgrid stratiform clouds is further complicated by a necessary assumption on cloud overlap statistics (Jakob and Klein, 1999). This situation appears to be less complex in high-resolution mesoscale models with grid spacings of less than about 10 km. Frontal stratiform clouds are well resolved and bulk microphysical parameterizations similar to those used in cloud resolving models (e.g. Kessler, 1969; Lin et al., 1983, Rutledge and Hobbs, 1983) may be applied. In these grid-scale schemes, only the cloud condensate is predicted by budget equations and the cloud cover is set to 100% whenever condensate occurs.

Except cumulus convection, which is parameterized by dedicated schemes, all other non-resolved clouds in mesoscale models are of stratocumulus-type. A direct hydrological impact of these clouds may be neglected for NWP purposes, but not the interaction with radiation. In LM, we use a traditional scheme that diagnoses a cloud fraction and a corresponding liquid water content in terms of relative humidity, pressure and convective activity. Clearly, subgrid-scale cloudiness will become less important with increasing model resolution.

Ice-phase processes play a significant role in mid-latitude frontal cloud systems and their impact should be taken into account by parameterization schemes. Two mechanisms of precipitation enhancement are of particular importance: the Bergeron-Findeisen process and the Seeder-Feeder mechanism, which both are based on the presence of supercooled liquid water. Nucleation of ice in a water saturated environment will cause a rapid growth of the ice crystals by deposition (because of the ice supersaturation) and riming (because of the precence of supercooled cloud droplets); the ice particle growth is at the expense of liquid water, but if the cloud is kept at water saturation by thermodynamic forcings, high precipitation rates may result from this Bergeron-Findeisen process. The Seeder-Feeder mechanism describes precipitation enhancement due to ice particles falling from a higher cloud into a lower cloud containing supercooled droplets; in this case, the droplets will also be converted into ice by deposition and riming, resulting in a more efficient removal of cloud water than by the collision-coalesence growth of water droplets.

Two gridscale cloud and precipitation schemes that include ice phase processes have been implemented in LM. They are described in the following sections and a shortcoming resulting from a simplified numerical treatment of precipitation fallout is also discussed. Both schemes neglect hail and graupel since these ice particle types are not relevant for precipitation formation in stratiform clouds at the current model resolution. The future application of LM on the mesoγ scale, however, will require a corresponding extension of the schemes.

2 The Operational Scheme

The default parameterization scheme for the formation of grid-scale clouds and precipitation is based on a Kessler-type bulk formulation and uses a specific grouping of various cloud and precipitation particles into broad categories of water substance. The particles in these categories interact by various microphysical processes which are parameterized in terms of the mixing ratios as the dependent model variables. Four categories of water substance are considered: water vapour, cloud water, rain and snow. Cloud water is treated a bulk phase with no appreciable terminal fall velocity relative to the airflow, whereas single-parameter exponential size-spectra and empirical size-dependent terminal fall velocities are assumed for raindrops and snow crystals.

To simplify the numerical solution of the budget equations for rain and snow, quasi-equilibrium in vertical columns is assumed by neglecting 3-d advective transport and by prescribing stationarity. The resulting balance between the divergence of the precipitation fluxes and the microphysical sources and sinks allows for a very efficient diagnostic calculation of P_r and P_s. While this assumtion is well justified for large-scale models (Ghan and Easter, 1992), it is clearly not adequate for the meso-γ and smaller scales. Work on a prognostic treatment of the precipitation phases is in progress. With these key assumptions, the equations for the hydrological cycle can be formulates as.

$$
\begin{aligned}
\frac{\partial T}{\partial t} &= A_T + \frac{L_V}{c_{pd}}\left(S_c - S_{ev}\right) + \frac{L_S}{c_{pd}} S_{dep} + \frac{L_F}{c_{pd}}\left(S_{nuc} + S_{rim} + S_{frz} - S_{melt}\right) \quad , \\
\frac{\partial q^v}{\partial t} &= A_{q^v} - S_c + S_{ev} - S_{dep}\,, \\
\frac{\partial q^c}{\partial t} &= A_{q^c} + S_c - S_{au} - S_{ac} - S_{nuc} - S_{rim} - S_{shed}\,, \\
\frac{1}{\rho\sqrt{G}}\frac{\partial P_r}{\partial \zeta} &= -S_{ev} + S_{au} + S_{ac} + S_{melt} - S_{frz} + S_{shed}\,, \\
\frac{1}{\rho\sqrt{G}}\frac{\partial P_s}{\partial \zeta} &= S_{nuc} + S_{rim} - S_{melt} + S_{frz} + S_{dep}\,.
\end{aligned}
\tag{1}
$$

The A_ψ-terms abbreviate advective and turbulent transport. L_V, L_S and L_F denote the latent heat of vapourization, sublimation and freezing, respectively. The other symbols have their usual meaning. The following table describes the microphysical prosesses which are parameterized by corresponding mass transfer rates S_x.

Symbol	Definition / Description
S_c	Condensation and evaporation of cloud water.
S_{au}	Autoconversion of cloud water to form rain.
S_{ac}	Accretion of cloud water by rain.
S_{nuc}	Initial formation of snow due to nucleation from cloud water.
S_{rim}	Accretion of cloud water by snow (riming), $T < 273.16K$.
S_{shed}	Accretion of cloud water by snow to form rain (shedding), $T \geq 273.16K$.
S_{dep}	Depositional growth of snow.
S_{melt}	Melting of snow to form rain, $T > 273.16K$.
S_{frz}	Heterogenous freezing of rain to from snow, $T < 267.16K$.
S_{ev}	Evaporation of rain in subcloud layers.

Both the Bergeron-Findeisen process and the Seeder-Feeder mechanism are represented explicitly by this scheme. The calculation of cloud water condensation and evaporation is based on instantaneous adjustment to water saturation. From the latter assumption, however, a number of major drawbacks result:

(a) Clouds will always exist at water saturation independent of temperature. That is, only mixed phase clouds – made up of cloud water, snow and rain – can be simulated below freezing point.

(b) The cloud ice-phase is neglected by assuming a fast transformation from cloud water to snow. Thus, the glaciation of clouds cannot be simulated and cirrus will be at a wrong thermodynamic state. Also, the precipitation enhancement from the Bergeron-Findeisen mechanism may be overestimated.

(c) High-level clouds usually exist at or close to ice saturation. Since the scheme requires water saturation for cloud formation, the initial conditions must be artificially adapted to avoid long spin-up periods: In the analysis scheme, the specific humidity obtained from measurements is increased by the ratio of the saturation vapour pressure over water and over ice for temperature below $0°C$. This affects the high-level humidity structure in an unphysical way.

To overcome these problems, a new scheme including cloud ice has been developed.

3 Description of the LM Cloud-Ice Scheme

Many ice-phase schemes used in NWP-models solve only one prognostic equation for cloud condensate. Hence, the distinction of the water and the ice phase has to be determined diagnostically. This is done by (i) prescribing the liquid fraction in the total condensate as a function f_l of temperature and (ii) assuming that both ice and water are in thermodynamic equilibrium with respect to a hypothetical saturation vapour pressure given by $e_s = f_l\, e_s^w + (1-f_l)\, e_s^i$, where e_s^w and e_v^i are the saturation vapour pressure over water and ice, respectively.

The function f_l for the liquid fraction is usually choosen to be 1 for $T > T_0 = 0°C$ and 0 for tempeatures below a threshold T_{ice} with a linear or quadratic decrease with temperature in the range $T_{ice} < T < T_0$. Various values for T_{ice} are assumed in different schemes, ranging from -15 $°C$ to - 40 $°C$. Figure 1 shows an example for f_l used in the UKMO Unified Model together with some aircraft observations taken in frontal and non-frontal stratiform clouds. The observational data show low liquid fractions below about - 15 $°C$. A climatology shown by Feigelson (1978), however, suggests that there is plenty of supercooled water in the range - 15 to - 30 $°C$.

Ice-schemes with a presribed liquid fraction are widely in use but have a number of conceptional drawbacks. First, the assumption of thermodynamic equilibrium of both water and ice at temperatures below T_0 is not in accordance with physical principles. Second, for $T < T_{ice}$ a saturation adjustment is done for the calculation of condensate; since the number of cloud ice crystals is very small, such an instantaneous adjustment has no physical basis. Third, effects from the Bergeron-Findeisen process cannot be considered explicitly, since the ice-phase is in thermodynamic equilibrium. Fourth, the Seeder-Feeder mechanism is not represented: deep clouds are more likely to be glaciated than thin clouds at the same temperature (Ryan, 1996). Also, ice falling from above into subfreezing layers is forced to melt in order to maintain the prescribed liquid fraction. This is not very realistic.

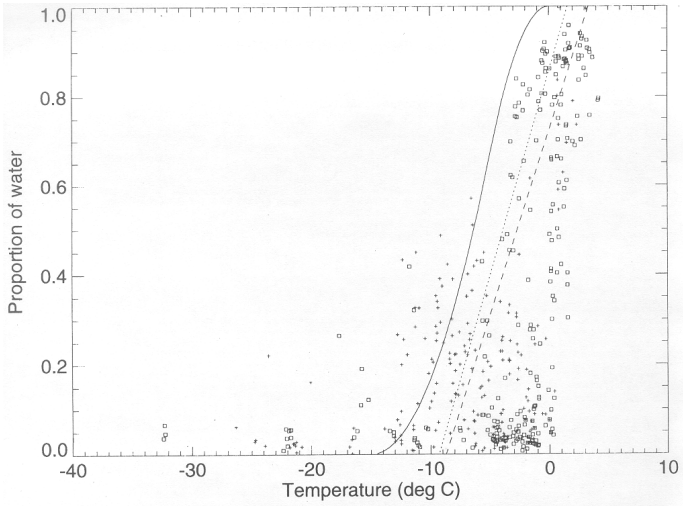

Figure 1: Liquid fraction from aircraft observations against temperature, as described by Bower et al. (1996). Crosses indicate clouds in continental clouds and squares indicate clouds in maritime clouds. The solid curve represents a parameterization used in the UKMO Unified Model. A similar parameterization is used in the ECMWF Model but with a threshold temperature of $-25°C$. The dotted lined is the best fit to the data for continental clouds and the dashed line for maritime clouds. Reproduced from Ryan (1996).

Bearing in mind these difficulties, the new LM parameterization scheme was designed to take into account cloud ice by a separate prognostic budget equation. Cloud ice is assumed to be in the form of small hexagonal plates that are suspended in the air and have no appreciable fall velocity. As a novel feature of the scheme, we formulate the depositional growth of cloud ice as a non-equilibrium process and require, at all temperatures, saturation with respect to water for cloud liquid water to exist. Ice crystals which are nucleated in a water saturated environment will then grow very quickly by deposition at the expense of cloud droplets. Depending on local dynamic conditions, the cloud water will either evaporate completely, or will be resupplied by condensation. For strong dynamical forcings it is expected that water saturation will be maintained, resulting in a mixed phase cloud. In case of a comparatively weak forcing, the cloud will rapidly glaciate to become an ice cloud existing at or near ice saturation (i.e. at subsaturation with respect to water). Figure 2 gives an overview on the hydrological cycle and the microphysical processes considered by the scheme.

The explicit calculation of cloud ice depositional growth as a non-equilibrium process is based on the mass-growth equation of a single pristine crystal and requires assumptions on the shape, size and number density of the ice crystals:

- We assume a monodispers size distribution for cloud ice particles with the mean crystal mass

$$m_i \;=\; \rho q^i N_i^{-1}\,, \tag{2}$$

being diagnosed from the the predicted mixing ratio q^i and the number density N_i of cloud ice particles.

- The number density $N_i(T)$ of cloud-ice particles is prescribed as a function of ambient air temperature using the relation

$$N_i(T) \;=\; N_0^i \exp\{\,0.2\,(T_0 - T)\}\,, \qquad N_0^i \;=\; 1.0 \cdot 10^2 m^{-3}\,, \tag{3}$$

which is an empirical fit to data obtained by aircraft measurements in stratiform clouds (Hobbs and Rangno, 1985, and Meyers et al., 1992). For a given temperature, the ex-

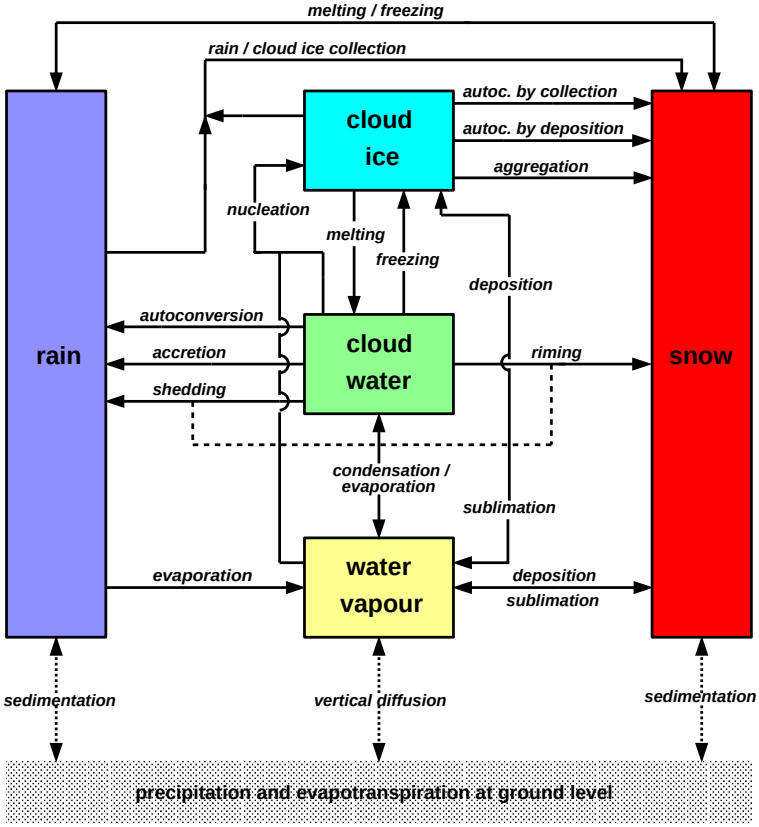

Figure 2: Hydrological cycle and microphysical processes in the LM cloud ice scheme

perimental data may scatter by about two orders of magnitude. Nevertheless, we assume that (3) represents a meaningful average value for the cloud ice crystal concentration in cold stratiform clouds.

- Cloud ice crystals are assumed to be in the form of thin hexagonal plates with diameter D_i and thickness h_i, where the maximum linear dimension D_i is smaller than about 200 μm. This constant aspect ratio growth regime yields the following relation to calculate the size D_i of cloud ice particles from the diagnosed mean mass m_i,

$$D_i \;=\; (m_i)^{1/3}\,(a_m^i)^{-1/3}\,, \tag{4}$$

where $a_m^i = 130$ kgm^{-3}. A temperature dependency of the form factor a_m^i is neglected.

Using (2), (3) and (4) in the mass-growth equation for a single crystal, the total deposition rate of cloud ice, $S_{dep}^i = N_i \dot{m}_i/\rho$, may then be formulated by

$$S_{dep}^i \;=\; c_i\, N_i\, m_i^{1/3}\,(q^v - q_{si}^v) \tag{5}$$

in terms of ice supersaturation (or subsaturation for sublimation). q_{si}^v is the specific humidity at ice saturation. The factor $c_i = 4G_i d_v \sqrt[3]{a_m}$ varies slowly with temperature and pressure due to the Howell factor G_i and the diffusivity d_v of water vapour. Here, c_i is approximated by the constant value of $1.5 \cdot 10^{-5}$.

Cloud ice is initially formed by heterogeneous nucleation or homogeneous freezing of supercooled droplets. The latter process is parameterized by instantaneous freezing of cloud

water for temperatures below $-37°C$. To formulate heterogeneous nucleation, we simply assume that the number of ice forming nuclei activated within a time step Δt is given by Eq. (3) and that the temperature is below a nucleation threshold (set to $-7°C$). We will also neglect nucleation whenever ice is already present since this has been found to be of minor importance. Recent field experiments show that ice nucleation is not likely to occur in regions of the atmosphere which are subsaturated with respect to water, except for very low temperatures. In the present version of the scheme we thus require water saturation for the onset of cloud ice formation above a temperature threshold T_d (set to $-30°C$). For temperatures below T_d, deposition nucleation may occur for ice supersaturation. All other conversion rates are parameterized in a similar way as in the operational scheme. For 3-dimensional advection of cloud ice, the positive definite Lin and Rood (1996) algorithm is used. A more detailed description of the scheme can be found in the LM Scientific Documentation (Doms and Schättler, 1999).

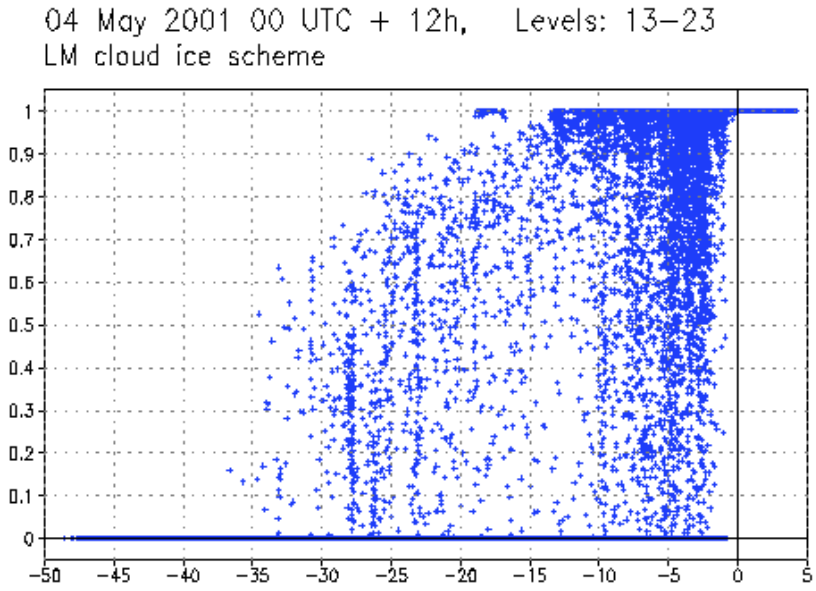

Figure 3: Variation with temperature of the liquid fraction for 4 May 2001 00 UTC + 12 h.

4 Preliminary Results

The LM cloud ice scheme has been tested for a number of case studies. Figure 3 shows the variation with temperature of the liquid fraction $f_l = q^c/(q^c + q^i)$ generated by the scheme. The values of f_l were obtained from a single time step after the model was run for 12 h starting from the 4 May 2001 00 UTC analysis. For temperatures warmer than about $-10°C$, there are cloudy grid-boxes which are composed of either liquid water or ice, and there is a large number of boxes indicating a mixed phase. Below $-10°C$, the there is still a large number of mixed phase clouds with supercooled droplets, but the liquid fraction drops off with temperature. Below about $-35°C$ only ice clouds exist. There is a good qualitative agreement with the observations for stratiform clouds in Figure 1, but the model indicates a larger number of mixed phase clouds for temperatures below about $-15°C$. In Figure 3, however, not only stratiform clouds but all cloudy grid points are counted. For the convective 4 May 2001 case, a large number of gridpoints from anvils and embedded cold frontal convection contribute to the scatter plot. At such points, strong dynamical forcing can keep the air at water saturation allowing for mixed phase clouds at low temperatures. This example shows that with the new scheme the liquid fraction adjusts reasonable in

response to dynamical forcing and microphysical processes.

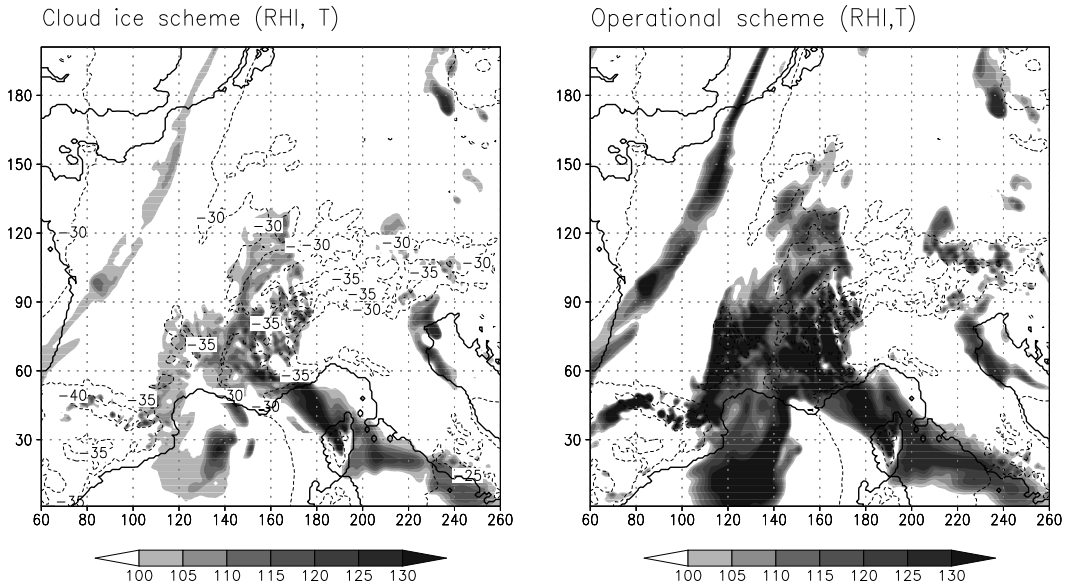

Figure 4: Relative humidity over ice (shaded, in %) and temperature ($°C$, isolines) for 4 May 2001 00 UTC + 12 h at model level 14. Left: cloud ice scheme. Right: operational scheme.

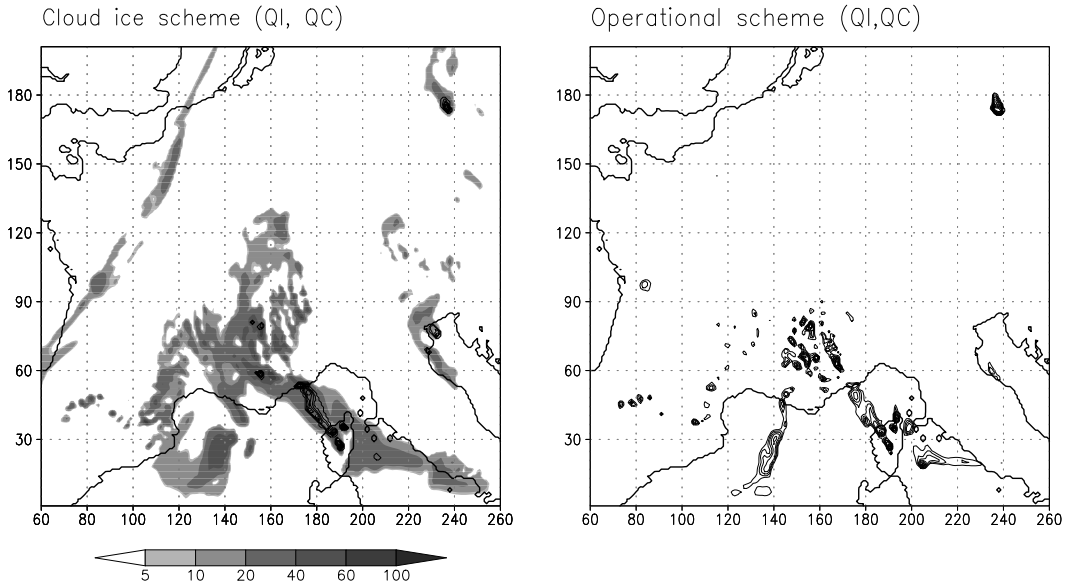

Figure 5: Specific cloud ice content (shaded, in mg/kg) and cloud water content (isolines at 10 mg/kg intervals) for 4 May 2001 00 UTC + 12 h at model level 14. Left: cloud ice scheme. Right: operational scheme.

There is also a large impact to the humidity structure of the upper atmosphere. To illustrate this, the relative humidity over ice obtained from runs with the cloud ice and the operational scheme is shown in Figure 4 for the same case and forecast time. Figure 5 displays the corresponding specific cloud ice and cloud water contents. The fields are plotted for a model subdomain at level 14, corresponding to a height of about 7000 m with temperatures ranging from -30 to $-40°C$. The operational run reveals high ice superaturation of about 20 - 40 % in two regions: a band-like structure over western France which is associated with a cold front, and a more unstructered region in the warm sector ahead of the front. Here,

widespread deep convection occurs which by vertical transport generates and maintains high humidity.

With the operational scheme, there is no ice but only cloud water by definition (Fig. 5, right). Since saturation with respect to water is required for grid-scale cloud formation, cloud water is found only at those gridpoints where dynamic forcing by convection drives the atmosphere to water saturation (at a temperature of $-35°C$, this will occure at about 35 % ice-supersaturation). However, these points are rather scattered whereas satellite images indicate a region of merged anvils above the northern Mediteranean Sea and southern France (not shown). This high level cloudiness is simulated much more realistic by the cloud ice scheme (Figures 4 and 5, left). Here, cloud ice is initially formed also at gridpoints which are at or near water saturation. Subsequently, however, it can be advected into regions which are ice-supersaturated but are below water saturation. In these regions, cloud ice will continue to grow by vapour deposition, thereby reducing the humidity to values more close to ice saturation (Fig. 4, left). Thus, a much larger region with grid-scale anvils – mostly composed of ice – is simulated than with the operational scheme. In the warm sector region, some mixed-phase clouds do also exist at gridpoints, where strong convective forcing maintains water saturation. Also, high-level ice clouds appear along cloud front.

5 Summary and Plans

For the test cases considered so far, there was no remarkable impact to the predicted precipitation. The total precipitation amount can increase or decrease by about 10 %, depending on the weather situation. The main advantage of the scheme is a more physically based representation of ice and mixed-phase clouds, allowing for a direct simulation of cloud glaciation. The phase composition of high-level clouds appears to be well captured, which is important for a better cloud-radiation interaction. And in particular, the formation, growth and spreading of grid-scale anvil clouds can be simulated explicitly.

Following further testing it is planned to introduce the cloud ice scheme operationally in spring 2002. To provide consistent boundary conditions from the driving model, the scheme has also been implemented in our global model GME. A rerun of a one-year period during 2000/2001 revealed an overall benefial impact of the cloud ice scheme, with a significant reduction of current imbalances in the average radiation an water budgets.

References

Bower, K. N., S. J. Moss, D. W. Johnson, T. W. Choularton, J. Latham, P. R. A. Brown, A. M. Blyth and J. Cardwell, 1996: A parameterizaion of the ice water content observed in frontal and convective clouds. *Quart. J. Roy. Meteor. Soc.*, 122, 1815-1844.

Doms, G., U. Schättler, 1999: The Nonhydrostatic Limited-Area Model LM (Lokal-Modell) of DWD. Part I: Scientific Documentation. Deutscher Wetterdienst (DWD), Offenbach (available at www.cosmo-model.org).

Feigelson, E. M., 1978: Preliminary radiation model of a cloudy atmosphere. Part I: Structure of clouds and solar radiation. *Beitr. Phys. Atmos*, 51, 203-229.

Ghan, S. and R. Easter, 1992: Computationally efficient approximations to stratiform cloud and microphysics parameterization. *Mon. Wea. Rev.*, 120, 1572-1582.

Hobbs, P. V. and A. L. Rango, 1985: Ice particle concentrations in clouds. *J. Atmos. Sci.*, 42, 2523-2549.

Jacob, C. and S. A. Klein, 1999: The role of vertically varying cloud fraction in the parameterization of microphysical processes in the ECMWF model. *Quart. J. Roy. Meteor. Soc.*, 125, 941-965.

Kessler, E., 1969: On the distribution and continuity of water substance in the atmospheric circulations. *Meteor. Monogr.*, 10, No. 32, Amer. Met. Soc., 84pp.

Lin K. N., R. D. Farley and H. D. Orville, 1983: Bulk-parameterization of the snow field in a cloud model. *J. Clim. Appl. Meteor.*, 22, 1065-1092.

Lin, S.-J. and R. B. Rood, 1996: Multidimensional flux-Form semi-Lagrangian transport schemes. *Mon. Wea. Rev.*, 124, 2046-2070.

Myers, M. P., P. J. DeMott and W. R. Cotton, 1992: New primary ice-nucleation parameterization in an explicit cloud model. *J. Appl. Meteor.*, 31, 708-721.

Rasch, P. J., and J. E. Kristjansson, 1998: A comparison of the CCM3 model climate using diagnosed and predicted condensate parameterizations. *J. Clim.*, 11, 1587-1614.

Rutledge, S. A. and P. V. Hobbs, 1983: The mesoscale and microscale structure and organization of clouds and precipitation in mid-latitude cyclones. VIII: A model for the 'seeder-feeder' process in warm-frontal cloud bands. *J. Atmos. Sci*, 40, 1185-1206.

Ryan, B. F. 1996: On the global variation of precipitating layer clouds. *Bull. Americ. Met. Soc.*, 77, 53-70.

Smith, R. N. B., 1990: A scheme for predicting layer clouds and their water content in a general circulation model. *Quart. J. Roy. Meteor. Soc.*, 116, 435-460.

Sundquist, H., 1988: Parameterization of condensation and associated clouds in models for weather prediction and general circulation simulation. *Physically-based modelling and simulation of climate and climate change*, M.E. Schlesinger, Ed., Kluwer Academic Publishers, 433-461.

Tiedtke, M., 1993: Representation of clouds in large-scale models. *Mon. Wea. Rev.*, 121, 3040-3061.

Three Closure Conditions for the Massflux Convection Parameterization

Erdmann Heise

Deutscher Wetterdient, Offenbach am Main, Germany

Abstract

Three closure conditions are tested in the framework of the operational Tiedtke massflux parameterization of convection. The first one is the well known Kuo-type closure. The second one uses the convective available potential energy, while the third one uses the vertical integral over the turbulent kinetic energy. A situation with airmass convection over Germany was used to test the three closure conditions.

1 Introduction

The parameterization of convection poses serious problems in numerical models of the atmosphere, and in fact convection seems to be an ill-posed parameterization problem. Parameterizations have to rely on the assumption of a statistical equilibrium between the resolved scales and the parameterized scales. This requires at least a spectral gap between resolved and parameterized processes. Typical space and time scales of convection are in the order of 10 km and 10 minutes and more, respectively. The horizontal resolution of present day numerical weather prediction models is of the same order and the time step is of the order 1 min. Neither in the horizontal scale nor in the time scale a spectral gap exists between resolved scales and convection. Nevertheless, experience shows that a parameterization of deep convection is necessary in models of the aforementioned resolution. Model results are seriously degraded if the parameterization is omitted.

But even with a parameterization included, the resulting distribution of convective precipitation - especially in cases of airmass convection - is often unsatisfactory. A common problem of parameterized convection in cases of airmass convection is a biased diurnal cycle. The peak convective activity occurs around noon, i. e. 4 to 5 hours too early. In addition, even if only the daily precipitation amount in convective situations is considered, the distribution of predicted precipitation often deviates significantly from the observed distribution. In many situations with airmass convection the parameterization fails to provide any convection in large areas of observed convective activity.

Therefore, an attempt was made to improve the results of the convection parameterization in the Lokal-Modell (LM) of the German Weather Service without moving to a different parameterization method. A modification of the closure condition of the operational parameterization seemed to be a promising method to improve the results.

2 The Convection Parameterization

The operational NWP models of the German Weather Service use a massflux parameterization for convection based on the parameterization in the ECMWF model (Tiedtke, 1989). The starting point for a massflux parameterization is the horizontally averaged equations for dry static energy $s = c_pT + gz$ and for specific humidity q_v (the vertical exchange of momentum by convection is not considered in this Report). If the overbar denotes the horizontal

average, we arrive at

$$\frac{\partial \overline{s}}{\partial t} = A(\overline{s}) - \frac{1}{\overline{\rho}}\frac{\partial}{\partial z}(\overline{\rho w' s'})_{conv} + L(\overline{c}_{conv} - \overline{e}_{conv}) \tag{1}$$

$$\frac{\partial \overline{q}_v}{\partial t} = A(\overline{q}_v) - \frac{1}{\overline{\rho}}\frac{\partial}{\partial z}(\overline{\rho w' q_v'})_{conv} - (\overline{c}_{conv} - \overline{e}_{conv}) \tag{2}$$

Here the A-terms denote all processes not connected to convection, $(\overline{\rho w' \psi'})_{conv}$, with $\psi = s$ or q_v, are the subgrid-scale vertical transports of dry static energy and of specific humidity, respectively, c and e represent condensation and evaporation, respectively.

The convective cloud is assumed to consist of two distinct areas, an updraft area, index u, and a downdraft area, index d. In the updraft area the vertical profiles of dry static energy and specific humidity correspond to a moist adiabate through the lifting condensation level of near surface air. Moist saturated downdrafts with negative buoyancy can be initiated in the upper part of the cloud. The negative buoyancy is maintained through evaporation of precipitation. Assuming top hat profiles, the subgrid-scale transports by convection can be formulated as

$$\frac{1}{\overline{\rho}}\frac{\partial}{\partial z}(\overline{\rho w' \psi'})_{conv} = \frac{1}{\overline{\rho}}\frac{\partial}{\partial z}[M_u \psi_u + M_d \psi_d - (M_u + M_d)\overline{\psi}] \tag{3}$$

The vertical profiles of the massfluxes M in the updraft and in the downdraft areas are determined by entrainment and detrainment processes:

$$\frac{\partial M_{u,d}}{\partial z} = E_{u,d} - D_{u,d} \tag{4}$$

3 Closure Conditions

To solve (4) for the vertical profile of the massflux, a boundary condition at cloud base has to be prescribed (downdrafts are initiated with a constant fraction of the updraft massflux at cloud base). In addition to the operational Kuo-type closure two alternative forms were tested.

i) Kuo-type closure (Kuo-closure)

In LM, operationally the well-known Kuo-type closure (Kuo, 1965) is used. Neglecting here - for the sake of simplicity - the downdrafts, this closure reads

$$(M_u)_{z_b} = -\frac{1}{C_{kuo}(q_{v,u} - q_v)_{z_b}} \int_{z_s}^{z_b} \left(\rho \mathbf{v} \cdot \nabla q_v + \frac{\partial F^{q_v}}{\partial z} \right) dz \quad , \tag{5}$$

where z_s and z_b are the heights of the surface and of the cloud base, respectively, and F^{q_v} is the turbulent vertical flux of specific humidity. Other symbols have their common meaning. This closure additionally expresses a vanishing time derivative of specific humidity below cloud base, as long as the dimensionless tuning parameter $C_{kuo} = 1$.

ii) Convective available energy closure (CAPE-closure)

The convective available potential energy (E_{cp}) is defined as the vertical integral over the buoyancy of cloud air (e. g. Kreitzberg and Perkey, 1976):

$$E_{cp} = \int_{z_b}^{z_{top}} \frac{g}{\theta_{v,e}}(\theta_{v,u} - \theta_{v,e}) dz \quad , \tag{6}$$

where index e denotes values in the environment of the cloud, which are assumed to be identical to the grid-scale variables, and z_{top} is cloud height. In this case equation (5) is replaced by

$$(M_u)_{z_b} = C_{cp}\rho_{z_b}\sqrt{E_{cp}} \quad . \tag{7}$$

C_{cp} is a dimensionless tuning parameter.

iii) Turbulent kinetic energy closure (TKE-closure)

The second alternative closure is based on the vertical average of turbulent kinetic energy (TKE). In the present operational version (at DWD) of the LM, a level 2.5 turbulence parameterization is included, and TKE is a predicted variable. In conditionally unstable situations the vertical average over cloud depth

$$E_{tke} = \frac{1}{z_{top} - z_b}\int_{z_b}^{z_{top}} q^2 dz \tag{8}$$

(q^2 is the turbulent kinetic energy) is used in the closure condition for cloud base massflux. In this case equation (5) is replaced by

$$(M_u)_{z_b} = \frac{\rho}{g}E_{tke}/C_{tke} \quad , \tag{9}$$

where C_{tke} is a time constant, acting as a tuning parameter. The rationale for this closure method is the close connection between the convective available energy and the buoyant production term in the prognostic equation for turbulent kinetic energy. This latter term is normally parameterized by $-(g/\overline{\theta_v})K_h(\partial\overline{\theta_v}/\partial z)$. If this term is positive and large, there will also be a considerable amount of convective available energy, as the difference between the updraft temperature and the environmental temperature will be large. Therefore, large values of convective available energy are connected to large buoyant production of TKE. If this term dominates the tendency of TKE, a growth of TKE is possible, postponing the time of the maximum convective activity.

A drawback of this closure became obvious in preliminary tests: A very small value of the time constant $C_{tke}(< 1s)$ has to be chosen in order to get a realistic order of magnitude for the cloud base massflux. This value of the time constant is obviously not appropriate for convective processes with characteristic time scales of the order of 10 minutes and more.

For all three closure conditions a maximum value for the cloud base massflux of $1kg/(m^2 s)$ is prescribed. Additionally, threshold values for $E_{cp}(E_{cp,min} = 1J/kg)$ and for $E_{tke}(E_{tke,min} = 0.05J/kg)$ are prescribed in order to inhibit the onset of convection at low values of these energies. The tuning parameters are $C_{kuo} = 1$, $C_{cp} = 0.01$, and $C_{tke} = 0.1s$, respectively, if not otherwise stated.

4 Experiments

The different parameterizations were tested in a couple of 24 hour LM-forecasts. In all experiments the currently operational LM-version of DWD was used. The level 2.5 turbulence closure (prognostic turbulent kinetic energy) and the new treatment of the surface layer were included. One experiment uses this operational LM with the Kuo-closure, the second one replaces the Kuo-closure by the CAPE-closure, and the third one replaces the Kuo-closure by the TKE-closure.

The following day with pronounced convective activity was chosen:

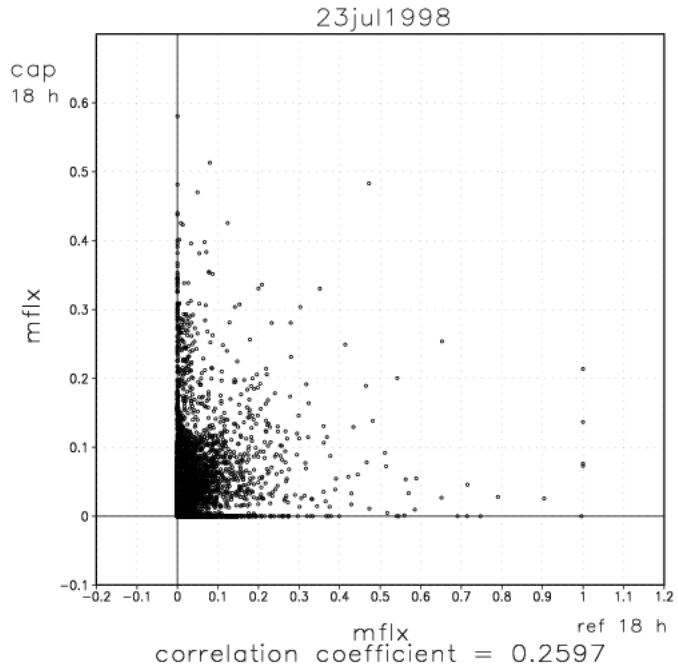

Figure 1: Scatter-plot of cloud-base massflux $[kg/(m^2s)]$ for the area in southern Germany as shown in Figure 3. The plot compares the Kuo-closure (reference version, abscissa) and the CAPE-closure (ordinate).

On 23 July 1998 severe convective activity developed during the afternoon in the northern parts of Bavaria (the area south of 50^o N between 10^o E and 12.5^o E in Figure 3), locally causing storm damage. The convection started at about 15.00 UTC and came to an end around midnight. No hint for this event was provided by the then operational Deutschland-Modell. The affected region was nearly free of precipitation in the forecast.

5 Results

First some general investigation of the results using different closure conditions was undertaken. Using the tuning parameters as given above, a comparison of cloud base massflux determined with the Kuo-closure and with the CAPE-closure is presented in Figure 1. Obviously there is no significant correlation between the results of the two runs. Of course we have to bear in mind that the atmospheric state of the two simulations may be different in this comparison. Therefore, in Figure 2 the results of two different closure variables in one single run are compared. For this comparison a run with the TKE-closure is used. The moisture convergence, the basis of the Kuo-closure, is compared to the convective available energy, the basis of the CAPE-closure. (Note that in LM the output variable 'moisture convergence' is defined as $g\rho$ times the vertical integral in (5). This gives the dimension $kg/(ms^3)$.) Again, there is no clear correlation between the two closure variables. This means that in regions with a large amount of moisture convergence there is not necessarily also a large value of potential instability and vice versa. Similar results are obtained with other combinations of variables. It might be argued that the comparison performed here is based on snapshots of atmospheric states. The convective development might take place at slightly different time scales. This could lead to a good correlation between different variables at slightly differing

reference times. But, nevertheless, the unpleasant consequence of these results is: *For a given atmospheric state the resulting convective activity depends very much on the chosen closure condition.*

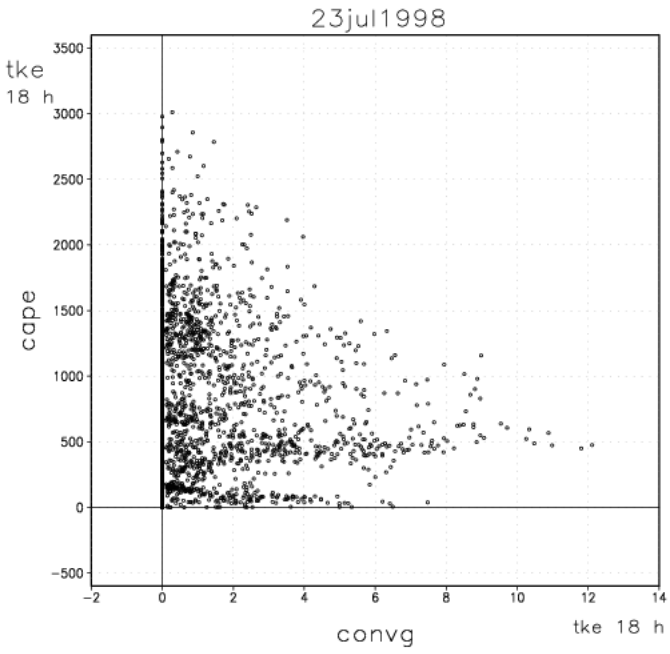

Figure 2: Scatter-plot of moisture convergence $[0.001kg/(ms^3)]$ (abscissa) and convective available energy $[J/kg]$ (ordinate) for an experiment using the TKE-closure for the area in southern Germany as shown in Figure 3.

If we look at the distribution of convective precipitation of the 6 hour interval centered around 18.00 UTC, indeed much of these differences are smoothed out (Figure 3). We see rather similar distributions in both experiments. The same is also true if we use the TKE-closure (not shown). To some degree this alleviates the problem of choosing between different closure conditions.

A couple of different tuning parameters have been tested for this situation. In all cases the Kuo-type closure (the reference version) was left unchanged ($C_{kuo} = 1$). Figure 4 shows some of the results, here using the convective precipitation amounts for 3 hour intervals, averaged over the whole LM area. For the Kuo-closure as well as for the CAPE-closure we see the well known problem of convective activity peaking around noon. Increasing the CAPE-closure tuning parameter from to $C_{cp} = 0.01$ ($Cape01$) to $C_{cp} = 0.05$ ($Cape05$) simply shifts the respective curve to higher precipitation values. A very small improvement of this behaviour can be achieved by using a considerably higher value of $E_{cp,min}$ (not shown). The TKE-closure behaves differently. With the tuning parameter as given above ($TKE10$) rather low convective precipitation amounts are simulated. In preliminary tests a larger value of the tuning parameter $C_{tke} = 1s$ ($TKE1$) was used. In this case convection is suppressed around noon and does not start before the early afternoon hours. This is clearly superior to the behaviour of the other schemes. But in general the convective precipitation rates are very low for the TKE-closure. If we use lower values of C_{tke} to enhance the precipitation rates, the superiority of a later maximum of convective precipitation disappears.

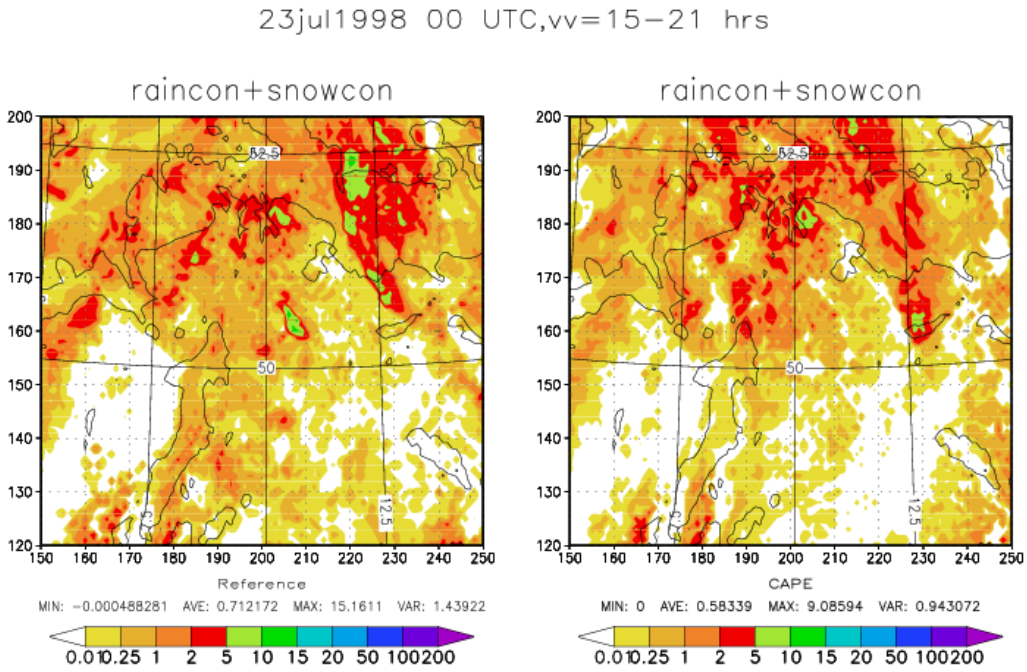

Figure 3: Convective precipitation ($mm/6h$) for the Kuo-closure (left part) and for the CAPE-closure (right part) in southern Germany. The black lines show the 50m, 200m, and 750m heights of the orography.

If we compare the predicted precipitation distributions (Figure 3) with reality (severe convection in the northern parts of Bavaria, locally causing storm damage), the results are disappointing. In all versions we only get some small amount of convective precipitation in part of the area without any hint for severe convection. Therefore, we have a second unpleasant result: *Neither of the two alternative closure conditions significantly improves the predicted precipitation distribution in this case.*

6 Summary and Conclusions

Two alternative closure conditions were used to examine their potential to improve the results of the operational Tiedtke massflux convection parameterization with a Kuo-type closure. The main disadvantages of the operational version occur in cases of airmass convection:

- The convective activity peaks too early (around noon).
- The model often completely fails to predict the observed distribution even of daily precipitation amounts.

The first alternative closure condition uses the convective available energy as a closure variable (CAPE-closure). The second one is based on the vertical integral over cloud depth of the predicted turbulent kinetic energy (TKE-closure).

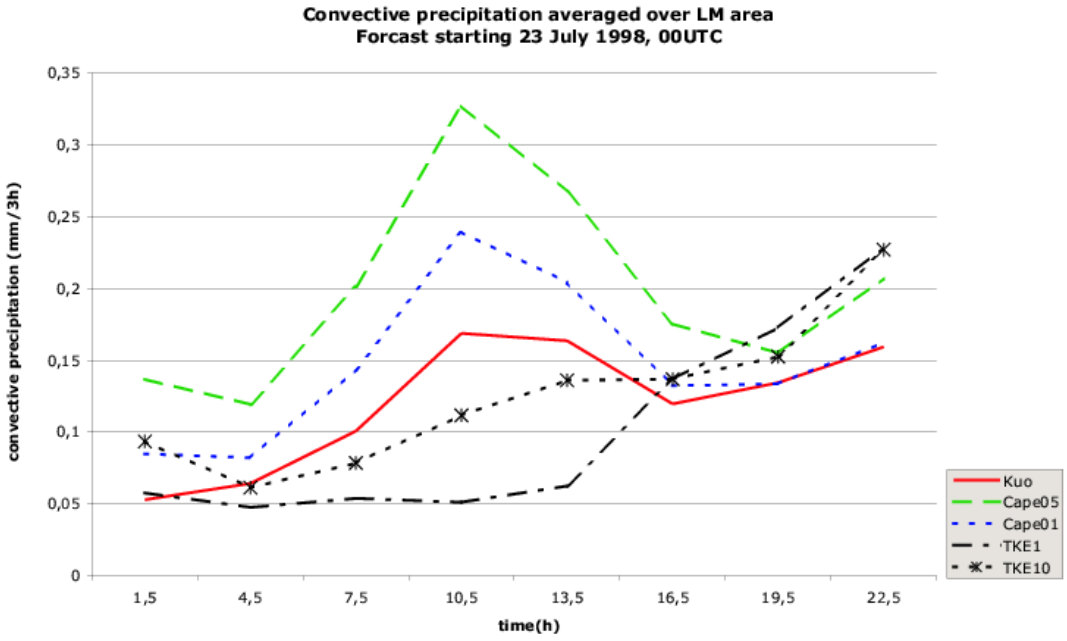

Figure 4: Diurnal course of convective precipitation for different closure conditions and different tuning parameters for the area in southern Germany as shown in Figure 3. See text for details.

It was shown that the TKE-closure is able to shift the peak convective activity to the evening, but at the expense of an underestimation of precipitation amount. Also, the time constant required as a tuning parameter is not appropriate for convective processes. The CAPE-closure provides results similar to the operational version. In general, the predicted precipitation distribution in all three versions fails to point to a situation of severe convective activity.

In view of the large effort required to change the operational scheme, on the basis of these results a change of the closure condition in the operational model could not be proposed.

A COSMO Technical Report is in preparation. This will show results of some more cases and especially deals more with the problem of the determination of the tuning parameters.

References

Kreitzberg, C. W., and D. J. Perkey, 1976: Release of Potential Instability: Part I: A Sequential Plume Model within a Hydrostatic Primitive Equation Model. Journ. Atm. Sci., Vol. 33, 456-475.

Kuo, H. L., 1965: On Formation and Intensification of Tropical Cyclones through Latent heat Release by Cumulus Convection. Journ. Atm. Sci., Vol. 22, 40-63.

Tiedtke, M., 1989: A Comprehensive Mass Flux Scheme for Cumulus Parameterization in Large-Scale Models. Mon. Weath. Rev., Vol. 117, 1779-1800.

Implementation of the Kain-Fritsch Convection Scheme

Marco Arpagaus

MeteoSwiss, Krähbühlstrasse 58, 8044 Zürich, Switzerland

Summary

The Kain-Fritsch convection scheme has been implemented into LM version 2.12 in a *preliminary* version.

Very first tests have been performed for MAP IOP 2 and show encouraging results.

The implementation needs to be consolidated and further case studies as well as longer parallel runs are needed to explore the potential of the scheme. An operational version will be completed in 2002.

First experiments

The Kain-Fritsch cumulus parameterization scheme (Kain and Fritsch (1993)) is being implemented into the LM as an optional convection scheme, to be used alternatively to the already available scheme by Tiedtke (1989). A *preliminary* version has been incorporated into LM version 2.12 and will be available with the next LM source-code release.

Very first tests to compare the Kain-Fritsch scheme with the Tiedtke scheme have been performed for MAP IOP 2a and 2b (17.09.1999 12 UTC – 21.09.1999 00 UTC; c.f. http://www.-map.ethz.ch), with the following technical specifications:

- no smoothing of forcing fields for both schemes
- no momentum feedback to grid-scale for both schemes
- EM boundary conditions, $289 * 289 * 45$ grid points
- unfiltered orography

Note that we expect relatively noisy fields due to the unfiltered orography and the absence of any smoothing of the forcing fields! – Figure 1 shows the 24h sum of total rain and snow in mm, whereas Figure 2 depicts the 24h sum of *convective* rain and snow in mm, both for forecast times +30h and LM runs initialized at 17.09.1999 00 UTC (MAP IOP 2a). The left panel refers to the LM run with the Kain-Fritsch scheme, the right panel to the forecast using the Tiedtke scheme.

Both forecasts do not validate particularly well against observations for both the general precipitation pattern and — even more so — the total amount of precipitation. However, they both give a reasonable forecast, and, more remarkably, the Kain-Fritsch scheme accounts slightly better for the convective activity observed in the northern part of the Po Valley. A comparison of the two schemes for MAP IOP 2b shows similar results.

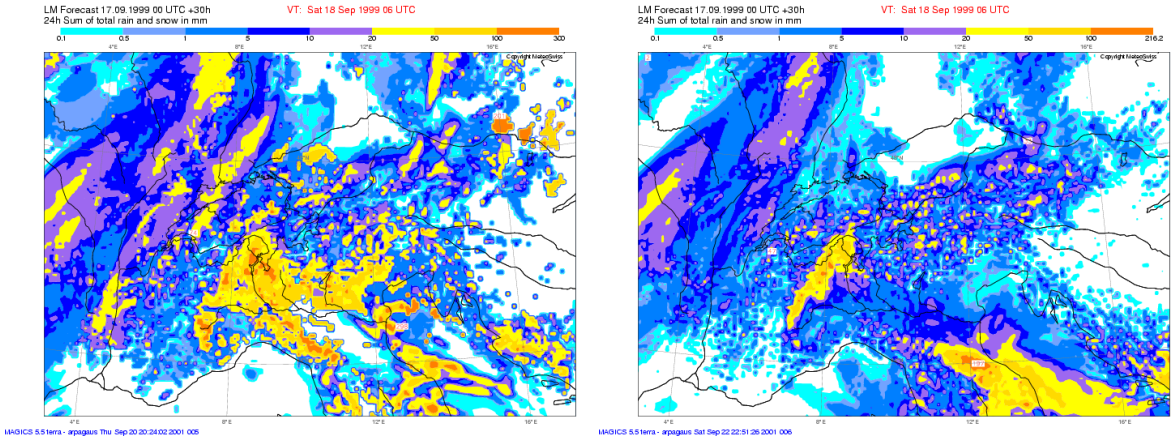

Figure 1: The 24h sum of total rain and snow in mm at forecast time +30h for LM runs with the Kain-Fritsch scheme (left) and the Tiedtke scheme (right), respectively. The run was initialized at 17.09.1999 00 UTC.

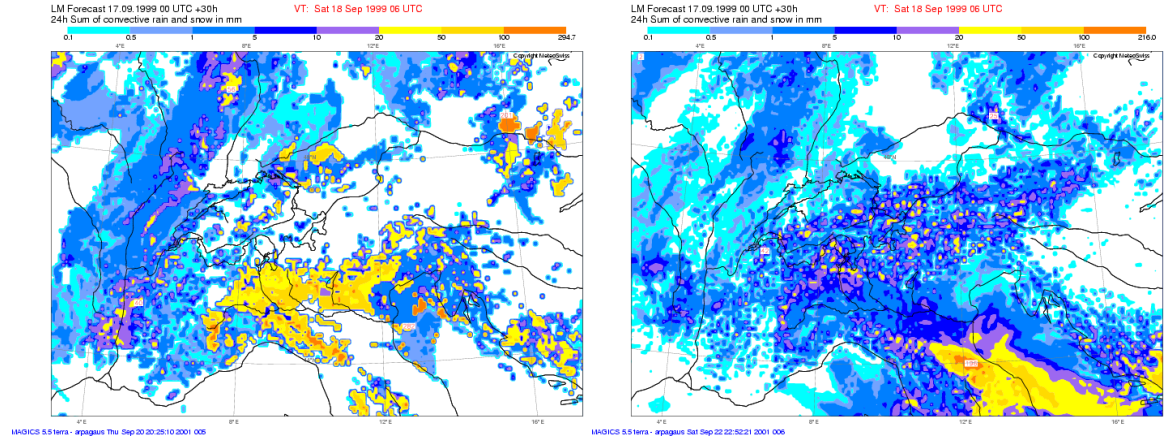

Figure 2: The 24h sum of convective rain and snow in mm at forecast time +30h for LM runs with the Kain-Fritsch scheme (left) and the Tiedtke scheme (right), respectively. The run was initialized at 17.09.1999 00 UTC.

These first comparisons are too preliminary to prove any strength (or weaknesses) of the two schemes, but are an encouraging start to invest more time into further case studies, longer parallel runs and parameter tuning exercises!

A final, operational version of the Kain-Fritsch cumulus parameterization scheme will be available in 2002, at which time a more detailed report on the obtained results will also be published.

References

Kain, J. S. and J. M. Fritsch, 1993: Convective Parameterization for Mesoscale Models: The Kain-Fritsch Scheme. *In: The Representation of Cumulus Convection in Numerical Models. Meteorological Monographs No 46*, American Meteorological Society, 165–170.

Tiedtke, M., 1989: Comprehensive Mass Flux Scheme for Cumulus Parameterization in Large-Scale Models. *Monthly Weather Review,* 117, 1779–1800.

The Water Surface Roughness Length for Temperature: an Observational Study

Dmitrii Mironov, Frank Beyrich, Erdmann Heise and Matthias Raschendorfer

Deutscher Wetterdienst, Offenbach am Main, Germany

Data from observations in the atmospheric surface layer taken over a small fresh water lake (the Kossenblatter See field station of the German Weather Service located near the Lindenberg Meteorological Observatory, Land Brandenburg, Germany) and over the Baltic Sea (the Östergarnsholm field station of the University of Uppsala located ca. 4 km east of the Island of Gotland) are used to analyse the roughness length of the water surface with respect to potential temperature. Using data from direct flux-profile measurements and the surface layer similarity relations, we have estimated the ratio of the roughness length with respect to the wind velocity, z_{0u}, to the roughness length with respect to the temperature, z_{0T}, or, alternatively, the increment of the temperature across the roughness layer, $(\theta_0 - \theta_s)/\theta_* \equiv \delta\theta/\theta_* = (Pr_n/\kappa)\ln(z_{0u}/z_{0T})$. Here, θ_s is the potential temperature at the surface, θ_0 is the potential temperature extrapolated logarithmically down to the level $z = z_{0u}$, $\theta_* = -Q_s/u_*$ is the potential-temperature scale, Q_s is the surface kinematic sensible heat flux, u_* is the surface friction velocity, κ is the von Kármán constant, and Pr_n is the Prandtl number at neutral static stability. We have tested several theoretical formulations for $\delta\theta/\theta_*$ agains data.

For the aerodynamically rough flow over the water surface, the "roughness" Reynolds number, $Re_0 = u_* z_{0u}/\nu$, ν being the kinematic molecular viscosity of the air, has been used as a relevant governing parameter, and a number of power-law formulations, Re_0^n, have been suggested to date (Kantha and Clayson 2000). Empirical estimates of the exponent n tend towards 0.5. Theoretical values of n vary with the writer. The value of $n = 1/2$ has been advocated by several authors (a summary is given by Zilitinkevich et al. 2001), although other values have also been suggested (e.g. Brutsaert 1982).

Beljaars (1994) took an "empirical" approach (in the sense that he attempted to develop an empirical recipe that gives a good fit to observations) and adopted the simplest assumption that the roughness length with respect to the temperature, z_{0T}, scales on the depth of the conduction sub-layer, χ_h/u_*, χ_h being the molecular temperature conductivity of the air, no matter how large the surface friction velocity. For the rough regime of the flow over the water surface, his formulation reads

$$\delta\theta/\theta_* = (Pr_n/\kappa)\,(0.92 + \ln Re_0)\,. \tag{1}$$

Zilitinkevich et al. (2001) presented fresh scaling arguments and experimental data in support of the following expression for the roughness lengths for temperature:

$$\frac{\delta\theta}{\theta_*} = \begin{cases} -2 & \text{at } \; Re_0 \le 0.1 \\ 4.0 Re_0^{1/2} - 3.2 & \text{at } \; Re_0 \ge 0.1, \end{cases} \tag{2}$$

with the 1/2 power-law dependence at large values of the roughness Reynolds number. The small-Reynolds-number formulation in the above expression corresponds to the smooth

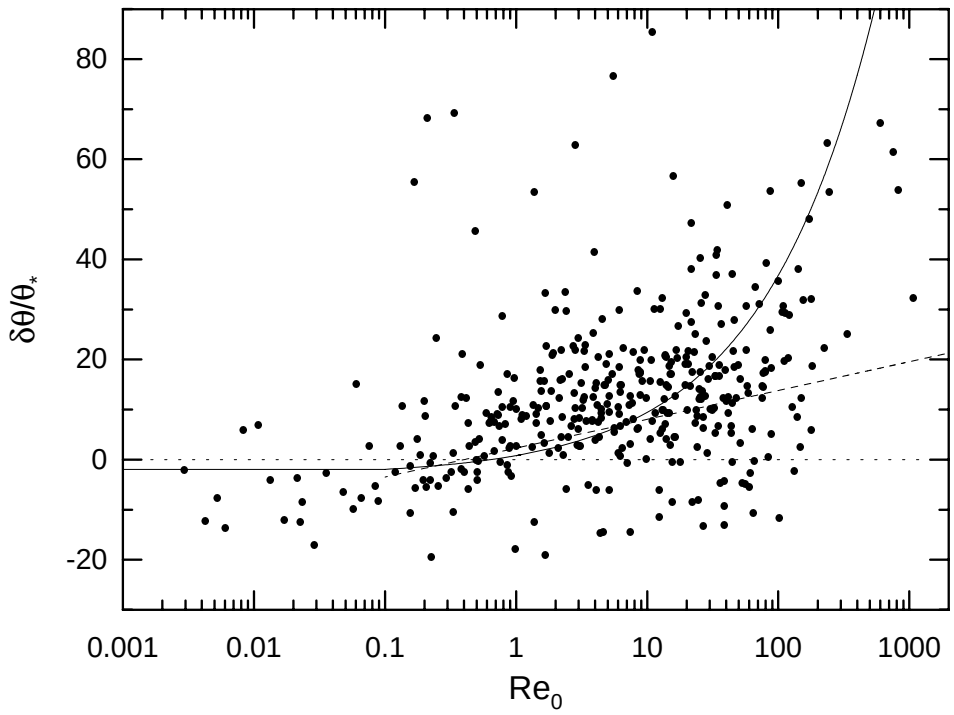

Figure 1: Dimensionless temperature increment across the roughness layer, $\delta\theta/\theta_*$, versus the roughness Reynolds number, Re_0. Solid curve shows the Zilitinkevich et al. (2001) formulation. Dashed curve shows the logarithmic law, Eq. (1), proposed by Beljaars (1994). Symbols show data from measurements taken over Kossenblatter See, Land Brandenburg, Germany, 6, 13 and 15 August and 12 October 1999 (Beyrich 2000, Beyrich et al. 2000).

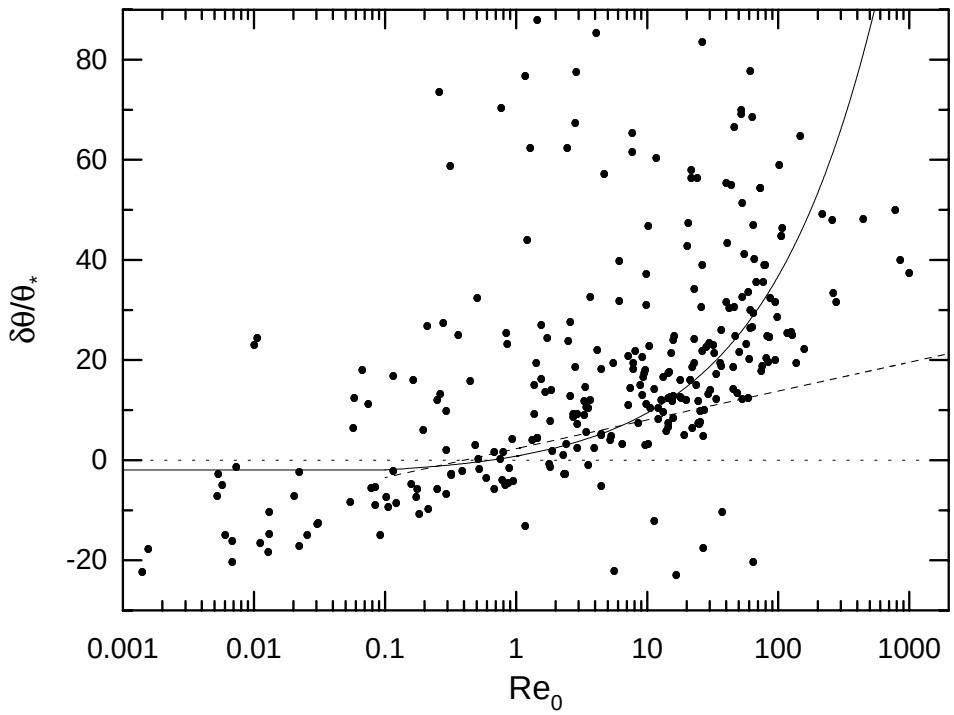

Figure 2: Dimensionless temperature increment across the roughness layer, $\delta\theta/\theta_*$, versus the roughness Reynolds number, Re_0. Solid curve shows the Zilitinkevich et al. (2001) formulation. Dashed curve shows the logarithmic law, Eq. (1), proposed by Beljaars (1994). Symbols show data from measurements taken over Baltic Sea, Field Station Östergarnsholm, from 1 November to 30 November 1998 (Rutgersson et al. 2001).

regime of the flow, where z_{0T} is known to scale on the depth of the near-surface conduction sub-layer.

Figures 1 and 2 show the dimensionless temperature increment across the roughness layer as function of the roughness Reynolds number. In spite of the wide scatter of points, the data demonstrate a pronounced tendency to follow a 1/2 power law. The Zilitinkevich et al. (2001) formulation, Eq. (2), appears to compare well with empirical data. The Beljaars (1994) logarithmic dependence of $\delta\theta/\theta_*$ on Re_0, Eq. (1), tends to underestimate data at large values of Re_0.

The $Re_0^{1/2}$ holds for both the Kossenblatter See data and for the Östergarnsholm data in spite of the significant difference in the aerodynamic roughness, z_{0u}, of the lake surface and of the surface of the Baltic Sea. This difference is accounted for through Re_0 that incorporates the roughness length with respect to the wind velocity. Hence the water-surface roughness length for temperature can be estimated rather accurately through fairly simple formulations like that given by Eq. (2) provided that z_{0u} is known to a good approximation. To put this another way, major problems in parameterizing both the momentum transfer and the scalar transfer near the surface are associated with the aerodynamic roughness of the water surface. Notice that the situation over land surfaces is essentially different. There the aerodynamic roughness does not present major difficulties whereas parameterizing the roughness lengths for scalars is very tricky (e.g. Raschendorfer 1999).

References

Beljaars, A. C. M., 1994: The parameterization of surface fluxes in large-scale models under free convection. *Quart. J. Roy. Meteorol. Soc.*, **121**, 255–270.

Beyrich, F., (Ed.), 2000: *LITFASS-98 Experiment. 25.51998 – 30.6.1998. Experiment Report.* Arbeitsergebnisse Nr. 62, Deutscher Wetterdienst, Geschäftsbereich Forschung und Entwicklung, Offenbach am Main, Germany, 78 pp.

Beyrich, F., S. H. Richter, U. Weisensee, W. Kohsiek, F. Bosveld, H. Lohse, H. de Bruin, O. Hartogensis, J. Bange, and R. Vogt, 2000: The LITFASS-98 Experiment: fluxes over a heterogeneous land surface. Proc. 14th Symp. on *Boundary Layers and Turbulence*, 7 – 11 August 2000, Aspen, USA, P 1.3.

Brutsaert, W., 1982: *Evaporation into the Atmosphere.* D. Reidel, Dordrecht, etc. 299 pp.

Kantha, L. H., and C. A. Clayson, 2000: *Small Scale Processes in Geophysical Fluid Flows.* Academic Press, San Diego, etc., 888 pp.

Raschendorfer, M., 1999: Special topic: The new turbulence parameterization of LM. *Quarterly Report of the Operational NWP-Models of the Deutscher Wetterdienst*, No. 19, Deutscher Wetterdienst, Offenbach am Main, Germany, 3–12.

Rutgersson, A., A.-S. Smedman, and A. Omstedt, 2001: Measured and simulated latent and sensible heat fluxes at two marine sites in the Baltic Sea. *Boundary-Layer Meteorol.*, **99**, 53–84.

Zilitinkevich, S. S., A. A. Grachev, and C. W. Fairall, 2001: Scaling reasoning and field data on the sea surface roughness lengths for scalars. *J. Atmos. Sci.*, **320**, 320–325.

A New Multi-Layer Soil-Model

Reinhold Schrodin and Erdmann Heise

Deutscher Wetterdient, Offenbach am Main, Germany

For land surfaces, the LM soil model TERRA provides the surface temperature and the specific humidity at the ground. The ground temperature is calculated by solving the equation of heat conduction with the EFR (extended force-restore) method after Jacobsen and Heise (1982). Two soil layers with adjusted depths for optimal response to dual frequency harmonic forcing are used. In practical application, there are three major shortcomings of this scheme:

- the thermal thickness of the soil layers depends on soil type,
- different thicknesses have to be used for water transport, resulting in an inconsistent interaction of thermal and hydrological transport, and
- due to the relatively large thickness of the upper soil layer, freezing and melting of soil water has to be excluded in order to avoid a significant suppression of temperature changes if phase transitions occur. This, on the other hand, enhances the temperature response in an unrealistic way.

Thus a new multi-layer version (TERRA_LM) has been developed which is based on the direct numerical solution of the heat conduction equation (HCE-method). With the HCE-method, the soil can rapidly react to high frequency changes of the atmospheric forcing. A great advantage of the multi-layer version is the formulation of hydrological and thermal processes with exactly the same layer distribution, simplifying the formulation of feedback processes between the thermal and hydrological parts of the model. A major improvement results also from the inclusion of phase transitions in the soil layers.

Numerical experiments have shown that six active layers with increasing thicknesses of 0.01, 0.03, 0.06, 0.12, 0.24 and 0.48 m from top to bottom are sufficient for numerical weather prediction models. The results become useless if the the number of active layers is reduced to less than four, and with additional layers close to the soil surface the results do not differ remarkably, even if freezing and melting occurs. A seventh inactive layer, the so-called climate layer, is added with prescribed temperature and water content. Figure 1 shows the structure of the new soil model.

Two versions for the representation of phase transitions in the soil layers have been implemented:

(a) freezing and melting occurs at a threshold temperature T_{thr} equal to the freezing point $T_0 = 0°C$; this gives the maximum effect of phase transitions.

(b) freezing and melting occurs at a threshold temperature T_{thr} depending on soil water content and soil type following Flerchinger and Saxton (1989); this gives the minimum effect of phase transitions. For details of this formulation, see Schrodin and Heise (2001).

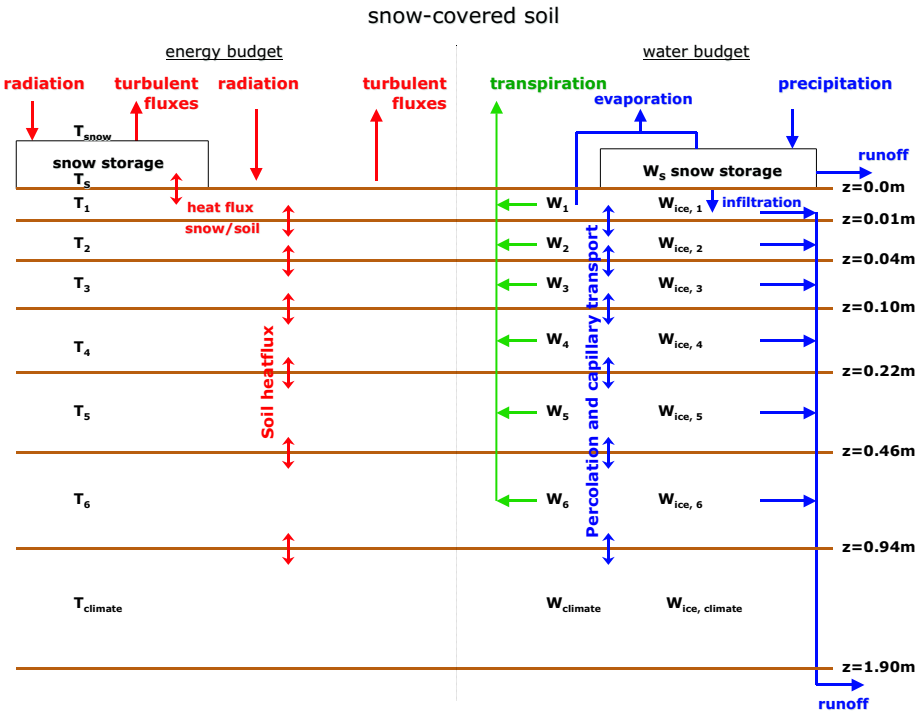

Figure 1: The multi-layer grid of the soil model TERRA_LM: General structure and physical processes considered in case of a snow covered soil.

To investigate the general effect of freezing/melting and especially the effect of the two different definitions of the threshold temperature, one dimensional simulations with a stand alone soil model were performed. In all test cases an artificial diurnal cycle of the thermal forcing at the soil surface is prescribed. A vertically constant temperature profile is assumed initially, and the integrations are repeated cyclically until a quasi-stationary state is reached. As no analytical solution of the heat conduction equation is available for this type of experiments, a 200-layer-version of the multi-layer soil model with layer thicknesses of 0.005 m is used as a reference. In all cases the soil-type loam is used. Simulations for three different values of the soil water content (0.8 W_{por}, 0.5 W_{por}, 0.2 W_{por}, vertically constant) are performed.

In Figure 2 the results with $T_{thr} = T_0$ are shown. In the 200-layer-version (left) with high values of soil water content (0.8 W_{por}) the soil surface temperature remains at T_0 for a considerable part of the day. Compared to a run without freezing/melting the temperature amplitude is reduced by about 70 %. With decreasing soil water content the duration of the periods with surface temperatures fixed to T_0 decrease and the amplitude of the diurnal temperature curve increases. If the freezing/melting of one layer has been completed, the temperature can decrease/increase until the next layer starts with this process, fixing the surface temperature again, now on a deeper/higher temperature. Of course this effect is coarsened in the 6-layer-version (Figure 2, right). The freezing/melting of the second layer now also forces the surface temperature to be fixed to a quasi constant value over some hours if the soil water content is rather high. Taking the results of the 200-layer-version as the truth, temperature amplitudes are somewhat too large in the 6-layer-version.

If instead of $T_{thr} = T_0$ we use the water content dependent threshold temperature, the effect of freezing/melting is reduced very much (Figure 3). Now there is no effect at all in the case of a dry soil as this low water content can not freeze until the temperature is extremely low. For the wetter soils, the periods of quasi constant surface temperature are much shorter

compared to the version with $T_{thr} = T_0$, both in the 200-layer (Figure 3, left) and in the 6-layer version (Figure 3, right). In general this gives the temporal course of temperature a somewhat smoothed appearance.

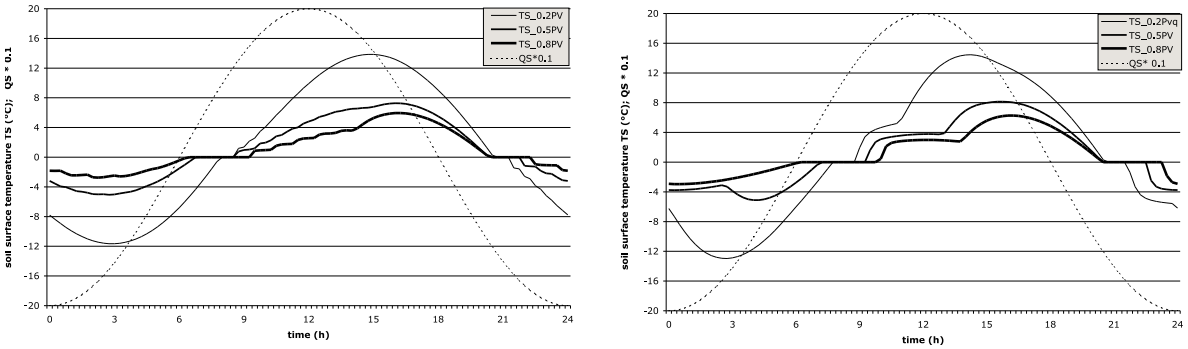

Figure 2: Soil surface temperature (°C) for a harmonic thermal forcing (dotted) and different water contents (see text). Freezing and melting at freezing point. Left: 200-layer version. Right: 6-layer version.

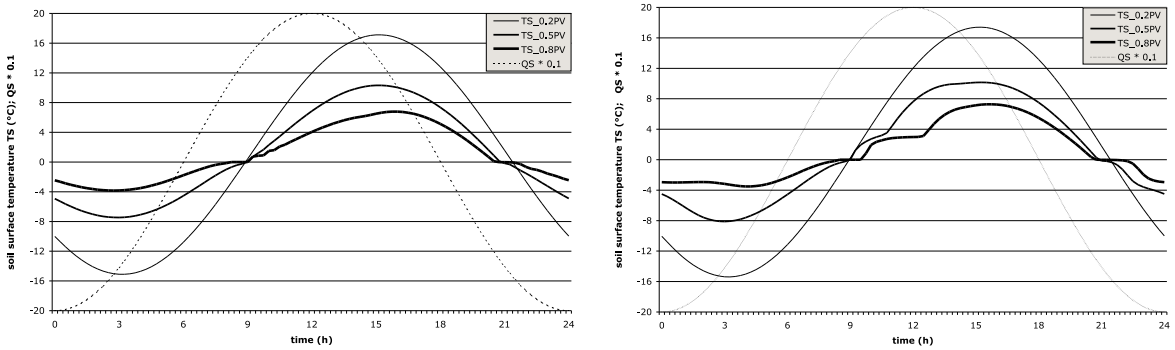

Figure 3: Soil surface temperature (°C) for a harmonic thermal forcing (dotted) and different water contents (see text). Freezing and melting at a threshold temperature depending on soil moisture and soil type. Left: 200-layer version. Right: 6-layer version.

These tests show that the inclusion of freezing/melting has a significant effect on the soil surface temperature. In this aspect, the HCE-method performs superior to the former EFR-method and in practical applications a beneficial impact in the prediction of 2m-temperature during the early and late winter season is expected (the operational application of the multi-layer soil model is scheduled for spring 2002). The two different methods to calculate phase transitions in the new multi-layer soil model, however, give significantly different results. It will be left to modelling experience with daily temperature verification to decide about the right way to include freezing/melting effects.

References

Flerchinger, G. N. and K. E. Saxton, 1989: Simultaneous heat and water model of freezing snow-residue-soil system. I. Theory and development. *Transactions of the ASEA*, 32, 2, 565 - 571.

Schrodin, R. and E. Heise (2001): The Multi-Layer Version of the DWD Soil Model TERRA_-LM. *Cosmo Technical Report*, No.2 (available at www.cosmo-model.org).

Ensemble Prediction and Statistical Postprocessing of Weather Parameters for the LM

S. Theis, A. Hense, U. Damrath[1)] and V. Renner[1)]

Meteorologisches Institut, University Bonn, Germany

[1)] *Deutscher Wetterdienst, Offenbach, Germany*

Abstract

Experimental ensemble predictions with the LM show that small spatial features of only a few gridboxes' scale might not be predictable in a deterministic way. Therefore, the direct output of the LM has to be interpreted statistically. Methods for the statistical postprocessing of LM output are being developed. A neighbourhood method transforms the model output into a probabilistic forecast at every grid point. The probabilistic forecast at a certain grid point is based on the model output within a spatial region surrounding the grid point and within a certain time interval. Preoperational tests of the method are under way. Additionally, the development and investigation of an alternative method based on wavelet analysis has started.

1 Introduction

At the German Weather Service (DWD) a new numerical weather forecasting system became operational in December 1999. The system consists of the global model GME and the non-hydrostatic limited area model "Lokal-Modell" (LM). The LM has a horizontal resolution of Δx =7 km and produces forecasts for a time period of 48 hours. The DWD is planning to further increase the horizontal resolution of the LM to 2.8 km within the next few years.

Since the weather does exhibit considerable variability even on spatial scales of only a few kilometers, the increase of model resolution is certainly a project worth striving for. When doing so, an eye has to be kept on the predictability of the atmosphere, though. The atmosphere is a chaotic system. In principle, this aspect has always to be taken into account whenever an atmospheric forecast is produced and interpreted. In short-range forecasts small spatial features of only a few gridboxes' scale might not be predictable in a deterministic way. In a high-resolution model output small-scale features rather contain a certain amount of stochastic information. For some variables like precipitation or cloud cover it has to be expected that these stochastic characteristics will noticeably influence the characteristics of the forecast.

One possibility of dealing with the intrinsic uncertainty of a forecast is the generation of ensemble predictions. The aim of ensemble prediction is to forecast the impact of the uncertainty of initial conditions on the uncertainty of the forecast. This is usually done by running several numerical forecasts from slightly different initial states. Certainly, one could also imagine to vary other parameters than the initial conditions, for example the surface parameters, such as roughness length or albedo. This method is especially interesting in the context of limited-area, high-resolution atmospheric models which are nested within a global model. The improvement of the high-resolution forecast in comparison with the low-resolution global forecast is substantially governed by the quantitative specification of

the surface parameters. Many of these surface parameters cannot be quantified with downright certainty. We have produced ensemble predictions by slightly perturbing the roughness length z_0 and the orographic height of the LM.

Ensemble prediction, however, is often not feasible in operational use, because it demands a prohibitive amount of computer capacities. Nevertheless, the direct model output has to be interpreted in a statistical way, whenever it contains a non-negligible amount of stochastic information. As a temporary remedy, the DWD in cooperation with the University of Bonn has started to develop methods which interpret the LM direct model output statistically. The methods require the data of one numerical simulation only. They aim at the transformation of the direct model output into a probabilistic forecast.

2 Ensemble Prediction

The aim of ensemble prediction is to forecast the impact of uncertainties in the input data and/or model formulation on the uncertainty of the forecast. Theoretically, all components should be perturbed which are subject to uncertainty or which can be formulated in several ways (i. e. initial conditions, lateral boundary conditions from the global model, model physics, surface parameters, etc.). Only then an ensemble can be expected to produce an ensemble spread which resembles the skill of the forecast.

For the sake of simplicity, we constrain ourselves to the perturbation of the aerodynamic roughness length z_0 and orographic height only. We must be aware, though, that such an ensemble does not produce a realistic spread. It will just reflect the impact of the uncertainty in the specification of roughness length and orographic height on the forecast. Thus, it provides an estimate of the minimum content of stochastic information in the forecast.

2.1 Random Perturbation of Surface Parameters

Among the numerous surface parameters in the LM, we perturb the aerodynamic roughness length z_0 and the orographic height. In the following, we only describe the perturbation of roughness length. The orographic height is perturbed in an analogue way.

The definition of a roughness length value is of statistical nature. Estimated values of roughness length are subject to uncertainty. The roughness length value at a certain grid point represents the mean of the processes within the gridbox. Unresolved processes are not taken into account explicitly. Every estimate of a mean is associated with a variance. Therefore, we consider the roughness length to be a random variable instead of a fixed value.

We assume that the roughness length at each grid point is distributed according to a log normal probability density function (*pdf*) with special treatment of the level zero. The *pdf* is fully characterized by its mean and its variance. The mean of the *pdf* at a grid point is taken to be the roughness length value which is prescribed by the operational version of the LM (see Figure 1). The variance of the *pdf* is supposed to represent the uncertainty which is associated with the determination of a roughness length value at this grid point. We assume it to be a function of the local gridscale spatial variability of roughness length.

We specified the log-normal *pdf* of the roughness length at each grid point individually. According to these *pdf*s we produced five random realizations of the roughness length at each grid point. Together with the original field of roughness length, these fields form an ensemble of six members. Figure 2 shows the standard deviation of the six realizations at each grid point.

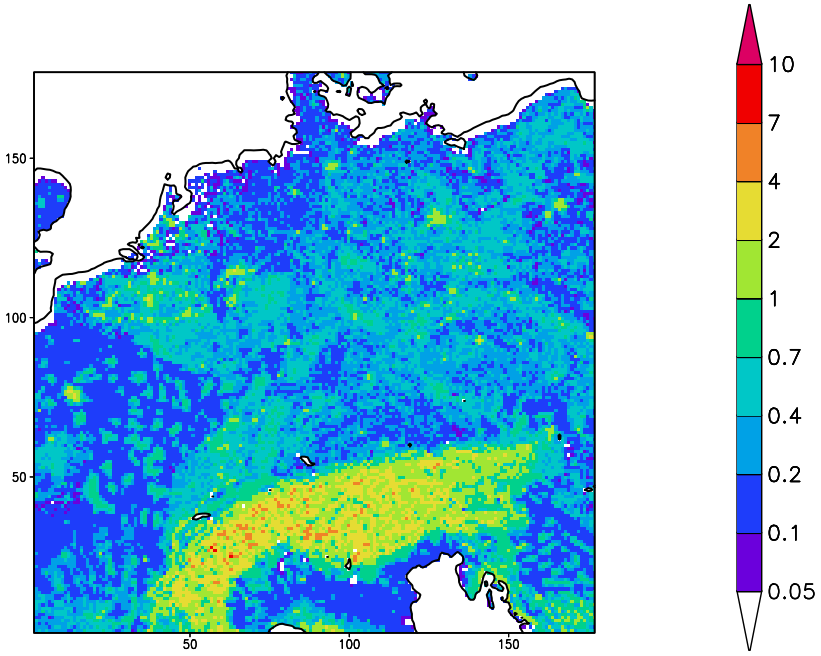

Figure 1: LM unperturbed roughness length z_0. Unit: m. Horizontal resolution: 7 km.

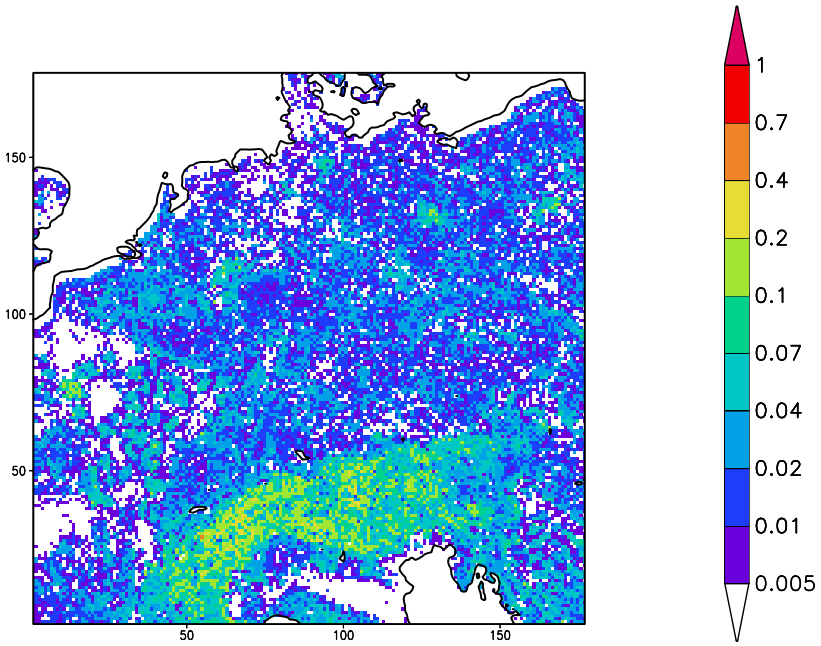

Figure 2: Standard deviation of the six realizations of perturbed roughness length z_0. Unit: m. Horizontal resolution: 7 km.

The standard deviation amounts to only 5%–10% of the original values (Figure 1). Thus, the magnitude of the perturbation is relatively small compared to the real uncertainty range of an estimated roughness length value (cf. e. g. Martano, 2000).

The realizations of the roughness length field were used to run six different LM-simulations of the same day. In some case studies perturbations of the orographic height were introduced additionally (see Table 1). Thus, the setups of the six LM-simulations only differ in terms of roughness length z_0 or in terms of roughness length z_0 and orographic height.

Table 1: The case studies.

Date	Situation	Perturbation of ...
July 4th, 1994	heavy convective precipitation over Central Europe	roughness length
May 21st, 1999	heavy gridscale precipitation on the northern side of the Alps	roughness length and orographic height
December 26th, 1999	severe storm "Lothar" in France and western Germany	roughness length and orographic height

2.2 Results of the Ensemble Forecast

We have produced ensembles for three case studies (Table 1) and we investigated the following forecast variables: hourly sums of precipitation at the ground, temperature 2 m above the ground, wind speed and gusts 10 m above the ground and total cloud cover.

In the following we focus on the precipitation forecast on July 4th, 1994, 12 UTC (see Figure 3). Figure 4 shows an enlarged area of this forecast field. The size of a grid box is 7 km × 7 km.

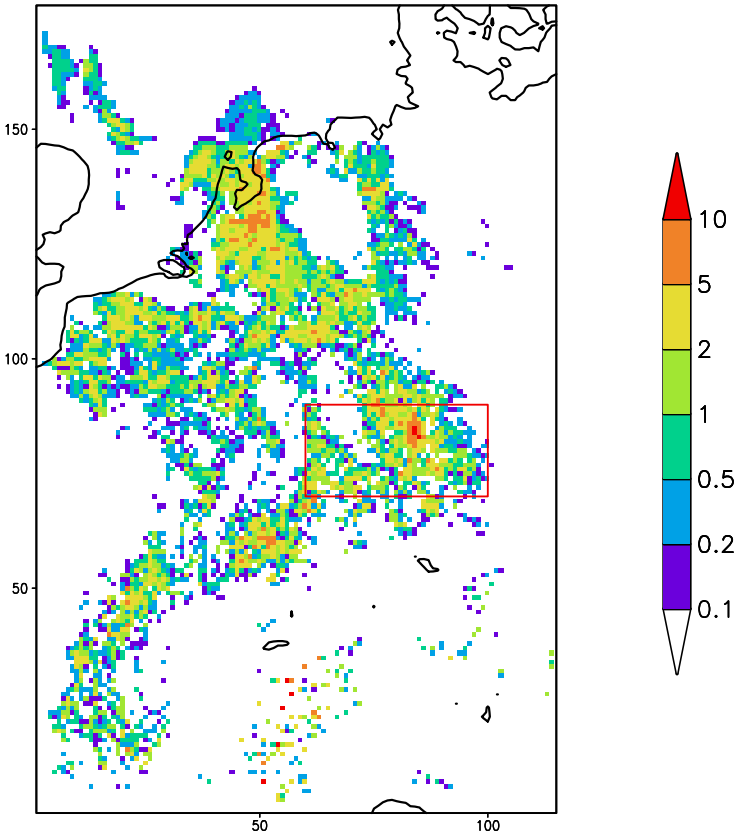

Figure 3: LM direct model output (unperturbed roughness length) of a convective situation over Central Europe at 12 UTC on July 4th, 1994. Forecast variable: Accumulated precipitation of the preceding hour. Unit: mm. Lead time of the forecast: 12 hours. Horizontal resolution: 7 km.

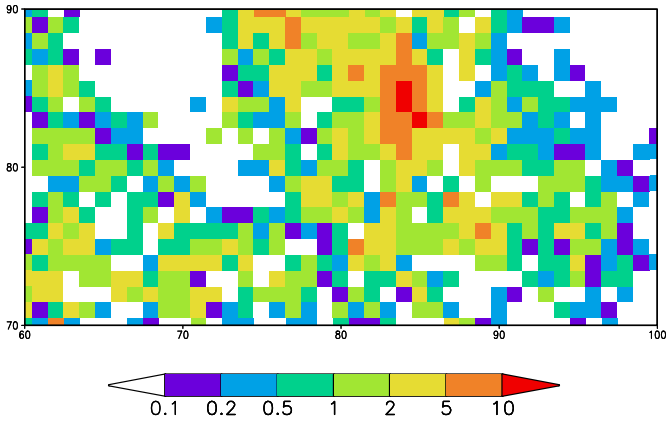

Figure 4: Zoom of the area which is marked in Figure 3. Simulation with unperturbed roughness length.

Figure 5 shows the standard deviation of the six ensemble members. At many grid points the standard deviation amounts to 50% of the original forecast values in Figure 3. The differences between the ensemble members must be caused by the slight perturbation of roughness length. The standard deviation of the ensemble forecast is a lower bound of the stochastic information which is contained in the direct model output of a single simulation of the LM. The relatively high values of the standard deviation in our ensemble forecast suggest a non-neglegible amount of stochastic information in an operational precipitation forecast of the LM. Due to this stochastic information the LM-forecast might be unreliable.

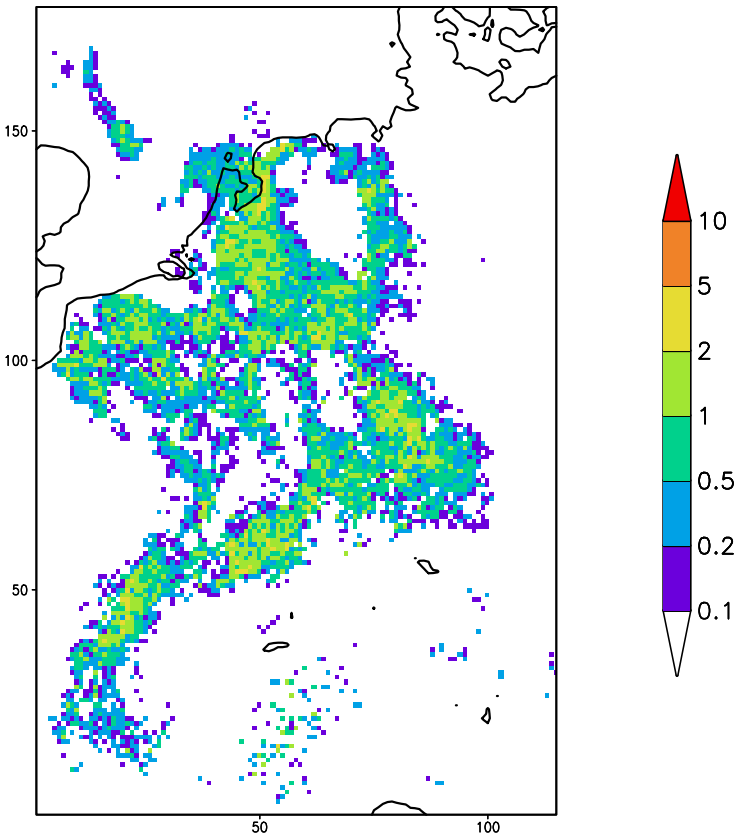

Figure 5: Standard deviation of the six ensemble members at 12 UTC on July 4$^{\text{th}}$, 1994. Forecast variable: Accumulated precipitation of the preceding hour. Unit: mm.

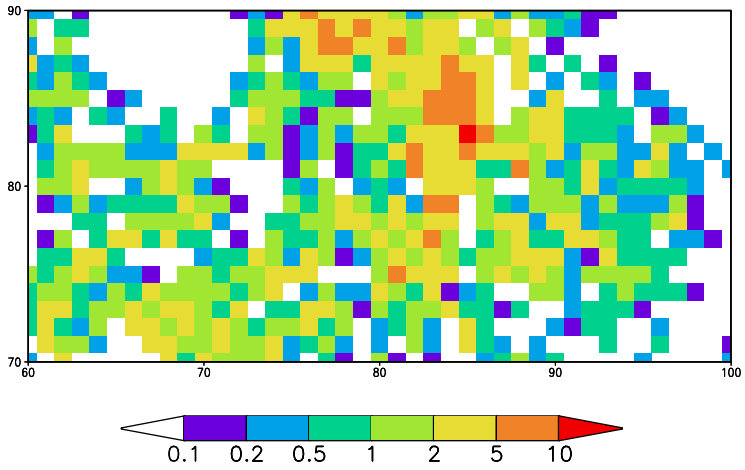

Figure 6: Zoom of the area which is marked in Figure 3. Example of a simulation with perturbed roughness length.

The differences between the ensemble members prevail in the smallest spatial scales of the forecast. If the forecasts of the individual ensemble members are spatially smoothed before they are compared with each other, the differences between the ensemble members become much smaller. As an example, Figure 6 shows the forecast of one of the simulations with perturbed roughness length. The area is the same as in Figure 4. A comparison of Figure 4 with Figure 6 illustrates that the exact position of heavy precipitation events is not predictable in a deterministic way. At the most, it is possible to predict *areas* which contain heavy precipitation events. The *exact* position within this area is a random feature.

The other two case studies (Table 1) lead to similar results, even though they mainly contain grid-scale precipitation instead of convective precipitation. Other variables (i. e. total cloud cover and wind/temperature near the ground) behave differently in comparison with precipitation. Wind is only slightly affected by a perturbation of roughness length/orographic height. In cases of high wind speed, though, this slight uncertainty proves to be non-neglegible, if the potential wind damage is forecast. The temperature forecast also responds to the perturbation of roughness length and orographic height. The response is correlated with the response of precipitation. Finally, the forecast of total cloud cover is strongly influenced by the perturbation of roughness length/orographic height, if it is caused by convection.

3 Statistical Postprocessing

The operational use of a high-resolution, limited-area, short-range ensemble prediction system would create an almost prohibitive demand on computer capacities. Therefore, at present, we restrict ourselves to the statistical postprocessing of the operational LM run only.

Two methods are being developed: the *neighbourhood method* (Section 3.1) and the *wavelet method* (Section 3.2). Whereas the wavelet method is still in its infancy, the neighbourhood method is already undergoing a pre-operational test phase.

3.1 Neighbourhood Method

The method intends to estimate properties of the probability distribution of the forecast at each grid point of the LM. In order to obtain information about the probability distribution

of the forecast at a certain grid point, an appropriate sample of this forecast is needed. Since we have to restrict ourselves to only one forecast simulation, we need to make a general assumption in order to generate the sample.

3.1.1 Key Assumption

Imagine a certain grid point called A. Around grid point A we define a spatial *neighbourhood* (Figure 7) of circular shape or elliptic shape (cf. Section). All grid point values are modified values of the LM direct model output (cf. Section).

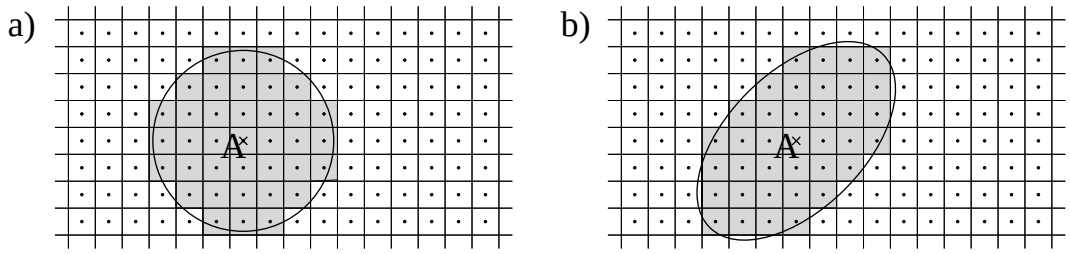

Figure 7: The spatial neighbourhood of grid point A. a) isotropic neighbourhood, b) anisotropic neighbourhood. Grid point values of the shaded gridboxes are assumed to form a random sample of the forecast at grid point A.

The key assumption of the neighbourhood method is as follows: Grid point values of the shaded gridboxes are assumed to constitute the sample of the forecast at grid point A. In other words, all grid point values within the neighbourhood are assumed to be independent and identically distributed according to the probability density function of the forecast at grid point A.

Currently, the diameter of the circle enclosing the spatial neighbourhood is chosen to be $6 \times \Delta x = 42\,\mathrm{km}$ in case of an isotropic neighbourhood. In the case of an anisotropic neighbourhood the area of the ellipse is approximately the same as the area of the isotropic neighbourhood.

Additionally, forecasts of neighbouring points in time are included in the sample. Thus, the neighbourhood also extends into the time dimension and the circle in Figure 7 is actually a sphere or an ellipsoid (not shown in Figure 7). Only forecasts on the full hours are taken into account. Currently, the temporal diameter of the neighbourhood is chosen to be 3 hours.

3.1.2 Deterministic Factors

In some cases the assumption (Section) obviously would not hold, if a circular neighbourhood was used or if the original LM forecast values directly served as the the grid point values within the neighbourhood. For example, imagine grid point A is located over the sea and a coastline runs through its neighbourhood. Then the temperature forecasts on grid points which are located over land are generally *not* representative of the temperature forecast on grid point A. A similar example is the dependence of the forecast on orographic height. The problem occurs whenever there are variables that

- are dynamically relevant and
- vary on a small spatial or temporal scale and
- are independent of the short-range forecast.

We refer to such variables as *deterministic factors*.

The disturbing influence of the deterministic factors has to be alleviated. This is done in several ways:

1. The shape of the spatial neighbourhood (Figure 7) is modified according to the orographic height. We allow the spatial neighbourhood to have the form of an ellipse. The shape of the ellipse minimizes the variance of orographic height within the neighbourhood. The centre of the ellipse is restricted to remain at grid point A and the area of the ellipse is forced to be the same as the area of the original circle.

2. We modify the forecasts in the neigbourhood with respect to the deterministic factors. For each neighbourhood a linear regression between forecast and orographic height is performed. Then the forecasts of the neighbourhood are linearly adjusted to the orographic height at grid point A.

3. The neighbourhood is cut off at coastlines. If grid point A is situated on land, then all grid points situated on the sea are excluded and vice versa.

4. For the statistical postprocessing of temperature the neighbourhood is cut off at boundaries of snow cover. If grid point A is covered by snow, then all grid points without snow are excluded and vice versa.

3.1.3 Quantile Estimator

The linearly modified forecasts within the elliptic neighbourhood serve as a random sample of the forecast at grid point A. Once we have generated a sample, we can estimate properties of its probability distribution function F.

We have decided to estimate the quantile function x. The quantile function x is a function of probability p. It is the inverse of the probability distribution function F. Hence, there is a probability p that the quantile $x(p)$ is greater than the correct forecast.

The estimation of the quantile function follows a method by Müller (1991). Müller (1991) proposes a non-parametric kernel quantile estimator. The calculation of the estimator is directly based on the sample. Moon and Lall (1994) present an application of this method.

3.2 Wavelet Method

The wavelet method assumes that small spatial scales of the forecast field are not deterministically predictable. Therefore, they must be removed from the forecast in order to achieve a more reliable forecast.

The LM model output is transformed with respect to a wavelet basis. Then all wavelet coefficients which belong to wavenumbers greater than a certain threshold value are set to zero. The threshold value may vary with location in space. Finally, the inverse wavelet transformation is carried out, so we get the grid point values of the postprocessed forecast field. For the wavelet transformation we use the *fast wavelet transform* by Sweldens (1996).

3.3 Example

An example of the statistical postprocessing via the neighbourhood method is presented. At each grid point the LM direct model output is transformed into a probabilistic forecast. We choose the forecast of heavy convective precipitation on July$^{\text{th}}$, 1994 (see Figure 3). The enlarged area in Figure 4 demonstrates the extreme spatial variability of the direct model output. It is unlikely indeed that the exact spatial location of these small-scale precipitation patterns can be predicted in a deterministic way.

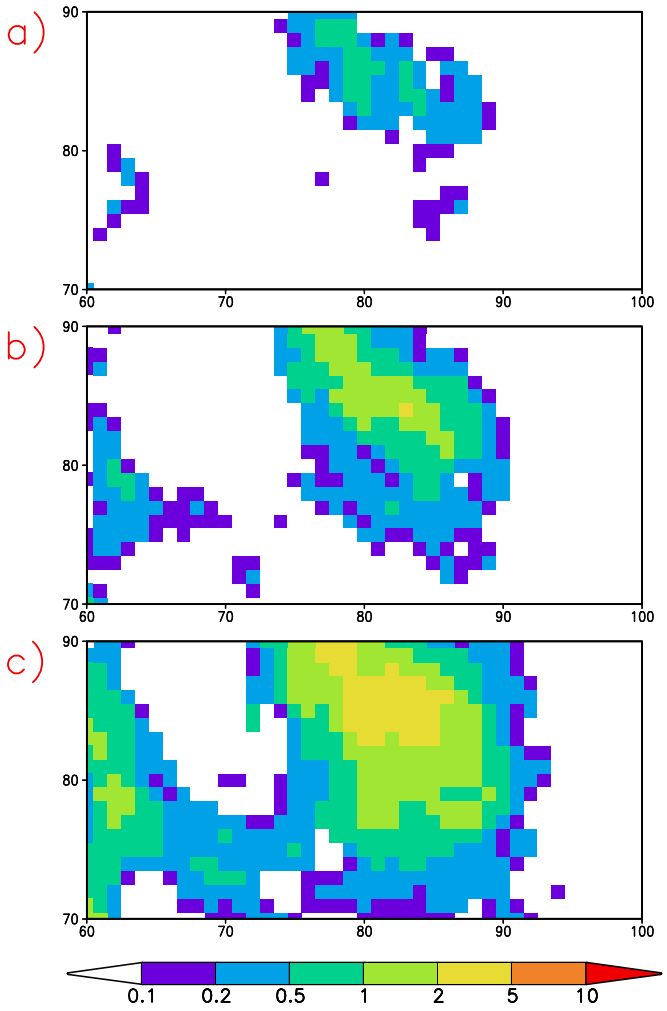

Figure 8: Result of the statistical postprocessing: Quantile estimates of the precipitation forecast shown in Figure 4. a) Quantiles for the probability $p = 0.25$. b) Quantiles for the probability $p = 0.5$. c) Quantiles for the probability $p = 0.75$. Unit: mm.

Figure 8 shows three quantile estimates that result from the statistical postprocessing of the precipitation forecast in Figure 4. The quantile estimators were calculated for the probabilities $p = 0.25$, $p = 0.5$ and $p = 0.75$, respectively. For example, at each grid point there is a probability of 25% that the correct forecast is less than the corresponding 0.25-quantile in Figure 8a. Similarly, there is a probability of 50% that the correct forecast is less than the quantile in Figure 8b and there is a probability of 75% that the correct forecast is less than the quantile in Figure 8c.

The quantiles must be interpreted for each gridbox individually. Note that the chances are far less than 25% that the correct precipitation forecast will fall below the corresponding 0.25-quantile (Figure 8a) at *all* grid points simultaneously. We expect the correct precipitation forecast to exceed the 0.25-quantile only at about 75% of the grid points. Similarly, at about half of the grid points the correct precipitation forecast will be less than the 0.75-quantile and greater than the 0.25-quantile.

The differences between the three quantiles in Figure 8 reflect the range of uncertainty associated with the prediction of small-scale patterns. We would like to emphasize, though, that the differences between the three quantiles do not necessarily predict the *overall* skill of the LM forecast. The quantiles are restricted by the assumption that the large-scale

precipitation forecast is perfect. For example, if the global model GME provides a wrong forecast at the lateral boundaries of the LM, then the resulting forecast errors of the LM will not become visible through the statistical postprocessing of the LM output.

4 Outlook

At present, pre-operational tests using the neighbourhood method are being conducted. This work mainly concentrates on the development of a procedure that will evaluate representative ("statistically smoothed") precipitation values.

Subjects of the ongoing development of the methods are - amongst others - the simultaneous, consistent treatment of several parameters, the derivation of probabilistic information by the wavelet method, and the calibration of both methods by comparing their results to those of a larger set of experimentally conducted ensemble forecasts.

References

Martano, P., 2000: Estimation of Surface Roughness Length and Displacement Height from Single-Level Sonic Anemometer Data. *J. Appl. Meteor*, 39, 708-715.

Moon, Y.-I. and U. Lall, 1994: Kernel quantile function estimator for flood frequency analysis, *Water Resour. Res.*, 30(11), 3095-3103.

Müller, H.-G., 1991: Smooth optimum kernel estimators near endpoints. *Biometrika*, 87(3), 521-530.

Sweldens, W., 1996: Wavelets and the lifting scheme: A five minute tour. *Z. Angew. Math. Mech.*, 76 (Suppl.2), 41-44.

First Results with COSMO–LEPS (Limited-area Ensemble Prediction System) During the MAP Season

Andrea Montani, Chiara Marsigli, Fabrizio Nerozzi and Tiziana Paccagnella

ARPA–SMR (Numerical Modelling Group), Bologna, Italy

1 Introduction and Methodology

The Ensemble approach allows to associate a probability of occurrence to meteorological events, providing further scope to quantitative precipitation forecasting. Current operational implementations of the Ensemble Prediction technique are currently based upon GCMs essentially covering the global scale. In the limited area model environment, it appears to be difficult to produce perturbations of the initial conditions which can efficiently grow for time ranges longer than 12–24 hours, depending on the size of the integration domain, possibly due to the driving/damping effects of the lateral boundary conditions. The natural approach to regionalize and adapt the global-scale EPS on the local scale should be to nest limited-area models in each EPS member. The obvious drawback of this procedure is connected to the large amount of computer resources required and to the intense data-flow necessary if the LAM integrations are not performed in the same centre where the EPS is produced.

At ARPA-SMR, the dynamical adaptation of the ECMWF EPS on the local scale through Limited Area Model nesting, is founded on an ensemble reduction technique where only few members of the entire global ensemble are selected to drive LAM integrations (Marsigli et al., 2001; Molteni et al., 2001; Montani et al., 2001). The reduction procedure is carried on by performing, on a restricted area (53-35N; 5W-25E), an independent cluster analysis of the 51 EPS members by a complete linkage method, where clustering is based on dynamic and thermodynamic fields in the lower-to-middle troposphere. The number of clusters is fixed to 5. A Representative Member (RM) for each of the 5 clusters is then defined by selecting the cluster member with the minimum distance from the other members of the same cluster and the maximum distance from all the remaining EPS members. These 5 RMs provide initial and boundary conditions for 5 LAM integrations up to three-to-five days ahead. The 5 individual LAM integrations generate a high–resolution **L**imited–area **E**nsemble **P**rediction **S**ystem (**LEPS**) and are used to compute a–priory probability of occurrence of meteorological events of interest, e.g. the exceeding of a given accumulated precipitation threshold, by combining them with weights proportional to the population of the cluster they represent.

Another practically important feature of the ARPA-SMR methodology is the use of the concept of "super-ensemble". Rather than using only one ECMWF EPS set, more (up to three) consecutive daily EPS sets, progressively lagged in time, are used, providing initial sets of up to 153 individual members (see fig. 1 in case of two lagged ensembles). From preliminary evaluations, the use of the super-ensemble technique increases the reliability of the computed a-priory probability of occurrence of the predicted event (surpassing of a precipitation threshold). In the first part of the experimentation, the limited area model employed was LAMBO (Limited Area Model BOlogna), the hydrostatic limited-area model in operational use at ARPA-SMR. LAMBO is based on the NCEP ETA model and has an operational horizontal resolution of 10 or 20 km with 32 vertical levels. Since the beginning

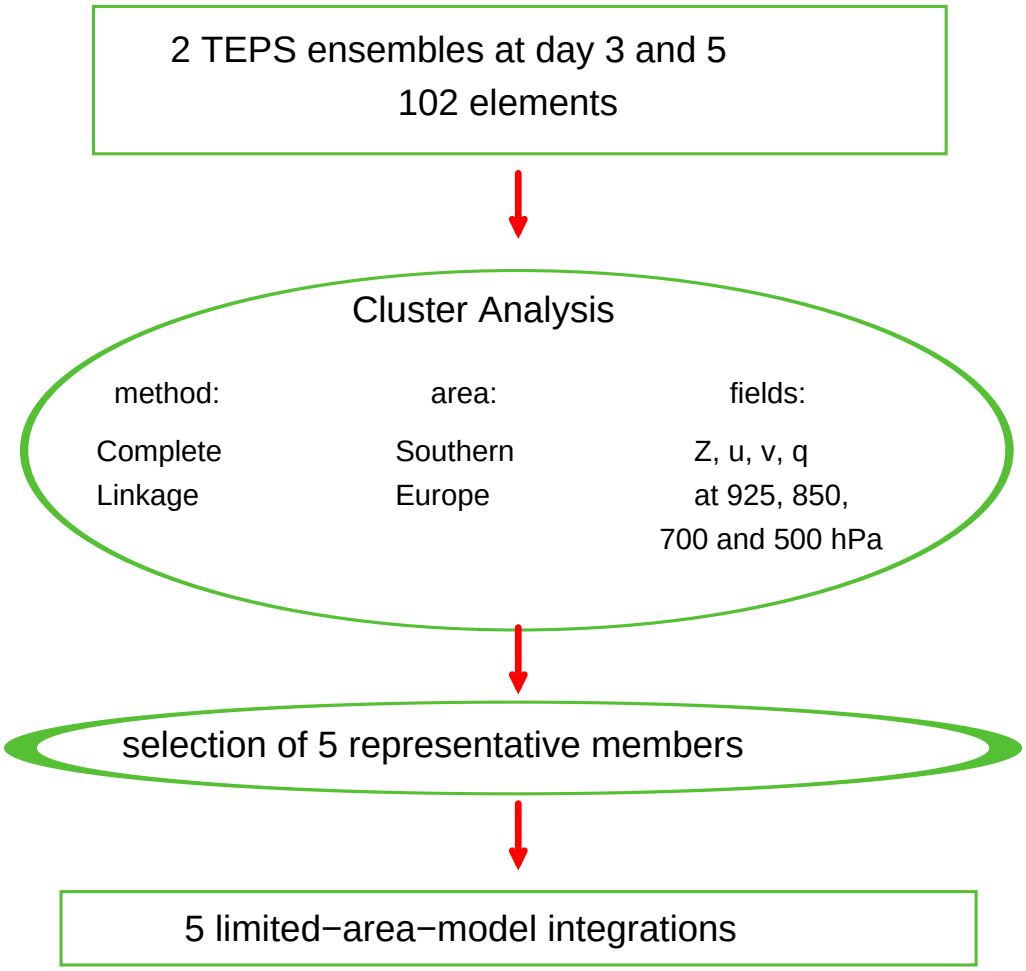

Figure 1: Super–ensemble methodology with two lagged ensembles.

of 2001, the first "COSMO–LEPS" experiments have been performed, using Lokal Model (LM) at the horizontal resolution of 14 km and with 32 vertical levels.

The LEPS technique is under evaluation on a set of individual case studies of severe precipitation events in Europe so as to improve short to medium–range probabilistic forecasts of localised weather events. A systematic statistical verification of LEPS performance is also ongoing for the period Sept–Oct–Nov 1999, during which special observational data-set are available in correspondence of the Special Observing Period of the MAP Programme. For this period, LEPS is integrated using the Targeted Ensemble Prediction System (T_L159 L40, $\Delta x \simeq 120$ km), developed at ECMWF mainly by KNMI (Hersbach et al., 2000) with the aim to enhance the ensemble spread over Europe in the short and early medium range.

2 Case study: MAP IOP 8 (Alpine region)

As an example, the performance of LEPS system is assessed for the precipitation event of IOP 8, during the MAP season. Fig. 2 shows the amount of precipitation observed over the 24–hour period ending at 6 UTC of 21 October 1999. High values of precipitation were recorded over Corsica and, especially, over Southern France, with peaks above 200 mm/day at about 45N 4E. This caused local floods and widespread damages.

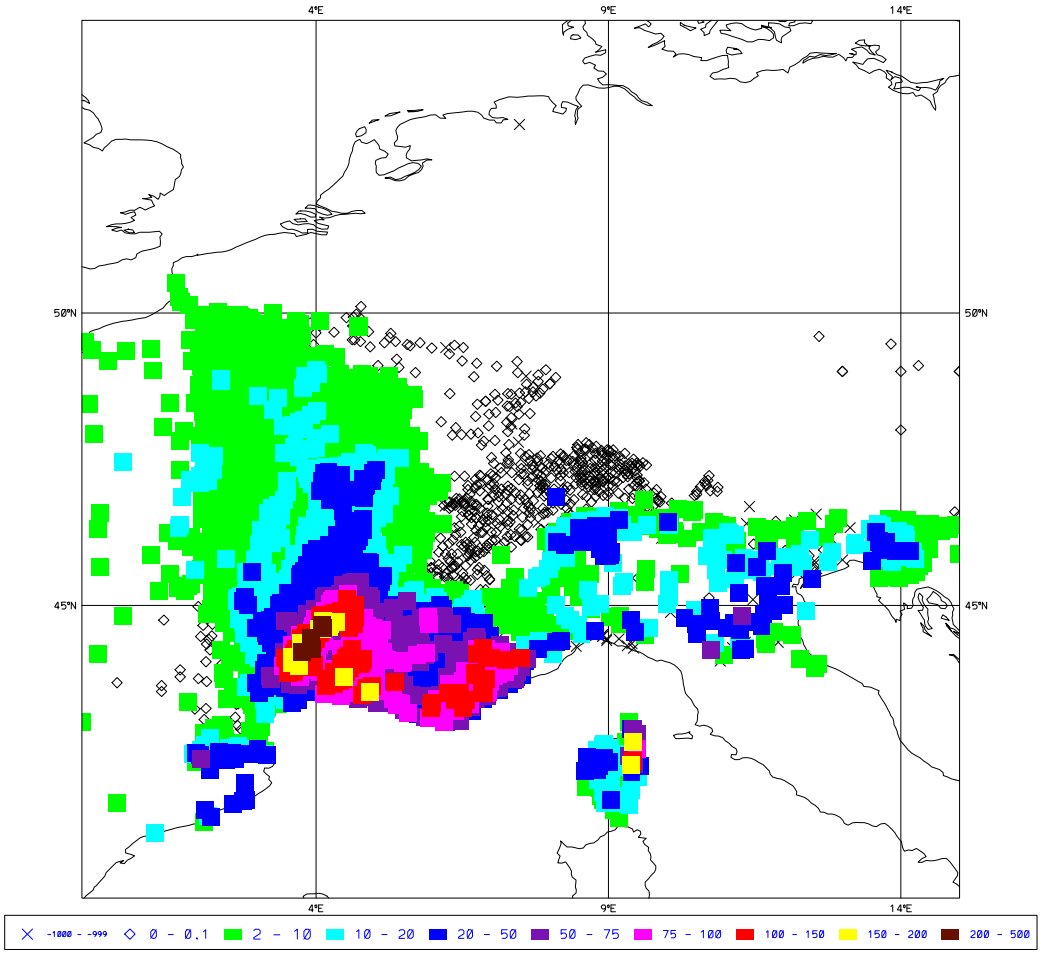

Figure 2: Observed rainfall over the 24–hour period ending at 6UTC 21/10/1999

The performance of ECMWF global ensemble for this event is not particularly satisfactory: the rainfall probability maps for precipitation exceeding 20 and 50 mm/day (left and right panel of the fig.3 , respectively) show that, according to the 66–hour forecast, the regions most likely to be affected by precipitation are partly misplaced to the west (in comparison with the observations of fig. 2). In addition to this, the amount of precipitation is highly underestimated: the probability of rainfall exceeding 50 mm is about 24% (and in the wrong area) and the probability at higher thresholds is below 10%. Therefore, there is no indication of a heavy precipitation event in any of ECMWF ensemble forecasts (at least for this range).

On the other hand, the performance of the LEPS is much more accurate. Thanks to the higher horizontal resolution, mesoscale and orographic–related processes are better resolved and, despite the small ensemble size, the quality of the probabilistic products is very good. Once the 5 RMs are selected within the 5–day and 3–day ECMWF ensembles and used to provide initial and boundary conditions to 5 LM integrations, the so–generated high–resolution ensemble provides better results. Fig. 4 shows the rainfall probability maps for precipitation exceeding 20, 50, 100 and 150 mm/day. It can be noticed that the regions most likely to be affected by heavy precipitation are very close to those where the rainfall peaks are observed (as in fig. 2). The bottom–right panel of the figure shows a probability of about 60% for 24–hour rainfall exceeding 150 mm. Therefore, the possibility of a flood event is clearly highlighted by the LEPS forecast. Since this type of information could be available 66 hours before the weather event, it would be possible to issue flood warning so as to alert the local population and maybe mitigate the flood consequences.

ECMWF PROBABILITY MAPS ($\Delta x \simeq 120$ km)

RAINFALL > 20 mm

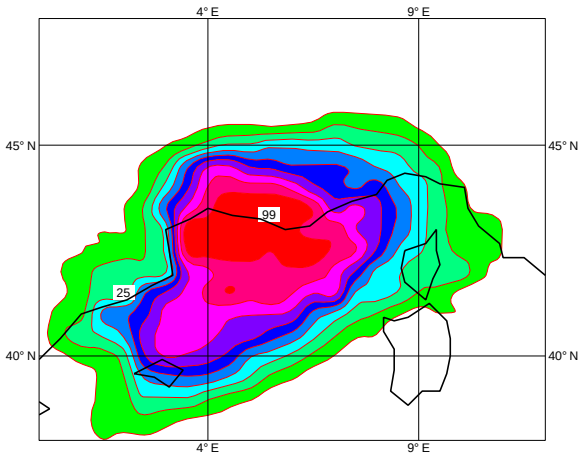

RAINFALL > 50 mm

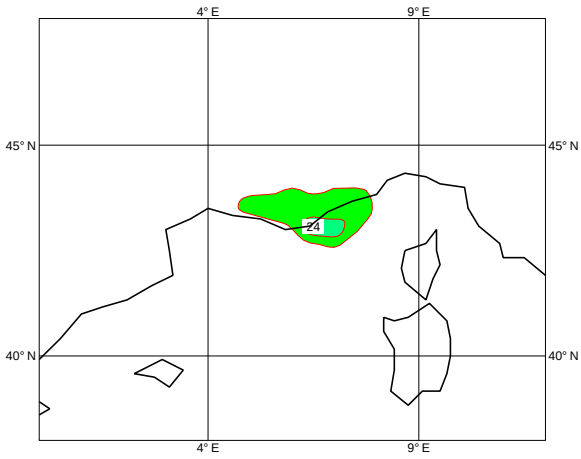

Figure 3: TEPS rainfall probability maps (66–hour forecast: VT: 21/10/1999, 6UTC).

LM PROBABILITY MAPS ($\Delta x \simeq 14$ km)

RAINFALL > 20 mm

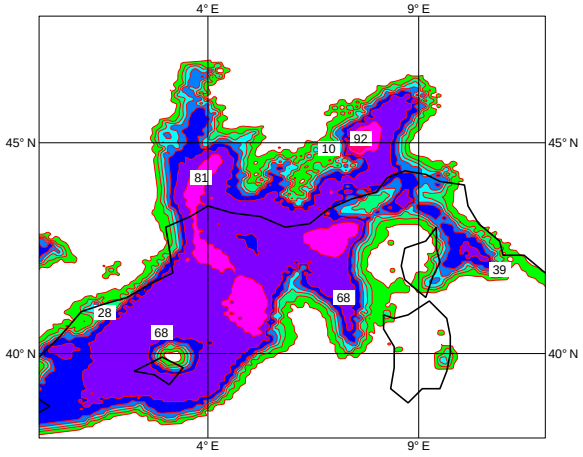

RAINFALL > 50 mm

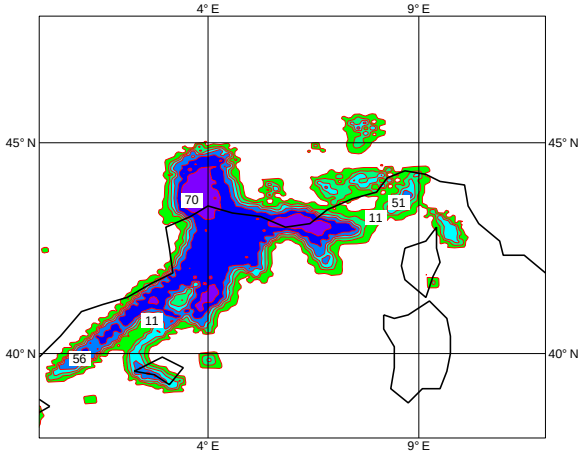

RAINFALL > 100 mm

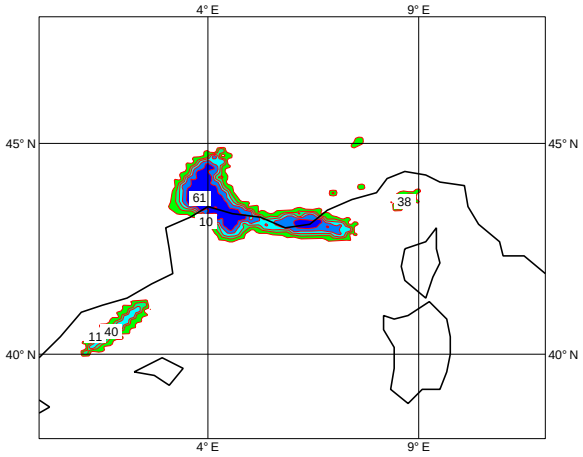

RAINFALL > 150 mm

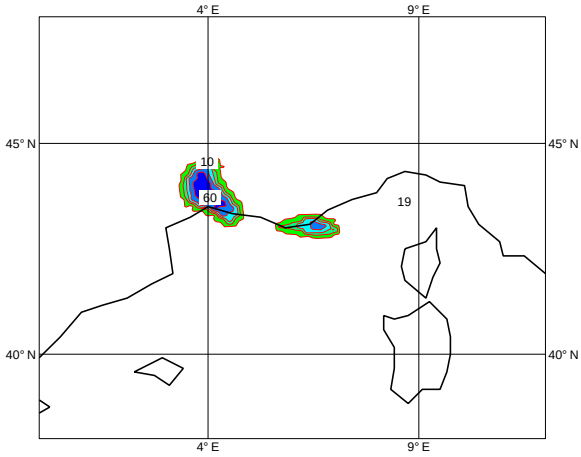

Figure 4: LM rainfall probability maps (66–hour forecast; VT: 21/10/1999, 6UTC).

3 Preliminary Conclusions

For this case study, the performance of LEPS has been shown to be more accurate than the global–model TEPS. The possibility of a flood event is clearly highlighted by LM integrations and the probability maps could be of great assistance to a hypothetical forecaster to issue flood alerts. Similar results have been obtained in other cases of heavy precipitation over localised area, this showing the benefits of running a high–resolution limited–area ensemble. The verification of COSMO–LEPS performance during MAP 1999 is still ongoing, but the preliminary results are encouraging. The feasibility of COSMO–LEPS on an operational basis at ECMWF (possibly on VPP5000) is being tested and it is hoped to implement LEPS system during 2002 over a super–domain which includes all the countries involved in COSMO.

5 References

Hersbach, H., Mureau, R., Opsteegh, J. D. and Barkmeijer, J., 2000: A short–range to early–medium–range Ensemble Prediction System for the European Area. *Mon. Wea. Rev.*, 128, 3501–3519.

Marsigli, C., Montani, A., Nerozzi, F., Paccagnella, T., Tibaldi, S., Molteni, F. and Buizza, R., 2001: A strategy for high–resolution ensemble prediction. Part II: limited–area experiments in four Alpine flood events. *Quart. J. Roy. Meteor. Soc.*, 127, 2095–2115.

Molteni, F., Buizza, R., Marsigli, C., Montani, A., Nerozzi, F. and Paccagnella, T., 2001: A strategy for high–resolution ensemble prediction. Part I: definition of representative members and global–model experiments. *Quart. J. Roy. Meteor. Soc.*, 127, 2069–2094.

Montani, A., Marsigli, C., Nerozzi, F., Paccagnella, T. and Buizza, R., 2001: Performance of the ARPA–SMR limited–area ensemble prediction system: two flood cases. *Nonlin. Proc. Geophys.*, 8, 387–399.

Comparison of Model and Radar Precipitation Fields Using a Simple Pattern Matching Method

Andrea M. Rossa

MeteoSwiss, Krähbühlstrasse 58, 8044 Zürich, Switzerland

Abstract

A complementary approach to traditional methods for precipitation verification of mesoscale model forecasts is presented that makes use of composited radar-observed precipitation estimates over Switzerland. A simple pattern matching technique is applied to search for radar-observed precipitation patterns in the model-predicted field. The aim of the method is to detect systematic position errors and to judge the model's capability of producing realistic structures. In particular, this approach is helpful in dealing with the double penalty problem traditional verification methods are faced with.

For this study an evaluation of one year of 24 hourly precipitation accumulations from 1 March 1998 to 28 February 1999 has been performed. Distinct systematic position errors have been found in the Swiss Model, operational NWP model of the Swiss national weather service, for frontal cases approaching Switzerland from the west and northwest. The model has a tendency to shift precipitation patterns onto the Alpine topography, as well as to position them to the west of the observed patterns.

1 Introduction

The systematic validation of mesoscale numerical weather prediction (NWP) models, particularly with respect to precipitation, is acknowledged to be an important and necessary step to improve the model's performance. One difficulty emerges from the gap between the density of traditionally used rain gauge observations and the simulated model data. Radars, on the other hand, offer precipitation estimates with high spatial resolution and have not yet been widely used for operational NWP model verification. Today, the European operational radar networks consist of well over a hundred radars – many of them with Doppler capabilities, a few of them polarimetric – and provide a unique basis for the use of radar information (Collier 2001). The COST-717 Action 'Use of radar observations in hydrological and NWP models' (Rossa 2000) seeks to exploit these data for operational application.

Radar data are, however, increasingly used for NWP verification and validation for research purposes, e.g. for subjective comparisons of precipitation structures (e.g. Yu et al. 1998, Keil and Volkert 2000). Goeber and Wilson (2001) use radar data to perform categorical statistics on every model gridpoint where radar data are available.

Traditional verification methods that rely on pairs of single observation and model gridpoint values are faced with the double penalty problem (Fig. 1). An attempt of a high-resolution model to forecast small-scale structures, when misplaced on the scale of its dimensions, is penalized in terms of higher root mean square errors and lower correlation values. A null forecast, therefore, which does not contain any information about the structure at all, is judged a better performance. Anthes (1983) noted that a more significant statement on the model's quality could be made when taking into account displacements of coherent precipitation structures in a model simulation with respect to observations. Hoffman et al. (1995) decomposed forecast errors into three components, i.e. into a displacement, amplitude, and

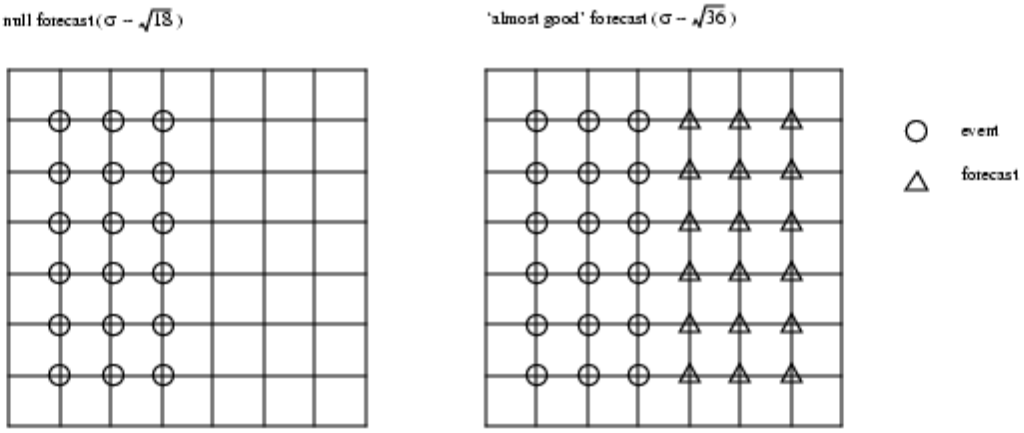

Figure 1: Illustration of the double penalty problem in verifying high-resolution NWP models. The variance is lower for a null forecast containing no information on the event than to an 'almost good' forecast with a positional error, which contains information on the event that is useful to the forecaster but degrades the statistical performance of the model.

structural error. Recently, Ebert and McBride (2000) made a comprehensive study on entity-based precipitation verification making use of this decomposition. The method is applied for precipitation as derived from gauges and radars to four years of model output of the Australian regional model.

In this paper we present a systematic comparison between simulated precipitation fields of the former operational NWP model of the Swiss National Weather Service MeteoSwiss, the Swiss Model (SM), and estimates of the Swiss radar network (SRN, Joss et al. 1998).

In Section 2 the description of the data set and methodology is given, while in Section 3 first results are presented. A summary and outlook on future work is provided in the final Section 4.

2 Data Sets and Methodology

i) Data set: Swiss Radar Network (SRN) and Swiss Model (SM)

For the present study 24 hour precipitation sums from 06 UTC to 06 UTC of the consecutive day as derived from estimates of the Swiss radar network and predictions of the Swiss Model are compared for frontal cases within the period 1 March 1998 to 28 February 1999. The selection of the days with frontal precipitation was done subjectively and based on the radar observations.

The SM, the former operational NWP model of MeteoSwiss, is a hydrostatic limited area model run at a horizontal resolution of 14 km with 20 vertical levels (see f.i. Majewski 1991 for more details). SM total precipitation sums of the operational 00 UTC integrations are taken for the forecast range +06 h to +30 h for every grid point.

MeteoSwiss-operated SRN is a third generation radar network consisting of three C-band Doppler radars of the same type, that provide full volume information every 5 minutes. The data are preprocessed and available on a Cartesian grid with a resolution of 1x1x1 km^3 for single radar sites and 2x2x1 km^3 for the network composite (Joss et al. 1998). The precipitation estimates are taken from the maximum reflectivity projection product. For the purpose of comparison 24-hour sums have been averaged and interpolated onto the model grid with a mesh size of 14 x 14 km^2.

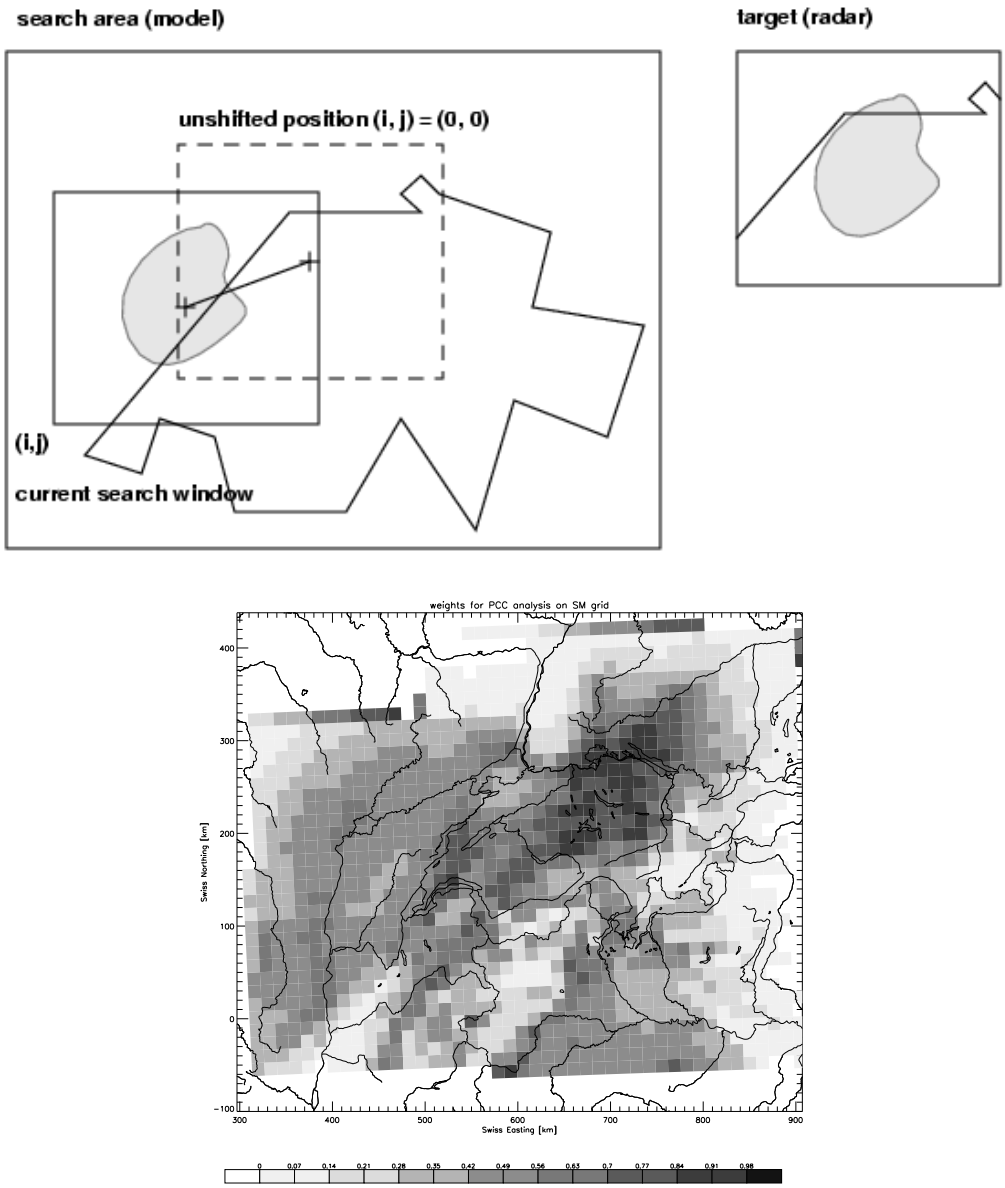

Figure 2: The pattern correlation coefficient (PCC) method is based on a field of correlation values of a target and a corresponding window in the search area (top panel). The calculation of the correlation has been modified using the weights shown in the lower panel.

ii) Pattern Matching Method

To tackle the double penalty problem referred to in the introduction section it appears unavoidable to use some sort of pattern matching and perhaps a pattern identification technique. For the present study a simple correlation technique has been chosen following an application in satellite meteorology to derive cloud motion vectors (Schmetz and Nuret 1987). This technique is referred to as pattern correlation coefficient (PCC) method in the following. The method is illustrated in Fig. 2. A correlation value is calculated for each position, or displacement, of the target within the search area, yielding a PCC field, which then is analysed. Thereby the rain is assumed to follow an approximate log-normal distribution and, hence, a transformation $r \rightarrow a \cdot \log(1 + r)$ into 16 classes has been applied to the precipitation intensities in order to calculate the correlation. The PCC analysis is insensitive to the absolute value of the fields and can be used as independent measure to judge position and structure of a forecast. The fixed target for this study has subjectively been chosen to

cover northwestern Switzerland, an area which is frequently exposed to frontal systems that are associated with Atlantic disturbances.

The quality of radar data can be highly variable, particularly in complex terrain, where the radar beam is shielded by mountain ranges, that prevent it to observe precipitation near the ground. The same is true, independently of orography, at long ranges from the radar. In order to limit the influence of pixels with scarce visibility a static weight is introduced into the calculation of the correlation field defined as:

$$w(\vec{x}) = e^{-z(\vec{x})/H} \tag{1}$$

where z denotes the minimum visibility height above ground of a pixel and H a scale height chosen as 2000 m (Rossa et al. 1998). Accordingly, the correlation fields have been modified to:

$$CC(p_r, p_m) \rightarrow PCC(\sqrt{w}/\sqrt{\|w\|}p_r, \sqrt{w}/\sqrt{\|w\|}p_m) \tag{2}$$

where the norm of $\|w\|$ is used to normalize the weights; the multiplication is pixelwise. The lower right panel in Fig. 2 shows the geographical distribution of the weights, exhibiting two major blind spots of the SRN in southern and eastern Switzerland.

iii) Interpretation of the PCC Field

In the case of tracking features in time, as done in determining cloud motion vectors, for instance, the patterns to be matched are relatively similar provided the time differences used for the tracking are small compared to the feature's life time. The search radius in space can hence be limited by the maximum possible displacement of the tracked feature. Therefore, the resulting PCC field is often relatively smooth yielding a distinct single maximum, whose position uniquely determines the displacement vector.

Our purpose, however, is to compare two precipitation fields of different origin which can be rather dissimilar. Also, there is no physical measure to limit the search area. This time, the resulting PCC field can be very complex and difficult to interpret, in that it does not necessarily feature high correlation values, and can exhibit several relative maxima which may or may not be connected with a sensible matching of the precipitation patterns.

As a first approach to interpreting the PCC fields all relative maxima with a value greater or equal than 80 % of the maximum correlation value achieved were selected in order to catch several possible 'good' matches. 'Bad' matches with high correlation values, i.e. matches that happen between unrelated precipitation systems (e.g. Fig. 4 upper panels), are not filtered at present so that they may contaminate the method. However, when selecting frontal cases with a clear and coherent signal the 'good' matches appear to dominate.

Traditional verification is based on pairs of single observation and model gridpoint values and measures only amplitude errors. More generally, the quality of a model precipitation forecast can be judged by the three parameters describing its amplitude as measured by intensity, shape as measured by the correlation value, and position, as measured by the displacement vector (Hoffman et al. 1995). The PCC method offers a handle on the parameters of shape and position. Figure 3 illustrates schematically one possibility of how these measures can be represented for a large numbers of events in terms of a histogram of the displacements merged with an average correlation value. If, like in panel (a), the displacement histogram shows a peak in the origin, i.e. for no displacement, and features a high correlation value, this means that the model produces correct structures at the correct location. In panel (b) the model would produce correct structures which are, however, systematically placed in a wrong position. Generally low correlation values indicate the model's inability to produce realistic structures, for which then it is not very helpful to define a displacement (panel c).

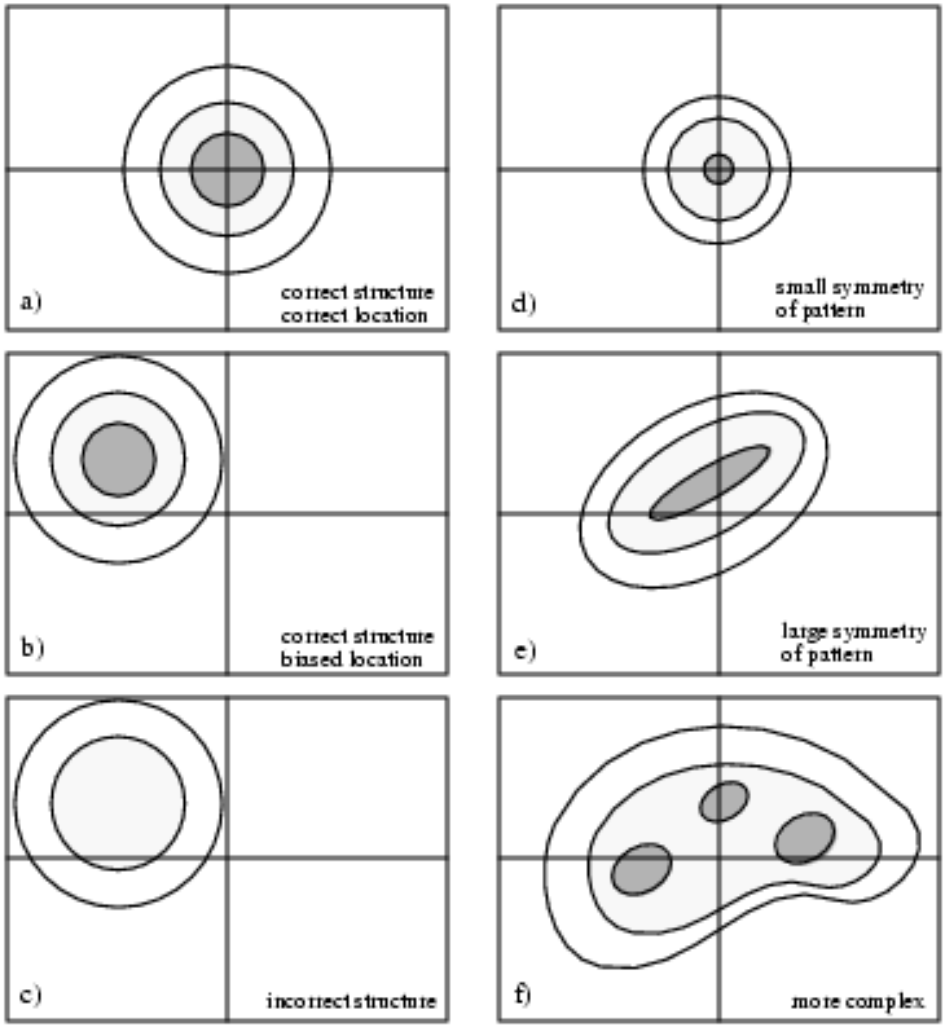

Figure 3: Possible measures of forecast quality. The schematic fields denote some measure of average correlation as a function of the displacement vectors. Similarly, they can be viewed as histograms of the displacements. For explanation see text.

A sharp correlation peak in the histogram, as shown in panel (d) denotes a small symmetry of the structures, whereas panel (e) indicates some symmetry in the patterns along the ridge of high correlation values. Panel (f), finally, is an example of a more complex situation. This analysis, applied to our data set, is presented in Fig. 6.

3 First Results

In Fig. 4 the method's performance is displayed for a selection of three single days, which can be considered typical cases of moderate to intense frontal precipitation events. For these cases the PCC fields are relatively smooth, and exhibit some sort of ridge with relatively high correlation values which reflects the symmetry of the frontal precipitation system. The position of the respective correlation maximum defines a displacement vector that describes the likely position error of the model precipitation prediction. With the exception of the case of 27 May 1998, all the relative maxima lie on a ridge. The positive subjective judgement of the model performance for these cases by a bench forecaster helps to interpret the absolute correlation values of larger than 0.7 as 'quite good' quality. Note that for the case of 28

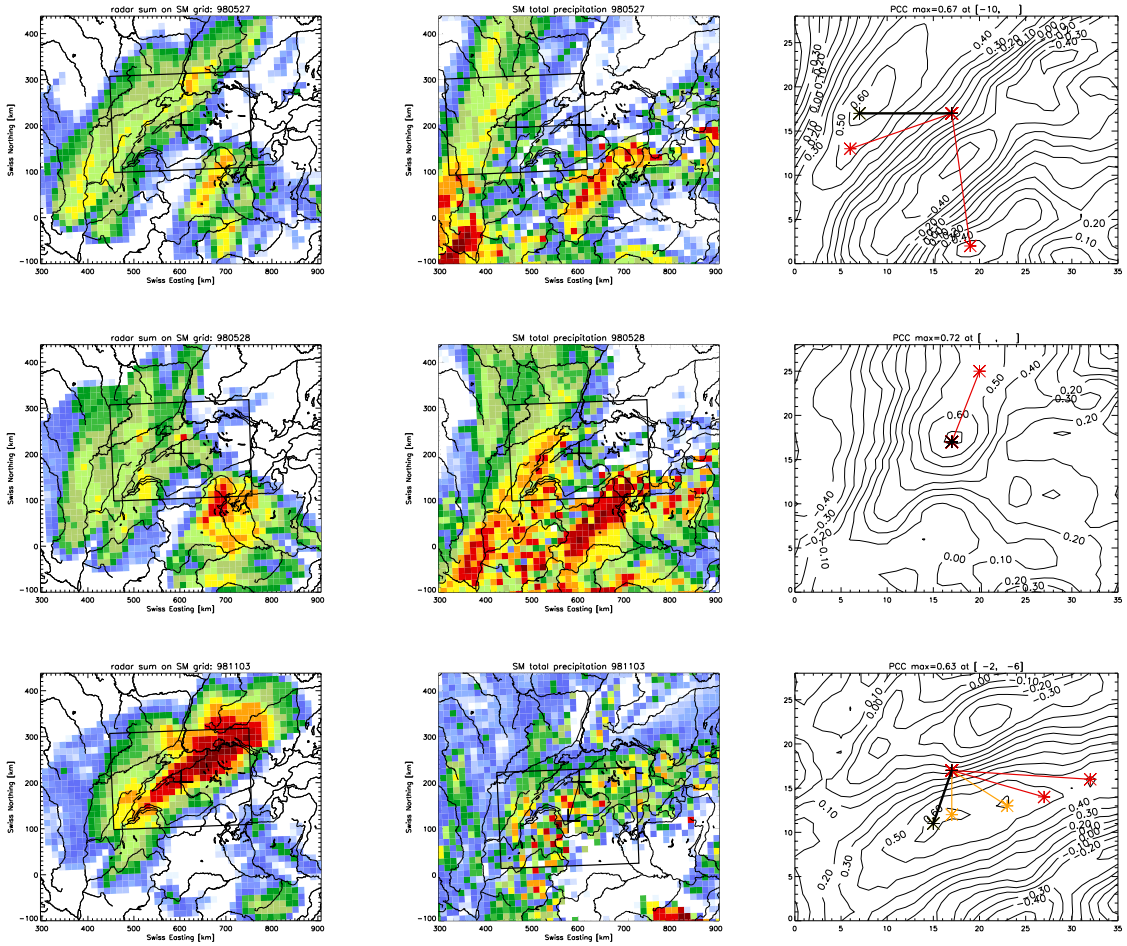

Figure 4: Upper, middle, and lower row show 24 h precipitation sums starting from 27, 28 May and 3 Nov 1998 06 UTC, respectively, for the SM (left column) and the SRN (middle column). Shading values are 1, 1.6, 2.5, 4, 6.3, 10, 16, 25, 40, 63, 100, and 160 mm). The right column displays the PPC fields, including the displacement vectors to the all the relative correlation maxima (coloured lines) that are greater or equal than 80 % the maximum correlation value (black line). The rectangles in the left column denote the fixed target in the radar field, whereas in the middle column they highlight the position corresponding to the highest correlation value.

May 1998 the maximum correlation occurs at the unshifted location. Maximum correlation values drop substantially when the precipitation field becomes less coherent and intense (not shown).

For a systematic comparison it is necessary to evaluate a large number of days. The most obvious representation is to overlay the displacement vectors obtained for each day in one single plot (Fig. 5 a). An alternative is to draw the displacement vectors of the centres of gravity of the respective precipitation fields (Fig. 5 b). The advantage of the latter is that the displacements are more closely related to the precipitation structures as opposed to the fixed target window. With the underlying model topography it is possible to recognize locations of preferred model position errors as, for instance, the Alpine crest. It shows the model's tendency to produce precipitation events preferably on the orography and is consistent with the well known difficulty of capturing structures that are limited to the Swiss Plateau. Also, there is a tendency for the model to position the frontal precipitation in a sector to the southwest to northwest.

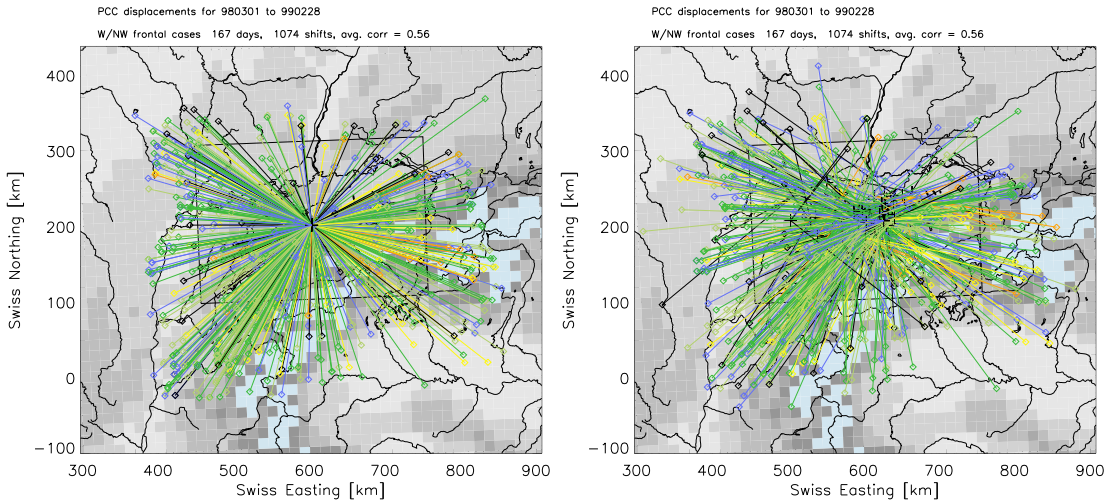

Figure 5: Overlay of displacement vectors for 167 days of north/northwest frontal precipitation in the target area (solid rectangle). The underlying greyscales denote the SM model orography, the color coding of the vectors the corresponding correlation value (black and blue vectors for high correlation value, yellow and red for low values). In panel (a) the displacements are drawn from the centre of the target to the centre of the shifted rectangle, whereas in panel (b) the displacements are drawn from the respective centres of gravity of the radar and model precipitation fields. There are a total of 679 vectors in the plots with an average correlation value of 0.56.

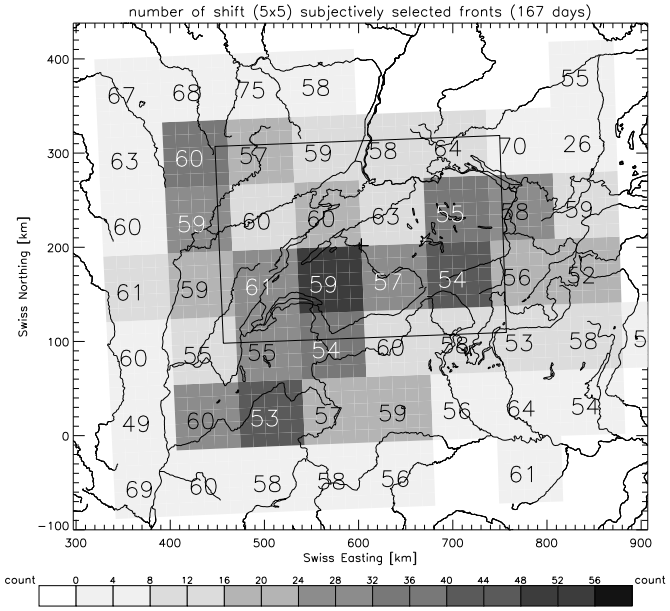

Figure 6: Histogram of the displacement vectors for the 167 cases of frontal precipitation. The shading denotes the number of shifts into a class, which is made up of 5x5 meshes of the SM. The numbers denote the corresponding average correlation values in %.

Yet another, simpler, representation of this analysis, as described in Section 2 (Fig. 3) is obtained using a two dimensional histogram based on the displacements and merged with a measure for the correlation of the members of each class (Fig. 6). It can be seen quite clearly that the model has a tendency to misplace precipitation onto the Alpine topography and to the west northwest. The correlation values are relatively uniform, with somewhat lower values for displacements onto the topography. This is consistent with the fact that the model precipitation pattern is substantially modulated by the underlying topography.

4 Summary, Discussion, and Outlook

A method was proposed for verification of model precipitation forecasts with radar observations. A simple pattern matching technique was used to identify systematic position errors in the model forecasts for one year of data. For the period of 1 March 1998 to 28 February, 167 cases of frontal precipitation associated with Atlantic disturbances systems approaching Switzerland and the Alps from the west were selected. It was found that for these cases the SM has a tendency to place precipitation onto the Alpine topography, as well as to misplace precipitation to the west north west.

Using one fixed target for the pattern matching algorithm is a limitation of this study, as it does not focus on meteorological entities. On the other hand it does focus on a target region of interest for the duty forecasters in Switzerland. The SRN composite is relatively small on the scale of the SM domain as well as on that of synoptic-scale weather, so that it would be highly desirable to include radars into a larger composite. The method will be further developed to include:

- a filter for discarding 'bad' displacement vectors suggested by the pattern matching;
- alternative pattern matching method(s), e.g. minimum total squared error instead of maximum correlation, as suggested by Ebert and McBride (2000);
- multiple target areas, to capture the model's performance in flow regimes that are frequent and important for Switzerland and the Alps;
- targets automatically adapted to precipitation structures.

Acknowledgments

The author gratefully acknowledges the patience and expertise of Drs Jürg Joss and Urs German for direction on the careful use the radar observations. Thanks are due to Dr Peter Binder for his encouraging advice, and Dr Marco Arpagaus for fruitful discussions, and his helpful comments on the manuscript.

5 References

Anthes, R. A., 1983. Regional Models of the Atmosphere in Middle Latitudes. *Mon. Wea. Rev.*, 111, 1306-1335.

Collier, C. G. (Ed.), 2001. COST Action 75. Advanced weather radar systems, Final report of the Management Committee. *Commission of the European Communities*, ISBN 92-828-6712-9, 326pp.

Ebert, E. E., and J. L. McBride, 2000. Verification of precipitation in weather systems: determination of systematic errors. *J. Hydrol.*, 239, 179-202.

Goeber, M. and S. Milton, 2001. On the Use of Radar data to verifiy the long term performance of the UK Met Office Mesoscale Model forecasts. AMS NWP Conference 2001.

Joss, J., B. Schaedler, G. Galli, R. Cavalli, M. Boscacci, E. Held, G. Della Bruna, G. Kappenberger, V. Nespor, and R. Spiess, 1998. Operational use of radar for precipitation measurements in Switzerland, Final Report of NRP 31. vdf Hochschulverlag an der ETH Zurich, 108 pp., ISBN 3 7281 2501 6, http://vdf.ethz.ch.

Hoffman, R. N., Z. Liu, J.-F. Louis, and C. Grassoti, 1995. Distortion Representation of Forecast Errors. *Mon. Wea. Rev.*, 123, 2758-2770.

Keil, C., and H. Volkert, 2000. Precipitation in the northern Alpine region: Case-study-type validation of an operational forecast model. *Meteorol. Atmos. Phys.*, 72, 161-173.

Majewski, D., 1991. The Europa model of the Deutscher Wetterdienst. *Proc. ECMWF Seminar on numerical methods in atmospheric models*, Vol II, 147-191.

Rossa, A. M., F. Schubiger, and P. Binder, 1998. Towards a more comprehensive verification of high-resolution NWP precipitation fields using radar data. *MAP newsletter*, 9, 82-83, available at MeteoSwiss or at http://www.map.ethz.ch.

Rossa, A. M., 2000. COST-717. Use of radar observations in hydrological and NWP models. *Physics and Chemistry of the Earth, Part B*, 10-12, 1221-1224.

Schmetz, J., and M. Nuret, 1987. Automatic tracking of high-level clouds in METEOSAT infrared images with a radiance windowing technique. *ESA Journal*, 11, 275-286.

Yu, W., C. A. Lin, R. Benoit, and I. Zawadzki, 1998. High resolution model simulation of precipitation and evaluation with Doppler radar observation. *Wat. Sci. Tech.*, 37, 179-186.

High Resolution Verification of Hydrostatic and Non-Hydrostatic LAM Precipitation Forecasts in Italy

Carlo Cacciamani[1] , Patrizio Emiliani[2], Massimo Ferri[2] and Enrico Minguzzi[3]

[1] *ARPA-SMR, Bologna, Italy*

[2] *UGM, National Weather Service, Rome, Italy*

[3] *Regione Piemonte, Torino, Italy*

1 Abstract

High resolution Quantitative Precipitation Forecast (QPF) obtained by hydrostatic LAMBO model, the non hydrostatic Lokal Model (LM, used in the framework of the COSMO Consortium between Germany, Switzerland, Italy and Greece), both of them used at ARPA-SMR in Bologna and finally the HRM model, routinely used at UGM (Rome, Italy) have been verified against the network of GTS stations (Synop reports) covering the territory of Italy. ECMWF QPF have been also used to compare LAM results. Standard schemes of precipitation verification, based essentially on the evaluation of contingence tables for different precipitation thresholds, from which it is possible to deduce verification indices like Probability of Detection (POD), False Alarm Rate (FAR), Threat score (TS) etc.. have been used. These QPF verification procedure are based on the direct comparison between the couples of observed precipitation at the station points and the nearest LAM- predicted grid point values.

Furthermore, a study based on the verification of the precipitation forecasts of LM, (the version operationally produced by DWD, hereafter named DWD-LM), have been carried on using the ITAMAP data set, constituted by the hourly observations of the non-GTS stations available in Northern Italy, belonging to different regional weather services, which have been made available during the MAP (Mesoscale Alpine Programme) field phase (September-November 1999). The availability of this high dense network of non-GTS stations allowed us to study the sensitivity of the QPF verification results to different station density. It was also tested the impact on the QPF verification scores of different spatial averaging procedures applied to the predicted and observed precipitation, within grid box of different size included in Northern Italy.

As a second exercise, the high resolution precipitation forecast operational produced by DWD-LM have been verified using the raingauge networks belonging to several administrative regions of Northern Italy. In particular in the Piedmont region, located in the north-western part of the Po Valley, a very dense network of raingauges is available and makes possible a high resolution verification of precipitation. In addition to the standard verification procedure mentioned before, a "river catchment" verification have been performed over this region. The observed and predicted precipitation were averaged over each of the 10 sub-domains and then contingency tables were built, considering each averaged value as a single super-observation; these "averaged" values are of crucial importance for hydrological forecasts based, for example, on the application of rainfall-runoff model.

The study shows that higher resolution models are able to produce realistic precipitation patterns but it is also necessary to apply some spatial filter (i.e. spatial averaging) to

the predicted values in order to have a better and sensible utility of the LAM output. A straightforward and direct use of the QPF produced by LAM is of questionable application because of the high variability, in time and space, of the LAM precipitation patterns. Small errors in positioning in time and/or in space, of the precipitation structures, produce big errors in terms of the common-used verification scores (POD or TS for example).

2 Introduction

The verification of the quality of high resolution (5-10 Km.) Quantitative Precipitation Forecast (hereafter QPF) produced by Limited Area Models (LAMs), is one of the major task of any weather service that uses numerical models for operational forecasting purposes. One of the main problem arising in this activity is the general inadequacy of the observing network used to control the quality of the LAM products. The density of GTS stations is in fact generally too low and therefore small scale structures produced by LAM, sometime showing high amplitude meteorological values, cannot be properly verified. A big improvement of the observing capabilities comes out by the new radar platforms, which are more and more available and operative in many countries. On the other side, the problem to deduce precipitation from radar reflectivity is not easy and now not completely solved up to now.

As a second problem, the use of common verification indices, to evaluate the quality of the LAM simulations, may be not completely satisfactory when the resolution of the models increases. In general, LAM are able to produce small scale features, often of large amplitude, as they are observed in the real atmosphere. The problem is that quite always these features are not well displaced in space and/or in time and, therefore, large errors arise when common verification indices (ex.: mean error, root mean errors, hit or false alarm rates) are used to quantify the accuracy of the LAM simulations. This problem is particularly true for QPF; precipitation is in fact a very high variable (in time and space) parameter showing sometime a very complex spatial pattern. New methods to investigate the quality of QPF LAM simulations should probably be used, in order to minimise these problems and to allow a better judge of the quality of high resolution LAM. A direct use of these scores probably penalises high resolution LAMs with respect to coarser LAM (or even GCMs) which produce smoother fields.

In this paper we will discuss the results obtained in the verification of QPF produced by different LAMs used in Italy. As regards the hydrostatic LAM, we have taken into account LAMBO model, that is operationally used at ARPA-SMR, and the HRM model (an italian version of the hydrostatic LAM used in the recent past at DWD), used at the Italian Meteorological Office of the Military Air Force. Also the non hydrostatic LM model, used in a pre-operational form since May 2001 at ARPA-SMR (hereafter named ARPA-LM), and the version used at DWD (hereafter named DWD-LM) have been used. ECMWF-GCM QPF is also considered to have a direct comparison of the LAM performances.

In the first section we will describe results obtained making use of all the italian SYNOP stations, available on the WMO-GTS. After that, we will describe the results of a second and higher resolution verification exercise achieved using different non-GTS and more dense observation data set. One of this data set is available operationally in the Piedmont region of northern Italy; the other data set used is constituted by the high resolution non-GTS data available during the Mesoscale Alpine Programme (MAP) field phase (Sep-Nov 1999). The availability of these high resolution non-GTS station networks has allowed us to study the sensitivity of the verification scores to modification in the number of the stations used. The results obtained give a clear picture of the importance of using station networks with similar spatial density of the distribution of the LAM grid point and furnish also give also

clear indications about the more correct methods to use LAM QPF, in order to obtain the maximum useful information.

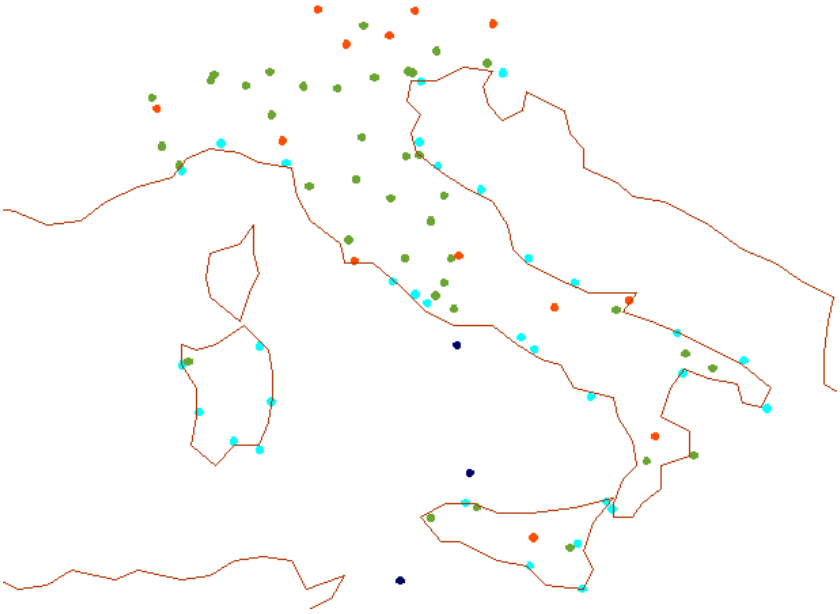

Figure 1: Italian Synop Stations - Type Classification. Blue and Cyan: Coastal; green: Lowland; orange: Mountain H > 700m.

3 Verification against SYNOP Report in Italy

In this first part of the study we show the results of the QPF (6 hours total accumulated precipitation) verification of Lambo, ARPA-LM and ECMWF models, all of them starting at 00GMT. The verification period covers the "extended" 2000-2001 winter period (December to March). At ARPA-SMR Lambo model is used in a double nesting chain (40 and 20 Km. Res.) using ECMWF analyses and operational forecast as Initial and boundary conditions of the former run at 40 Km. Res. As regards ARPA-LM, global analyses and forecast from GME, (runned at DWD) are used to provide initial and boundary condition. ARPA-LM doesn't make use of any data assimilation procedure.

Figure 1 shows the distribution of the Synop stations, divided in classes according to their geographical location, used for verification. In order to define contingence tables for QPF we used the nearest grid point to a given Synop station, provided that the grid point was a land type and its altitude mismatch with the station height was lower than 100 m. If one of these two conditions was is not satisfied, we have chosen among the four surrounding grid-point the one that was land type and that minimised the altitude mismatch.

The main results for the winter 2000-2001 are shown in Figure 2 and Figure 3, which show Probability of Detection (POD) and False Alarm Rate (FAR), both derived from the contingence tables for all the stations used as a function of the precipitation threshold. Respect of 6 h cumulated precipitation it possible to note the advantage of ARPA-LM respect to others in term of POD at higher thresholds. We can see that, together with POD, also FAR increases even if it is about on the same level of other models. In general the quality of QPF is better for smaller precipitation threshold and ECMWF GCM gives the best results for these small precipitation amounts.

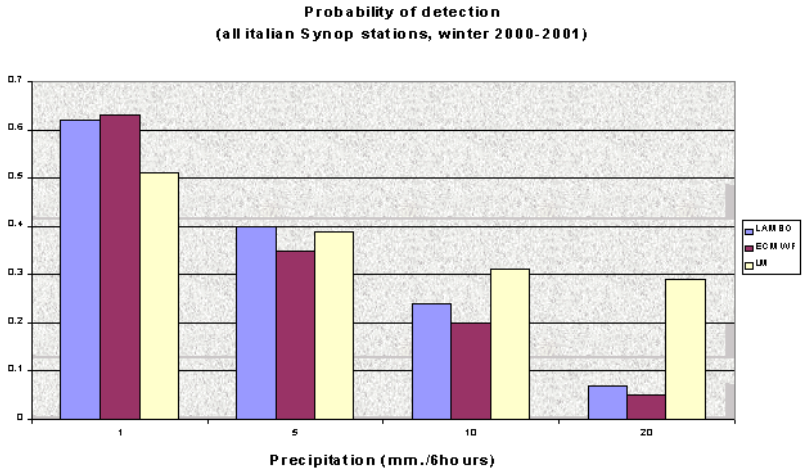

Figure 2: Probability of Detection (POD) computed for 6h TP at different threshold for Lambo (blue), ECMWF (red) and Lokal Model (yellow).

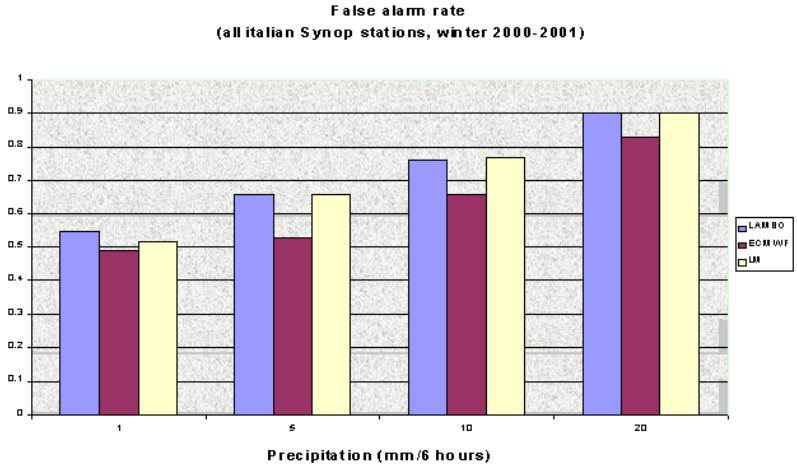

Figure 3: False Alarm Rate (FAR) computed for 6h TP at different threshold for Lambo (blue), ECMWF (red) and Lokal Model (yellow).

Figure 4 shows results of the verification of QPF of HRM, the LAM used operatively at UGM, Rome, against italian SYNOP reports, shown in Figure 1. The verification period is a little different with respect to the previous one so only a qualitative comparison can be done. Several statistical indices (Threat score, Kuiper score, POD, FAR, BIAS) are shown for different precipitation thresholds. As it can be expected all the scores indicate a decrease of the QPF quality for higher thresholds. Again ECMWF is the best for small precipitation thresholds.

As common results, these studies indicate the existence of a series of causes responsible for evident failures. First of all, a systematic overestimation affects on some mountain stations and a prevalent underestimation affects the stations located in valleys or along the coasts. Apart from topography, other important aspects influence the model performances: the synoptic flux (usually model overestimates upwind obstacles while underestimates downwind) and the kind of frontal system (prevailing overestimation in warm fronts and in pre-frontal areas, underestimation in cold fronts).

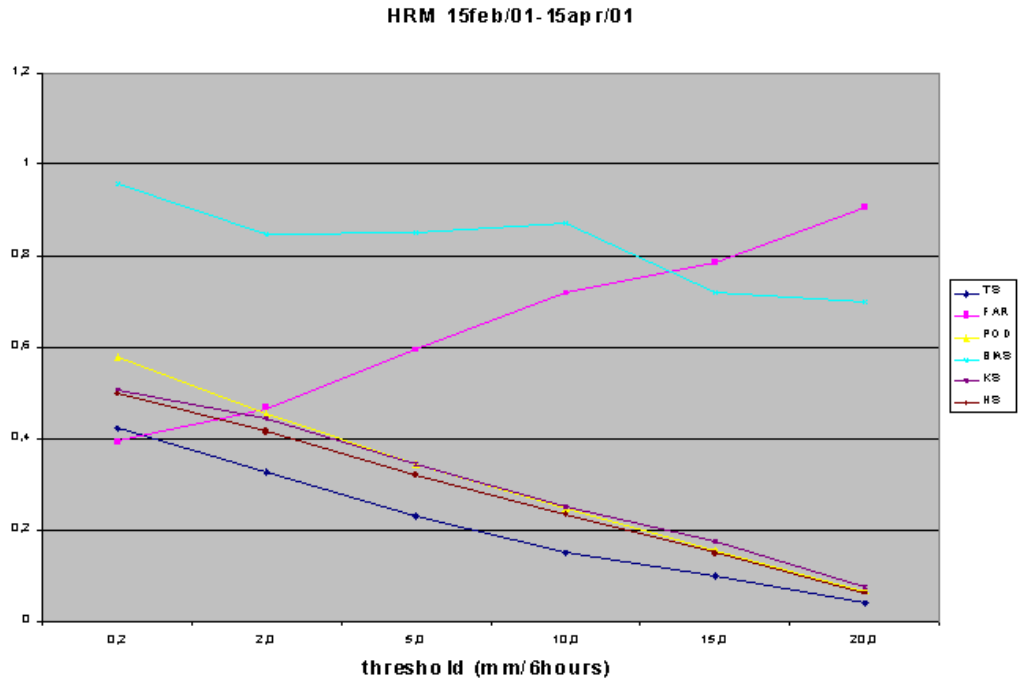

Figure 4: QPF verification scores for HRM model used at UGM against SYNOP reports for accumulated precipitation thresholds.

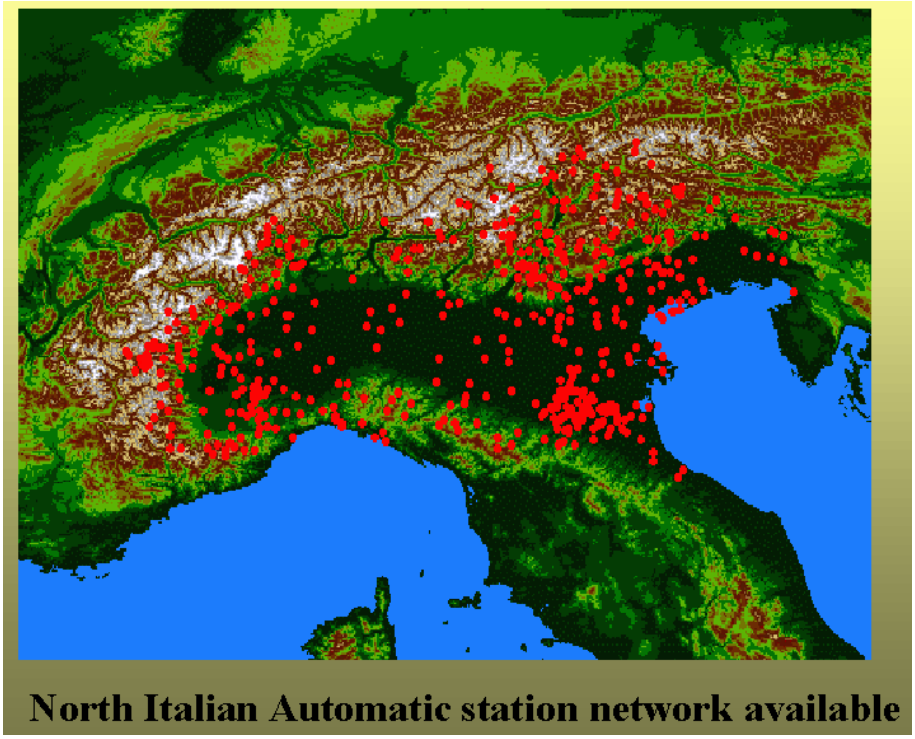

Figure 5: ITAMAP station network available during the MAP field phase (Sep. - Nov. 1999). The points indicate non-GTS data, observed every 1 hour interval, available at the MAP web site (www.map.ethz.ch).

4 High Resolution QPF Verification in Sub-Regions Against Non-GTS Data

4.1 Verification of Lokal Model in the MAP Period

During the MAP field phase (September-November 1999) a large number of non-GTS surface data, belonging to several national and regional weather/hydrological services operating in Northern Italy has been transferred in real time to the MAP Project Operation Centre (POC) in Milano at a hourly frequency (see the MAP web site: www.map.ethz.ch for details of the MAP campaign). All of these non-GTS data have been coded in a common "synop-like" ASCII format (Surfcode) and constitute the ITAMAP data set, available at the MAP web site. In the actual release (ITAMAP 1.2) the total number of non-GTS stations available is around 500, ten times larger than the number of the GTS weather stations available in Northern Italy. Furthermore, the density of this non-GTS station network is almost homogeneous (see Figure 5 that shows the distribution of the stations in Northern Italy) and makes possible a very efficient verification of the main meteorological parameters, like precipitation (accumulated in intervals of 1 hours).

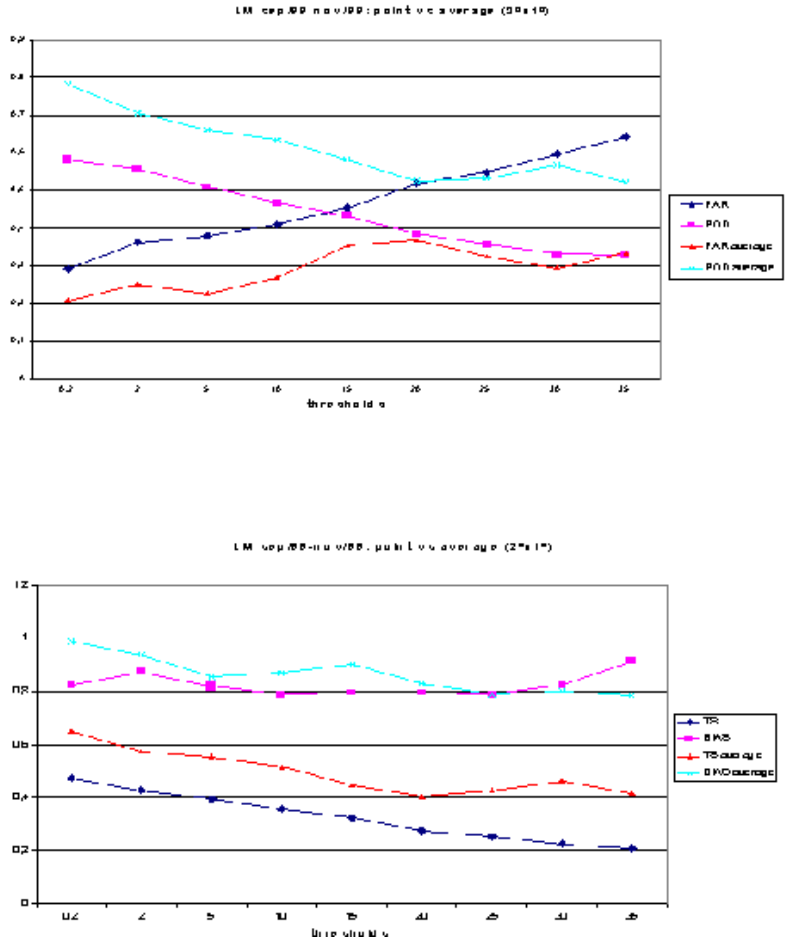

Figure 6: Plots of POD, FAR (upper panel), threat score (TS) and BIAS (lower panel) as a function of precipitation thresholds, for both punctual and averaged scores in areas of 1x2 degrees.

In particular, we used this high density data set to verify the QPF of DWD-LM. The high density of the station network available for the MAP period allowed us to study the sensitivity of the scores to different methods to evaluate them. We calculated contingence tables and then verification scores deduced by these tables, using all the couples of grid-point/stations

(hereafter named "punctual scores") in the domain and also making spatially averaged values of both grid point forecasts and observations (hereafter named "averaged scores") within square box of variable size. In Figure 6 we can see the plots of POD, FAR (upper panel), threat score (TS) and BIAS (lower panel) as a function of precipitation thresholds, for both punctual and averaged scores. It is evident that averaged values are sensitively better than punctual ones, especially for high precipitation thresholds. POD doesn't decrease under 0.5 even for the highest precipitation threshold and also the FAR increases at a lower rate. Averaged TS are much better than punctual TS and indicate that if averaged values are used DWD-LM gives extremely useful forecast also at high precipitation threshold.

4.2 Verification of DWD-LM in the Piedmont Region.

In the Piedmont region a high dense network of non-GTS stations is available (see Figure 7) and allows a very refined verification of DWD-LM QPF. Common contingence tables (and then standard scores like POD, FAR, BIAS, TS etc..) have been evaluated for all the year 2000). Even in this case the evaluation have been performed in two ways: 1) for all the couples of grid-point/station points (hereafter named again "point" evaluation) and also, 2) making before a spatial averaging of the observed and predicted precipitations in each of the 10 hydrological basins of the Piedmont region (hereafter named "basin" evaluation), shown again in Figure 7.

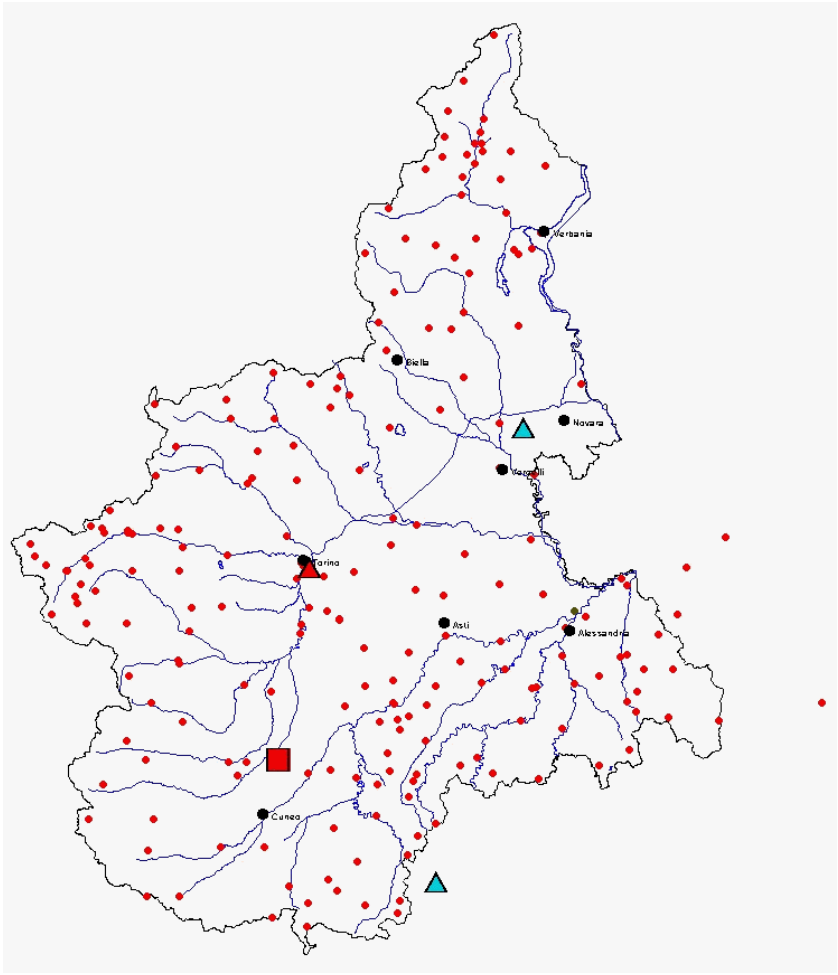

Figure 7: The network of non-GTS stations available in the Piedmont region and the main river catchement.

Figure 8 and Figure 9 show DWD-LM QPF verification results for "basin" and "points" evaluation of the scores, respectively. ECMWF model and persistence results are also shown and allow a evaluation of the relative improvement of DWD-LM against them. It is evident that averaging the observed and predicted precipitation amount in river catchment has a tremendous impact to the quality of the QPF. If we look to the usual scores evaluated using all the couples of grid-pint/station points (Figure 9) we see that LM doesn't give very useful results. ECMWF is always better, especially for small precipitation amounts, as one can expect. If we see the results obtained making spatial averages within hydrological basins (Figure 8) we notice, on the contrary, that LM is better than ECMWF for the highest precipitation thresholds (over 10mm/24 hours).

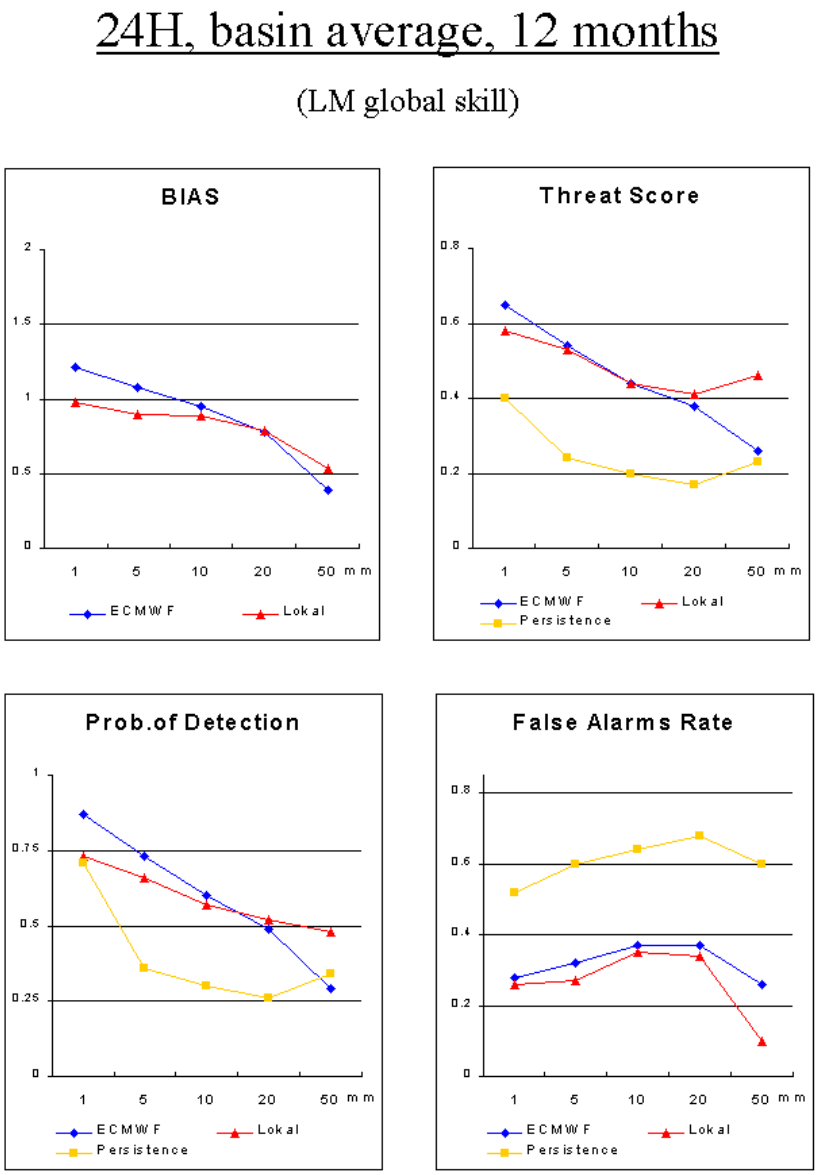

Figure 8: QPF verification scores for 24 hours accumulated precipitation (BIAS, Threat score, POD and FAR), deduced by contingence tables for the year 2000. Scores are evaluated after averaging observed (at the station points) and predicted (Lokal Model grid points) precipitation values within the 10 hydrographic basins ("basin" averaging) of the Piedmont region

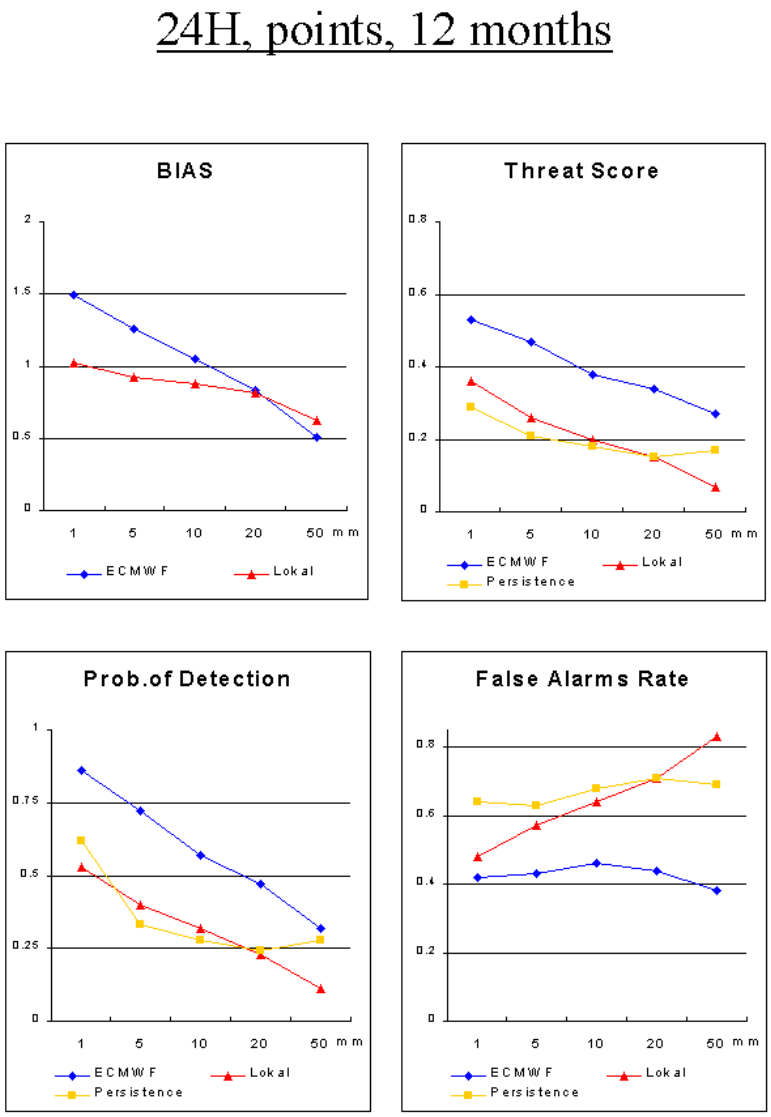

Figure 9: As in Figure 8 but without any averaging process applied to observed and predicted precipitation values. All the couples of station/nearest grid point are considered to evaluate first contingence tables and then the shown scores.

If we look to the results of the QPF during the integration time (48 hours, Figure 10 and Figure 11), we see again that the averaging procedure applied to predicted and observed values allow to have usable QPF prediction of DWD-LM, at least for the first 12-18 hours integration and for high precipitation thresholds (25mm/24 hours). For these high precipitation values the scores of DWD-LM are much better than ECMWF that, on the contrary, gives the best results only for small precipitation amounts. That is evident if we compare, for example, the TS for "basin" (Figure 10, lower-right panel) and "points" (Figure 11, lower right panel).

5 Conclusions

In this report we have discussed the results of the verification of QPF produced by different Limited Area Models (LAM) and compared results of their products with ECMWF global

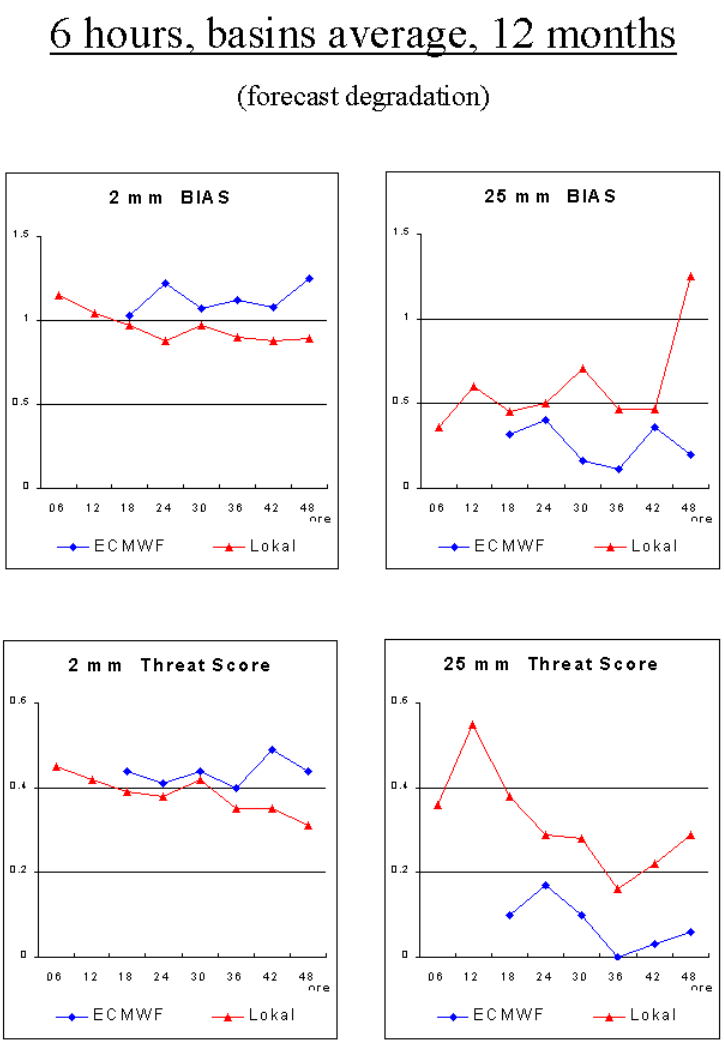

Figure 10: Diurnal cycle during the integration time of the verification scores for QPF for 6-hours accumulated precipitation during the integration time. Scores are evaluated after the averaging process discussed in the text (and in Figure 8).

model. Data used for this study are the common SYNOP reports available on GTS and non-GTS data available for the period of the MAP field phase (Sep-to-Nov 1999) in northern Italy (ITAMAP data set available at the MAP web site: www.map.ethz.ch) and also in some sub-regions of Italy. One of this is the Piedmont Region in the western part of Northern Italy where a dense network of non-GTS data is available.

The results of the study indicate some interesting points to be matter of debate and future investigation:

1. GTS data is not sufficient to catch the mesoscale structure of the precipitation field produced by high resolution hydrostatic and non-hydrostatic LAMs;

2. Common verification scores like Probability of Detection, False Alarm rate, Threat scores etc., deduced by contingence tables obtained comparing couples of station points and nearest grid points are probably non completely suitable for the verification of precipitation. Small phase errors in the positioning, in space and/or in time, of precipitation maxima, for example, produce big errors as evaluated by these scores, even

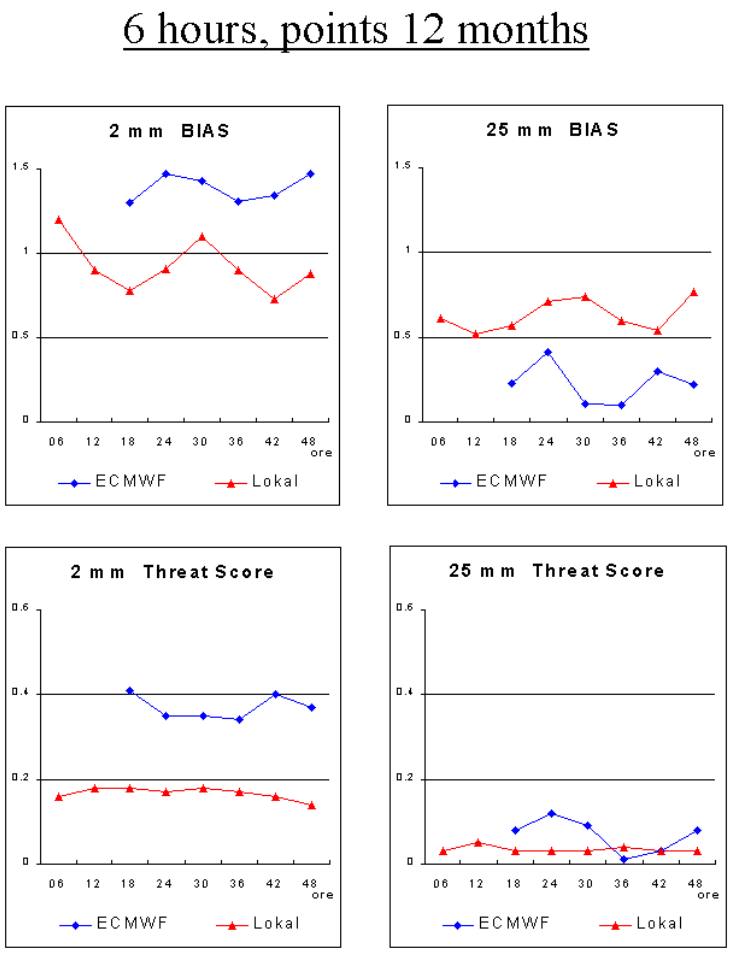

Figure 11: As in Figure 10 but without any averaging process applied to observed and predicted precipitation values (see text and Figure 9).

if the mesoscale structures of the precipitation fields are well captured by the LAM outputs;

3. Using these indices it comes out that global model (ECMWF) gives better results than the used LAMs (hydrostatic: LAMBO; non hydrostatic: Lokal Model). This is particularly true for small precipitation thresholds;

4. A substantial improvement in the quality of the LAM QPF simulation is obtained when spatial averaged (predicted and observed) values are considered and the abobe mentioned scores are evaluated after the averaging process. For example, spatial averaging performed within hydrological basins of the Piedmont region allows to have very useful QPF by DWD-LM, much better than what produced by ECMWF precipitation forecats. For high values of precipitation thresholds and for the first 12-18 integration time the LM outputs are the only that are usable for application in areas like the evaluation of hydrological risk and/or as input for rainfall/runoff models.

Comparison of Forecasts with and without Nudging: Surface Parameters over Switzerland for April - December 2001

Francis Schubiger

MeteoSwiss, Krähbühlstrasse 58, 8044 Zürich, Switzerland

1 Introduction

Since 1 April 2001 a testchain with forecasts issued from the nudging-assimilation runs at 00 UTC. A short introduction in nudging assimilation is presented in Section 3.2 of this Newsletter.

The forecasts with nudging are compared to those without nudging (i.e. initial fields transformed from GME) and the results are also compared to the forecasts from DWD (which run also from nudging assimilation). For differences between the MeteoSwiss and DWD model set-up, see Tables 9 and 7 in Section 7 of the Newsletter.

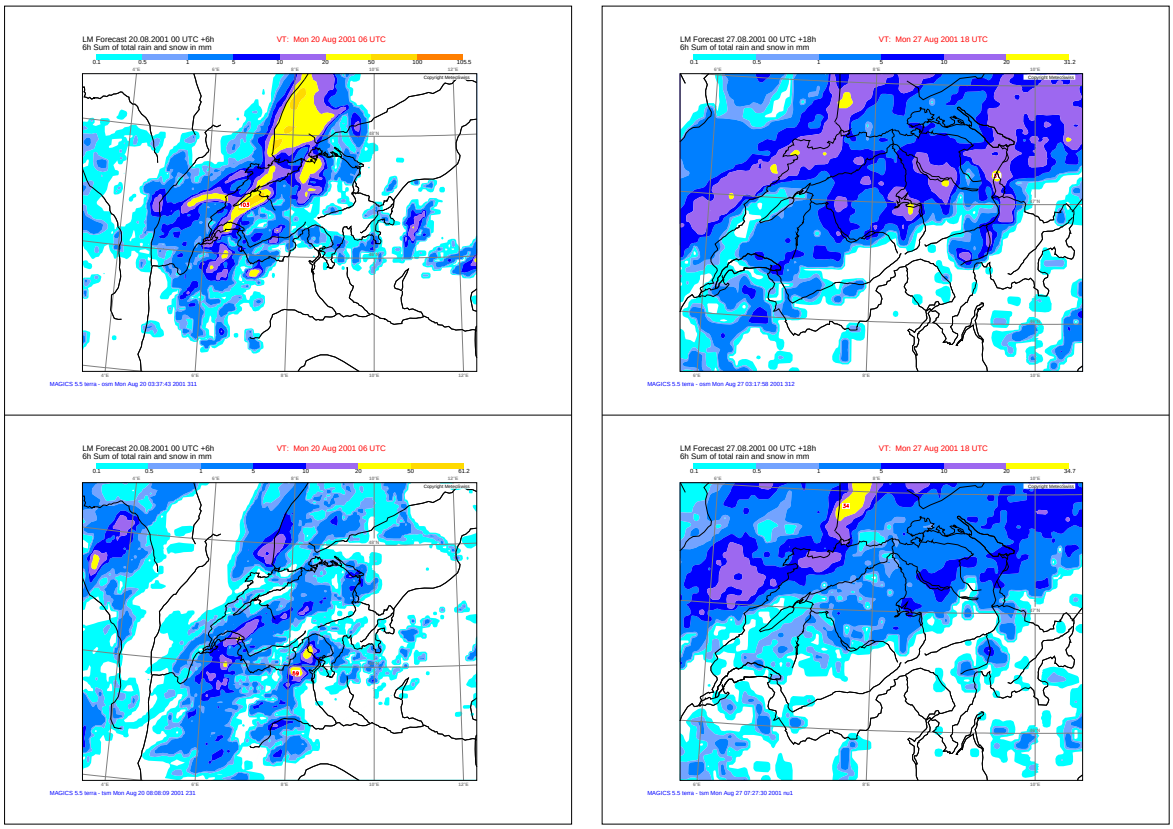

Figure 1: 6-h precipitaion amounts for 20 August 2001 00UTC from +0h to +6h (left) and from +12h to +18h (right). Top panel: without nudging. Bottom panel: with nudging.

The improvement with nudging for precipitation is well visible on single cases: the forecasts without nudging often give much too much precipitation in the first forecast hours (even up to 12-18 hours). Figure 1 shows 6h-sums of precipitation (above) without nudging and (below) with nudging: The left hand side of Figure 1 for the 6h-sum +0h to +6h from

forecast of 20 August 2001 00 UTC and the right hand side for the 6h-sum +12h to +18h from forecast of 27 August 2001 00 UTC. The exaggerated sums over the Jura are eliminated with nudging.

Summarized results are presented for:

1. surface verification over Switzerland,
2. precipitation over extended swiss domain, and
3. subjective verification by bench forecasters.

A separated report of verification of the vertical profiles at +0h summarizes the results for temperature, geopotential, humidity and wind profiles. This report (by Marco Arpagaus) is available at the COSMO web-site (member area). The main result form this comparison is that the nudging scheme provides better initial temperature profiles (with respect to bias and standard deviation) than by interpolation of the GME analysis. Also, the relative humidity is well assimilated, except very close to the surface. The improved analysis has an impact on the forecast error (BIAS) out to +12 hours. An effect on the forecast spread (standard deviation) can not be seen.

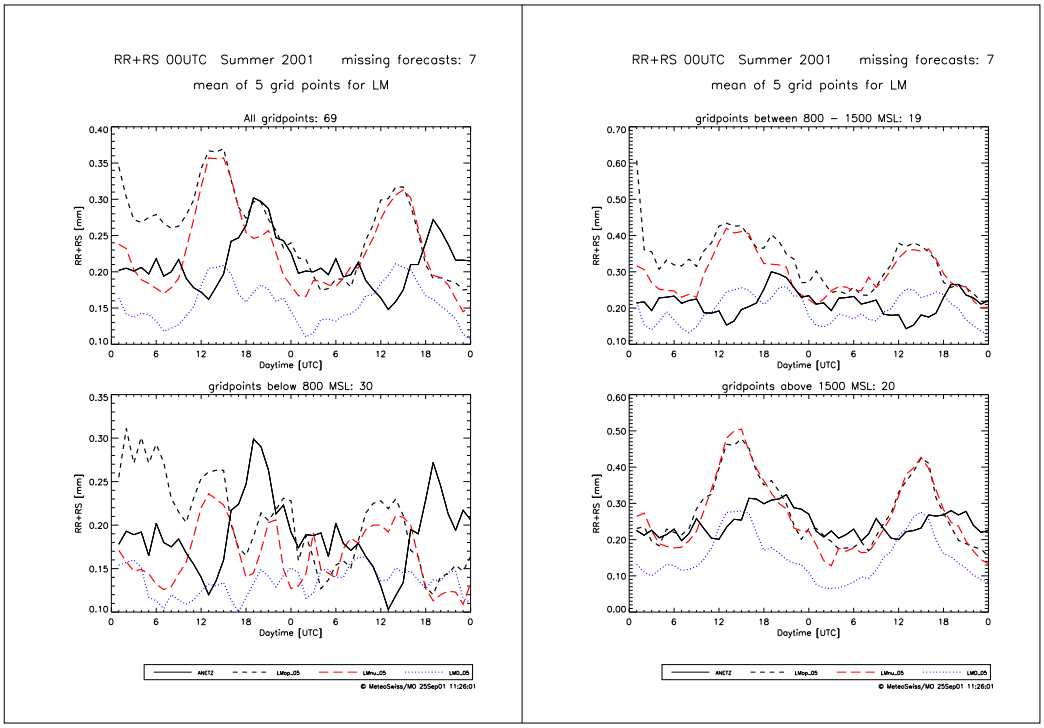

Figure 2: Mean diurnal cycle of precipitation at ANETZ stations in Switzerland for Summer 2001. Full black line: ANETZ observations. Dashed black line: aLMo-GME. Dashed red line: aLMo-nudging. Dotted blue line: LM-DWD. Top left: all 69 stations. Bottom left: for gridpoints below 800m. Top right: for gridpoints between 800m and 1500m. Bottom right: for gridpoints above 1500m.

2 Verification of Daily Cycle with ANETZ

At MeteoSwiss the verification package with hourly surface observations over Switzerland runs for (a) aLMo forecasts (i.e. from MeteoSwiss) and (b) LM forecasts from DWD.

Results of the three model versions have been analysed. In the following, differences due to the new nudging assimilation-scheme are presented. Note that differences between aLMo and LM-DWD are also due to the different physics package used at DWD and at MCH.

These differences are *not* commented in this report. See the report "Verification results of aLMo with and without the new TKE-scheme (14.08.01-06.11.01)" in this Newsletter that explains these differences in wind and dewpoint depression. The main results for nudging vs no nudging are summarized below.

Precipitation

The mean diurnal variation for Summer 2001 (Figure 2) and Autumn 2001 (Figure 3) show much too high sums in the first forecast hours for gridpoints < 1500m in the forecasts without nudging. This spin up in precipitation is removed with nudging; see also below (in Section 3) the reduced amounts of precipitation on a domain of 57x39 gridpoints over Switzerland.

- spinup in the first 9h removed.
- no more 50% overestimation of high amounts of precipitation (> 10 mm/6h) in the first 6-12h.

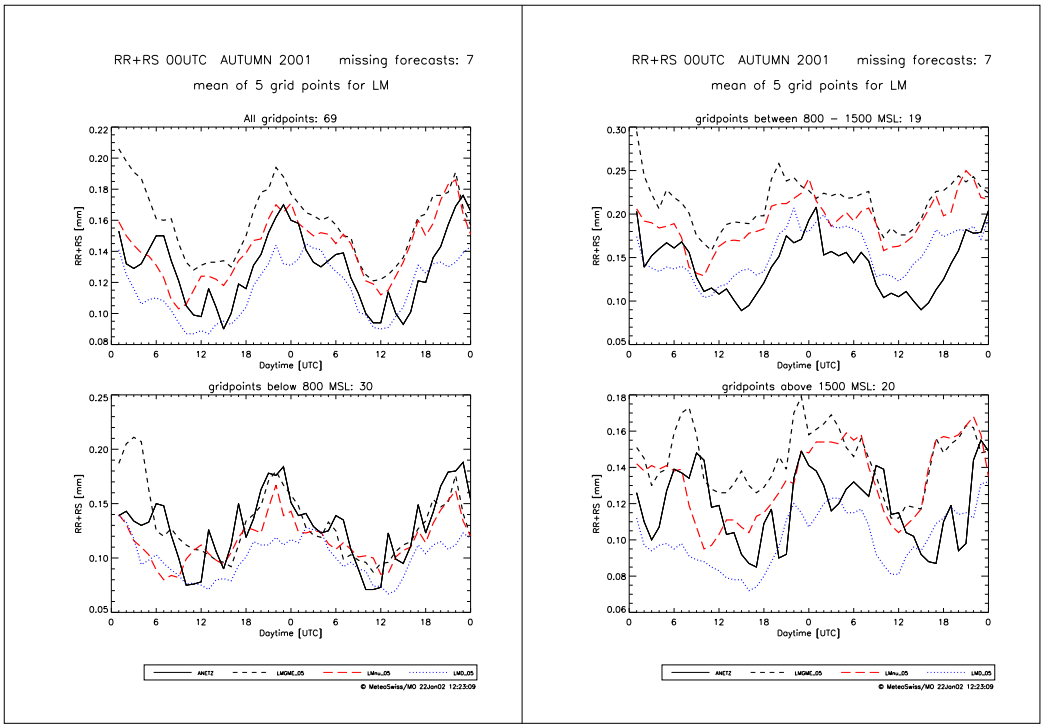

Figure 3: As in Figure 2 but for Autumn 2001.

Total Cloudiness

The mean diurnal variation is shown for Summer 2001 (Figure 4) and Autumn 2001 (Figure 5). The nudging assimilation gives an increased amount of cloudiness at analysis time (+0h) and up to 6-9 hours of forecast. At +0h the amount of cloudiness is $\sim$ 1 octas higher with nudging. This higher amount of cloudiness was visible during all the months and has also been observed during winter 2000/2001 between LM-DWD (nudging) and aLMo (without nudging). This higher amount is not only due to high clouds: there are more high, medium and low clouds at +0h with nudging assimilation.

- $\sim$ 1 octas more at +0h; after +9h similar

- higher amount of clouds at +0h at all levels: in August 2001 (+1.3 octas for total cloudiness) higher amounts of 0.8 octas for high and medium clouds and 0.6 octas for low clouds.

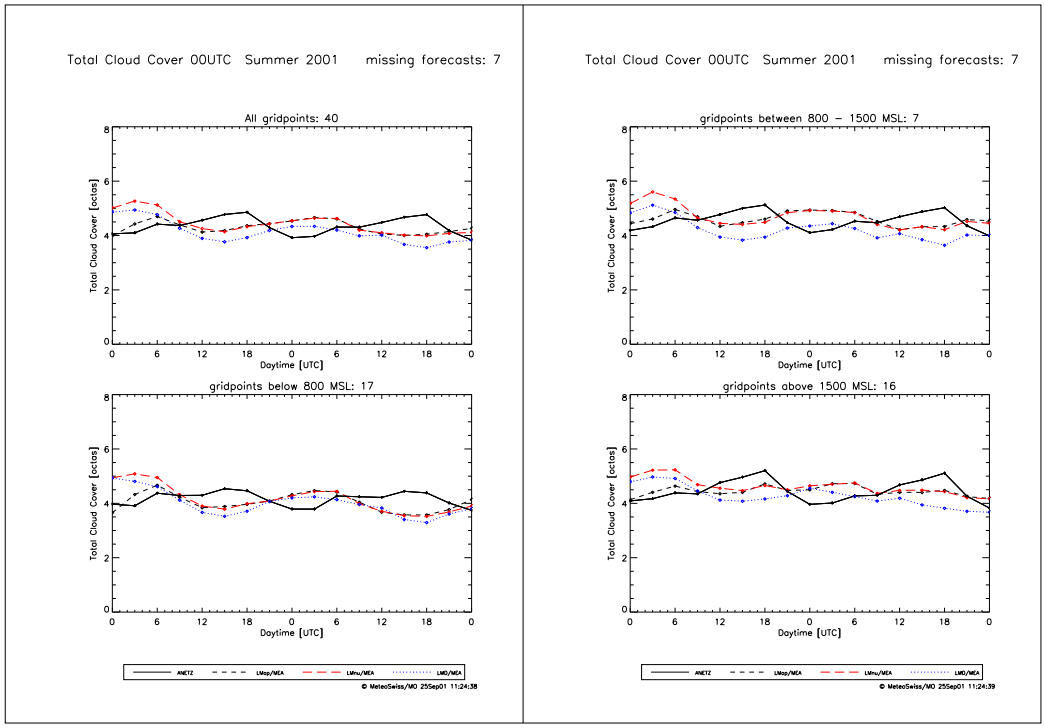

Figure 4: Mean diurnal cycle of total cloud cover at ANETZ stations. Legend as in Figure 2

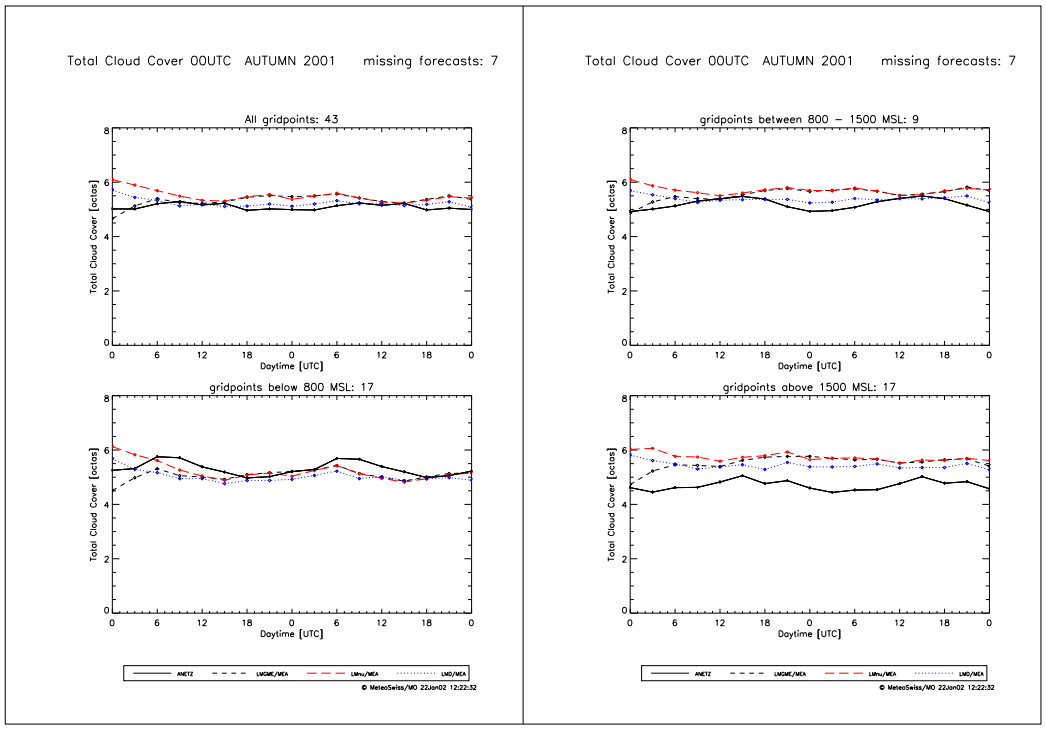

Figure 5: As in Figure 4 but for Autumn 2001.

10m-Wind

The mean diurnal variation for the period April-August 2001 (aLMO with/without nudging) for 10m-wind speed and 10m-wind direction for all representative stations (above) and those < 800m (below) show an amelioration in the first forecast hours. The results for Summer 2001 and Autum 2001 reveal a similar behaviour. Figure 6 shows the verification results for Summer 2001 (left) and Autumn 2001 (right) for 10-m wind speed. The corresponding results for 10-m wind direction are shown in Figure 7.

10m-windspeed has no longer a spinup in the very first forecast hours (this behaviour was not seen with the transformed fields from EM [i.e. in program EM2HM], it seems to be a "bug" in the program GME2LM). The 10m-wind direction show a reduced error in standard deviation up to +9 hours of forecast (in the period till August 2001).

- speed (for gridpoints < 800m): no spinup in the first 3h (GME2LM bug?)
- direction: std dev of errors in first 6h a little bit better, similar in bias

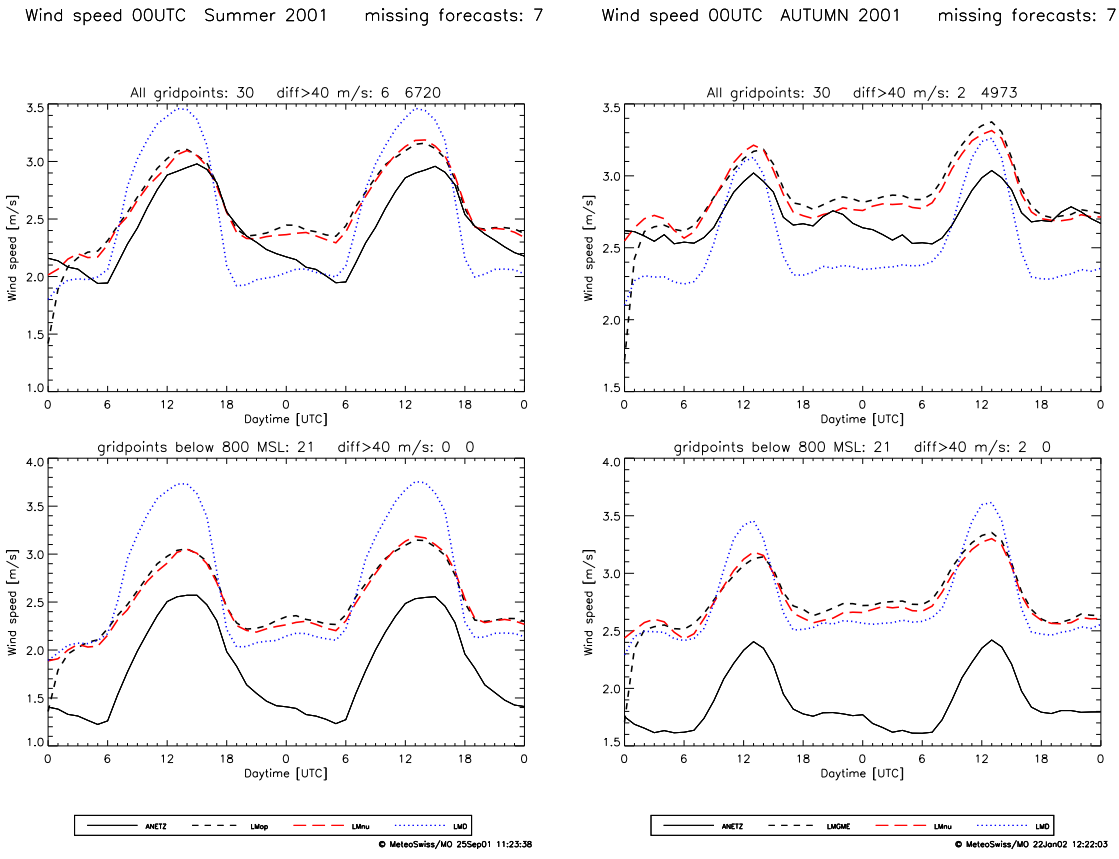

Figure 6: Mean diurnal variation of the 10-m wind speed at ANETZ stations for Summer 2001 (left) and Autumn 2001 (right). Full black line: ANETZ observations. Dashed black line: aLMo-GME. Dashed red line: aLMo-nudging. Dotted blue line: LM-DWD. Bottom panel: for gridpoints below 800m. Top panel: all gridpoints.

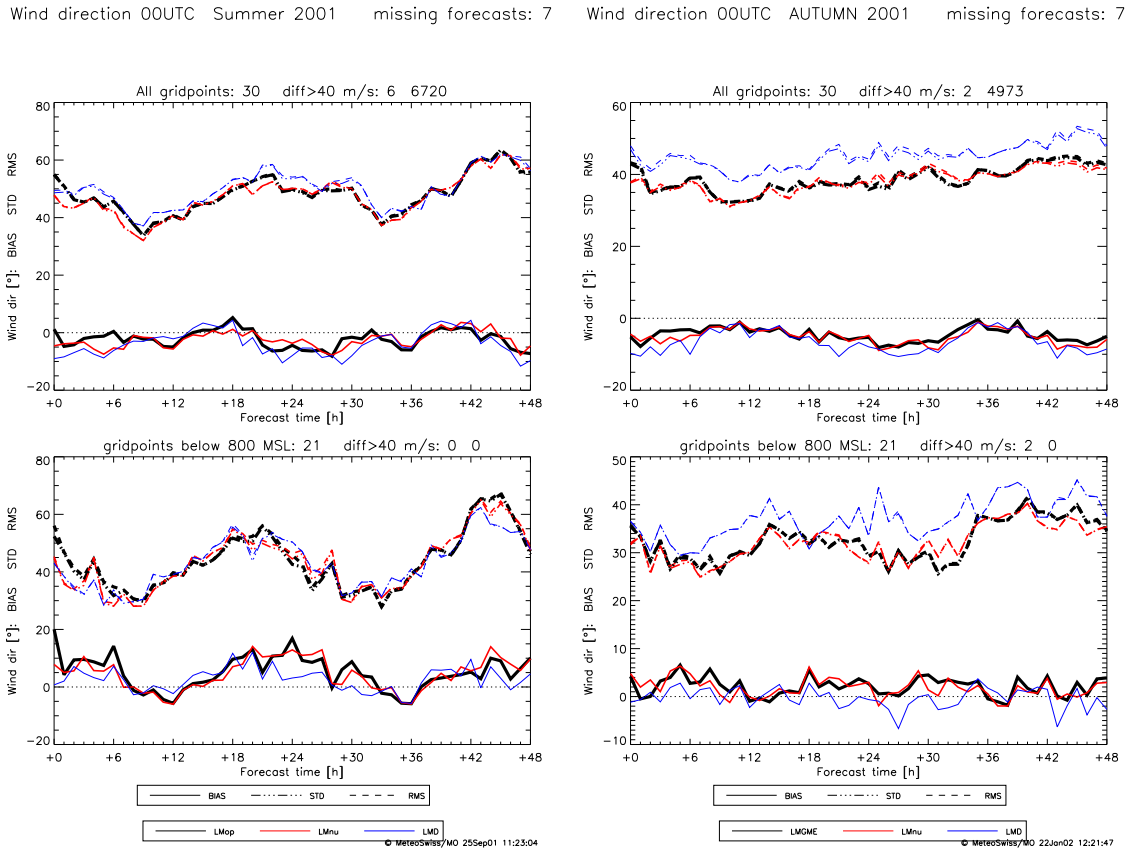

Figure 7: Mean diurnal variation of bias (full lines), standard deviation (dash-dotted lines) and rmse (dashed lines) of 10-m wind direction at ANETZ stations for Summer 2001 (left) and Autumn 2001 (right). Black line: aLMo-GME. Red line: aLMo-nudging. Blue line: LM-DWD. Bottom panel: for gridpoints below 800m. Top panel: all gridpoints.

2m-Temperature

Results with/without nudging are similar in Summer and Autum 2001. In Spring differences have been noticed at some locations, namely in the alpine valleys or at mountain gridpoints. Figure 8 show these results for the gridpoint near Interlaken: above mean diurnal cycle, below statistical coeeficients of errors, and on the left for the period April-August 2001 and on the right only for June-August 2001. At this location in Spring the standard deviation of errors was much reduced with nudging (but not in Summer!).

- similar results
- in Spring 2001: better scores of std dev of errors at locations in mountains or in valleys

2m-Dew Point Depression

The verification of aLMo with/without nudging for the period April-August 2001 for the gridpoints < 800m revealed that the mean diurnal variation is much more realistic with nudging assimilation. The analog results for Summer and Autumn 2001 are shown in Figure 9.

- at +0h better and more realistic
- similar results (a little bit drier, i.e. better in daytime)

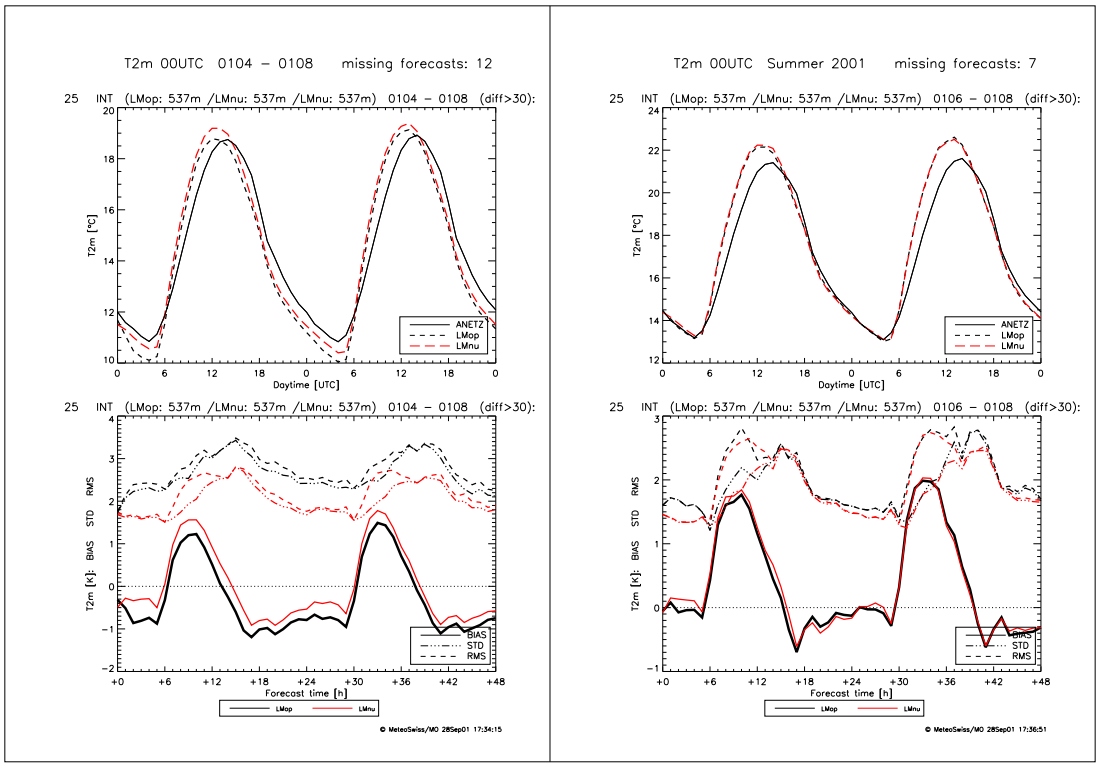

Figure 8: Mean diurnal cycle at gridpoint Interlaken of 2-m temperature (top panel) and of of bias, standard deviation and rmse of 2-m temperature (bottom panel), colours and lines as in Figur 7. Left: April-August 2001. Right June-August 2001

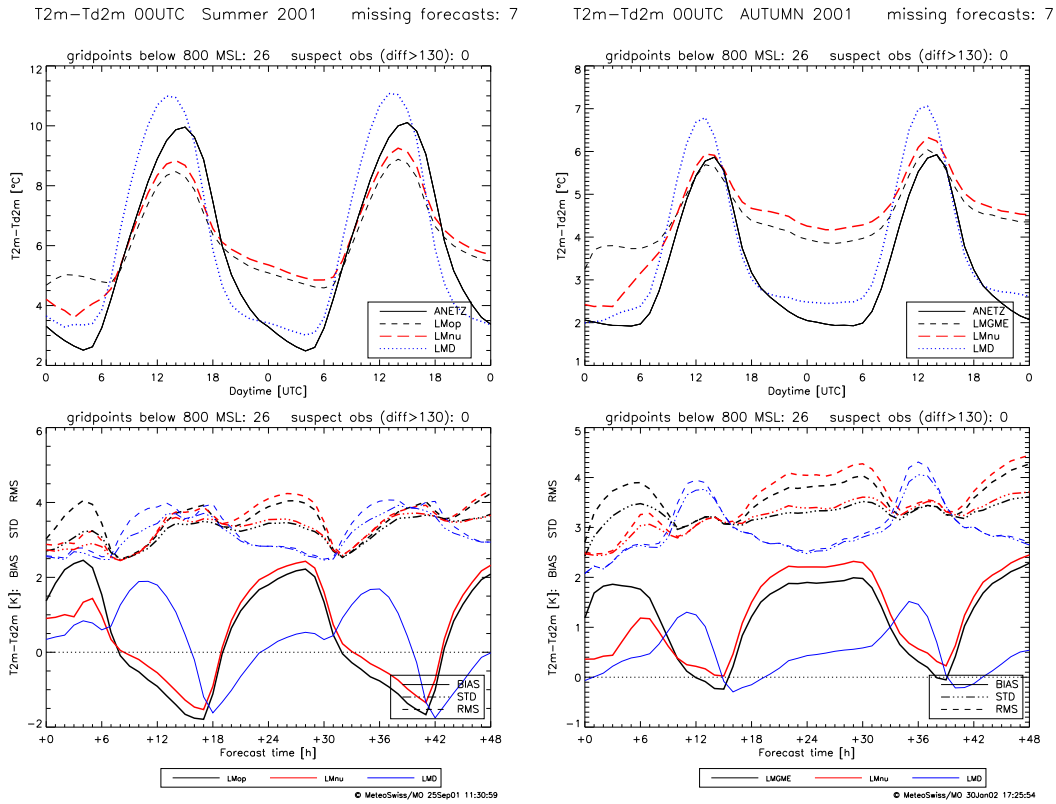

Figure 9: Mean diurnal variation of the 2-m dew point depression (top panel, colors and lines as in Fig. 7) and of bias, standard deviation and rmse (bottom panel, colors and lines as in Fig. 8) at ANETZ stations for Summer 2001 (left) and Autumn 2001 (right).

3 Precipitation over Extended Swiss Domain

Figure 10 (Summer 2001) and Figure 11 (Autumn 2001) show the mean diurnal cycle of precipitation for a domain extract over Switzerland (57x39 gridpoints) for all gridpoints (left above), gridpoints < 800m (left below), gridpoints 800-1500m (right above) and gridpoints > 1500m (right below). With nudging the precipitation sums are much redudced in the first 12 hours of forecast for gridpoints < 1500m (for those < 800m reduction of $\sim$ 1/3 in the first 6 hours).

As has been shown above for the verification at ANETZ-locations (Figure 2 and 3), this reduction results in a much improved cycle for the first 9-12 hours of forecast (no more spin up). The differences in Autum 2001 (Figure 11) between aLMo with/without nudging are more pronounced than in Spring and Summer 2001: the forecasts without nudging give more precipitation up to +30h (!). In the time range +6..+18h forecasts without nudging gives 15% more precipitation than those with nudging the for the gridpoints < 800 m and even 25% for the gridpoints > 1500 m. The verification with ANETZ (mean diurnal variation shown on Figure 3) gives better scores for the nudging forecasts, except for the high amounts of precipitation (> 10mm/6h) for gridpoints < 800m which were underestimated in both cases, but even more with nudging (frequency bias in the time range +06..+18h for threshold 10mm/6h gives an underestimation with nudging by 40"only" 25%).

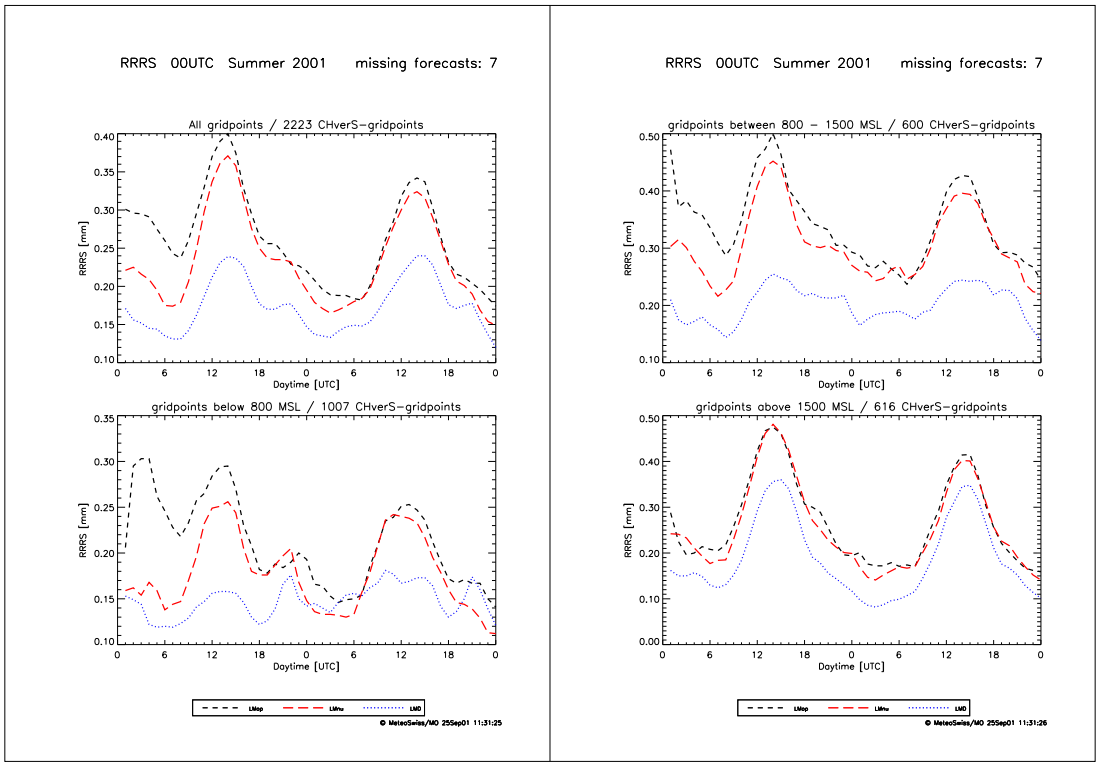

Figure 10: Mean diurnal cycle of area-average precipitation for a subdomain over Switzerland for Summer 2001. Dashed black line: aLMo-GME. Dashed red line: aLMo-nudging. Dotted blue line: LM-DWD. Top left: all gridpoints. Bottom left: for gridpoints below 800m. Top right: for gridpoints between 800m and 1500m. Bottom right: for gridpoints above 1500m.

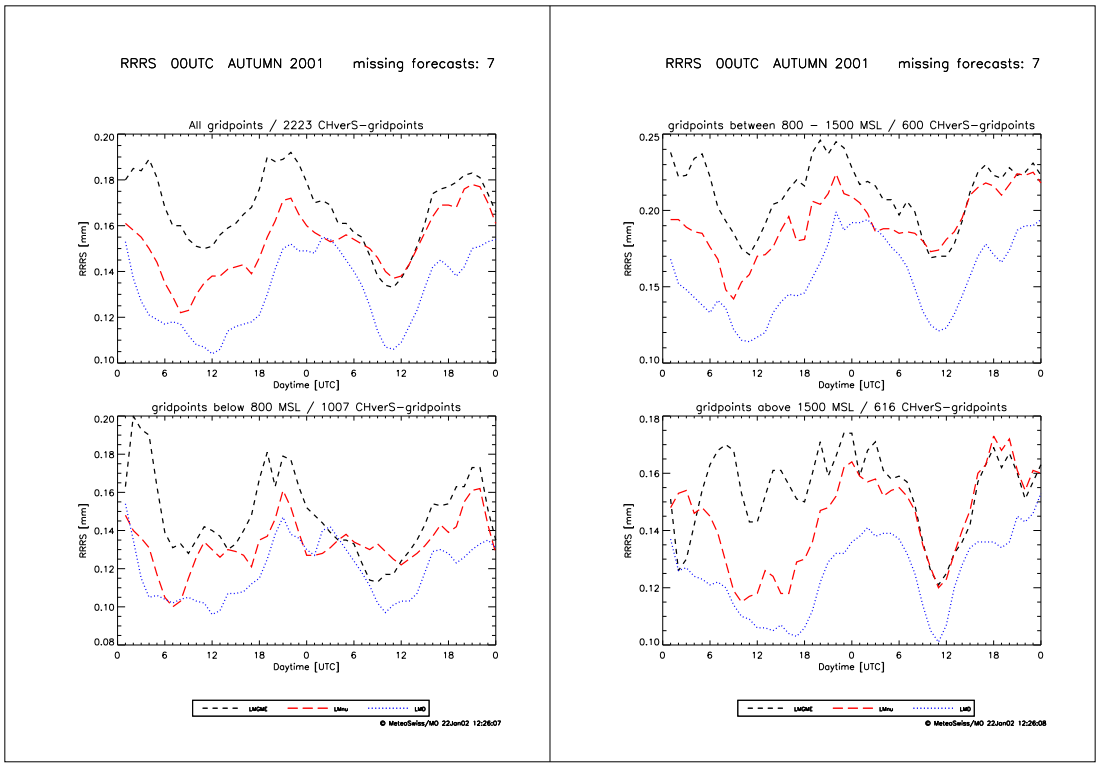

Figure 11: As in Figure 11 but for Autumn 2001.

Subjective verification by bench forecasters in Geneva
aLMo with nudging vs aLMo without nudging

parameters		domain	period
fronts	structure	Europe	+0..+18h
	timing	Europe	+0..+18h
precipitation	maxima	Switzerland	+0..+18h
	distribution	Switzerland	+0..+18h
	timing	Switzerland	+0..+18h
10m-wind		Switzerland	+0..+18h
low cloud cover		Switzerland	+0..+18h
vertical profile		Payerne	+12h

Results for: 63 aLMo-forecasts of 03.07.01 - 30.09.01
Results for: 98 aLMo-forecasts of 01.10.01 - 13.01.02

- **all parameters**: "better", i.e. superior forecasts with nudging in **27 (14)** % of the cases, "similar", i.e. no big differences in quality in **61 (71)** % of the cases, "less good" in **12 (15)** % --> **nudging better**

- **precipitation** (max, distr., timing) **nudging better**
  35 (19) % better, **52 (57)** % similar, **13 (24)** % less good

- **10m windfield**: **nudging better**
  27 (14) % better, **69 (80)** % similar, **4 (6)** % less good

- **profiles**: **nudging better**
  26 (14) % better, **57 (76)** % similar, **17 (10)** % less good

- **low cloud cover similar with/without nudging**
  18 (16) % better, 64 (67) % similar, 18 (17) % less good

- **fronts** (structure, timing) **similar with/without nudging**
  11 (6) % better, **76 (86)** % similar, **13 (8)** % less good

Figure 12: Results of a subjective verification by bench forecasters at MeteoGeneve for aLMo with nudging against aLMo withour nudging (see text).

4 Subjective Verification by Bench Forecasters

Bench forecasters at MeteoGeneve began at 3 July 2001 with a subjective verification of aLMo with nudging vs aLMo without nudging for the first 18 hours of forecast. Figure 12 summarizes these results which show a clear improvement with the nudging assimilation. In red are the results for 03.07.01-30.09.01 and in blue for 01.10.01-13.01.02: the forecasts with nudging gave especially in summer an improvement in precipitation. This is in agreement with the results shown above: in Autumn 2001 the high amount of precipitation have been more underestimated with nudging and in December 2001 (not shown) there is no spin up in the first 6-9 hours in the forecasts without nudging (i.e. no differences between nudging/no nudging).

5 Summary

The results of the objective and subjective verification show an *overall improvement in the quality for the first 12-18 hours with forecasts issued from nudging assimilation.* This improvement is most pronounced for precipitation: there is no more a spin up (no more exaggerated amounts in the first forecast hours). But also humidity and 10m-wind give better scores in verification in the first 12 hours. Cloudiness give higher amounts at analysis time. The expected improvement in low cloudiness by stable high pressure situations in wintertime will be examined in Winter 01/02.

Verification results of aLMo with and without new TKE-scheme: 14 August - 6 November 2001

FRANCIS SCHUBIGER

MeteoSwiss, Krähbühlstrasse 58, 8044 Zürich, Switzerland

1 Introduction

Since 4 April 2001 LM at DWD runs with the new TKE-scheme (see COSMO Technical Report No. 1). Preliminary results for LM-DWD with the new TKE-scheme and aLMo without the TKE-scheme are available in a separate verification report for April 2001 (at the COSMO web-site, member area): the differences between the two model-versions were compared to those obtained in the earlier months (i.e. when LM-DWD run without the new TKE-schme, i.e. same physics in both model-versions [DWD and MCH]).

At MeteoSwiss the new TKE-scheme has been run on a testchain with the 00 UTC-forecasts between 14 August 2001 and 6 November 2001. Results are presented for:

- Vertical profiles for the two aLMo-versions (with/without TKE) for the period 14.08 - 22.09.01,
- Surface verification over Switzerland for the three model versions (aLMo with/without TKE and LM-DWD) for the period 14.08 - 06.11.01.

2 Vertical Profiles (for aLMo with/without TKE)

The main results of the comparison of verification results of vertical proviles (TKE vs no TKE with aLMo) are summarized below.

- humidity:
  - greater positive bias up to 700 hPa at 12 UTC (i.e. at +36h, see Figure 1) as well as at 00 UTC (i.e. at +48h, not shown)
  - Minor differences in standard deviation of errors
- temperature:
  - greater bias in the lower PBL at 12 UTC (i.e. at +36h, see Figure 2) At 00 UTC (i.e. at +48h) similar results except for the lowest layer and at the surface
  - over Alpine region greater negative bias up to 850 hPa (despite better results at surface!): see results at 00 UTC (i.e. at +48h, see Figure 3)
- wind:
  - for direction a little bit reduced bias in PBL up to 800 hPa at 12 UTC (i.e. at +36h, see Figure 4) and up to 950 hPa at 00 UTC (i.e. at +48h)
  - no differences in wind speed (not shown)

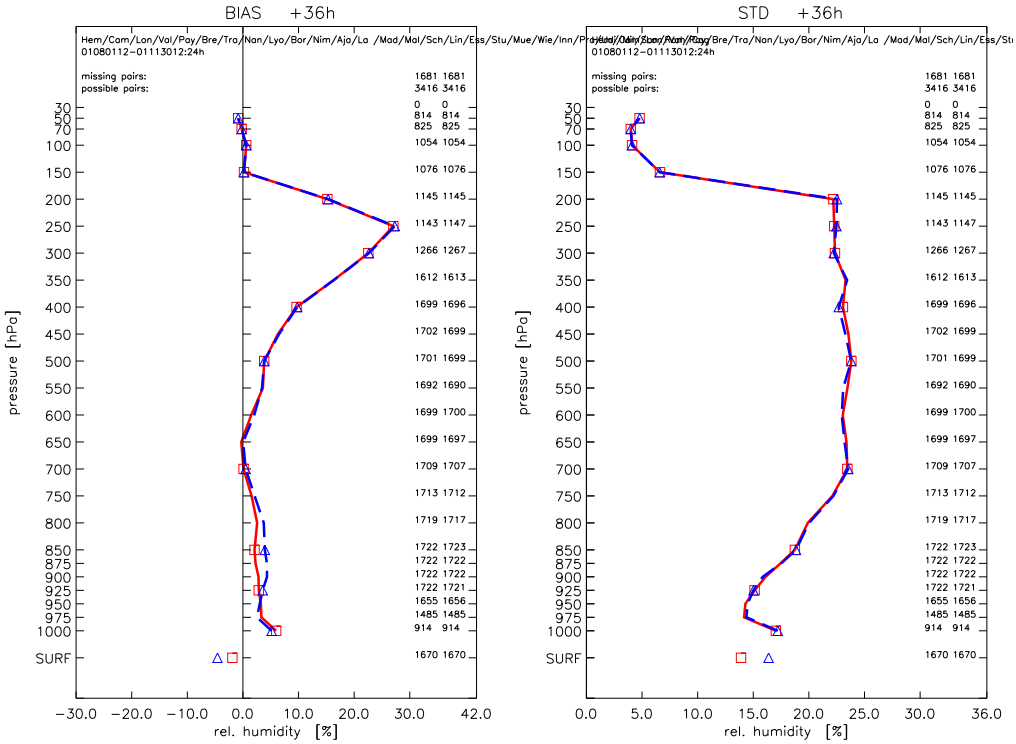

Figure 1: Mean error (BIAS, left) and standard deviation (STD, right) of relative humidity for verification time 12 UTC (+36h forecaste time). Time period: 14 August – 22 September 2001). Red line: operational aLMo without TKE, blue dashed line: aLMo with TKE; all soundings.

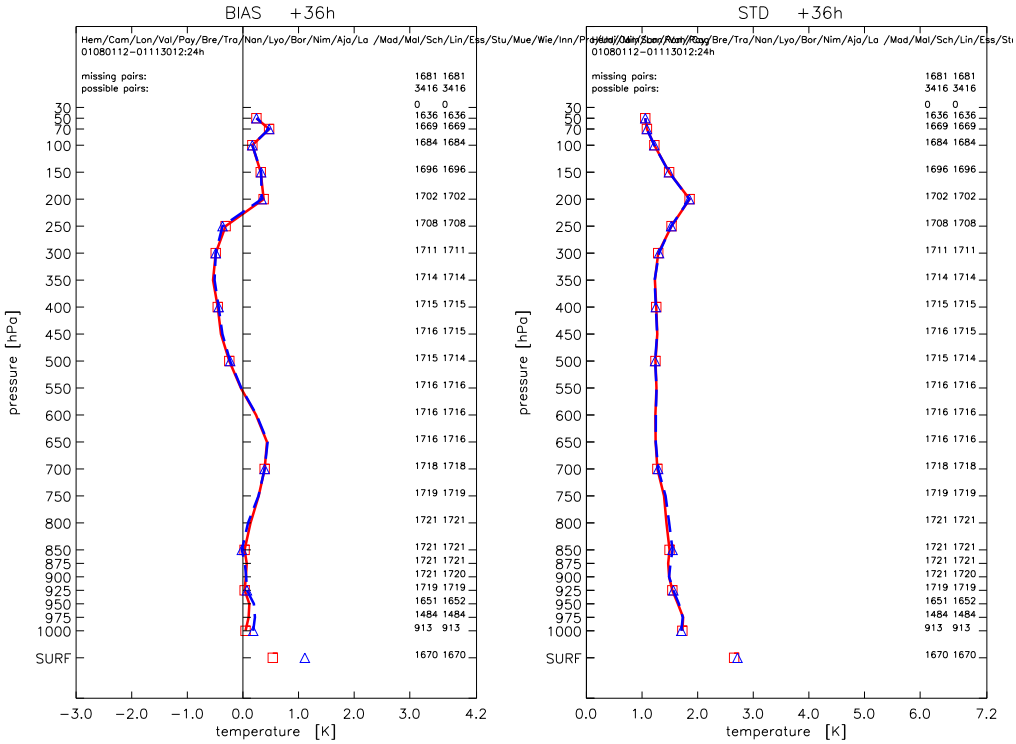

Figure 2: Mean error (BIAS, left) and standard deviation (STD, right) of temperature for verification time 12 UTC (+36h forecaste time). Time period: 14 August – 22 September 2001). Red line: operational aLMo without TKE, blue dashed line: aLMo with TKE; all soundings.

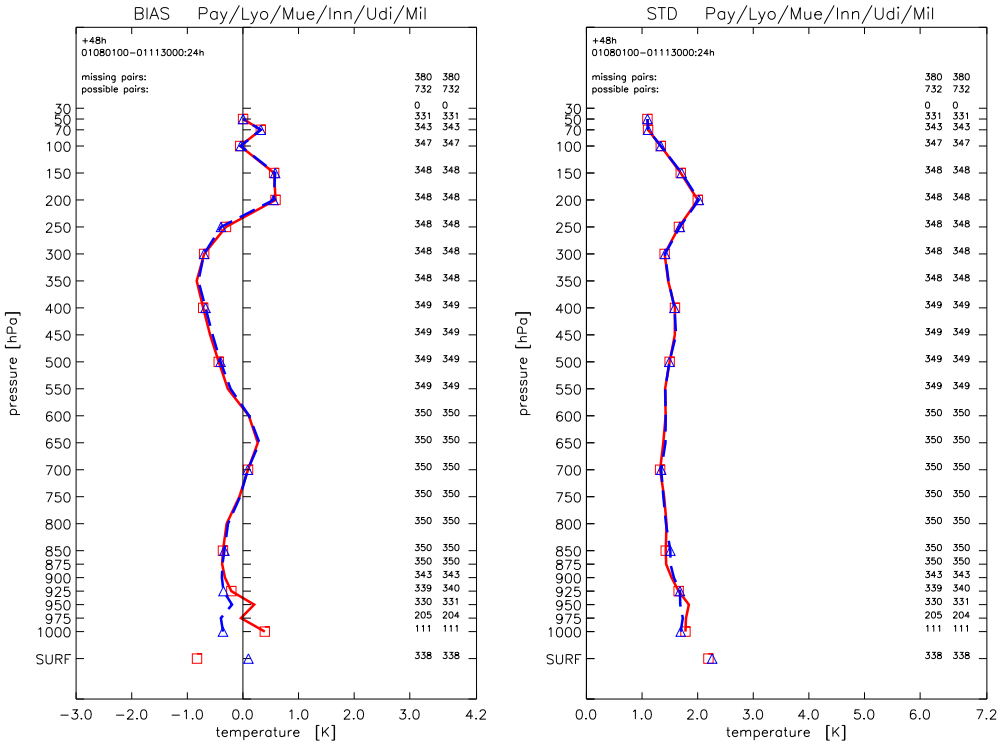

Figure 3: Mean error (BIAS, left) and standard deviation (STD, right) of temperature for verification time 12 UTC (+36h forecaste time). Time period: 14 August – 22 September 2001). Red line: operational aLMo without TKE, blue dashed line: aLMo with TKE; only soundings from the Alpine region.

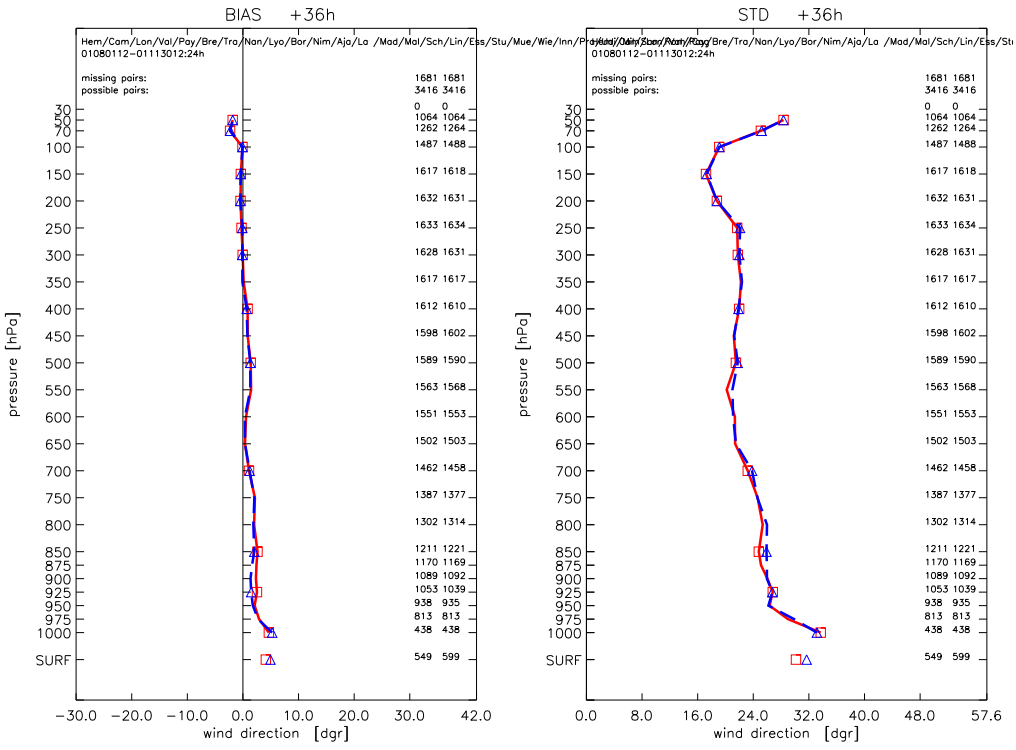

Figure 4: Mean error (BIAS, left) and standard deviation (STD, right) of wind direction for verification time 12 UTC (+36h forecaste time). Time period: 14 August – 22 September 2001). Red line: operational aLMo without TKE, blue dashed line: aLMo with TKE; all soundings.

2 Verification of Daily Cycle with ANETZ (for aLMo with/without TKE and LM-DWD)

Results for the three model-versions have been analysed and the differences compared to those obtained in earlier months (i.e. when LM-DWD run without the new TKE-scheme, i.e. same physics in all model-versions). In the following only differences that seem to be due to the new TKE-scheme will be discussed. The main results are (TKE vs no TKE):

2m-Dewpoint Depression

The mean diurnal variation for stations < 800m (Figure 5, bottom left) and for stations > 1500m (Figure, 5 bottom right) show the much more realistic diurnal amplitude with the new TKE-scheme. For the gridpoints in the mountains, there is a negative bias (too wet). There is a great difference at +0h between aLMo-TKE and aLMo-OPR, despite the fact that both model-versions have the same analysed fields from GME2LM. These big differences at +0h must come from the initialisation (?).

2m-temperature

The mean diurnal variation for stations < 800m (Figure 5 top left) and > 1500m (Figure 5 top right) show no improvement with TKE. The diurnal amplitude is a little bit larger (but this was already too large without TKE).

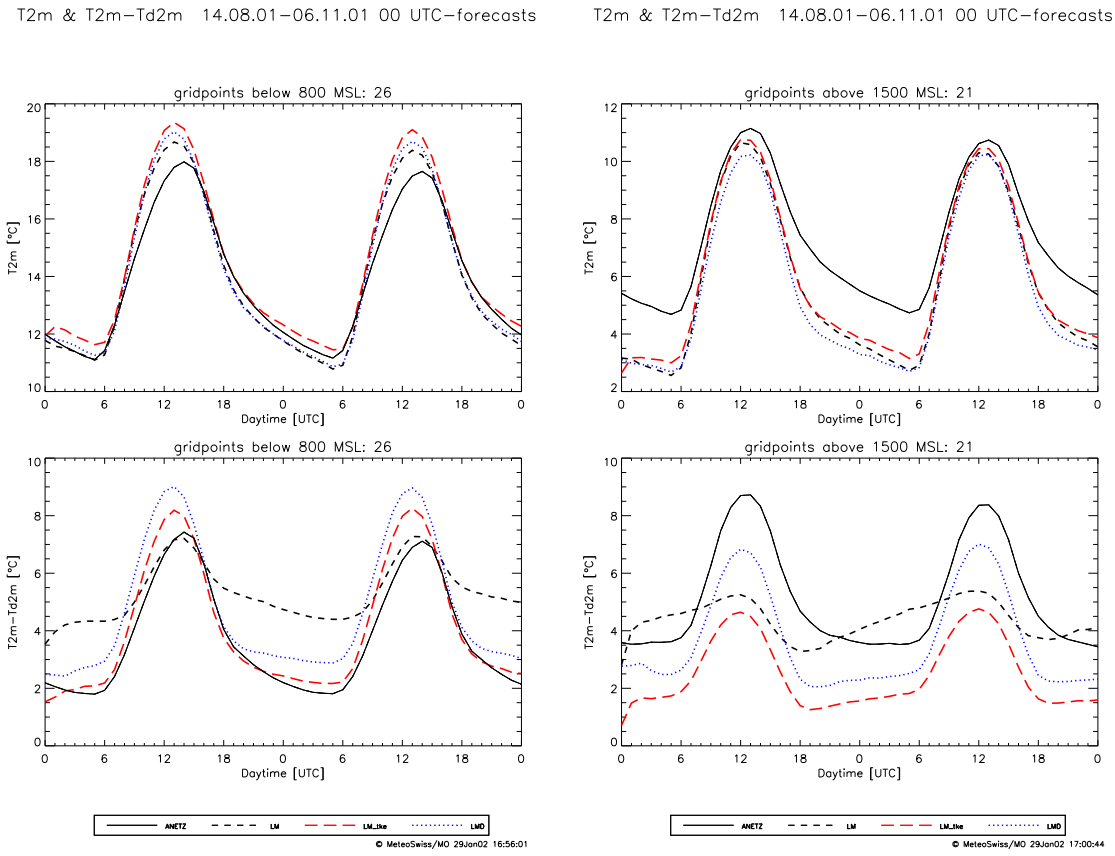

Figure 5: Mean diurnal variation of the 2-m temperature (top panel) and 2-m dew point depression (bottom panel) at ANETZ stations for the period 14 August – 6 November 2001. Left for stations below 800m, right for stations above 1500m. Full line: ANETZ observations. Black dashed line: operational aLMo. Red dashed line: aLMo with TKE. Blue dotted line: LM-DWD with TKE.

10m-wind

Figure 6 shows the mean diurnal variation of 10m-windspeed for those stations where 10m-wind direction was representative for SM-verification (i.e. no stations in the inner alpine valleys): upper part for gridpoints < 800 m, lower part for gridpoints > 1500 m. Verification of 10m-windspeed make sense only for gridpoints < 800m: the new TKE-scheme gives a more realistic diurnal amplitude, but higher values in daytime (i.e. a greater positive bias). On mountain gridpoints (> 1500 m) the windspeed should not be verified with obs (model windspeed much too reduced due to the PBL parametrisation), but the comparison of the windspeed for the 3 model-versions is interesting: there is a reduction by a factor of 3 with TKE (on the graphics for only 5 gridpoints where 10m-wind direction is representative). The reduction in 10m-wind speed is even of factor 5 (!) for all 21 gridpoints > 1500m corresponding to an ANETZ-station (not shown).

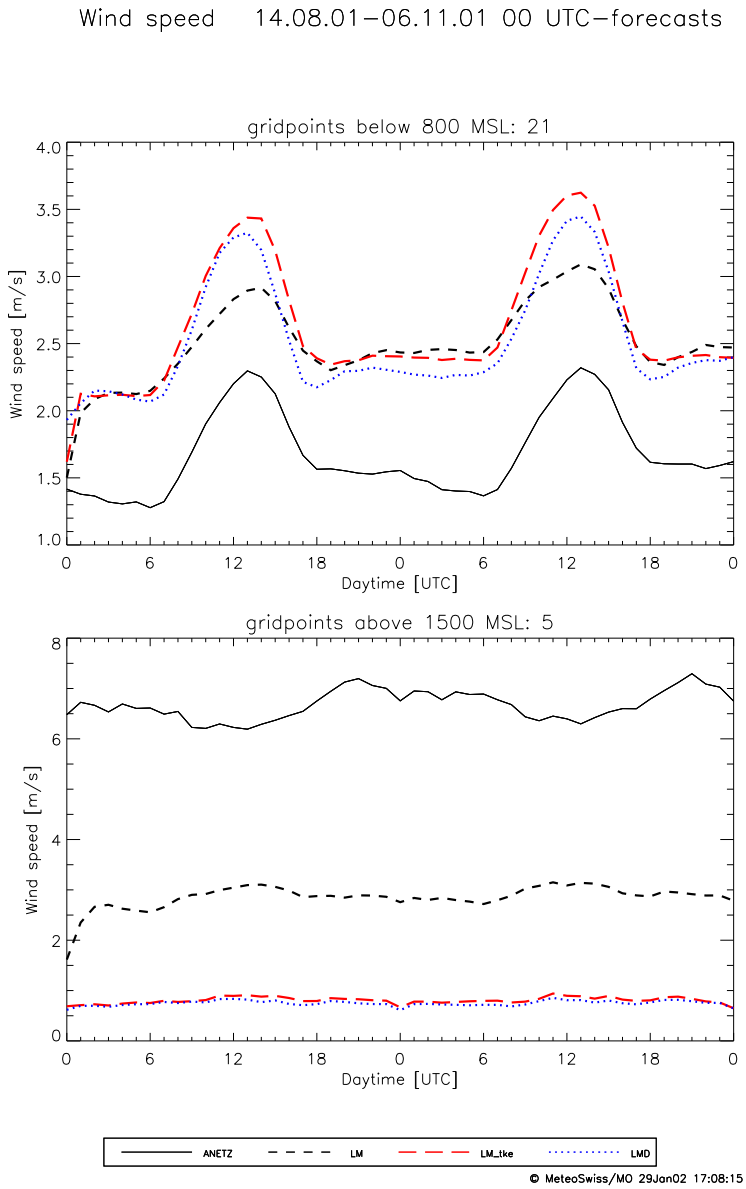

Figure 6: Mean diurnal variation of 10-m wind speed at ANETZ stations for the period 14 August – 6 November 2001. Top for stations below 800m, bottom for stations above 1500m. Full line: ANETZ observations. Black dashed line: operational aLMo. Red dashed line: aLMo with TKE. Blue dotted line: LM-DWD with TKE.

For 10m-wind direction there are some differences, but the explanation - with this little dataset (only observed 10m-wind speed > 3 m/s considered for the statistics) - is not obvious. Figure 4 shows the mean diurnal variation of 10m-wind direction for the representative stations (i.e. no stations in the inner alpine valleys). A longer verification period will be needed to interpret the differences. The differences between aLMo-TKE and aLMo-OPR for the gridpoints > 1500m was mainly obtained at the end of the period at locations over the Jura (October 2001).

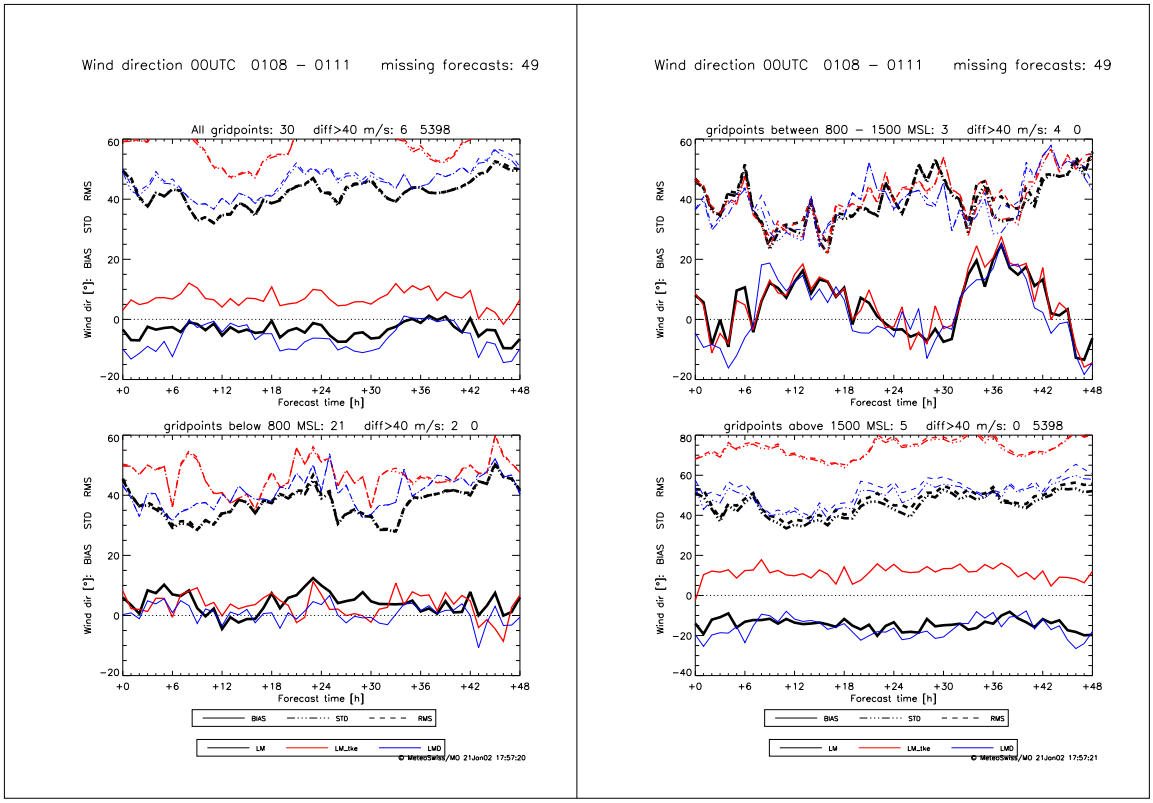

Figure 7: Mean diurnal variation of bias (full lines), standard deviation (dash-dotted lines) and rmse (dashed lines) of 10-m wind direction at ANETZ stations for the period 14 August – 6 November 2001. Black line: aLMo-operational. Red line: aLMo-TKE. Blue line: LM-DWD. Top left: all gridpoints. Bottom left: gridpoints below 800m. Top right: gridpoints between 800 and 1500m. Bottom right: gridpoints above 1500m.

Precipitation and total cloudiness

No significant differences between the runs with and without TKE can be noticed.

3 Summary

The verification results discussed above are summarized as:

- The new TKE-scheme shows a clear improvement in the diurnal amplitude for 2m-dewpoint (and 2m-dewpoint depression) and for 10m wind speed.
- The vertical profiles of humidity and temperature give a deterioration in the lower PBL.
- The other verified parameters show no (clear) differences (no improvement/no deterioration).

10 Collaboration and External Users of LM

All national weather services of COSMO are members of EUMETNET, the network of meteorological services within Europe. EUMETNET provides a framework to organize co-operative programmes between the Members in the various fields of basic meteorological activities such as observing systems, data processing, basic forecasting products, research and development, and training (*www.eumetnet.eu.org*). COSMO's activities are embedded in this network and are especially related to EUMETNET programmes such as MAP-NWS (Mesoscale Alpine Programme - National Weather Services) and EUCOS (EUMETNET Composite Observing System).

Since the 1st of January 2000, EUMETNET provides a Coordinator for the SRNWP (Short Range Numerical Weather Prediction) Group. Representatives of the NWP branches of European National Meteorological Services meet in this group on a yearly basis to organize co-operative activities in development of numerical atmospheric models. The present SRNWP-coordinator is J. Quiby from MeteoSwiss. Within the SRNWP Group, Lead Centres have been selected for different topics. The Lead Centres have the responsibility to organize intercomparisons, workshops and to ensure the flow of information between participants. DWD has taken the role as the Lead Centre for Nonhydrostatic Modelling (responsible for this LC is Jürgen Steppeler from DWD). For more information on SRNWP and its Lead Centres see *http://srnwp.cscs.ch*.

All COSMO partners are also members of EWGLAM (European Working Group on Limited Area Modelling). This group meets once a year to exchange information on the current status and on recent developments in high-resolution numerical weather prediction.

Another type of collaboration with other European meteorological services is via COST, an intergovernmental framework for European *Co-operation in the field of Scientific and Technical Research*, allowing the co-ordination of nationally funded research on an European level (for more information about COST see *www.netmaniacs.com/cost*).

10.1 International Projects

This section lists the current participation of COSMO partners in international research projects which are related to LM. This list will be updated in the forthcoming issues.

- **CLIWA-NET** *Cloud Liquid Water Network.*
  Type: EU-project with funding.
  DWD contribution: *Supply of special LM-output for intercomparison with observations and other models.*
  Information: www.knmi.nl/samenw/cliwa-net (with online results from LM)

- **COST 717** *Use of Radar Observations in Hydrological and NWP models.*
  Type: COST concerted research action
  MeteoSwiss contribution: *Chairmanship of COST 717 Action (A. Rossa).*
  DWD contribution: *Chairmanship of COST 717 Working Group 2: Using radar observations in parameterization and validation of atmospheric models (D. Frühwald).*
  MeteoSwiss contribution: *Assimilation of three-dimensional radar reflectivities into a nonhydrostatic NWP model.*
  DWD contribution: *Development of an on-line adjustment scheme.*
  Information: www.smhi.se/cost717

- **COST 716** *Exploitation of Ground-Based GPS for Climate and Numerical Weather Prediction Applications.*
  Type: COST concerted research action
  DWD contribution: *Validation of integrated water vapour from ground-based GPS observations and their assimilation in the LM of DWD.*
  Information: www.oso.chalmers.se/geo/cost716.html

- **EFFS** *An European Flood Forecasting System.*
  Type: EU-project with funding.
  DWD contribution: *Hindcasting of flood events, input to flood forecasting models, analysis of precipitation (24-h totals) based on rain gauge data and radar estimates.*
  Information: http://effs.wldelft.nl

- **ELDAS** *Development of an European Land Assimilation System to Predict Floods and Droughts.*
  Type: EU-project with funding.
  DWD contribution: *Design and application of a variational assimilation scheme.*
  Information: no homepage yet

- **EUROGRID** *Application Testbed for European GRID Computing.*
  Type: EU-project with funding.
  DWD contribution: *Implementation of a relocatable LM using the EUROGRID environment.*
  Information: www.eurogrid.org

- **SEAROUTES** *Advanced Decision Support for Shiprouting Based on Full-Scale Ship Specific Responses as well as Improved Sea and Weather Forecasts Including Synoptic, High Precision and Realtime Satellite Data*
  Type: EU-project with funding.
  DWD contribution: *a) Supply of LM-data over the Baltic Sea for the development of a high-resolution sea wave model at GKSS (Geesthacht); b) Supply of sea-state information of the Mediterranean sea wave model (MSM) for verification against Altimeter data and for driving ship response models.*
  Information: www.tu-berlin.de/fb10/MAT/searoutes

Furthermore, a number of activities of COSMO members are related to the *Mesoscale Alpine Project* (MAP). For more information, see the MAP homepage at *www.map.ethz.ch.*

10.2 National Projects and Collaboration

This section lists LM-related projects and collaboration of COSMO members on a national level. At present, the list is by no means complete. Please inform the editors on such activities, especially those with national funding, in order to get a more complete list in the next COSMO newsletter.

- **DWD/University of Bonn** *Use of Radar Information for Initialization of LM*
  Type: bilateral project, funded by DWD.

- **DWD/University of Bonn** *Special Investigations in Statistical Model Interpretation*
  Type: bilateral project, funded by DWD.

In autumn 2001, the German community on regional climate modelling decided to use the Lokal-Modell as a basis for a new regional climate model. The CLM (Climate Version of the LM) will be derived from the release 2.14 of LM. You find information on this modelling group and the related model developments at the CLM web-site *http://w3.gkss.de/CLM/index.html.*

10.3 External Users of LM

The source code of the LM-package is available free of charge for scientific and educational purposes to third parties outside COSMO. Such external users, however, must register and sign a special agreement with a COSMO meteorological service. For questions about the request and the agreement, please contact M. Capaldo (massimo.capaldo@iol.it) or D. Frühwald (dieter.fruehwald@dwd.de) from the COSMO Steering Committee.

Meanwhile, a number of universities and research institutes have received the model software. Once a year, there is a *User Workshop on Scientific Applications of the LM* organized by J. Steppeler at DWD (contact: juergen.steppeler@dwd.de, see also Section 7.4). There is, however, not always a feedback on the activities or on results and problems. Table 1 lists the current registered users of the LM (outside the COSMO group).

Table 1: ***Registered Scientific Users of LM outside COSMO***

Institution	**Research Activities**
Academy of Science, Hydrometeorological Institute, Bulgaria	unknown
Academy of Science, Institute for Physics of the Atmosphere, Prague, Czech Republic	Clouds and precipitation at high resolution
Alfred Wegener Institut, Bremerhaven, Germany	Cloud physics
Frontier Research, Institute for Global Change Research, Japan	Tests on time-splitting methods
German Aerospace Centre, Institute of Atmospheric Physics, Oberpfaffenhofen, Germany	Turbulence studies, model intercomparison
GKSS Research Centre Geesthacht, Germany	GEWEX cloud system studies, regional climate simulations
Institute for Tropospheric Research (IFT), Leipzig, Germany	Z-coordinate, turbulence studies
Konrad-Zuse Institut, Berlin, Germany	Scientific visualization
Meteorological Research Institute, Japan	Model comparison
Meteorological Research Institute, Korea	unknown
National Institute of Meteorology and Hydrology, Romania	Test simulations
Norwegian Meteorological Institute (DNMI), Oslo, Norway	Model intercomparison

Institution	**Research Activities**
Potsdam Institute for Climate Impact Research (PIK), Potsdam, Germany	Regional climate studies, low Mach-number dynamics
Swiss Institute of Technology (ETH), Zürich, Switzerland	Regional climate studies
Turkish State Meteorological Service, Turkey	Test simulations for coastal winds
University of Ljubljana, Slovenia	Latent heat nudging
University of Berlin, Germany	unknown
University of Bern, Switzerland	Land use and regional climate
University of Bonn, Germany	Physical initialization, statistical postprocessing regional evaporation and land use water resource management
University of Bremen, Germany	unknown
University of Cologne, Germany	unknown
University of Dresden, Germany	unknown
University of Frankfurt, Germany	Numerics and cloud physics
University of Hamburg, Germany	unknown
University of Hannover, Germany	Icing, atmosphere-surface interaction
University of Karlsruhe, Germany	Soil modelling, case studies
University of Leipzig, Germany	Cloud physics, hydrology
University of Ljubljana, Slovenia	Latent heat nudging
University of Munich, Germany	Model comparison, case studies
University of Trento, Italy	Numerics, shaved elements

References

Davies, H. C. and R. E. Turner, 1977: Updating prediction models by dynamical relaxation: An examination of the technique. *Quart. J. Roy. Meteor. Soc.*, 103, 225-245.

Doms, G., U. Schättler, 1999: The Nonhydrostatic Limited-Area Model LM (Lokal-Modell) of DWD. Part I: Scientific Documentation. Deutscher Wetterdienst (DWD), Offenbach. January 1999.

Doms, G., 2001: A scheme for monotonic numerical diffusion in the LM. *Cosmo Technical Report*, No.3 (available at www.cosmo-model.org).

Dudhia, J., 1993: A nonhydrostatic version of the Penn State / NCAR mesoscale model: Validation tests and simulation of an Atlantic cyclone and cold front. *Mon. Wea. Rev.*, 121, 1493-1513.

Gassmann, A., 2001: Filtering of LM-Orography. *COSMO Newsletter*, No.1, 71-78 (available at www.cosmo-model.org).

Hess, R., 2001: Assimilation of screen-level observations by variational soil moisture analysis. *Meteor. Atmos. Phys.*, 77, 155-166.

Jacobsen, I. and E. Heise, 1982: A new economic method for the computation of the surface temperature in numerical models. *Contr. Atmos. Phys.*, **55**, 128-141.

Kessler, E., 1969: On the distribution and continuity of water substance in the atmospheric circulations. *Meteor. Monogr.*, 10, No. 32, Amer. Met. Soc., 84pp.

Klemp, J. B. and R. Wilhelmson, 1978: The simulation of three-dimensional convective storm dynamics. *J. Atmos. Sci.*, 35, 1070-1096.

Lorenc, A. C., R. S. Bell and B. Macpherson, 1991: The Meteorological Office analysis correction data assimilation scheme. *Quart. J. Roy. Meteor. Soc.*, 117, 59-89.

Louis, J.-F., 1979: A parametric model of vertical eddy fluxes in the atmosphere. *Bound. Layer Meteor.*, **17**, 187-202.

Lynch, P., D. Girard and V. Ivanovici, 1997: Improving the efficiency of a digital filtering scheme. *Mon. Wea. Rev.*, **125**, 1976-1982.

Majewski, D., 1998: The new global icosahedral-hexagonal grid point model GME of the Deutscher Wetterdienst. *ECMWF Seminar on Numerical Methods in Atmospheric Models*, 1998.

Mellor, G. L. and T. Yamada, 1974: A hierarchy of turbulence closure models for planetary boundary layers. *J. Atmos. Sci.*, 31, 1791-1806.

Mellor, G. L. and T. Yamada, 1982: Development of a turbulence closure model for geophysical flow problems. *Rev. Geophys. and Space Phys.*, 20, 831-857.

Raschendorfer, M. and D. Mironov, 2001: Evaluation of empirical parameters of thenew LM surface-layer parameterization scheme. Results from numerical experiments including the soil-moisture analysis. *Cosmo Technical Report*, No.1 (available at www.cosmo-model.org).

Raymond, W. H., 1988: High-order low-pass implicit tangent filters for use in finite area calculations. *Mon. Wea. Rev.*, **116**, 2132-2141.

Ritter, B. and J. F. Geleyn, 1992: A comprehensive radiation scheme for numerical weather prediction models with potential applications in climate simulations. *Mon. Wea. Rev.*, **120**, 303-325.

Schraff, C., 1996: Data assimilation and mesoscale weather prediction: A study with a forecast model for the Alpine region. Publication No. 56, Swiss Meteorological Institute.

Schraff, C., 1997: Mesoscale data assimilation and prediction of low stratus in the Alpine region. *Meteorol. Atmos. Phys.*, **64**, 21-50.

Schrodin, R. and E. Heise, 2001 : The Multi-Layer Version of the DWD Soil Model TERRA_LM. *Cosmo Technical Report*, No.2 (available at www.cosmo-model.org).

Skamarock, W. C. and J. B. Klemp, 1992: The stability of time-split numerical methods for the hydrostatic and the nonhydrostatic elastic equations. *Mon. Wea. Rev.*, **120**, 2109-2127.

Sommeria, G. and J. W. Deardorff, 1977: Subgrid-scale condensation in models of non-precipitating clouds. *J. Atmos. Sci.*, 34, 344-355.

Stauffer, D. R. and N. L. Seaman, 1990: Use of four-dimensional data assimilation in a limited-area mesoscale model. Part I: Experiments with synoptic-scale data. *Mon. Wea. Rev.*, 118, 1250-1277.

Stauffer, D. R. and N. L. Seaman, 1994: Multiscale four-dimensional data assimilation. *J. Appl. Meteor.*, 33, 416-434.

Thomas, S., C. Girard, G. Doms and U. Schättler, 2000: Semi-implicit scheme for the DWD Lokal-Modell. *Meteorol. Atmos. Phys.*, **75**, 105-125.

Tiedtke, M., 1989: A comprehensive mass flux scheme for cumulus parameterization in large-scale models. *Mon. Wea. Rev.*,**117**, 1779-1799.

Wicker, L. and W. Skamarock, 1998: A time-splitting scheme for the elastic equations incorporating second-order Runge-Kutta time differencing. *Mon. Wea. Rev.*, **126**, 1992-1999.

Appendix A: The GRIB Binary Data Format used for LM I/O

All input and output arrays of the LM and of the preprocessor programs providing interpolated initial conditions and the boundary values are stored in a compressed binary data format called GRIB-code. GRIB means "gridded binary" and is designed for the international exchange of processed data in the form of grid-point values expressed in binary form.

The GRIB-code is part of the FM-system of binary codes of the World Meteorological Organization (WMO). Currently, we use Edition 1 of the GRIB-code with number FM 92-VIII. For coding details, see the *Manual on Codes, International Codes, Volume 1.2* of WMO (WMO Publication No. 306, 1995). In this section, we describe only the basic features of the GRIB code which are relevant for the I/O of the LM-system.

A.1 Code Form

Each GRIB-coded record (analysis or forecast field) consists of a continuous bit-stream which is made up of a sequence of octets (1 octet = 8 bits). The representation of data by means of series of bits is independent of any particular machine representation. The octets of a GRIB messsage are grouped in sections (see Table 1, where the length of the record and the length of the sections are expressed in octets. Section 0 has a fixed length of 4 octets and section 5 has a fixed length of 4 octets. Sections 1, 2, 3 and 4 have a variable length which is included in the first three octets of each section.

Table 1: *Form of GRIB-code*

Section number	Name	Contents
0	Indicator Section	"GRIB"; length of record; GRIB edition number
1	Product Definition Section	Length of section; identification of the coded analysis/forecast field
2	Grid Description Section (optional)	Length of section; grid geometry, as necessary
3	Bit-map Section (optional)	Length of section; the bit per grid-point, placed in suitable sequence
4	Binary Data Section	Length of section; data values
5	End Section	7777

Octets are numbered 1, 2, 3, etc., starting at the beginning of each section. Bit positions within octets are referred to as bit 1 to 8, where bit 1 is the most significant bit and bit 8 is the least significant bit. Thus, an octet with only bit 8 set to 1 would have the integer value 1.

A.2 Indicator and End Section

The Indicator Section has a fixed length of 8 octets. The first four octets shall always be character coded as "GRIB" (according to the CCITT International Alphabet No.5). The remainder of the section shall contain the length of the entire GRIB-record (including the Indicator Section) expressed in binary form over the left-most 3 octets (i.e. 24 bits in octet 5-7), followed by the GRIB edition number (currently 1), in binary, in the remaining octet 8.

The End Section has a fixed length of 4 octets. These octets are character coded as '7777' according to the International Alphabet No.5.

Thus, the beginning and the end of a GRIB-record can be identified by the character coded words "GRIB" and "7777". All other octets included in the code represent data in binary form. Each input or output array defined on the rotated lat/lon grid of the LM (e.g the surface pressure or the temperature at a specified model level) is coded as a GRIB-record. Various such records can be combined in a single GRIB-file.

A.3 Product Definition Section

The Product Definition Section (PDS) contains the necessary information to identify the binary coded field contained in the GRIB-record. The most important octet in this section is the indicator of the meteorological parameter. The indicator relates a specific meteorological element to an integer number. This indicator number is also referred to as GRIB-number or element-number and is defined in a separate code table. More than one indicator code tables may be used in GRIB-code. Thus, one can have the same element-number but different code table numbers for various fields. The element-numbers and code tables used by LM are described below.

The program `grbin1` of the supplementary GRIB-library `griblib` of the LM-system can be used to decode GRIB binary code. Besides the decoded data set, this program does also retrieve the contents of the octets of the PDS in an integer array `ipds`. To illustrate the structure of the PDS, Table 2 shows the contents of the product definition section of a binary coded LM output array, the total cloud cover (CLCT). The GRIB-record for this field is valid for 28.10.1998 00 UTC + 11 h and was created at 28.10.1998 7.04 UTC by an LM forecast.

Octet 4 (ipds(2)) assigns a table number to the parameter indicator number given in octet 9. Currently, we use 3 additional code tables besides the WMO-table (see Table 3). A full list of variables defined by these tables is available from DWD.

Octet 6 (ipds(4)) indicates the process identification number which is allocated by the originating centre. Currently, we use only two different process numbers for forecasts or analyses (see Table 4).

The level or layer for which the data are included in the GRIB-record is coded in octets 10 - 12 (ipds(8) - ipds(9)), where octet 10 indicates the type of level and octets 11 and 12 indicate the value of this level. Table 5 shows the code figures used for LM. For reserved values, or if not defined, octets 11 and 12 shall contain zero.

All 3-D variables of LM except the vertical velocity are defined on terrain-following main levels. In GRIB, these main levels are coded as level-type 110: hybrid layers between two adjacent hybrid levels - which are the LM half levels, i.e the layer interfaces. In this case, octet 11 contains the level index of the upper half level and octet 12 contains the level index of the lower half level. The vertical velocity and the height of the half levels are coded as level type 109: hybrid levels, i.e. the LM half levels. In this case, octet 11 contains zero and octet 12 contains the level index of the model half level. Pressure levels (ipds(8) = 100) and height levels (ipds(8) = 105) are used when the interpolation from model to specified p- or z-surfaces is switched on for model output.

Table 2: ***Contents of the Product Definition Section***

array ipds(i)	Octet number	Contents of PDS Value	Remarks
1	1-3	54	Length of the PDS (in octets)
2	4	2	Version number of the GRIB indicator table (see Table 3)
3	5	78	Identification of originating/generating centre (DWD has WMO number 78)
4	6	132	Generating process identification number (allocated by originating centre, see Table 4)
5	7	255	Number of grid used - from catalogue defined by the originating centre. Octet 7 set to 255 indicates a non-cataloged grid, in which case the grid is defined in the grid description section.
6	8	128	Block-flag; the value 128 indicates that the grid description section is included.
7	9	71	Indicator of parameter (element number) from GRIB-table in ipds(2); see Section 3.7
8	10	1	Indicator of type of level, see Table 5
9-10	11-12	0	Value of level (height, pressure, etc.) for which the data are included (see Table 5)
11	13	98	Year (start time of forecast; analysis time)
12	14	10	Month (start time of forecast; analysis time)
13	15	28	Day (start time of forecast; analysis time)
14	16	0	Hour (start time of forecast; analysis time)
15	17	0	Minute (start time of forecast; analysis time)
16	18	1	Indicator of unit of time range (see Table 6)
17	19	11	P1 - period of time (number of time units);
			time units given by octet 18 (ipds(16))
18	20	0	P2 - period of time (number of time units);
			time units given by octet 18 (ipds(16))
19	21	0	time range indicator (see Table 7)
20	22-23	0	Number of forecasts included in average, when octet 21 (ipds(19)) indicates an average or accumulation of forecasts (or analyses); otherwise set to zero.
21	24	0	Number of forecasts missing from averages or accumulations.
22	25	20	Century of reference time of data given by octets 13- 17
23	26	255	Sub-centre identification, national use
24	27-28	0	Units decimal scale factor (D)
25-36	29-40	0	Reserved: need not to be present
37	41	254	Octets 41-54 are reserved for the originating centre. The integer value 254 indicates that additional data follow. We use this part as follows:
38	42	0	not used
39	43-45	0	not used
40	46	0	not used
41	47	0	Additional indicator for a GRIB element number
42	48	98	Year of production of GRIB-record
43	49	98	Month of production of GRIB-record
44	50	11	Day of production of GRIB-record
45	51	2	Hour of production of GRIB-record
46	52	0	Minute of production of GRIB-record
47	53-54	1	Version number, currently 1 for LM

Table 3: *GRIB-tables for parameter (element) indicator number*

Version number of GRIB-table; ipds(2)	**Comment**
2	WMO-table of indicator parameters
201	national table of DWD for internal use
202	national table of DWD for internal use
203	national table of DWD for internal use

Table 4: *Process identification numbers*

process id-number; ipds(4)	**Comment**
131	LM-analyses from data assimilation cycle
132	LM-forecasts and initialized analyses

Table 5: *Types of fixed levels or layers used by LM*

level type ipds(8)	**Meaning**	**ipds(9)**	**ipds(10)**
1	Ground or water surface	0	0
2	Cloud base level	0	0
3	Level of cloud tops	0	0
4	Level of $0°C$ isotherm	0	0
8	Top of atmosphere	0	0
100	Pressure (isobaric) level	0	Pressure in hPa
102	Mean sea level	0	0
103	Specified height above mean sea level	0	Height in m
105	Specified height level above ground	0	Height in m
109	Hybrid level (half levels)	0	Level number (k)
110	Hybrid layer (main level) between two hybrid levels	Level number of top (k)	Level number of bottom (k+1)
111	Depth below land surface	0	Depth in cm
112	Layer between two depths below land surface	Depth of upper surface in cm	Depth of lower surface in cm

Octets 13-17 contain the reference time of the data: the start of a forecast, the time for which an analysis is valid or the start of an averaging or accumulation period. The year of the century is coded in octet 13 and the century (100 years) in octet 25. For a reference time within the year 2000, octet 13 will contain the integer value 100 and octet 25 will contain the integer value 20.

The time or time interval for which the data are valid with respect to the reference time is coded in octets 18-21 (ipds(16)-ipds(19)). Octets 19 and 20 contain two periods of time, P1 and P2. The units of the values of P1 and P2 are defined in octet 18. Currently, we use hours as the time unit, but other values may be more appropriate for special applications of the model as the maximum integer number in an octet is 256. Thus, for long-term climate runs or short-term cloud simulations, other time units must be chosen. The WMO code-table for the unit of time in P1 and P2 is given in Table 6.

Table 6: *Code table for unit of time*

ipds(16)	Meaning	ipds(16)	Meaning	ipds(16)	Meaning
0	Minute	5	Decade	11	6 hours
1	Hour	6	Normal	12	12 hours
2	Day	7	Century	13-253	Reserved
3	Month	8-9	Reserved	254	Second
4	Year	10	3 hours		

The meaning of the time period P1 in octet 19 (ipds(17)) and of the time period P2 in octet 20 (ipds(18)) - given in the units coded in octet 18 - depends on the time-range indicator, which is contained in octet 21 (ipds(19)). The WMO code-table allows for a large number of indicators including averages and accumulation over a number of forecasts and analyses. For the LM-system, we use only a few standard indicators as shown in Table 7.

Table 7: *Time range indicators used by LM*

ipds(19)	Meaning
0	Forecast product valid for reference time + P1 (if P1 > 0) or uninitialized analysis product valid for reference time (P1 = 0)
1	initialized analysis product valid for reference time (P1 = 0)
2	Product with a valid time ranging between reference time + P1 and reference time + P2
3	Average from reference time + P1 to reference time + P2
4	Accumulation from reference time + P1 to reference time + P2; product valid for reference time + P2

A.4. Grid Description Section

Section 2 of a GRIB-record, the grid description section GDS, contains all information about the geometry of the grid on which the data are defined. For all input and output files of the LM, this section is coded completely for every field contained in the file. The program `grbin1` of the supplementary GRIB-library `griblib` retrieves the contents of the GDS in an integer array `igds`.

The contents of the grid description section of an LM GRIB-record is illustrated in Table 8 for the model domain used operationally at DWD. The octets corresponding to the integer array `igds` are numbered relative to this section.

Table 8: ***Contents of the Grid Description Section***

array igds(i)	Octet number	Contents of GDS Value	Meaning
1	1-3	202	Length of GDS (in octets) including the vertical coordinate parameters. (here for $ke = 35$ layers, i.e. $ke + 1 = 36$ half levels)
2	4	40	NV: Number of vertical coordinate parameters (four base state parameters + $(ke + 1)$ values of the vertical coordinates of the half levels)
3	5	43	PV: Location (octet number) of the list of vertical coordinate parameters
4	6	10	Data representation type according to WMO code-table 6; '10' assigns a rotated latitude/longitude grid
5	7-8	325	Number of gridpoints in 'zonal' direction
6	9-10	325	Number of gridpoints in 'meridional' direction
7	11-13	-17000	Rotated latitude of the first gridpoint in millidegrees
8	14-16	-12500	Rotated longitude of the first gridpoint in millidegrees
9	17	0	Resolution flag according to WMO code-table 7; '0' means that the grid spacing is not given
10	18-20	3250	Rotated latitude of the last gridpoint in millidegrees
11	21-23	7750	Rotated longitude of the last gridpoint in millidegrees
12	24-25	0	Longitudinal direction increment (grid spacing in λ-direction, not given)
13	26-27	0	Meridional direction increment (grid spacing in ϕ-direction, not given)
14	28	64	Scanning mode flag according to WMO code-table 8 '64' means that points scan in +i and +j direction and adjacent points in i-direction are consecutive
15-19	29-32	0	Reserved (set to zero)
20	33-35	-32500	Geographical latitude of rotated southern pole in millidegrees
21	36-38	10000	Geographical longitude of rotated southern pole in millidegrees
22	39-42	0	Angle of rotation
26-65	43-202	.....	List of vertical coordinate parameters, each packed on 4 octets (length = 4 x NV octets). first the three parameters defining the base state: `igds(26)=p0sl`, `igds(27)=t0sl`, `igds(28)=dt0lp`; then the parameter `igds(29)=vcflat` of the hybrid coordinate system; and finally the $ke + 1$ values of the vertical coordinate $\eta(k)$ of the model half levels for $k = 1, \ldots, ke + 1$ in `igds(30)`,..., `igds(65)`.

Appendix B: Available LM Output Fields

This appendix summarizes the GRIB parameter indicators (element numbers), the table numbers and the dimensions of the direct model output variables. Any changes will be updated in the next COSMO Newsletter.

B.1 General Remarks

For direct model output, we distinguish between so-called *multi-level fields* which are defined on model layers or levels or on fixed pressure or height levels, and *single level fields* which are defined at the surface or on another fixed level.

The fields contained in the model output GRIB-files can be freely chosen by the user: The names of the model variables to be written out have to be specified on the following NAMELIST input character arrays:

- `yvarml` for output on the model grid and for single level data,
- `yvarpl` for output on constant pressure levels
- `yvarzl` for output on constant height levels.

If latter two variables are empty, the model-internal interpolation to pressure and height levels is omitted. If they are set, the values of the corresponding pressure and height levels can be specified by the NAMELIST input arrays `plev` and `zlev`. By default, some multi-level variable are interpolated to 10 pressure levels and 4 height levels:

- p-levles: 1000, 950, 850, 700, 600, 500, 400, 300, 250, 200 hPa.
- z-levles: 1000, 2000, 3000, 5000 m (above sea level).

B.2 Element and Table Numbers used by LM

The name of an input/output field is specified as a CHARACTER variable (in capital letters, names must be 8 characters long, filled with blanks) in NAMELIST input. The model then relates this name internally to a corresponding GRIB element number and table number as well as the corresponding global model variable (which has usually the same name but with small letters). However, some names of output variables are not related to a globally defined model variable. In these cases, the output array is calculated locally only at the output time step.

Table 1 shows the GRIB-element numbers (ee) and table numbers (tab) for the multi-level fields available for LM output files. The level-types (lty) and the corresponding values in octet 11 (lvt) and octet 12 (lv) as well as the physical units (unit) are also included. For variables with level-types 109 and 110, the integer level numbers denoted by k (and k+1) are stored in octets 11 and 12. For pressure levels the constant pressure value in hPa is stored in octet 12 (denoted by pres), and for height levels the constant height level in m above sea level (denoted by z) is stored in octet 12.

Some of the multi-level fields in Table 1 can only be put on the output list if certain parameterization schemes are switched on. These variables are denoted as optional fields. All variables on the list for constant pressure and constant height levels are in the default output list.

Table 1: ***Multi-level fields of LM GRIB-output***

Name	Meteorological Element	ee	tab	lty	lvt	lv	unit
Multi-level fields on model layers/levels k							
U	Zonal wind component (rotated grid)	33	2	110	k	k+1	m/s
V	Meridional wind component (rotated grid)	34	2	110	k	k+1	m/s
W	Vertical wind component	40	2	109	-	k	m/s
P	Pressure	1	2	110	k	k+1	Pa
PP	Pressure perturbation	139	201	110	k	k+1	Pa
T	Temperature	11	2	110	k	k+1	K
QV	Specific humidity	51	2	110	k	k+1	kg/kg
QC	Specific cloud water content	31	201	110	k	k+1	kg/kg
CLC	Fractional cloud cover	29	201	110	k	k+1	%
HHL	Height of half levels (i.e. layer interfaces) constant with time, written only at t=0	8	2	109	-	k	m
Optional multi-level fields on model layers/levels k							
QI	Specific cloud ice content	33	201	110	k	k+1	kg/kg
TKE	Specific turbulent kinetic energy	152	201	109	-	k	m^2/s^2
TKVM	Turbulent diffusion coefficient for vertical momentum transport	153	201	109	-	k	m^2/s
TKVH	Turbulent diffusion coefficient for vertical heat transport	154	201	109	-	k	m^2/s
Multi-level fields interpolated on pressure levels pres (in hPa)							
U	Zonal wind component (rotated grid)	33	2	100	-	pres	m/s
V	Meridional wind component (rotated grid)	34	2	100	-	pres	m/s
OMEGA	Vertical motion	39	2	100	-	pres	Pa/s
T	Temperature	11	2	100	-	pres	K
RELHUM	Relative humidity	52	2	100	-	pres	%
GPH	Geopotential	6	2	100	-	pres	m^2/s^2
Multi-level fields interpolated on height levels z (in m)							
U	Zonal wind component (rotated grid)	33	2	103	-	z	m/s
V	Meridional wind component (rotated grid)	34	2	103	-	z	m/s
W	Vertical wind component	40	2	103	-	z	m/s
T	Temperature	11	2	103	-	z	K
P	Pressure	1	2	103	-	z	Pa
RELHUM	Relative humidity	52	2	103	-	z	%

Table 2 shows the GRIB-element numbers (ee) and table numbers (tab) for the single-level forecast fields available for LM output files. As in the previous table, the level-types (lty) and the corresponding values in octet 11 (lvt) and octet 12 (lv) as well as the physical units (unit) of the fields are also included. See Table 5 in Appendix A for the units of the numbers stored in lvt and lv for the corresponding level-type.

Table 2: ***Single-level fields of LM GRIB-output***

Name	Meteorological Element	ee	tab	lty	lvt	lv	unit
Single-level fields: valid at output time							
PS	Surface pressure	1	2	1	-	-	Pa
PMSL	Mean sea level pressure	2	2	102	-	-	Pa
U_10M	Zonal 10m-wind	33	2	105	-	10	m/s
V_10M	Meridional 10m-wind	34	2	105	-	10	m/s
T_2M	2m-temperature	11	2	105	-	2	K
TD_2M	2m-dewpoint temperature	17	2	105	-	2	K
T_G	Temperature at the interface surface-atmosphere	11	2	1	-	-	K
T_SNOW	Temperature of snow surface (surface temperature if no snow)	203	201	1	-	-	K
T_S	Temperature below snow (surface temperature if no snow	85	2	111	-	0	K
T_M	Temperature at the bottom of first soil layer	85	2	111	-	9	K
QV_S	Specific humidity at the surface	51	2	1	-	-	kg/kg
W_SNOW	Water content of snow	65	2	1	-	-	kg/m^2
W_I	Water content of interception store	200	201	1	-	-	kg/m^2
W_G1	Water content of upper soil layer	86	2	112	0	10	kg/m^2
W_G2	Water content of middle soil layer	86	2	112	10	100	kg/m^2
TCM	Turbulent transfer coefficient for momentum at the surface	170	201	1	-	-	-
TCH	Turbulent transfer coefficient for heat and moisture at the surface	171	201	1	-	-	-
Z0	Roughness length (land and water)	83	2	1	-	-	m
ALB	Surface albedo for shortwave radiation	84	2	1	-	-	%
CLCT	Total cloud cover	71	2	1	-	-	%
CLCH	High cloud cover (0 - 400 hPa)	75	2	1	-	-	%
CLCM	Middle cloud cover (400-800 hPa)	74	2	1	-	-	%
CLCL	Low cloud cover (800hPa-surface)	73	2	1	-	-	%
CLCT_MOD	Total cloud cover (modified for graphics)	204	203	1	-	-	-
CLDEPTH	Normalized cloud depth (modified for graphics)	203	203	1	-	-	-
HTOP_DC	Top height of dry convection (height above mean sea level)	82	201	1	-	-	m
HZEROCL	Height of $0°C$ isotherm (above mean sea level)	84	201	1	-	-	m
MFLX_CON	Massflux at convective cloud base	240	201	1	-	-	kg/m^2s
CAPE_CON	Convective available potential energy	241	201	1	-	-	J/kg
QCVG_CON	Moisture convergence below convective cloud base	242	201	1	-	-	1/s
TKE_CON	Convective turbulent kinetic energy	243	201	1	-	-	J/kg
IWATER	Vertically integrated total water	41	201	1	-	-	kg/m^2
IWV	Vertically integrated water vapour	54	2	1	-	-	kg/m^2

Name	Meteorological Element	ee	tab	lty	lvt	lv	unit
Single-level fields: Accumulated since start of the forecast							
RAIN_GSP	Amount of grid-scale rain	102	201	1	-	-	kg/m^2
SNOW_GSP	Amount of grid-scale snow	79	2	1	-	-	kg/m^2
RAIN_CON	Amount of convective rain	113	201	1	-	-	kg/m^2
SNOW_CON	Amount of convective snow	78	2	1	-	-	kg/m^2
TOT_PREC	Total precipitation amount	61	2	1	-	-	kg/m^2
RUNOFF_S	Surface water run-off	90	2	112	0	10	kg/m^2
RUNOFF_G	Ground water run-off	90	2	112	10	100	kg/m^2
IDIV_HUM	Vertically integrated divergence of specific humidity	42	201	1	-	-	kg/m^2
AEVAP_S	Accumulated flux of surface moisture	57	2	1	-	-	kg/m^2
Single-level fields: Averaged over the forecast period							
AUMFL_S	Surface u-momentum flux	124	2	1	-	-	N/m^2
AVMFL_S	Surface v-momentum flux	125	2	1	-	-	N/m^2
ASHFL_S	Surface sensible heat flux	122	2	1	-	-	W/m^2
ALHFL_S	Surface latent heat flux	121	2	1	-	-	W/m^2
ASOB_S	Solar radiation budget at the earth surface	111	2	1	-	-	W/m^2
ASOB_T	Solar radiation budget at the top of the atmosphere	113	2	8	-	-	W/m^2
ATHB_S	Thermal radiation budget at the earth surface	112	2	1	-	-	W/m^2
ATHB_T	Thermal radiation budget at the top of the atmosphere	114	2	8	-	-	W/m^2
APAB_S	Budget of photosynthetic active radiation at the earth surface	5	201	1	-	-	W/m^2
Single-level fields: Extreme values over certain time intervals							
TMIN_2M	Minimum of 2m-temperature	16	2	105	-	2	K
TMAX_2M	Maximum of 2m-temperature	15	2	105	-	2	K
VMAX_10M	Maximum of 10m-wind speed	187	201	105	-	10	m/s
HTOP_CON	Top height of convective clouds (above mean sea level)	69	201	3	-	-	m
HBAS_CON	Base height of convective clouds (above mean sea level)	68	201	2	-	-	m
TOP_CON	Main-level index of convective cloud top	73	201	1	-	-	-
BAS_CON	Half-level index of convective cloud base	72	201	1	-	-	-
Single-level fields: Constant and climatological fields							
FIS	Geopotential of earth surface	6	2	1	-	-	m^2/s^2
HSURF	Geometrical height of surface	8	2	1	-	-	m
FR_LAND	Land fraction of a grid area	81	2	1	-	-	-
SOILTYP	Soil texture for land fraction (key number 1-8, over water =9)	57	202	1	-	-	-
PHI	Geographical latitude	114	202	1	-	-	° N
RLA	Geographical longitude	115	202	1	-	-	° E
PLCOV	Fractional plant cover	87	2	1	-	-	-
LAI	Leaf area index of vegetation	61	2	1	-	-	-

Name	Meteorological Element	ee	tab	lty	lvt	lv	unit
ROOTDP	Root depth of vegetation	62	202	1	-	-	m
FC	Coriolis parameter	113	202	1	-	-	s^{-1}
T_CL	Temperature of the lowest soil layer (climatological value)	85	2	111	-	36	K
W_CL	Water content of the lowest soil layer (climatological value)	86	2	112	100	190	kg/m^2
VIO3	Vertically integrated ozone	65	202	1	-	-	Pa O3
HMO3	Height of ozone maximum	64	202	1	-	-	Pa

All variables required on the input and boundary data files use also the corresponding GRIB table and element numbers from the above tables. The preprocessor programs to interpolate initial and/or boundary conditions to the LM-grid require the GRIB-files containing the external parameter data sets. The table and element numbers of the external parameter fields are shown in table 3.

Table 3: ***Single-level fields in the LM external parameter files***

Name	Meteorological Element	ee	tab	lty	lvt	lv	unit
FIS	Geopotential of earth surface	6	2	1	-	-	m^2/s^2
HSURF	Geometrical height of surface	8	2	1	-	-	m
FR_LAND	Land fraction of a grid area	81	2	1	-	-	-
Z0	Roughness length (land and water)	83	2	1	-	-	m
SOILTYP	Soil texture for land fraction (key number 1-8, over water =9)	57	202	1	-	-	-
PHI	Geographical latitude	114	202	1	-	-	° N
RLA	Geographical longitude	115	202	1	-	-	° E
PLCOV_V	Plant cover, vegetation period	67	202	1	-	-	%
PLCOV_V	Plant cover, rest period	68	202	1	-	-	%
LAI_V	Leaf area index, vegetation period	69	202	1	-	-	-
LAI_R	Leaf area index, rest period	70	202	1	-	-	-
ROOTDP	Root depth of vegetation	62	202	1	-	-	m

Appendix C: List of COSMO Newsletters and Technical Reports

All Newsletters and Technical Reports are available for download from the COSMO Website: www.cosmo-model.org.

COSMO Newsletters

Newsletter No.1, February 2001.

Newsletter No.2, February 2002.

COSMO Technical Reports

No. 1, Dmitrii Mironov and Matthias Raschendorfer (2001): *Evaluation of Empirical Parameters of the New LM Surface-Layer Parameterization Scheme. Results from Numerical Experiments Including the Soil Moisture Analysis.*

No. 2, Reinhold Schrodin and Erdmann Heise (2001): *The Multi-Layer Version of the DWD Soil Model TERRA_LM.*

No. 3, Günther Doms (2001): *A Scheme for Monotonic Numerical Diffusion in the LM.*